Deformation and Yield of Polymer Thin Films in Confined Geometries

A thesis presented to the University of Dublin, Trinity College for the degree of

Doctor of Philosophy in Physics

By

Owen Brazil

Under the supervision of Prof. Graham Cross

2019

Declaration

I declare that this thesis has not been submitted as an exercise for a degree at this or any other university and it is entirely my own work.

I agree to deposit this thesis in the University's open access institutional repository or allow the library to do so on my behalf, subject to Irish Copyright Legislation conditions of use and acknowledgement.

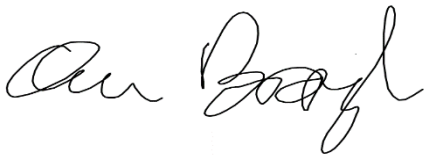

Owen Brazil – November 2018

Abstract

Polymer thin film mechanics represents a hugely promising field of research. Due to their versatility and ease of fabrication, polymer films and coatings rank among the most ubiquitous systems in all of nanotechnology. The ability to correctly characterise and mechanically pattern such small volumes of material is a significant step towards the development of the next generation of organic nanomechanical systems. In this work, the deformation and yield of polymer films is studied through a series of flat punch indentation and imprint experiments, where the film material becomes geometrically confined beneath features whose width are many times the initial thickness of the film.

A new methodology is developed for the extraction of the mechanical properties of supported thin films. Indentation of a polymer film by a well-aligned cylindrical flat punch whose diameter is several times the initial thickness of the film results in a state of uniaxial strain deformation, wherein lateral displacements are suppressed by the surrounding film. This method, called the *confined compression layer test*, allows for extraction of Young's modulus, Poisson's ratio, and the bulk modulus in a single test. Further, the test leads to a distinct confined yield event throughout the volume beneath the punch, in the absence of lateral flow. This yield event occurs within a highly uniform, pressure dominated stress field that is entirely unique at the nanoscale. The confined layer compression test is characterised here via indentation of atactic polystyrene films of 190 – 470 nm thicknesses with a 2050 nm diameter diamond flat punch and via finite element simulations. The test is also demonstrated in PMMA and amorphous selenium films.

The confined layer compression test is then extended to study aspects of non-equilibrium glass mechanics in polymer thin films. The effect of thermal history on the intrinsic stress-strain behaviour of polystyrene films is characterised, with well annealed films exhibiting higher confined yield stresses and greater resistance to plastic deformation. The effect of confined plasticity on the viscoelastic properties of polystyrene is studied, with a notable increase in creep compliance observed at yield. This is linked to higher segmental mobility.

An increase in yield stress for materials plastically deformed in the confined layer compression test is reported. This phenomenon is studied experimentally in polystyrene and via finite element simulations and is found to result from persistent residual stresses imparted to the material during confined yield. These residual stresses also result in an elastic densification of the confined material, with a maximum relative mass density increase of 3.4% being observed in a 203 nm polystyrene film indented to 0.84 GPa peak stress. This technique suggests the possibility of a new form of residual stress based mechanical lithography.

Finally, a significant improvement to the thermal nanoimprint technique is introduced. Shear flow of resist material confined directly beneath large aspect ratio imprint mold features is enhanced by the addition of a small (~10% of the feature size), oscillating lateral strain during normal loading. This leads to greater plasticity beneath mold features and a pumping action which aids flow into the surrounding cavities. This is demonstrated to enable high fidelity imprint below the glass transition temperature in 50 µm thick PMMA sheets, while significant improvements are also reported in 150 and 40 nm films imprinted with a 4 µm full pitch line pattern mold of 35 nm relief. The technology, called small amplitude oscillatory shear forming, is shown to enable low temperature, high fidelity pattern transfer over macroscopic sample areas, typically on the order 1 x 1 cm with a variety of mold geometries.

In summary, this work sets out to use stress and strain as control variables to extend our knowledge and understanding of glassy polymer films and find new ways of patterning and probing materials at small scales

It is good to have an end to journey toward; but it is the journey that matters, in the end

– **Ursula Le Guin**

I would hate to tell you what this lousy little book cost me in money and anxiety and time

– **Kurt Vonnegut**

Acknowledgements

I'd like to start by thanking my supervisor Prof. Graham Cross for giving the opportunity to work in his research group for the past four years. Aside from providing invaluable guidance and a really keen insight into how a physicist goes about approaching problems, I'd particularly like to thank him for his seemingly endless patience when it came to me dithering over data, breaking expensive equipment in the lab, and generally testing Murphy's law to its furthest limits.

Following on, I'd like to thank all the members past and present of the Cross nanomechanics group who have helped me in this work over years. In particular I'm grateful to James Annett and Victor Usov both on a personal and professional level for their unwavering assistance in the lab and in teaching me how to actually do science. I would also like to thank Johann de Silva for laying the groundwork for the work conducted in this thesis.

I have benefitted over the course of this work from collaborating with some truly excellent scientists. I'd like to thank Prof. Özgur Özer for his tireless efforts in trying to cook up an etching recipe for the PolLux. I'd also like to thank Prof. John Pethica for his guidance as we tried to make some sense of what any of our results meant.

On a personal level I'd like to thank all the friends I've made over the past four years, both inside and outside of college. There's always been a shoulder to cry on or someone to grab a beer with in good times. It's been a lot of fun.

Finally, I'd like to thank my family, and in particular my parents Kate and John. I have no idea how you put up with me. I love you very much.

Publications

Papers

1. O. Brazil, V. Usov, J. B. Pethica, and G. L. W. Cross. "Large area thermal nanoimprint below the glass transition temperature via small amplitude oscillatory shear forming." Microelectronic Engineering 182 (**2017**): 35-41.

2. A. Ajetunmobi, D. McAllister, N. Jain, O. Brazil, A. Corvin, Y. Volkov, D. Tropea, and A. Prina‐Mello. "Characterization of SH‐SY5Y human neuroblastoma cell growth over glass and SU‐8 substrates." Journal of Biomedical Materials Research Part A 105, no. 8 (**2017**): 2129-2138.

3. S. Varagnolo, N. Basu, D. Ferraro, T. Toth, M. Pierno, G. Mistura, G. Fois, B. Tripathi, O. Brazil, and G. L. W. Cross. "Effect of hair morphology and elastic stiffness on the wetting properties of hairy surfaces." Microelectronic Engineering 161 (**2016**): 74-81.

4. O. Brazil, J. P., deSilva, W. C. Oliver, J. Kilpatrick, J. B. Pethica, and G. L. W. Cross "Direct observation of elastic to plastic yield in thin films." In preparation.

5. O. Brazil, J. P., deSilva, M. Chowdhury, B. Watts, W. C. Oliver, J. B. Pethica, H. Ö. Özer, and G. L. W. Cross "Pressure densification of polymer films by confined plastic yielding." In preparation.

Table of Contents

Table of Figures

Commonly used Abbreviations and Symbols

AFM	Atomic force microscopy
CLCT	Confined layer compression test
CRR	Cooperatively rearranging regions
CSM	Continuous stiffness measurement
DCM	Dynamic contact module
FEA	Finite element analysis
FIB	Focused ion beam
KV	Kelvin-Voigt
LVE	Linear viscoelastic
M_w	Molecular weight
NIL	Nanoimprint lithography
OD	Optical density
OSA	Optical sorting aperture
PEL	Potential energy landscape
PLGA	Poly-lactic-co-glycolic acid
PMMA	Polymethylmethacrylate
PS	Polystyrene
PSD	Position sensitive diode
RIE	Reactive ion etch
SAOSF	Small amplitude oscillatory shear forming
SEM	Scanning electron microscopy
SLS	Swiss light source
STXM	Scanning transmission x-ray microspectroscopy
T_g	Glass transition temperature
VFT	Vogel Fulcher Tammann equation

a	Contact radius
$A(\lambda)$	Absorption coefficient
C	Confined elastic modulus
C^*	Confined plastic modulus
E	Young's modulus
G	Elastic shear modulus
$G(t)$	Shear relaxation modulus
h_0	Initial film thickness
I_0	Initial x-ray beam intensity
I_T	Transmitted x-ray intensity
$J(t)$	Creep compliance
K	Elastic bulk modulus
k_{film}	Vertical stiffness of a thin film
k_{frame}	Total background stiffness of support apparatus
P	Hydrostatic pressure
R_g	Radius of gyration
S	Indentation contact stiffness
S	Ratio of film and substrate Young's moduli
T	Temperature
$T_{imprint}$	Nanoimprint temperature
V^*	Eyring activation volume
Y	Yield stress in tension
Yc	Confined yield stress
α'	Yield surface pressure coefficient
δ	Departure from equilibrium
ε	Strain tensor
ε_{ij}	j^{th} component of strain on i^{th} face
Z	Nanoimprint mold fill factor
η	Viscosity
λ	Plastic scalar multiplier

$\boldsymbol{\mu}$	Static coefficient of friction
$\boldsymbol{\mu(\lambda)}$	Mass extinction coefficient
$\boldsymbol{\nu}$	Poisson's ratio
$\boldsymbol{\nu_f}$	Specific free volume
$\boldsymbol{\rho}$	Polymer mass density
$\boldsymbol{\sigma}$	Stress tensor
$\boldsymbol{\sigma_c}$	Applied creep stress
$\boldsymbol{\sigma_{ij}}$	j^{th} component of stress acting on i^{th} face
$\boldsymbol{\sigma_{VM}}$	Von Mises equivalent shear stress
$\boldsymbol{\tau_{oct}}$	Octahedral shear stress
$\boldsymbol{\chi}$	Punch diameter to film thickness ratio

Chapter 1:
Introduction

Nanomechanics is the study of the mechanical response of systems and materials whose smallest dimensions are on the order of 100 nm or less, and characterization of their elastic, plastic, viscous, and viscoelastic response to imposed loads and displacements. The accelerating pace of miniaturization of electronic, optical, and mechanical devices have made nanomechanics an increasingly important topic in materials science, both in the context of mechanical characterization of nano-structured systems such as thin films, and exploitation of unique nano-scale mechanical properties. Examples of such properties include superlubricity[1], dramatic increases in the strength of crystalline materials at the nanoscale[2,3], and the remarkable elastic strength of low dimensional materials such as graphene and carbon nanotubes[4,5]. These deviations from bulk behaviour are brought about through confinement effects, geometric considerations, and non-intuitive scaling of physical properties at very short length scales.

Despite being a relatively young research field, nanomechanical systems and technologies are already widely utilised and set to become more prevalent in all walks of life over the next half century. In integrated circuit design, epitaxial thin films are used to apply compressive and tensile strains to enhance electron/hole mobility in the transistor channel, boosting conductivity in a process known as strain engineering[6]. Nanomechanical systems of non-volatile memory boasting data densities greater than 1 Gb/mm^2 have been developed[7,8], while nanomechanical lithography techniques are set to form a major component of the fabrication process for next generation three-dimensional flash memory[9]. In medicine, nanomechanical technologies such as microcantilever array biosensors are expected to play a major role in the development of new antibiotics capable of fighting multi-drug resistant bacterial strains such as MRSA[10,11], with commercial applications already coming online[12]. In terms of fundamental physics, nanomechanics continues to expand the frontiers of what is measurable. Recent breakthroughs in the field have included the development of mass balances with yoctogram (10^{-21} g) precision capable of monitoring few-molecule chemical reactions[13], the measurement of persistent currents in resistive metal rings via

mechanical means[14], and observation of plastic yield in ^{4}He quantum crystals below 0.5 K[15].

Polymer thin films and coatings are nanomechanical systems of considerable technological and theoretical interest. Polymers are long molecular chains of covalently bonded atoms made up of smaller, repeating molecular units called monomers. Due to the considerable work of organic chemists over the past century, polymers are highly customizable, with properties such as electrical conductivity[16], biocompatibility and biodegradability[17], mechanical strength[18], and thermal resistivity[19], all tailorable for specific functions. Films can be made with sub-nm accuracy over a large thickness range through techniques such as spin coating[20] and chemical vapour deposition[21] and thermoplastic polymers may be moulded and formed to specific shapes with nm critical dimension with great ease[22,23]. Physically polymers may be found in many forms: viscous melts with temperature dependent flow properties, non-equilibrium amorphous glasses, semi-crystalline states where crystal domains may make 10-80% of the total structure[24], and liquid crystals which exhibit long range order is one or two dimensions, but not in three[25]. The transition from melt to amorphous state is called the glass transition (T_g) and involves a reduction of molecular mobility for individual segments of several orders of magnitudes, typically leaving the glass in a non-equilibrium frustrated state. The specific origins of this dramatic drop in molecular mobility over a short temperature range are still heavily debated[26], leading the glass transition to be considered one of the greatest mysteries remaining in condensed matter physics[27].

Exploitation of the unique properties of nano-structured matter requires that their properties of interest be well-established so that comparisons may be drawn with bulk materials and the operational limits of the system in question be known. Mechanical characterisation of thin films is usually performed via sharp-tipped nanoindentation[28,29], a technique initially developed for hard materials such as ceramics and metals[30]. Sharp tipped intenders are not ideally suited to quantify viscoelastic response of polymers due to the high stress gradients around the tip making interpretation of results difficult. Further, sharp tipped indenters may lack the required sensitivity to detect unique polymer sample size dependent effects in thin films such as T_g[31] and mobility[32] gradients close to the surface due to the small contact area at low indentation depths. As such, new tests are needed to quantify the mechanical response of polymer thin films.

In the field of glassy dynamics, significant uncertainty remains around the effects of pressure, stress, deformation, and thermomechanical history on the non-equilibrium response of bulk polymer systems[33]. Out of equilibrium polymers tend to evolve towards the equilibrium state in a process known as structural recovery[34], with changes in enthalpy[35], free volume[36] and segmental mobility[37] used as thermodynamic signatures of the glassy state. A popular interpretation of the effect of stress and strain on the thermodynamic state is that deformation increases mobility[38,39] and the free volume content of the system leading to "mechanical rejuvenation" of the system, reversing the effects of structural recovery and leaving it further from equilibrium. Recent experiments however have shown that mobility may increase in situations where free volume decreases[40], and that under certain loading conditions may decrease with increasing deformation[41]. This indicates that more experimental work is required to characterise the effects of stress and strain on glasses, particularly in previously neglected deformation modes.

Mechanical forming of polymer thin films has also been a subject of heavy research since the development of nanoimprint lithography by *Chou* in the mid 1990's[22,42,43]. Originally developed for the semiconductor industry and listed as a potential successor to optical lithography in the 2003 international technology roadmap for semiconductors[44], issues associated with scale up have prevented widespread industrial adoption of the technique outside of a relatively small number of applications. These have included defect control, mask fabrication, processing times and metrology of both master stamp and resist[45,46]. Work is needed therefore to refine the fundamentals of the process, introducing new techniques that will lower adhesion between the mold and resist and decrease thermally induced stress gradients to allow for more uniform forming.

The purpose of this thesis is to tackle the problems outlined in the previous three paragraphs: Mechanical characterisation of thin films, investigation of glassy polymer mechanics, and improved mechanical lithographic methods. A new test for the extraction of supported thin film mechanical properties is developed based on the flat punch geometry called the confined layer compression test. This same geometry is used to study the non-equilibrium dynamics of glassy films via constant contact area stress-controlled deformation experiments. The effect of confined mechanical yield on free volume and molecular mobility in thin films is considered and quantified via density measurements and creep compliance testing. A modification to the thermal

nanoimprint process is presented known as small amplitude oscillatory shear forming, wherein a lateral motion is applied to the stamp during imprint resulting in greater pattern replication at sub Tg temperatures.

1.2 Structure and outline of thesis

This thesis is divided into five chapters:

- The remainder of **chapter one** will introduce the fundamental concepts required to interpret the results of subsequent chapters. Section 1.3 focuses on the structure and dynamics of polymers, introducing concepts such as reptation theory, free volume, and the glass transition. Section 1.4 is devoted to continuum mechanics, developing the theories of linear elasticity, plasticity, and viscoelastic response and how they may be applied to the mechanical modelling glassy polymers.
- **Chapter two** will focus on the principal experimental techniques used in this work. Detailed explanations of the theoretical underpinnings and operating principles of nanoindentation and nanoimprint lithography are given, as they are the primary methods used herein to mechanically probe and manipulate polymer films. Other fabrication and characterisation techniques used heavily throughout this work such as atomic force microscopy and spin coating are also explained.
- In **chapter three**, a new test for the study of the mechanical properties of glassy thin films is introduced, called the *confined compression layer test*. The test relies on indentation of a thin film with a well-aligned cylindrical flat punch whose diameter is several the initial thickness of the film. A state of quasi-uniaxial strain is generated, where the film material around the contact area suppresses lateral flow. A distinct, confined yield event in the absence of lateral shear flow is observed that has not been reported before in nanostructured matter. The confined layer compression test and yield event are parameterised in terms of film thickness, substrate compliance, and frictional boundary conditions via indentation into polystyrene and finite element simulations.
- **Chapter four** looks to extend the confined layer compression test to examine the non-equilibrium dynamics of glassy polymer thin films. The effects of ageing

and yield on subsequent mechanical response is explored. Yielding in a confined geometry is found to increase the yield stress of the deformed volume on subsequent loading and results in a densification effect caused residual stresses imparted to the sample during plastic deformation. The coupling of a confining geometry to classical plasticity results in a stress memory effect, which persists over long times.

- In **chapter five** a technique called *small amplitude oscillatory shear forming* is used to enhance traditional thermal nanoimprint processes. This relies on the application of a small, lateral oscillatory motion to the stamp/mold during imprint. While this technique has been demonstrated before, this is the first time it is scaled up to technologically relevant sample sizes on the order of cm^2.
- Finally, a brief conclusion and future prospects/outlook section is included.

1.3 Polymer structure and dynamics

Polymers are among the most important classes of molecules found in nature. In biology, polymers form the building blocks of life, with nucleic acids, proteins and actin filaments all essentially being some form of polymer[47]. Technological usage of polymers reaches back 3,600 years to ancient Mesoamerica where natural rubbers were used to fashion footballs, medicines, rubber bands, and ritual figurines[48,49]. Polymers have become increasingly indispensable materials in day to day life since the creation of the first synthetic plastic, Bakelite[50], by Leo Baekeland in 1907. Materials such as polystyrene (PS), polymethylmethacrylate (PMMA), polycarbonate, and polypropylene are crucial components in fields as varied as construction[51], consumer goods, and packaging[52]. Polymers have played a key role in the digital revolution, allowing for sturdy, high precision parts and components to be mass produced at low cost, and are an important material in semiconductor fabrication as photoresists[53,54].

This section is divided into four portions. First the basics of polymer structure are introduced before the concepts of melt dynamics are briefly considered. The glass transition and phenomenological theories of its origin are discussed, before the section is closed with consideration of structural recovery in the glass state.

1.3.1 Basic polymer structure

The essential structure of a polymer is a macromolecule made up of one or more repeating units called monomers bonded together, as shown for polypropylene in figure 1.3.1 (a), where the monomer is highlighted in red[55]. Monomers are covalently bonded along the main chain, consisting exclusively of carbon atoms in this case, with molecules bonded off the main chain known as side groups. These side groups may be made up of different chemical species, as in the case of polypropylene, which means polymers of the same chemical formula may show dramatically different properties based on the ordering of the side groups. This phenomenon is known as stereoisomerism and is depicted in figure 1.3.1 (b). In the isotactic configuration all side groups of the same type (marked here as A's and B's) are on the same side of the main chain. The syndiotactic configuration sees side groups alternate with each subsequent monomer, while in the atactic configuration monomers are distributed randomly about the main chain. An example of the differences brought about by tactility is the propensity of isotactic PS to crystallise in conditions where atactic PS remains amorphous[56].

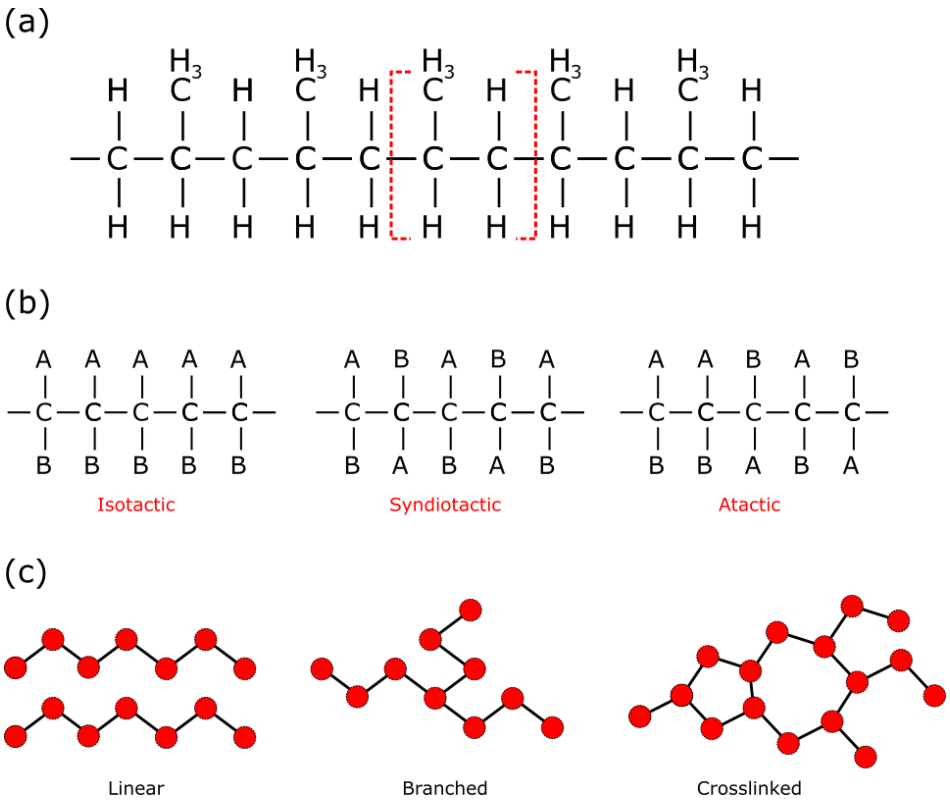

Figure 1.3.1 Molecular structure of simple polymers (a) Polypropylene, with the monomer highlighted in red. (b) Stereoisomers with the same chemical formula, but difference spatial order. (c) Different common molecular architectures.

The simplest and most commonly encountered molecular architecture in polymer physics is the linear chain, shown in 1.3.1 (c). Polymers may also exist in branched forms depending on their method of synthesis[57,58], or as cross-linked networks which are typically either thermally or chemically treated/cured causing the formation of covalent bonds between adjacent chains[59]. Branched polymers are often less dense and harder to crystallise than their linear counterparts, while crosslinked polymers lack the viscous flow properties seen in other architectures even at long times and high temperatures[18].

The polymers considered in this work are exclusively linear. It is therefore useful to consider this simplest form to derive the typical relations between polymer chemistry, mass, size, and conformation. A linear polymer consists of n monomers, each of molecular weight M_0. The total molecular weight M_w of the chain therefore is:

$$M_w = nM_0 \tag{1.3.1}$$

Each monomer has a fixed length, a, and a fixed bonded angle to the adjacent monomers, θ. The end to end length *along* the chain l is therefore given by[60]:

$$l = na\cos\left(\frac{\theta}{2}\right) \tag{1.3.2}$$

Each atom along the main chain is free to rotate however, meaning that the polymer adapts a complicated conformation in 3D space which is not well characterized by l. The mean square end to end distance $\langle R^2 \rangle$ is more descriptive and is given by:

$$\langle R^2 \rangle = na^2\left(\frac{1+\cos\theta}{1-cos\theta}\right) \tag{1.3.3}$$

An important observation is that the position vector $\boldsymbol{r}$ of the i^{th} chain is correlated to that of the j^{th} by:

$$\langle \vec{r_i} \cdot \vec{r_j} \rangle = a^2 \cos^{|j-i|}\theta \tag{1.3.4}$$

As the cosine term decays very quickly, the position vectors of chains far away from each other are effectively uncorrelated. This indicates that the chain may be divided into N statistically independent units, known as Kuhn monomers, of length b, where:

$$Nb^2 = na^2\left(\frac{1+\cos\theta}{1-cos\theta}\right) = \langle R^2 \rangle \tag{1.3.4 a}$$

$$Nb = na\cos\left(\frac{\theta}{2}\right) = l \qquad (1.3.4\ b)$$

The size of the persistence length b is effectively determined by the bond angle of the monomers and the bulkiness of the side groups. As the mean square end to end distance now scales only with the number of steps (Kuhn monomers) and step size (persistence length) chain conformation is described by an idealised random walk. Further, as chemical properties such as bond angle and side group makeup only influence the size of b, a general universality emerges in the properties of linear polymers so long as crystallisation is avoided. They all go through a glass transition and have broadly similar mechanical properties in their respective melt and glassy states, as well as similar time dependent viscoelastic response.

Another useful measure of chain size is the mean square radius of gyration, $<R_g^2>$, which is the average squared distance of any point within the chain to its centre of mass. This is given by:

$$\langle R_g^2 \rangle = \frac{1}{6}Nb^2 = \frac{1}{6}\langle R^2 \rangle \qquad (1.3.5)$$

$<R_g^2>$ is somewhat more physically intuitive than $<R^2>$ and is often used to characterize deviations from bulk behaviour encountered in ultra-thin polymer films[61], which typically emerge for film thicknesses on the order of $\sqrt{\langle R_g^2 \rangle}$[62–64]. The various lengths and chain size measures discussed in this section are shown in figure 1.3.2, with the sub-Kuhn monomer structure shown in the far left image and a chain as part of an entangled melt shown on the far right.

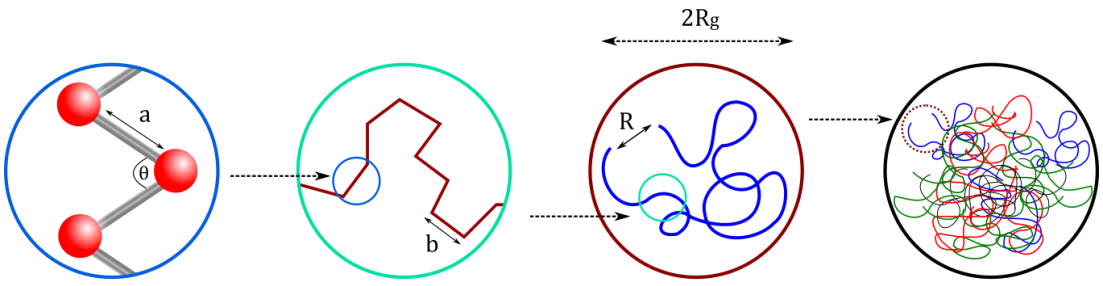

a = monomer/bond length, ***b*** = Kuhn monomer length, ***R*** = End to end chain distance, ***Rg*** = Radius of gyration

Figure 1.3.2 Structure of polymer chain in an entangled melt. From left to right: Structure of the polymer below the Kuhn persistence length. At intermediate lengths the chain is described by the persistence length b and obeys random walk statistics. On the single chain scale, the size of the macromolecule may be described either by the end to end chain distance or the radius of gyration. Finally, the single chain is shown as part of a dense entangled melt.

1.3.2 Melt dynamics

The relations arrived at in the previous section were for a single chain in isolation. For polymers in the melt phase, translational motion is considerably curtailed by the presence of surrounding chains, a phenomenon known as entanglement. The motions of chains in such an environment is described by the reptation model[65], developed by *Edwards*, *Doi*, and *de Gennes*.

The essential idea of the reptation model is shown in figure 1.3.3 (a), where a single chain within a melt is shown as a black line surrounded by a red tube. The effect of local entanglements is to constrain the motion of monomers on the chain to within the red tube by introducing a quadratic potential energy cost *V(x)* associated with motion perpendicular to the local direction of the tube[66]. The diameter a of the tube is defined as the point where the potential curve is equal to the available thermal energy, k_BT:

$$V\left(\frac{a}{2}\right) = k_BT \tag{1.3.6}$$

Where k_B is the Boltzmann constant. This is illustrated in figure 1.3.3 (b). a is typically on the order of several nm, very much wider than the chain itself. As such, the polymer is free to adopt a random walk within this volume. For length scales < a, the chain is effectively unaware of confinement. It is useful therefore to divide the chain into N_e entanglement blobs of diameter a, with similar reasoning to that used when employing Kuhn monomers in equation 1.3.4. A schematic of these entanglement blobs within the Edwards tube is shown in 1.3.3 (c). The mean end to end length along the chain is now given by:

$$\langle l \rangle = a\frac{N}{N_e} = \frac{bN}{\sqrt{N_e}} \tag{1.3.7}$$

The chain now "wriggles" along the tube direction. This motion is known as reptation, deriving its name from the motion of snakes and reptiles[67]. A relaxation time τ_{rep} is defined as the amount of time required for a polymer chain to fully displace by <l>, or to completely move out from its original tube:

$$\tau_{rep} = \frac{\langle l^2 \rangle}{D_{tube}} = \frac{\xi b^2}{k_BT}\frac{N^3}{N_e} \tag{1.3.8}$$

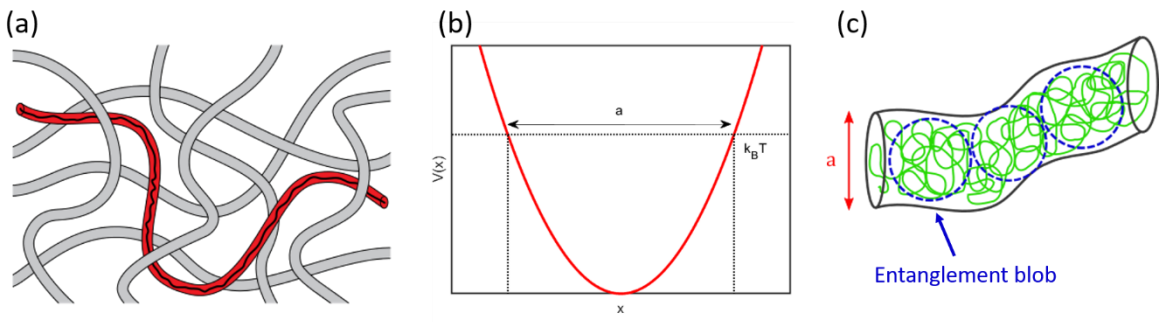

Figure 1.3.3 (a) Repetition model of entangled polymer dynamics. The motion of the black chain is confined to within the red tube by surrounding entanglements. Taken from Wikipedia under creative commons licence. (b) Lateral potential energy felt by monomers on the chain. The width of the Edwards tube is defined by where the potential V(x) is equal to the available thermal energy. (c) Entanglement blobs of diameter *a*.

Where D_{tube} is a diffusion coefficient along the tube and ξ is a monomer friction coefficient. The viscosity of the polymer η is found to linearly depend on τ_{rep}, related by a time dependent shear relaxation modulus, which shall be introduced shortly. For the time being it is sufficient to say:

$$\eta \propto \tau_{rep} \tag{1.3.9}$$

The relaxation time may be rewritten in terms of molecular weight by defining a Kuhn monomer molecular weight of $M_0^K = \frac{M_w}{N}$. Equation 1.3.8 may now be written as:

$$\tau_{rep} = \frac{\xi b^2}{N_e k_B T}\left(\frac{M_w}{M_0^K}\right)^3$$

$$\eta \propto (M_w)^3 \tag{1.3.10}$$

This scaling of viscosity with M_w^3 is found to agree reasonably well with experimental value of 3.4, as shown in figure 1.3.4 (a) which plots log(M_w) versus log(η) for a host of linear polymers[68]. A crossover in viscosity-M_w dependency is observed at a critical molecular weight M_{wc}, below which the scaling is linear. Below M_{wc} the chains are effectively too short to entangle. This scenario was described by *Rouse*, who modelled a single chain as a series of Brownian particles connected by harmonic springs existing in a viscous background fluid[69,70]. Rouse calculated the viscosity as:

$$\eta_{Rouse} = \frac{\xi}{b}\frac{M_w}{M_0}, \qquad M_w < M_{wc} \tag{1.3.11}$$

A schematic of the Rouse model is shown in figure 1.3.4 (b). The polymers used in this work generally have $M_w > M_{wc}$ and can therefore be described using the reptation model.

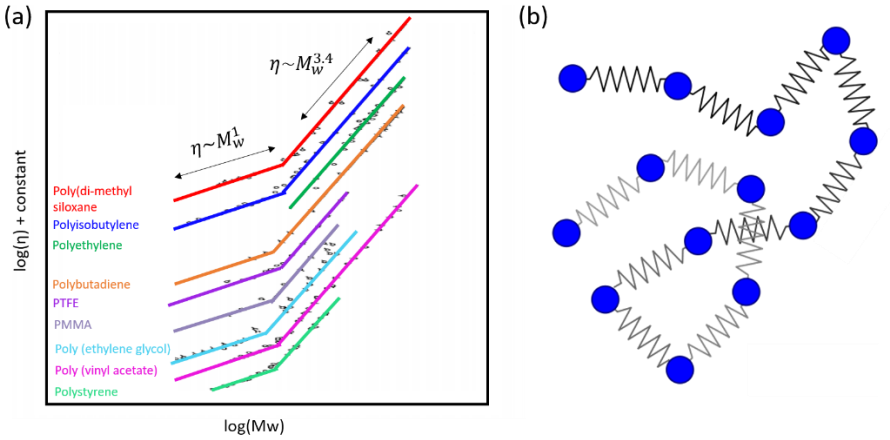

Figure 1.3.4 (a) Scaling of viscosity with molecular weight for various polymer melts. For molecular weights above the critical entanglement weight M_{wc}, the viscosity scales as $Mw^{3.4}$ due to the constraining effects of entanglement of nearby chains. This behaviour is predicted by the reptation model of melt dynamics. Below Mwc chains are too short to entangle, meaning their dynamics can be described by the Rouse model, in which the chain is described as a series of Brownian particles connected by harmonic potentials in a viscous background medium. Data originally from [68] (b) Schematic of the Rouse model of polymer dynamics.

Polymer dynamics are made up of several independent relaxation mechanisms, whose relaxation times can stretch from nanoseconds to several years at a given temperature[71]. These range from large scale translational modes such as reptation which are responsible for flow, through sub-entanglement scale mechanisms such as Rouse dynamics and co-operative segmental motion, to local monomer vibrations and side-group rotations[72]. This spectrum of relaxations is best illustrated through the shear relaxation modulus, $G(t) = \sigma_{xy}(t)/\gamma_{xy}$, a measure of the amount of the stress required to maintain a fixed shear deformation γ_{xy}. This is plotted for an amorphous thermoplastic in figure 1.3.5[73]. At long times (or equivalently high temperatures) *G(t)* is vanishingly small as flow occurs due to chain slippage and reptation. At intermediate times flow is prevented by the presence of entanglements, and as such *G(t)* plateaus at approximately 10^5 Pa. At shorter times and lower temperatures there is either insufficient time or thermal energy available for translational movement through co-operative segmental motion and the mechanical response of the polymer is that of a solid with a modulus on the order of 10^9 Pa. This changeover from viscoelastic liquid to solid behaviour is known as the glass transition and has been considered one of the greatest intellectual challenges in solid state physics[74]. The glass transition sees a dramatic drop in molecular mobility of several orders of magnitude over a relatively narrow temperature range and with only modest accompanying changes in local

density[75]. Further, the glass transition sees the polymer fall out of equilibrium, as chains no longer have sufficient thermal energy to explore all energetically equivalent configurations and conformations over experimentally accessible timescales. The glass transition and phenomenological models explaining it are the focus of the next section.

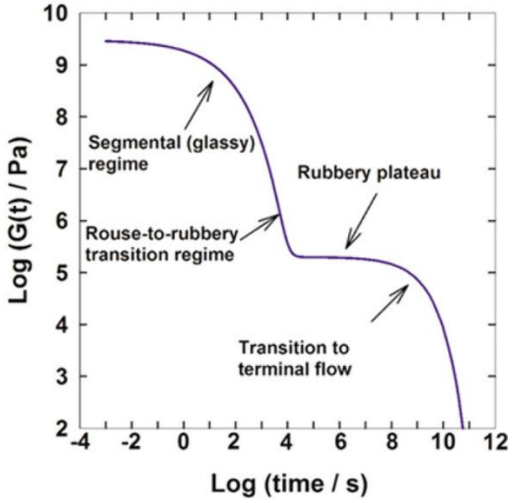

Figure 1.3.5 Shear relaxation modulus as a function of time for a model amorphous thermoplastic at a fixed temperature. The shear relaxation modulus encompasses a wide range of relaxation mechanisms, ranging from short timescale phenomena such as side group rotation and segmental vibration, through large scale translational motions such as reptation, which are responsible for flow. Reproduced with permission from [77]

1.3.3 The glass transition

Fundamentally, the glass transition is a kinetic transition[73,76]. While there is a dramatic decrease in molecular mobility, there is no fundamental local change in structure, with the glassy solid retaining a liquid-like lack of long range order[77]. Further, the glass transition is not a phenomenon unique to polymers. Several small molecule systems display glass transitions, as well as colloidal[78,79] and metallic glasses[80]. The nature of the glass transition therefore cannot be strongly linked to chain connectivity, further evidenced by the weak dependence of the glass transition temperature, T_g, on M_w[81]. Phenomenology, the glass transition is best illustrated through monitoring thermodynamic variables such as volume and enthalpy upon cooling from the equilibrium melt state[71]. This is shown in figure 1.3.6. Focusing on volume, above T_g *V(T)* is linear, representing thermal expansion of the liquid. At T_g, the system falls out of equilibrium and is no longer able to explore all possible configurations due to a lack of sufficient thermal energy, becoming non-ergodic. The

system now enters the glassy state, and *V(T)* is again linear, following the glassy thermal expansion line, typically about half the magnitude of the equilibrium melt line. T_g is observed to be cooling rate dependent, with slower rates resulting in a lower T_g. This is as greater time is allotted to the system to achieve an equilibrium state during cooling.

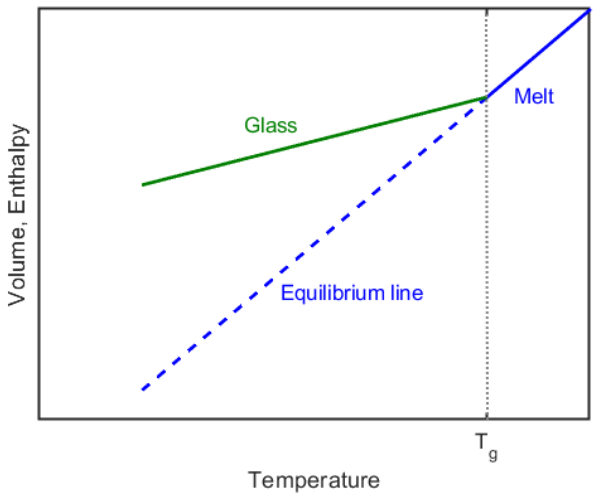

Figure 1.3.6 The glass transition as defined in terms of the thermodynamic quantities volume and enthalpy. T_g is marked by the change in equilibrium to glassy behaviour. In terms of volume, it is the point where the slope of V(T) changes from the equilibrium melt thermal expansion coefficient, to the glassy coefficient.

In understanding the glass transition, it is first useful to consider the 'supercooled' melt state[82,83], covering a temperature range of approximately $T_g - T_g + 50°$. In this region, thermal energy is insufficient to allow reptation over experimental timescales, and as such the primary mode of relaxation is the segmental scale α-relaxation. Mathematically, the alpha relaxation time τ_α is described by the Vogel-Fulcher-Tammann (VFT) equation[84,85]:

$$\tau_{alpha} = \tau_0 \exp\left(\frac{B}{T - T_0}\right) \tag{1.3.12}$$

Where B and τ_0 are empirical fitting constants and T_0 is the so-called Vogel temperature, the temperature at which all α-relaxation ceases - typically 30-50° below T_g. The VFT equation is considered 'super-Arrhenius' in form[86]. The Arrhenius equation describes a rate activated process with a temperature independent activation energy, E_A:

$$\tau_{Arrhenius} \propto \exp\left(\frac{E_A}{k_B T}\right) \tag{1.3.13}$$

In this context, the VFT equation essentially contains a temperature dependent activation energy, which increases in size as T is decreased, leading to sluggish dynamics as τ_α increases rapidly at low temperature. τ_α and $\tau_{Arrhenius}$ are plotted as functions of inverse temperature in figure 1.3.7 (a), normalised such that they diverge at 1.0. The origin in this dramatic slowdown in dynamics is the mechanism behind the α-relaxation; segmental cooperative motion[87,88].

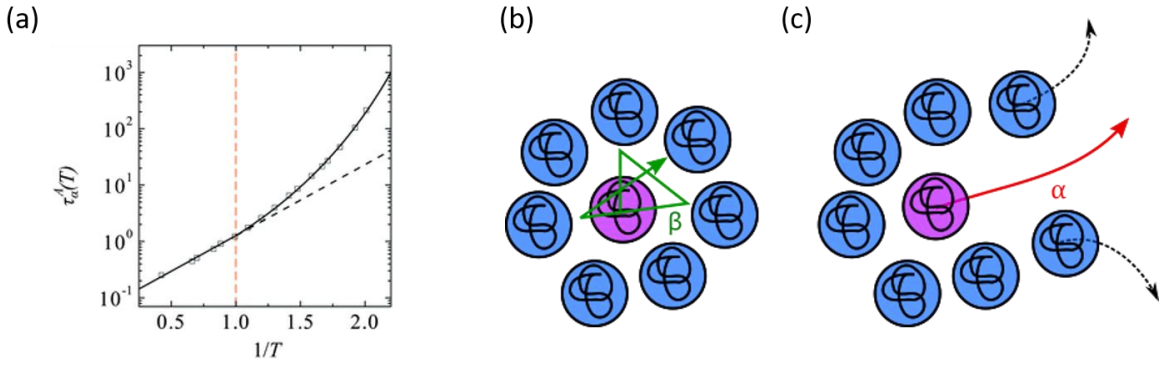

Figure 1.3.7 (a) Alpha relaxation time as a function of inverse temperature for a simulated glass former. Due to the super-Arrhenian nature of the VFT equation, τ_α increases much faster than Arrhenius behaviour (dashed line) at low temperatures. Reproduced under creative commons licence from [90] (b) Beta relaxation cage rattling at low temperature. (c) Alpha relaxation through cooperative motion, where the central segment escapes the cage due to the motion of surrounding segments.

A simplified representation of the cooperative motion mechanism is shown in figure 1.3.7 (b) and (c), drawn from the ideas of mode-coupling theory[89,90]. In the supercooled regime, the temperature has dropped, and density increased sufficiently that the central pink segment is trapped and may only 'rattle' locally in secondary β movements, as shown in (b). The α-relaxation occurs when surrounding segments move in a manner that breaks the cage surrounding the central segment, allowing it to escape. Two popular phenomenological theories exist to explain this process; the Adam-Gibbs[91] entropy formulation and the free volume theory originally proposed by *Turnbull* and *Cohen*[92]. In the Adam-Gibbs model, dynamics slow down due to a decrease in configurational entropy with decreasing temperature. Conformational changes require cooperative motion of segments in groups called cooperative rearranging regions (CRR),

containing $z^*(T)$ segments, where the number of segments in a CRR increases with decreasing temperature according to:

$$\frac{z^*(T)}{s_c^*} = \frac{N_A}{S_c(T)} \tag{1.3.14}$$

Where s_c^* is the entropy of the smallest CRR, N_A is Avogadro's number, and $S_c(T)$ is the macroscopic configurational entropy. Adam and Gibbs were able to formulate a relaxation time of the form:

$$\tau_{AG} = \exp\left(\frac{B}{TS_c(T)}\right),$$

$$B = \frac{N_A s_c^* \Delta\mu}{k_B C}, \qquad S_c = \int_{T_0}^{T} \frac{\Delta C_p(T')}{T'} dT' \tag{1.3.15}$$

Where $\Delta\mu$ is the energy barrier to rearrangement per segment, ΔCp is the configurational heat capacity, and C is the configurational heat capacity at the temperature where Sc is zero. Using the relation $\Delta C_p(T) = CT_0/T$ the VFT equation is recovered. Essentially the Adam-Gibbs model states that as temperature is lowered, the configurational entropy of the system drops, increasing the size of CRRs required for motion, leading to a temperature dependent energy barrier.

The basic assumption of the free volume model is that the motion of each segment requires vacant free volume, V_f. The total volume of the polymer sample V is:

$$V = V_{occ} + V_f \tag{1.3.16}$$

Where V_{occ} is the occupied volume. The fractional free volume per segment is therefore $\nu_f = V_f/N$. Above T_g, the fractional free volume of the system may be approximated as:

$$\nu_f = \nu_g + \alpha_f(T - T_g) \tag{1.3.17}$$

Where ν_g is the free volume content at T_g and α_f is the equilibrium free volume thermal expansion coefficient. A comprehensive study conducted by Lipson and White determined the free volume content of 51 thermoplastic polymers cooled from the melt state and found: $5\% < \nu_f < 15\%$ at their experimental T_g[93], indicating that the typical free volume content of a glassy polymer will be on the order of 10%. Cohen and Turnbull derived an expression for relaxation time of the form:

$$\tau_f = \tau_0 \exp\frac{b}{\nu_f} \tag{1.3.18}$$

The VFT equation is recovered by allowing:

$$B = \frac{b}{\alpha_f}, \qquad T_0 = T_g - \frac{\nu_g}{\alpha_f} \tag{1.3.19}$$

Both the free volume and configurational entropy models have their limitations. For example, careful dielectric experiments in PVAc have revealed that α-relaxation times diminish faster than can be accounted for by free volume reduction[94]. Several flavours and modifications to both theories exist incorporating factors such as hydrostatic pressure, spatial heterogeneity of relaxation times, and the shape of CRRs, with refinement being an ongoing process[95–97]. These further theories are beyond the scope of this work. The essential point is that the glass transition leaves the system in a non-equilibrium state. In response, the glassy systems sheds excess enthalpy and free volume, evolving towards equilibrium in a process known as structural recovery.

1.3.4 Structural recovery and physical aging

Structural recovery is the spontaneous evolution of the thermodynamic properties of a glass with sub-T_g annealing as it moves towards the equilibrium state[73]. The resultant changes in mechanical properties such as yield strength and creep compliance are referred to as physical ageing[98], where it is important to note that no change in chemical structure occurs. The structural recovery process is shown in temperature-volume/enthalpy space in figure 1.3.8. The glass is rapidly cooled (quenched) from the melt phase to an ageing temperature T_a in the glassy state. In terms of volume, during the quench phase the polymer contracts in accord with α_l and α_g, the liquid and glassy thermal expansion coefficients, when above and below T_g respectively. The temperature is then held constant at T_a and the volume decreases with time towards the equilibrium value, as shown by the red line. The instantaneous structure of the glass is quantified by two measures: the fictive temperature T_f, and the departure from equilibrium δ. T_f is the temperature at which the glass would intersect the equilibrium line if heated from its current state[99], as shown by the grey line in 1.3.8. δ[100] is defined as:

$$\delta = \frac{V(t) - V_\infty}{V_\infty} \tag{1.3.20}$$

Where $V(t)$ is the current sample volume and V_∞ the volume at equilibrium.

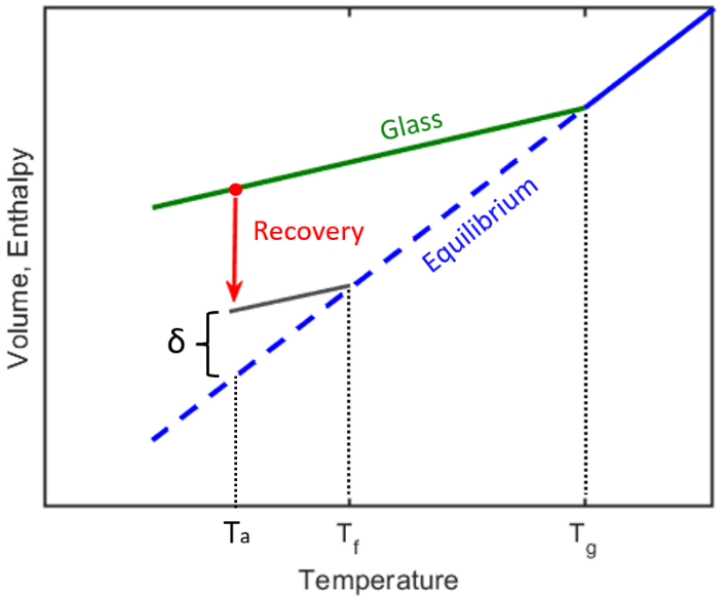

Figure 1.3.8 Structural recovery of a glass towards equilibrium. After a rapid quench to T_a, the glass evolves towards equilibrium, with reductions in volume in enthalpy. Recovery is quantified through the fictive temperature T_f and the departure from equilibrium δ.

Structural recovery is a complex, non-linear process that cannot be satisfactorily described through a single relaxation mechanism. This is best illustrated by a series of experiments originally performed by *Kovacs* in the 1960's; the intrinsic isotherm, asymmetry of approach, and memory tests/effects[101]. These are detailed below.

The intrinsic isotherm experiment consists of quenching the material from an equilibrium state either at or above T_g to T_a. The volume recovery response is then monitored and used to track δ[35]. By repeating the experiment which quenches to different T_a's a family of isotherms is formed. This process is shown in figure 1.3.9 (a), where each red line represents an isotherm. The results of such a test in polystyrene with a nominal T_g of 100°C is shown in (b). The important result is that δ decreases linearly with the log of ageing time. Further, while lower T_a's result in greater departures from equilibrium, it does not appear to affect ageing rate, at least over this narrow T range. For T_a's 10°C below T_g, ageing periods of over a week are still insufficient to return the sample to equilibrium.

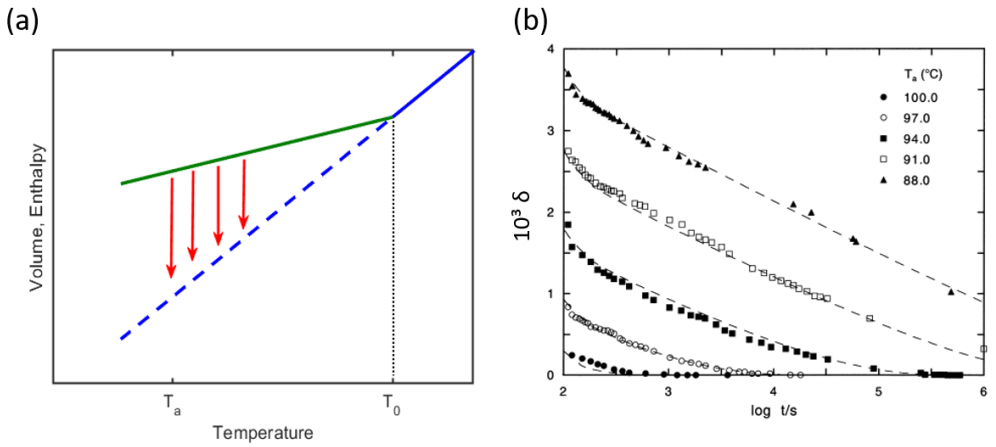

Figure 1.3.9 (a) The intrinsic isotherm experiment. The sample is quenched from above T_g to the aging temperature and δ monitored. By quenching to different T_a's a family of isotherms is built. (b) Evolution *of* δ in polystyrene at 5 ageing temperatures. Reproduced with permission from [35]

The asymmetry of approach experiment[102] consists of equilibrating the sample at two temperatures: $T_a - \Delta T$ and $T_a + \Delta T$. The sample is heated to T_a from $T_a - \Delta T$ and cooled from $T_a + \Delta T$ in what are termed up-jump and down-jump experiments respectively. The sample is then aged with δ monitored in each case. This experimental procedure is plotted in figure 1.3.10 (a). The response of a molecular glass to such a test as measured by Kovacs in his original work is shown in (b). It can be readily observed that the response is highly asymmetrical, with the down-jump test relaxing to equilibrium much faster than the up-jump. This indicates that the underlying kinetics of the glassy relaxation process are dependent on the current state/structure of the glass, with the up-jump relaxing more slowly due to it coming from a state of lower molecular mobility than the down-jump.

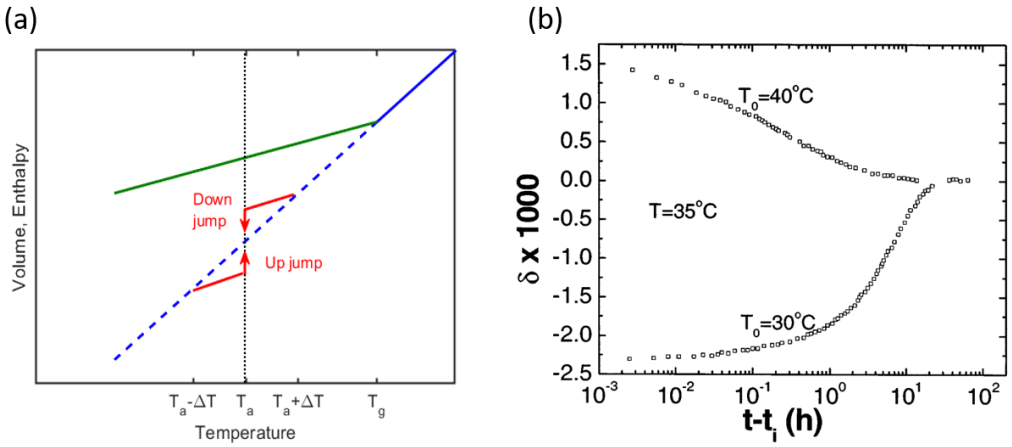

Figure 1.3.10 The asymmetry of approach experiment. (a) The material is equilibrated at temperatures $T_a - \Delta T$ and $T_a + \Delta T$. It is then heated/cooled to T_a and the evolution of δ monitored. (b) Response of a molecular

glass to this protocol. The up-jump step reaches equilibrium more slowly due to lower molecular mobility in the deeper glassy state Reproduced with permission from [105].

The last of Kovacs' signature experiments is the memory effect test. The sample is quenched to T_a and allowed to age part way to equilibrium. The sample is then heated to T_f, where $\delta = 0$. This procedure is plotted in figure 1.3.11 (a) for several aging temperatures.

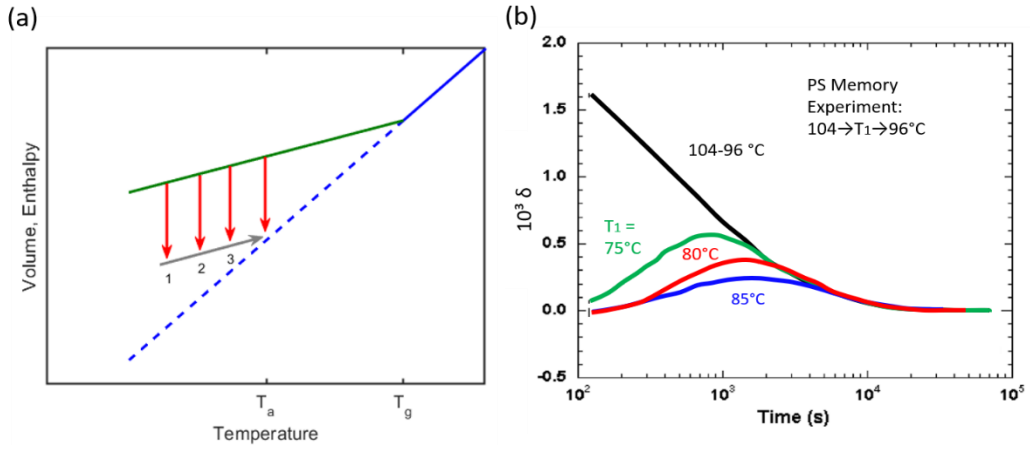

Figure 1.3.11 (a) The memory effect experiment. (a) The sample is quenched to T_a and allowed to partly recover. It is then heated to T_f. (b) Response of polystyrene. An overshoot of δ is measured, indicating the presence of more than one underlying relaxation mechanism. Reproduced with permission from [36]

Were there a single mechanism for structural relaxation there would be no further volume change following the up-jump as $\delta = 0$. However, as can be seen in (b), the material (in this case polystyrene[36]) overshoots, with δ increasing, before decaying in a similar fashion to a simple quench experiment, which is plotted in black. The magnitude of this overshoot is found to be proportional to the magnitude of the difference between T_a and T_f. This memory effect in which the sample's thermal history affects its behaviour despite being at thermal equilibrium is typically attributed to there being a spectrum of relaxation processes associated with the overall structural recovery processes, each with their own relaxation times and dependencies on the material state.

The effects of deformation and stress on the structural recovery process have been hotly debated for several years[103]. Typically, mechanical deformation results in an increase in molecular mobility and reduction of relaxation times[104]. This has led to the

mechanical rejuvenation hypothesis, in which ageing is erased by the introduction of stress and the material returned to a "younger" state. Recent direct optical measures of mobility during deformation by Ediger and others have revealed that mobility does indeed increase during deformation until yield, after which there is no further change[38,39,105]. In terms of a potential energy landscape perspective, it has been suggested that sub yield stresses act to tilt the energy landscape allowing for faster ageing, while post yield stresses push the material further up the energy landscape where barriers are more easily overcome[106]. This shall be expanded upon in chapter 4, where the role of compressive stresses on the thermomechanical behaviour of polystyrene is probed.

The study of polymer response to mechanical stimuli requires the ability to characterise the applied stresses and strains and how the material deforms in response. The next section is therefore devoted to continuum mechanics, which form the basis of three-dimensional stress-strain analysis.

1.4 Continuum mechanics

Continuum mechanics, as the name suggests, is the analysis of the mechanical behaviour of bodies treated as though they were composed of continuous mass distributions, as opposed to discrete particles. While some deviations from continuum behaviour have been reported at few and sub-nm scales[107,108], where intense stress fields may be concentrated over relatively few atoms, the stress and strain relations derived from continuum mechanics are generally accurate descriptors of nanomechanical systems for which the minimum length scale is above 10 nm. This is particularly true for materials lacking significant long-range order, such as the amorphous glassy polymers considered in this work. As such, the laws of elasticity, plasticity, fracture, and flow derived from continuum mechanics are powerful quantitative tools in the study of polymer nanomechanics. In this section, the basic laws of continuum mechanics are explained, including definition of the stress and strain tensors, linear isotropic elasticity, plastic yield conditions and flow rules, and linear and non-linear viscoelasticity. These shall form the basis of the mechanical analyses of polymer thin films in later chapters.

1.4.1 Stress, strain, and linear isotropic elasticity

The forces encountered in continuum mechanics can be broadly divided into two categories: body forces such as gravity which act throughout the whole volume, and surface forces generated from pushing/pulling, which result in non-uniform force distributions emanating from the loading point[109]. It is the latter which is of principal interest here. The relationship between the applied force/load and the resultant deformation in a body are typically expressed in terms of stress and strain, as these quantities relate the deformation to the intrinsic, non-dimensional properties of the material. An illustrative example of the concept of stress and strain is that of the simplest deformation mode; uniaxial tension of a linear elastic rectangular bar. This situation is shown in figure 1.4.1.

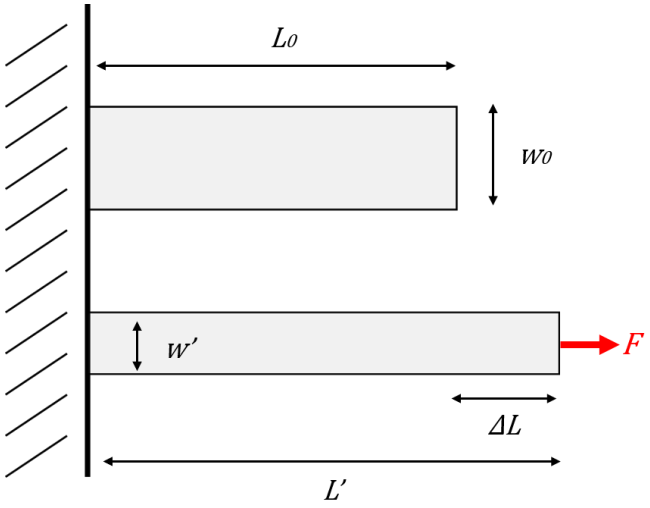

Figure 1.4.1 Uniaxial tensile deformation of an elastic rectangular block under a uniformly distributed force *F*.

A uniform tensile force F is applied across the free end of the bar. The engineering stress σ throughout the body is given by:

$$\sigma = \frac{F}{A_0} \tag{1.4.1}$$

Where A_0 is the undeformed cross-sectional area of the bar. The resultant engineering strain ε is given by the change in the bar's length divided by its initial length:

$$\varepsilon = \frac{\Delta\varepsilon}{\varepsilon_0} \tag{1.4.2}$$

The relationship between stress and strain is given by Hooke's law:

$$\sigma = E\varepsilon \tag{1.4.3}$$

Where E is the Young's modulus, a measure of the stiffness of the material. Typically, E falls between 1 – 4 GPa for most glassy polymers, while metals generally range between 50 – 500 GPa[110]. Accompanying strain parallel to the direction of applied force is a perpendicular contraction of the sample through the Poisson effect. This is quantified through Poisson's ratio ν, the ratio of lateral to normal strain:

$$\nu = \frac{\varepsilon_\perp}{\varepsilon} \tag{1.4.4}$$

Mathematically, ν is restricted to values between -1.0 and 0.5. Physically, values of $\nu >$ 0 correspond to lateral contraction of the sample upon tensile loading. The vast majority of real materials have Poisson's ratios between 0 and 0.5, while glassy polymers typically lie in the 0.2 – 0.4 range[111]. Negative values of ν correspond to lateral expansion of the sample and is seen in a special class of substances known as auxetic materials[112].

The strength of the stress-strain formulation is that it can be extended to more complex loading regimes and sample geometries, to completely describe the state of stress at any point within an arbitrarily shaped body. This scenario is considered in figure 1.4.2 for the body V subjected to loads F_1 and F_2. The stress state for an infinitesimal cubic element within V can be resolved into 9 components, with three acting on each orthogonal plane:

$$\boldsymbol{\sigma} = \begin{bmatrix} \sigma_{xx} & \sigma_{xy} & \sigma_{xz} \\ \sigma_{yx} & \sigma_{yy} & \sigma_{yz} \\ \sigma_{zx} & \sigma_{zy} & \sigma_{zz} \end{bmatrix} \tag{1.4.5}$$

$\boldsymbol{\sigma}$ is known as the stress tensor. Stresses acting parallel to the normal of a plane, i.e. σ_{xx}, σ_{yy}, σ_{zz} are referred to as normal stresses, while stresses acting perpendicular to the normal are called shear stresses. Equilibrium requires that the stress tensor be symmetric about the diagonal, reducing the number of components to six:

$$\boldsymbol{\sigma} = \begin{bmatrix} \sigma_{xx} & \sigma_{xy} & \sigma_{xz} \\ \sigma_{xy} & \sigma_{yy} & \sigma_{yz} \\ \sigma_{xz} & \sigma_{yz} & \sigma_{zz} \end{bmatrix} \tag{1.4.6}$$

It is often convenient to decompose $\boldsymbol{\sigma}$ into a hydrostatic component consisting of the mean of the normal stresses, and a deviatoric component made up of the remainder:

$$\boldsymbol{\sigma} = \begin{bmatrix} P & 0 & 0 \\ 0 & P & 0 \\ 0 & 0 & P \end{bmatrix} + \begin{bmatrix} \sigma_{xx} - P & \sigma_{xy} & \sigma_{xz} \\ \sigma_{xy} & \sigma_{yy} - P & \sigma_{yz} \\ \sigma_{xz} & \sigma_{yz} & \sigma_{zz} - P \end{bmatrix} \tag{1.4.7}$$

$$\boldsymbol{\sigma} = \boldsymbol{\sigma_H} + \boldsymbol{\sigma_D}$$

Where P is the hydrostatic pressure, and is equal to the first invariant of $\boldsymbol{\sigma}$:

$$P = \frac{1}{3} tr(\boldsymbol{\sigma}) = I_1 \tag{1.4.8}$$

This division of $\boldsymbol{\sigma}$ into hydrostatic and deviatoric components is pertinent as the hydrostatic component is responsible for volume change/dilation, while the deviatoric component, made up of shear terms, is responsible for shape change. Further, this division will be useful when considering plastic yield criteria, which are usually formulated in terms of the second invariant of the deviatoric stress tensor[113].

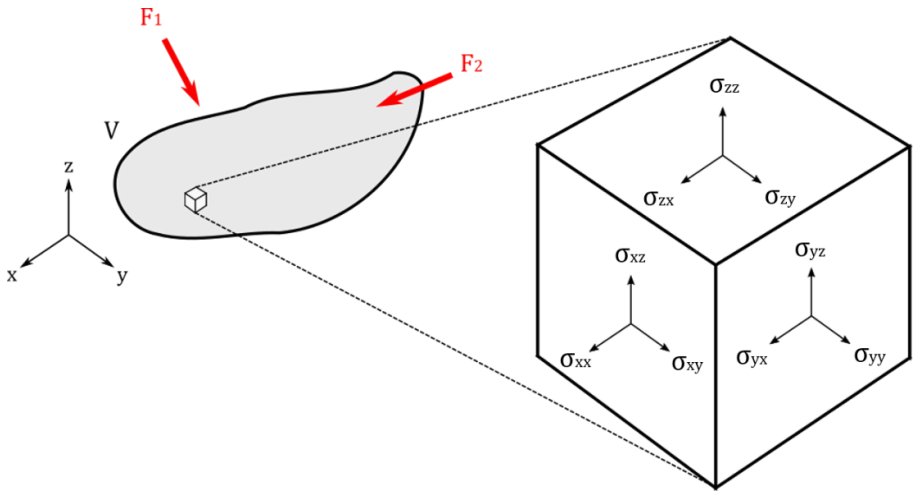

Figure 1.4.2 State of stress on an infinitesimal cubic element within the body *V*, subjected to arbitrary forces F_1 & F_2.

To create a local, generalised form of equation 1.4.2 for strain, stretching of the arbitrary volume V in the x-axis is considered, as shown in figure 1.4.3. Two points, P_1 and P_2, placed infinitesimally close together at x and $x + \partial x$ respectively undergo displacements $u_x(P_1)$ and $u_x(P_2)$, where u_x is a linear displacement field:

$$u_x = u_x(x, y, z) \tag{1.4.9}$$

The distance between P_1 and P_2 increases to $u_x(P_2) - u_x(P_1)$, and the strain is therefore given by:

$$\varepsilon_{xx} = \lim_{\partial x \to 0} \frac{u_x(P_2) - u_x(P_1)}{\partial x} = \frac{u_x(x + \partial x) - u_x(x)}{\partial x} \tag{1.4.10}$$

$$= \frac{\partial u_x}{\partial x}$$

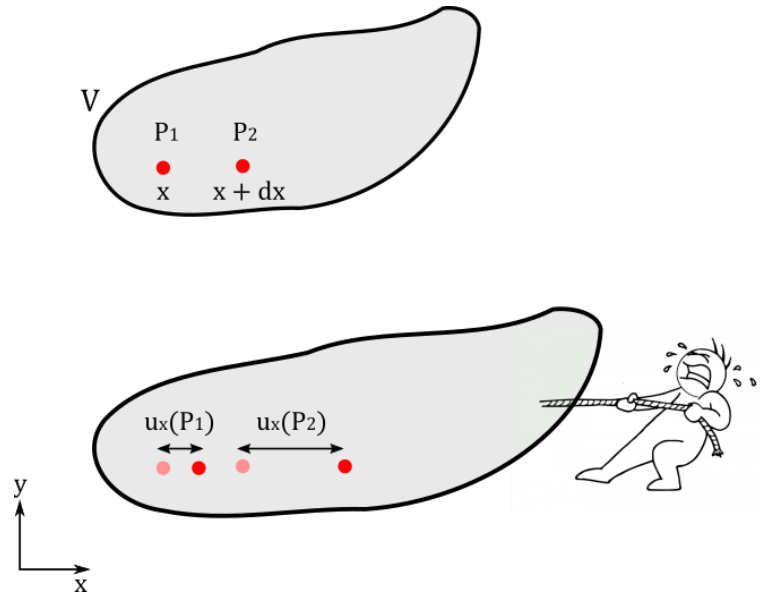

Figure 1.4.3 A displacement applied to the arbitrary volume *V* in the x-y plane. The points P_1 and P_2 placed at *x* and *x* + *dx* respectively undergo displacements $u_x(P_1)$ and $u_x(P_2)$

This definition is applicable to the normal strains ε_{xx}, ε_{yy}, *and* ε_{zz}, however as the displacement field defined above also contains rigid body rotations, these must be removed for an adequate definition of shear strains. For a displacement in the x-y plane, as shown in figure 1.4.4, it is rotations around the z-axis, ω_z, which must be factored out. This leads to the following definition of shear strain:

$$\varepsilon_{xy} = \frac{\partial u_y}{\partial x} - \omega_z = \frac{1}{2}\left[\frac{\partial u_y}{\partial x} + \frac{\partial u_x}{\partial y}\right] \tag{1.4.11}$$

As with stress, strain is most conveniently represented as a 2nd order symmetric tensor:

$$\boldsymbol{\varepsilon} = \begin{bmatrix} \varepsilon_{xx} & \varepsilon_{xy} & \varepsilon_{xz} \\ \varepsilon_{xy} & \varepsilon_{yy} & \varepsilon_{yz} \\ \varepsilon_{xz} & \varepsilon_{yz} & \varepsilon_{zz} \end{bmatrix} \tag{1.4.12}$$

Often it is convenient to express shear strain in terms of the engineering shear strain, γ_{ij}, where in the case of the x-y plane:

$$\gamma_{xy} = \left[\frac{\partial u_y}{\partial x} + \frac{\partial u_x}{\partial y}\right] = 2\varepsilon_{xy} \tag{1.4.13}$$

The differences between these two quantities are outlined in figure 1.4.4. The shear strain ε_{xy} is the average of the shear strain on the x face along the y direction, and on the y face in the x direction, whereas the engineering strain γ_{xy} is a measure of the total shear strain in the x-y plane. Generally, γ_{xy} is the more commonly used quantity, as it simply measured in experimental setups such as parallel plate rheometers.

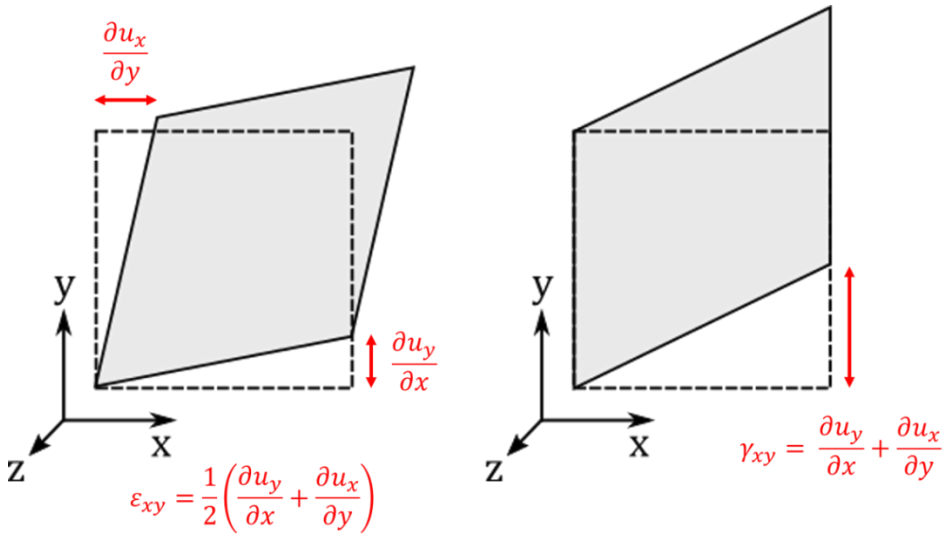

Figure 1.4.4 Differences between shear strain (left) and engineering shear strain (right). Shear strain is an average measure of the shear strains along each face, while engineering shear strain measures the total shear strain in the x-y plane. In both cases, rigid body rotation around the z-axis are removed.

The most general three-dimensional form of equation 1.4.3 that relates $\boldsymbol{\sigma}$ to $\boldsymbol{\varepsilon}$ is to assume that each independent stress is linearly related to each independent strain:

$$\begin{bmatrix}\sigma_{xx}\\ \sigma_{yy}\\ \sigma_{zz}\\ \sigma_{xz}\\ \sigma_{yz}\\ \sigma_{xy}\end{bmatrix} = \begin{bmatrix}C_{11} & C_{21} & C_{31} & C_{41} & C_{51} & C_{61}\\ C_{12} & C_{22} & C_{32} & C_{42} & C_{52} & C_{62}\\ C_{13} & C_{23} & C_{33} & C_{43} & C_{53} & C_{63}\\ C_{14} & C_{24} & C_{34} & C_{44} & C_{54} & C_{64}\\ C_{15} & C_{25} & C_{35} & C_{45} & C_{55} & C_{65}\\ C_{16} & C_{26} & C_{36} & C_{46} & C_{56} & C_{66}\end{bmatrix}\begin{bmatrix}\varepsilon_{xx}\\ \varepsilon_{yy}\\ \varepsilon_{zz}\\ \varepsilon_{xz}\\ \varepsilon_{yz}\\ \varepsilon_{xy}\end{bmatrix} \tag{1.4.14}$$

For amorphous materials such as non-crystalline glassy polymers, it can be assumed that the elastic response is isotropic and that no coupling exists between the normal

and shear stresses, nor between shear stresses and extensional strains[114]. This greatly simplifies equation 1.4.14 to the form:

$$\begin{bmatrix}\sigma_{xx}\\ \sigma_{yy}\\ \sigma_{zz}\\ \sigma_{xz}\\ \sigma_{yz}\\ \sigma_{xy}\end{bmatrix} = \begin{bmatrix} 1/E & -\nu/E & -\nu/E & 0 & 0 & 0\\ -\nu/E & 1/E & -\nu/E & 0 & 0 & 0\\ -\nu/E & -\nu/E & 1/E & 0 & 0 & 0\\ 0 & 0 & 0 & 1/2G & 0 & 0\\ 0 & 0 & 0 & 0 & 1/2G & 0\\ 0 & 0 & 0 & 0 & 0 & 1/2G\end{bmatrix}\begin{bmatrix}\varepsilon_{xx}\\ \varepsilon_{yy}\\ \varepsilon_{zz}\\ \varepsilon_{xz}\\ \varepsilon_{yz}\\ \varepsilon_{xy}\end{bmatrix} \tag{1.4.15}$$

Where G is the shear modulus, defined as:

$$G = \frac{E}{2(1+\nu)} \tag{1.4.16}$$

It is also useful to define the bulk modulus, K, which characterises the material response to purely hydrostatic loading:

$$K = \frac{E}{3(1-2\nu)} \tag{1.4.17}$$

The constants E, G, ν, and K fully describe an isotropic linear elastic material, however as they are interrelated, only two must be measured to characterise the elastic state.

Equation 1.4.15 is most succinctly expressed in index notation:

$$\sigma_{ij} = 2G\varepsilon_{ij} + \frac{2G\nu}{1-2\nu}\delta_{ij}\sum_{k}\sigma_{kk}\,, \qquad i,j,k = x,y,z \tag{1.4.18}$$

Where δ is the Kronecker delta. While equation 1.4.18 has been derived for a cartesian coordinate system, equivalent approaches may be adopted to obtain relationships for cylindrical or spherical coordinates.

The linear elastic relations derived above provide the simplest description of mechanical behaviour in a three-dimensional form and are accurate at describing the behaviour of glassy polymers well below their glassy transition temperature when subjected to low stresses at high loading rates. At higher stresses significant permanent deformation occurs as the material plastically yields. The relationships criteria describing yield and subsequent plastic flow are discussed in the next section for materials displaying no time dependent properties.

1.4.2 Plastic yield and flow rules

Within the elastic domain, all energy imparted to the system via distortion/strain is stored and is available to return the material to its original shape upon the removal of load. Upon reaching a critical stress defined by an appropriate yield criterion the material begins to deform permanently, involving the dissipation of energy through the sample in an irreversible process. The mechanisms for yield are numerous and will depend strongly on the material type. In crystalline materials dislocation motion and grain boundary migration featuring prominently[115], while in glassy polymers several mechanisms have been proposed, including deformation creating an excess of free volume, leading to material flowing locally in a viscous liquid-like manner in the shear transformation zone theory[116]. From a continuum mechanics perspective, the microscopic mechanism is somewhat irrelevant so long as the chosen criterion is phenomenologically accurate.

The one-dimensional stress-strain response of an elastic-perfectly plastic sample subjected to uniaxial tension is shown in figure 1.4.5. Unloading after the yield point σ_Y results in permanent sample length change, shown here by the residual plastic strain ε^p. For stresses above σ_Y there no longer exists an explicit relationship between stress and strain. As such, characterization of deformation in the plastic regime must be formulated in terms of an incremental theory, relating stress increments to increments of plastic strain $d\varepsilon^p$. Such a theory is called a plastic flow rule. This section shall focus on the operation of the Von Mises yield criterion and the Prandtl-Reuss flow equations, the most commonly used yield condition and flow rule combination.

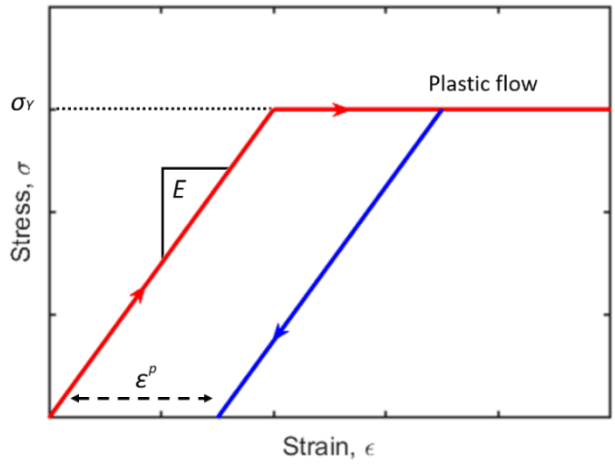

Figure 1.4.5 Stress-strain response of an elastic-perfectly plastic material under uniaxial tension.

The Von Mises criterion states that yield (the onset of irreversible deformation) occurs when the second invariant of the deviatoric stress tensor, J_2, reaches a critical value. Mathematically this is defined as:

$$J_2 = k^2 = \frac{\sigma_Y^2}{3} \tag{1.4.19}$$

Where k is the yield stress in pure shear. With the tensile test being the most common and well understood macroscopic deformation mode, it is practical to structure the yield condition so that yield occurs when whichever quantity is chosen to be monitored reaches a value of σ_Y, in an arbitrary mode of deformation. From equation 1.4.19 this implies that $\sqrt{3J_2}$ is the quantity of merit, and is termed the Von Mises equivalent stress, σ_{VM}:

$$\sigma_{VM} = \sqrt{3J_2} = \sqrt{\frac{1}{2}\left[\left(\sigma_{xx}^2 - \sigma_{yy}^2\right) + \left(\sigma_{yy}^2 - \sigma_{zz}^2\right) + \left(\sigma_{zz}^2 - \sigma_{xx}^2\right) + 6\left(\sigma_{xy}^2 + \sigma_{yz}^2 + \sigma_{xz}^2\right)\right]} \tag{1.4.20}$$

Yield therefore occurs when:

$$\sigma_{VM} = \sigma_Y \tag{1.4.21}$$

The Von Mises yield surface is shown in principal stress space in figure 1.4.6 as a cylinder centred around the hydrostatic axis. Importantly, the Von Mises surface is pressure invarient and the yield stress cannot be raised or lowered by the application of pressure. As such the Von Mises critereon serves only as a first order approximation for the behaviour of glassy polymers, whose yield properties may be strongly pressure

dependent. This point is revisited in chapter three, where glassy yielding in a hydrostatically dominated enviroment is encountered.

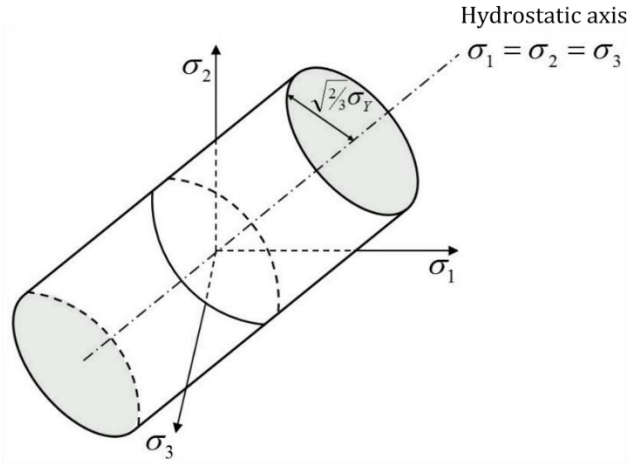

Figure 1.4.6 The Von Mises yield surface in principal stress space.

An important postulate of plasticity theory is that once a material begins to yield, further loading cannot increase J_2. As such, the material is bound to the yield surface in principal stress space and further loading may only increase the hydrostatic pressure content. Schematically, this is represented by sliding up and down the surface depicted in figure 1.4.6.

To arrive at a suitable incremental plastic flow rule it is first useful to decompose the total strain increment into elastic and plastic parts:

$$d\varepsilon = d\varepsilon^e + d\varepsilon^p \tag{1.4.22}$$

The plastic portion is again assumed to depend on the deviatoric stress tensor, $\boldsymbol{\sigma_D}$, with each component of plastic strain being linearly dependent on its corresponding $\boldsymbol{\sigma_D}$ component:

$$\frac{d\varepsilon_{xx}^p}{\sigma_{D_{xx}}} = \frac{d\varepsilon_{yy}^p}{\sigma_{D_{yy}}} = \frac{d\varepsilon_{zz}^p}{\sigma_{D_{zz}}} = \frac{d\varepsilon_{xy}^p}{\sigma_{D_{xy}}} = \frac{d\varepsilon_{yz}^p}{\sigma_{D_{yz}}} = \frac{d\varepsilon_{xz}^p}{\sigma_{D_{xz}}} = d\lambda \tag{1.4.23 a}$$

$$d\varepsilon_{ij}^p = \sigma_{D_{ij}} d\lambda \tag{1.4.23 b}$$

Where λ is the known as the plastic scalar multiplier. In terms of cartesian stress coordinates, this yields the Levy-Mises relations:

$$d\varepsilon_{xx}^{p} = \frac{2}{3}d\lambda\left[\sigma_{xx} - \frac{1}{2}\left(\sigma_{yy} + \sigma_{zz}\right)\right] \quad (1.4.24\ a)$$

$$d\varepsilon_{xy}^{p} = d\lambda\sigma_{xy} \quad (1.4.24\ b)$$

With equivalent terms for y and z. The total elastic-plastic response of a material undergoing yield may now be written as:

$$d\varepsilon_{ij} = \frac{1+\nu}{E}d\sigma_{ij} - \frac{\nu}{E}\delta_{ij}d\sigma_{kk} + d\lambda\sigma_{D\,ij} \quad (1.4.25)$$

Where the first two terms characterise the elastic response, and the latter the plastic response. Equation 1.4.25 is known as the Prandtl-Reuss flow rule and combined with the Von Mises yield criterion stated in equation 1.4.21 totally characterizes the plastic behaviour of a simple elastic-perfectly plastic material subjected to an arbitrary loading pattern.

The degree to which the mechanical response of glassy polymers can be accurately described by the elastic-plastic rules outlined above is highly dependent on the loading conditions to which they are subjected[117]. Well below the glass transition polymers typically show linear elastic behaviour followed by a plastic yield event. This shall form the basis of the analysis of the confined layer test in chapter three. Both the recorded moduli and the yield stress however are strain rate dependent. Further, both quantities are highly temperature dependent, decreasing with increasing temperature and effectively vanishing about the glass transition temperature. Polymers also display significant viscous flow properties which dominate the mechanical response above T_g and contribute significantly in the glassy domain. This combination of viscous and elastic response is termed viscoelasticity and derives from the highly entangled microstructure of amorphous polymers, covered in section 1.3. The next section shall introduce the essentials of linear viscoelastic (LVE) material modelling, as well as the idea of stress activated flow in the context of viscoelastic materials through the Eyring equation.

1.4.3 Linear viscoelasticity & the Eyring equation

A LVE material shows a time dependent strain response to an instantaneously applied stress, with both elastic and viscous flow properties present. This is shown in figure 1.4.7 (a), where a constant uniaxial stress σ is applied at t_0 and maintained until t_{end}.

The material contains an instantaneous (unrelaxed) elastic component, a delayed elastic component, and a viscous flow component, the last of which is not recovered upon removal of σ. The response of a perfectly elastic material is included for reference.

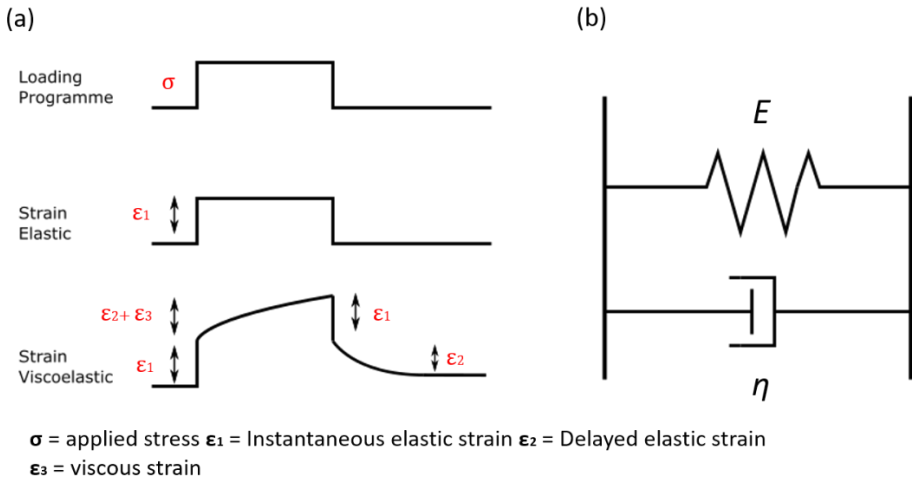

Figure 1.4.7 (a) Response of an elastic solid and a viscoelastic material to a step stress (b) Single component Kelvin-Voigt model of viscoelasticity. The material responds as a spring with stiffness *E* in parallel with a dashpot of viscosity η.

LVE is linear in the sense that each loading step makes an independent contribution to the final deformation and that these contributions may be added together to get the total deformation. LVE may be expressed in integral form via the Boltzmann representation in either relaxation (i) or retardation (ii) form[118]:

$$(i)\ \sigma(t) = \int_{-\infty}^{t} E(t-t')\dot{\varepsilon}(t')dt\,, \qquad (ii)\ \varepsilon(t) = \int_{-\infty}^{t} D(t-t')\dot{\sigma}(t')dt' \tag{1.4.26}$$

Where *E(t)* is the stress relaxation modulus and *D(t)* is the creep compliance. Time-dependent response of polymers shall be studied through stress-controlled creep tests in this work and therefore prominence is given to the retardation form here. The simplest form of LVE assumes that the Hookean elastic and Newtonian viscous responses are additive:

$$\sigma(t) = E\varepsilon + \eta\dot{\varepsilon} \tag{1.4.27}$$

This is the Kelvin-Voigt (KV) formulation and is represented schematically by an elastic spring and a viscous dashpot in parallel in figure 1.4.7 (b). The strain response of a KV material to a step stress is given by:

$$\varepsilon(t) = \frac{\sigma_0}{E}\left(1 - e^{-t/\tau_{KV}}\right) = \sigma_0 D(t), \qquad \tau_{KV} = \frac{\eta}{E} \tag{1.4.28}$$

Where τ_{KV} is the retardation time. As discussed in section 1.3.3 polymers display a spectrum of time dependent relaxation mechanisms. The KV model can be generalised to accommodate more than one mechanism by connecting several individual KV elements in series, as shown in figure 1.4.8 (a), where each ith element represents an individual relaxation mode, and D_0 and η_0 represent the immediate (unrelaxed) elastic and long-term flow responses respectively. Mathematically this is written as:

$$D(t) = D_0 + \left[\sum_{i=1}^{n} D_i\left(1 - e^{t/\tau_i}\right)\right] + \frac{t}{\eta_0} \tag{1.4.29}$$

D(t) for a typical thermoplastic is shown in figure 1.4.8 (b).

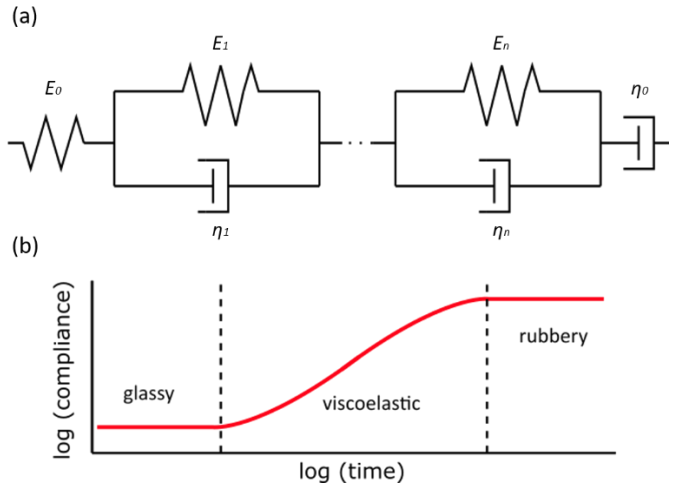

Figure 1.4.8 (a) Generalised Kelvin-Voigt model with *n* individual KV units. An instantaneous elastic spring and long term viscous flow dashpot are added for completeness. (b) Typical creep compliance response of a viscoelastic thermoplastic.

LVE implies that creep compliance is invariant with stress. In reality, this is found to be true only for a small regime of low stresses[119]. This is shown figure 1.4.9 (a). A solution to this problem was formulated by *Eyring*[120]. The viscosity of the dashpot in the KV model may be treated as stress-dependent under the following scheme: Eyring

supposed that macroscopic deformation of the polymer required segments/monomers to overcome a potential energy barrier ΔU to move locally in the direction of deformation. With no applied stresses, hops over ΔU in the forward and backward direction occur at the same frequency, given by:

$$\nu_{forward,backward} = \nu = \nu_0 \exp\left(\frac{\Delta U}{k_B T}\right) \tag{1.4.30}$$

Where ν_0 is a constant exponential pre-factor. When a stress is applied, the barrier is tiled so that hopping preferentially occurs in the direction in which σ is applied. This is shown pictorially in figure 1.4.9 (b) and results in a net forward hopping frequency of:

$$\nu_{net} = \nu_{forward} - \nu_{backward} = \nu_0 \exp\left(\frac{\Delta U}{k_B T}\right) \sinh\left(\frac{V^* \sigma}{k_B T}\right) \tag{1.4.31}$$

Where V^* is an activation volume for the segmental/monomer dislocation event. A viscosity $\eta(\sigma)$ may be calculated under the assumption that the macroscopic strain rate is of the same form as ν_{net}:

$$\eta(\sigma) = \frac{\sigma}{\dot{\varepsilon}(\sigma)} = \frac{\sigma}{\dot{\varepsilon_0} \exp\left(-\frac{\Delta U}{k_B T}\right) \sinh\left(\frac{\sigma V^*}{k_B T}\right)} \tag{1.4.32}$$

Where $\dot{\varepsilon_0}$ is a pre-factor similar to ν_0. This expression may be further simplified by introducing a characteristic stress σ^* and a zero-stress viscosity η_0:

$$\sigma^* = \frac{k_B T}{V^*}, \qquad \eta_0 = \frac{\sigma^*}{\dot{\varepsilon_0}} \exp\left(-\frac{\Delta U}{k_B T}\right) \tag{1.4.33}$$

The stress dependent viscosity becomes:

$$\eta(\sigma) = \eta_0 a_\sigma(\sigma), \qquad a_\sigma(\sigma) = \frac{\sigma/\sigma_0}{\sinh(\sigma/\sigma_0)} \tag{1.4.34}$$

Where a_σ is a stress dependent shift factor. At stresses below σ_0, $a_\sigma = 1$ and the viscosity is Newtonian. This defines the LVE regime. The total non-linear viscoelastic creep compliance may now be written as:

$$D(t) = D_0 + \left[\sum_{i=1}^{n} D_i \left(1 - e^{-t/\tau_i(\sigma)}\right)\right] + \frac{t}{\eta_0}, \qquad \tau_i(\sigma) = \tau_i a_\sigma(\sigma) \tag{1.4.35}$$

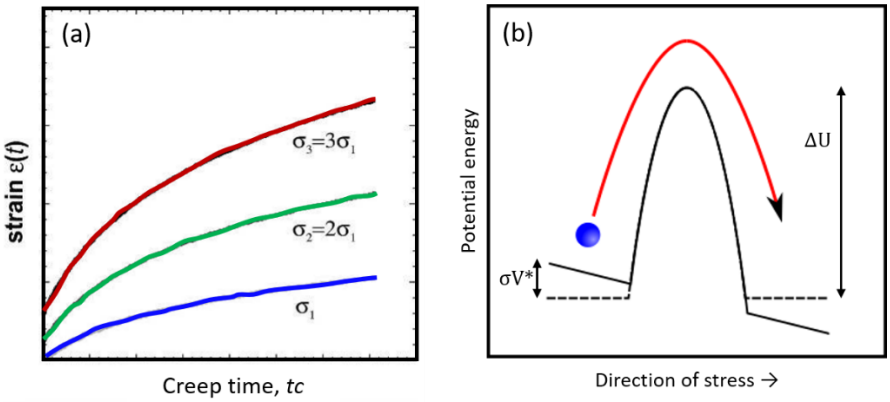

Figure 1.4.9 (a) Scaling of creep compliance with stress for a non-linear viscoelastic material. *D(t)* increases with increasing *σ*. Reproduced with permission from [119] (b) Effect of applied stress on segmental/monomer motion. *σ* shifts the potential energy landscape to promote motion in the direction of stress.

The topics covered in this chapter present a picture of the molecular origins of the mechanical behaviour of polymers in both the glassy and melt state. The mechanical framework needed to study polymer deformation in exotic geometries is also presented. While some specific topics (e.g. molecular mobility during deformation) are left to later research chapters, the contents of this chapter should provide a firm theoretical understanding for what is to follow. Chapter three will aim to provide a similar experimental footing.

Bibliography

1. Dienwiebel, M. *et al.* Superlubricity of Graphite. *Phys. Rev. Lett.* **92**, 126101 (2004).
2. Greer, J. R. & De Hosson, J. T. M. Plasticity in small-sized metallic systems: Intrinsic versus extrinsic size effect. *Prog. Mater. Sci.* **56**, 654–724 (2011).
3. Greer, J. R., Oliver, W. C. & Nix, W. D. Size dependence of mechanical properties of gold at the micron scale in the absence of strain gradients. *Acta Mater.* **53**, 1821–1830 (2005).
4. Lee, C., Wei, X., Kysar, J. W. & Hone, J. Measurement of the elastic properties and intrinsic strength of monolayer graphene. *Science* **321**, 385–8 (2008).
5. Treacy, M. M. J., Ebbesen, T. W. & Gibson, J. M. Exceptionally high Young's modulus observed for individual carbon nanotubes. *Nature* **381**, 678–680 (1996).
6. Oishi, A. *et al.* High performance CMOSFET technology for 45nm generation and scalability of stress-induced mobility enhancement technique. in *IEEE InternationalElectron Devices Meeting, 2005. IEDM Technical Digest.* 229–232 (IEEE, 2005). doi:10.1109/IEDM.2005.1609314
7. Vettiger, P. *et al.* The millipede nanotechnology entering data storage. *IEEE Trans. Nanotechnol.* **1**, 39–55 (2002).
8. King, W. P. *et al.* Atomic force microscope cantilevers for combined thermomechanical data writing and reading. *Appl. Phys. Lett.* **78**, 1300–1302 (2001).
9. Lapedus, M. Whatever Happened to Nanoimprint Litho? *Semiconductor Engineering* (2018).
10. Ndieyira, J. W. *et al.* Nanomechanical detection of antibiotic–mucopeptide binding in a model for superbug drug resistance. *Nat. Nanotechnol.* **3**, 691–696 (2008).
11. Fritz, J. *et al.* Translating biomolecular recognition into nanomechanics. *Science* **288**, 316–8 (2000).
12. Nanomechanical Analysis – Bio Nano. Available at: http://www.bio-nano-consulting.com/innovation-consulting/technical-due-diligence/nanomechanical-analysis. (Accessed: 16th August 2018)
13. Chaste, J. *et al.* A nanomechanical mass sensor with yoctogram resolution. *Nat. Nanotechnol.* **7**, 301–304 (2012).
14. Bleszynski-Jayich, A. C. *et al.* Persistent currents in normal metal rings. *Science* **326**, 272–5 (2009).
15. Cheng, Z. G. & Beamish, J. Plastic Deformation in a Quantum Solid: Dislocation Avalanches and Creep in Helium. *Phys. Rev. Lett.* **121**, (2018).
16. Kumar, D. & Sharma, R. C. Advances in conductive polymers. *Eur. Polym. J.* **34**, 1053–1060 (1998).
17. Anderson, J. M. & Shive, M. S. Biodegradation and biocompatibility of PLA and

PLGA microspheres. *Adv. Drug Deliv. Rev.* **28**, 5–24 (1997).

18. Ward, I. M. & Hadley, D. W. *An Introduction to the Mechanical Properties of Solid Polymers*. (John Wiley & Sons, 1993).

19. Saeidijavash, M. & Garg, J. High thermal conductivity polymers. *Bull. Am. Phys. Soc.* **Volume 60**, **Number 1**, (2015).

20. Hall, D. B., Underhill, P. & Torkelson, J. M. Spin coating of thin and ultrathin polymer films. *Polym. Eng. Sci.* **38**, 2039–2045 (1998).

21. Chen, N. *et al.* Nanoscale, conformal polysiloxane thin film electrolytes for three-dimensional battery architectures. *Mater. Horizons* **2**, 309–314 (2015).

22. Chou, S. Y., Krauss, P. R. & Renstrom, P. J. Nanoimprint Lithography. *J. Vac. Sci. Technol. B, Nanotechnol. Microelectron. Mater. Process. Meas. Phenom.* **14**, 4129–4133 (1996).

23. Zhang, N., Chu, J. S., Byrne, C. J., Browne, D. J. & Gilchrist, M. D. Replication of micro/nano-scale features by micro injection molding with a bulk metallic glass mold insert. *J. Micromechanics Microengineering* **22**, 065019 (2012).

24. Ehrenstein, G. W. (Gottfried W. & Theriault, R. P. (Richard P. . *Polymeric materials : structure, properties, applications*. (Hanser, 2001).

25. de Gennes, P. G. & Prost, J. *The physics of liquid crystals*. (Clarendon Press, 1993).

26. Roth, C. B. Mobility and stability of glasses. *J. Polym. Sci. Part B Polym. Phys.* **48**, 2558–2560 (2010).

27. Salez, T., Salez, J., Dalnoki-Veress, K., Raphaël, E. & Forrest, J. A. Cooperative strings and glassy interfaces. *Proc. Natl. Acad. Sci. U. S. A.* **112**, 8227–31 (2015).

28. Pharr, G. M. & Oliver, W. C. Measurement of Thin Film Mechanical Properties Using Nanoindentation. *MRS Bull.* **17**, 28–33 (1992).

29. Oliver, W. C. & Pharr, G. M. Measurement of hardness and elastic modulus by instrumented indentation: Advances in understanding and refinements to methodology. *J. Mater. Res.* **19**, 3–20 (2004).

30. Oliver, W. C. & Pharr, G. M. An improved technique for determining hardness and elastic modulus using load and displacement sensing indentation experiments. *J. Mater. Res.* **7**, 1564–1583 (1992).

31. Ellison, C. J. & Torkelson, J. M. The distribution of glass-transition temperatures in nanoscopically confined glass formers. *Nat. Mater.* **2**, 695–700 (2003).

32. Priestley, R. D., Ellison, C. J., Broadbelt, L. J. & Torkelson, J. M. Structural relaxation of polymer glasses at surfaces, interfaces, and in between. *Science* **309**, 456–9 (2005).

33. McKenna, G. B. Mechanical rejuvenation in polymer glasses: factor fallacy ? *J. Phys. Condens. Matter* **15**, S737 (2003).

34. Koh, Y. P., Gao, S. & Simon, S. L. Structural recovery of a single polystyrene thin film using Flash DSC at low aging temperatures. *Polymer (Guildf).* **96**,

182–187 (2016).

35. Simon, S. L., Sobieski, J. W. & Plazek, D. J. Volume and enthalpy recovery of polystyrene. *Polymer (Guildf).* **42**, 2555–2567 (2001).

36. Bernazzani, P. & Simon, S. L. Volume recovery of polystyrene: evolution of the characteristic relaxation time. *J. Non. Cryst. Solids* **307**–**310**, 470–480 (2002).

37. Echeverría, I., Kolek, P. L., Plazek, D. J. & Simon, S. L. Enthalpy recovery, creep and creep–recovery measurements during physical aging of amorphous selenium. *J. Non. Cryst. Solids* **324**, 242–255 (2003).

38. Bending, B., Christison, K., Ricci, J. & Ediger, M. D. Measurement of segmental mobility during constant strain rate deformation of a poly(methyl methacrylate) glass. *Macromolecules* **47**, 800–806 (2014).

39. Ediger, M. D., Lee, H. N., Paeng, K. & Swallen, S. F. Dye reorientation as a probe of stress-induced mobility in polymer glasses. *J. Chem. Phys.* **128**, (2008).

40. Riggleman, R. A., Lee, H. N., Ediger, M. D. & De Pablo, J. J. Free volume and finite-size effects in a polymer glass under stress. *Phys. Rev. Lett.* **99**, 1–4 (2007).

41. Kim, J. W., Medvedev, G. A. & Caruthers, J. M. Nonlinear stress relaxation in an epoxy glass and its relationship to deformation induced mobility. *Polymer (Guildf).* **54**, 3949–3960 (2013).

42. Chou, S. Y., Krauss, P. R. & Renstrom, P. J. Imprint of sub-25 nm vias and trenches in polymers. *Appl. Phys. Lett.* **67**, 3114–3116 (1995).

43. Chou, S. Y., Krauss, P. R. & Renstrom, P. J. Imprint Lithography with 25-Nanometer Resolution. *Science (80-.).* **272**, 85–87 (1996).

44. *International technology roadmap for semiconductors - 2003 edition: Lithography*.

45. *The International Roadmap for Semiconductors - 2013 Edition*.

46. Sotomayor Torres, C. M. Alternative lithography. *Mater. Sci.* 446 (2002). doi:10.1007/978-1-4419-9204-8_1

47. Jones, R. A. L. (Richard A. L. *Soft condensed matter*. (Oxford University Press, 2002).

48. Hosler, D., Burkett, S. L. & Tarkanian, M. J. Prehistoric polymers: rubber processing in ancient mesoamerica. *Science* **284**, 1988–91 (1999).

49. Scarborough, V. L. (Vernon L. & Wilcox, D. R. *The Mesoamerican ballgame*. (University of Arizona Press, 1991).

50. Baekeland, L. H. The synthesis, constitution, and uses of Bakelite. *Ind. Eng. Chem.* **1**, 149–161 (1909).

51. Pendhari, S. S., Kant, T. & Desai, Y. M. Application of polymer composites in civil construction: A general review. *Compos. Struct.* **84**, 114–124 (2008).

52. Barlow, C. Y. & Morgan, D. C. Polymer film packaging for food: An environmental assessment. *Resour. Conserv. Recycl.* **78**, 74–80 (2013).

53. Mack, C. A. Development of Positive Photoresists. *J. Electrochem. Soc.* **134**, 148

(1987).

54. Shaw, J. M., Gelorme, J. D., LaBianca, N. C., Conley, W. E. & Holmes, S. J. Negative photoresists for optical lithography. *IBM J. Res. Dev.* **41**, 81–94 (1997).

55. Sperling, L. . *Introduction to Physical Polymer Science*. (Wiley-Interscience, 2005).

56. E Karasz, by F. & Bair, E. Thermal Properties of Atactic and Isotactic Polystyrene. *J. Phys. Chem.* **69**, 2657–2667 (1965).

57. Hult, A., Johansson, M. & Malmström, E. Hyperbranched Polymers. in *Branched Polymers II* 1–34 (Springer Berlin Heidelberg, 1999). doi:10.1007/3-540-49780-3_1

58. Bauer, B. J. & Fetters, L. J. Synthesis and Dilute-Solution Behavior of Model Star-Branched Polymers. *Rubber Chem. Technol.* **51**, 406–436 (1978).

59. Nielsen, L. E. Cross-Linking–Effect on Physical Properties of Polymers. *J. Macromol. Sci. Part C* **3**, 69–103 (1969).

60. Gennes, P.-G. de. *Scaling concepts in polymer physics*. (Cornell University Press, 1979).

61. Rowland, H. D., King, W. P., Pethica, J. B. & Cross, G. L. W. Molecular Confinement Accelerates Deformation of Entangled Polymers During Squeeze Flow. *Science* 720–724 (2008).

62. Mukhopadhyay, M. K. *et al.* Thickness Induced Structural Changes in Polystyrene Films. *Phys. Rev. Lett.* **101**, 115501 (2008).

63. and, O. N. T. & Zbankov, R. G. FTIR Spectroscopic Evidence of Lowered Chain Interpenetration in Thin Polymer Films. (2004). doi:10.1021/MA049492G

64. Si, L., Massa, M. V., Dalnoki-Veress, K., Brown, H. R. & Jones, R. A. L. Chain Entanglement in Thin Freestanding Polymer Films. *Phys. Rev. Lett.* **94**, 127801 (2005).

65. de Gennes, P. G. Reptation of a Polymer Chain in the Presence of Fixed Obstacles. *J. Chem. Phys.* **55**, 572–579 (1971).

66. Doi, M. & Edwards, S. F. Dynamics of concentrated polymer systems. Part 1.—Brownian motion in the equilibrium state. *J. Chem. Soc., Faraday Trans. 2* **74**, 1789–1801 (1978).

67. Doi, M. (Masao) & Edwards, S. F. (Sam F. *The theory of polymer dynamics*. (Clarendon Press, 1986).

68. Berry, G. C. & Fox, T. . The viscosity of polymers and their concentrated solutions. in *Fortschritte der Hochpolymeren-Forschung* 261–357 (Springer-Verlag, 1968). doi:10.1007/BFb0050985

69. Rouse, P. E. A Theory of the Linear Viscoelastic Properties of Dilute Solutions of Coiling Polymers. *J. Chem. Phys.* **21**, 1272–1280 (1953).

70. Zimm, B. H. Dynamics of Polymer Molecules in Dilute Solution: Viscoelasticity, Flow Birefringence and Dielectric Loss. *J. Chem. Phys.* **24**, 269–278 (1956).

71. Roth, C. B. *Polymer glasses*. (CRC Press, 2016).

72. McKenzie, I. *et al.* Direct measurements of the temperature, depth and processing dependence of phenyl ring dynamics in polystyrene thin films by ß-detected NMR. *Soft Matter* (2018). doi:10.1039/C8SM00812D

73. McKenna, G. B. & Simon, S. L. *50th Anniversary Perspective* : Challenges in the Dynamics and Kinetics of Glass-Forming Polymers. *Macromolecules* **50**, 6333–6361 (2017).

74. Anderson, P. W. Through the glass lightly. *Science (80-.).* **267**, 1618–1618 (1995).

75. Debenedetti, P. G. & Stillinger, F. H. Supercooled liquids and the glass transition. *Nature* **410**, 259–267 (2001).

76. Angell, C. A., Ngai, K. L., McKenna, G. B., McMillan, P. F. & Martin, S. W. Relaxation in glassforming liquids and amorphous solids. *J. Appl. Phys.* **88**, 3113 (2000).

77. Angell, C. A. Formation of glasses from liquids and biopolymers. *Science* **267**, 1924–35 (1995).

78. Hunter, G. L. & Weeks, E. R. The physics of the colloidal glass transition. *Reports Prog. Phys.* **75**, 066501 (2012).

79. Schweizer, K. S. & Saltzman, E. J. Entropic barriers, activated hopping, and the glass transition in colloidal suspensions. *J. Chem. Phys.* **119**, 1181–1196 (2003).

80. Busch, R., Bakke, E. & Johnson, W. L. Viscosity of the supercooled liquid and relaxation at the glass transition of the Zr46.75Ti8.25Cu7.5Ni10Be27.5 bulk metallic glass forming alloy. *Acta Mater.* **46**, 4725–4732 (1998).

81. Santangelo, P. G. & Roland, C. M. Molecular Weight Dependence of Fragility in Polystyrene. *Macromolecules* **31**, 4581–4585 (1998).

82. Gotze, W. & Sjogren, L. Relaxation processes in supercooled liquids. *Reports Prog. Phys.* **55**, 241–376 (1992).

83. Stillinger, F. H. A Topographic View of Supercooled Liquids and Glass Formation. *Science (80-.).* **267**, 1935–1939 (1995).

84. Hecksher, T., Nielsen, A. I., Olsen, N. B. & Dyre, J. C. Little evidence for dynamic divergences in ultraviscous molecular liquids. *Nat. Phys.* **4**, 737–741 (2008).

85. McKenna, G. B. Diverging views on glass transition. *Nat. Phys.* **4**, 673–673 (2008).

86. Malins, A., Eggers, J., Tanaka, H. & Royall, C. P. Lifetimes and lengthscales of structural motifs in a model glassformer. *Faraday Discuss.* **167**, 405 (2013).

87. Starr, F. W., Douglas, J. F. & Sastry, S. The relationship of dynamical heterogeneity to the Adam-Gibbs and random first-order transition theories of glass formation. *J. Chem. Phys.* **138**, 12A541 (2013).

88. Pazmiño Betancourt, B. A., Douglas, J. F. & Starr, F. W. String model for the dynamics of glass-forming liquids. *J. Chem. Phys.* **140**, 204509 (2014).

89. Reichman, D. R. & Charbonneau, P. Mode-coupling theory. *J. Stat. Mech. Theory Exp.* **2005**, P05013 (2005).

90. Das, S. P. Mode-coupling theory and the glass transition in supercooled liquids. *Rev. Mod. Phys.* **76**, 785–851 (2004).

91. Adam, G. & Gibbs, J. H. On the Temperature Dependence of Cooperative Relaxation Properties in Glass-Forming Liquids. *J. Chem. Phys.* **43**, 139–146 (1965).

92. Cohen, M. H. & Turnbull, D. Molecular Transport in Liquids and Glasses. *J. Chem. Phys.* **31**, 1164–1169 (1959).

93. White, R. P. & Lipson, J. E. G. Thermodynamic treatment of polymer thin-film glasses. *Phys. Rev. E - Stat. Nonlinear, Soft Matter Phys.* **84**, 1–6 (2011).

94. Dlubek, G., Kilburn, D. & Alam, M. A. Comments to the paper "The need to reconsider tradional free volume theory for polymer electrolytes". *Electrochim. Acta* **49**, 5241–5247 (2004).

95. R. Casalini, †,‡, M. Paluch, †,§ and & C. M. Roland*, †. Dynamics of Salol at Elevated Pressure. (2003). doi:10.1021/JP0267297

96. Roland, C. M., Hensel-Bielowka, S., Paluch, M. & Casalini, R. Supercooled dynamics of glass-forming liquids and polymers under hydrostatic pressure. *Reports Prog. Phys.* **68**, 1405–1478 (2005).

97. Paluch, M., Roland, C. M., Pawlus, S., Zioło, J. & Ngai, K. L. Does the Arrhenius Temperature Dependence of the Johari-Goldstein Relaxation Persist above T g ? *Phys. Rev. Lett.* **91**, 115701 (2003).

98. Struik, L. C. E. *Physical aging in amorphous polymers and other materials*. (1977).

99. MOYNIHAN, C. T., EASTEAL, A. J., BOLT, M. A. & TUCKER, J. Dependence of the Fictive Temperature of Glass on Cooling Rate. *J. Am. Ceram. Soc.* **59**, 12–16 (1976).

100. Hutchinson, J. M. Physical aging of polymers. *Prog. Polym. Sci.* **20**, 703–760 (1995).

101. Kovacs, A. J. Transition vitreuse dans les polymères amorphes. Etude phénoménologique. in *Fortschritte Der Hochpolymeren-Forschung* 394–507 (Springer-Verlag, 1964). doi:10.1007/BFb0050366

102. and, Y. Z. & McKenna*, G. B. Structural Recovery in a Model Epoxy: Comparison of Responses after Temperature and Relative Humidity Jumps. (2003). doi:10.1021/MA025930C

103. McKenna, G. B. Mechanical rejuvenation in polymer glasses: fact or fallacy? *J. Phys. Condens. Matter* **15**, S737–S763 (2003).

104. Warren, M. & Rottler, J. Deformation-induced accelerated dynamics in polymer glasses. *J. Chem. Phys.* **133**, 164513 (2010).

105. Paeng, K., Swallen, S. F. & Ediger, M. D. Direct measurement of molecular motion in freestanding polystyrene thin films. *J. Am. Chem. Soc.* **133**, 8444–8447 (2011).

106. Chen, K. & Schweizer, K. S. Theory of aging, rejuvenation, and the nonequilibrium steady state in deformed polymer glasses. *Phys. Rev. E - Stat. Nonlinear, Soft Matter Phys.* **82**, 1–12 (2010).

107. Shimada, T., Ouchi, K., Chihara, Y. & Kitamura, T. Breakdown of Continuum Fracture Mechanics at the Nanoscale. *Sci. Rep.* **5**, 8596 (2015).

108. Tapasztó, L. *et al.* Breakdown of continuum mechanics for nanometre-wavelength rippling of graphene. *Nat. Phys.* **8**, 739–742 (2012).

109. Johnson, K. L. *Contact Mechanics*. (Cambridge University Press, 1985). doi:10.1017/CBO9781139171731

110. The Engineering Toolbox: Young's Modulus - Tensile and Yield Strength for common Materials. (2018). Available at: https://www.engineeringtoolbox.com/young-modulus-d_417.html. (Accessed: 11th October 2018)

111. Greaves, G. N., Greer, A. L., Lakes, R. S. & Rouxel, T. Poisson's ratio and modern materials. *Nat. Mater.* **10**, 823–837 (2011).

112. Evans, K. E. Auxetic polymers: a new range of materials. *Endeavour* **15**, 170–174 (1991).

113. Quinson, R., Perez, J., Rink, M. & Pavan, A. Yield criteria for amorphous glassy polymers. *J. Mater. Sci.* **32**, 1371–1379 (1997).

114. Ward, I. M. & Sweeney, J. *The Mechanical Properties of Solid Polymers*. (John Wiley & Sons, 2004).

115. Lubliner, J. *Plasticity theory*. (Dover Publications, 2008).

116. Argon, A. S. *The physics of deformation and fracture of polymers*. (Cambridge University Press, 2013).

117. Rottler, J. & Robbins, M. O. Yield conditions for deformation of amorphous polymer glasses. *Phys. Rev. E - Stat. Physics, Plasmas, Fluids, Relat. Interdiscip. Top.* **64**, 8 (2001).

118. Klompen, E. T. J. Mechanical properties of solid polymers: consitutive modelling of long and short term behaviour. (Technische Universiteit Eindhoven, 2005).

119. Tweedie, C. A. & Van Vliet, K. J. Contact creep compliance of viscoelastic materials via nanoindentation. *J. Mater. Res.* **21**, 1576–1589 (2006).

120. Eyring, H. Viscosity, Plasticity, and Diffusion as Examples of Absolute Reaction Rates. *J. Chem. Phys.* **4**, 283–291 (1936).

Chapter 2:
Experimental Techniques

This chapter outlines the principal experimental techniques and sample preparation methods used throughout the course of this work. The basic operating principles for each technique is outlined, however experiment specific details are left to the relevant chapter. In keeping with the general theme of this research, the principal techniques discussed are related to the fabrication, characterisation, and mechanical patterning of polymer thin films. Special attention is given to flat punch nanoindentation and thermal nanoimprint lithography, as these are the two techniques of primary investigation in this work. As each section of this chapter is written as a standalone piece, it may be used a reference for future chapters, or read independently.

2.1 Flat punch nanoindentation

Nanoindentation is a technique used to probe the mechanics of small volumes of materials and is the principle method for the measurement of the mechanical properties of nanostructured matter. The technique relies on compressive loads applied to the sample via a geometrically well-defined tip. Unlike traditional macroscopic hardness tests, nanoindentation provides in-situ measurement of the local displacement of the tip into the sample surface, and as such no independent measurement of residual strain is necessary. Coupling sub nanonewton load accuracy with a large dynamic load range, as well as sub nanometre displacement resolution, nanoindentation has been used to study the mechanics of all classes of materials. While originally developed for high hardness and stiffness materials such as metals and ceramics, nanoindentation has been extended to soft biological tissues and is capable of capturing the time-dependent mechanics encountered in polymer thin films.

2.1.1 General nanoindentation

Traditional microhardness tests such as the Brinell or Vickers tests rely on an external measure of the residual impression left in the sample to determine mechanical properties, typically performed via optical microscopy[1]. Increasing interest in the mechanics of sub-micron thin films and graded surfaces modified through processes such as ion implantation[2] in the latter half of the twentieth century necessitated the development of techniques independent of optical measurement, which produced excessive uncertainties at this scale[3]. Development of in-situ depth sensing techniques[4–8] and advances in the understanding of contact mechanics of sharp tipped indenters into elastic-plastic halfspaces[9–13] over the course of the 1970's and 80's lead to the emergence of nanoindentation as a method primarily for the extraction of Young's modulus and hardness at micron and nanometre scales. Conventionally this is performed via the *Oliver-Pharr*[14,15] method, wherein it is assumed that during unloading all recovery in the direction of the sample surface normal is elastic. The contact stiffness S at the initial portion of the unloading curve is used to calculate the Young's modulus via the relation:

$$S = \frac{dL}{dh} = \beta \frac{2}{\sqrt{\pi}} E^* \sqrt{A_{proj}} \tag{2.1.1}$$

Where L is the applied load, h is the depth of penetration into the surface, β is a dimensionless tip geometry correction factor A_{proj} is the projected area of contact, and E^* is the reduced modulus of the indenter and sample defined by:

$$\frac{1}{E^*} = \frac{1-\nu^2}{E} + \frac{1-\nu_i^2}{E_i} \tag{2.1.2}$$

For a perfect Berkovich indenter (a three-sided pyramid with an included half angle of 65.27°) A_{proj} is a function of the depth at which contact is made between the indenter and the surface when sink-in of the surrounding material is accounted for, h_c:

$$A_{proj}^{berk} = 24.5 h_c^2 \tag{2.1.3}$$

Experimentally, A_{proj} for a given tip is given in the series formulation:

$$A_{proj}(h_c) = \sum C_n (h_c)^{2-n} \tag{2.1.4}$$

Where the higher order constants are representative of imperfections in tip geometry. These are calculated via indentation of a reference material such as fused silica or

polished aluminium. hc is found to be a function of applied load and displacement of the tip into the surface via Sneddon's relationship[16]:

$$h_c = h_{max} - h_s = h_{max} - \epsilon\left(\frac{L}{S}\right) \tag{2.1.5}$$

Where h_s is the 'sink-in' of the surface surrounding contact, and ϵ is a constant dependent on the indenter geometry ($\epsilon = 0.75$ for a Berkovich tip.) Accurate tracking of L and h_{max} coupled with a well-defined tip geometry allows calculation of the Young's modulus via equation 2.2 and hardness H via:

$$H = \frac{L_{max}}{A_{proj}} \tag{2.1.6}$$

The described contact geometry is shown for an idealised conical indenter in figure 2.2.1 (a). A typical nanoindentation load displacement curve is shown in (b) for a Berkovich tip into fused silica, which yields a Young's Modulus of 72 GPa and a hardness at maximum load of 9.8 GPa.

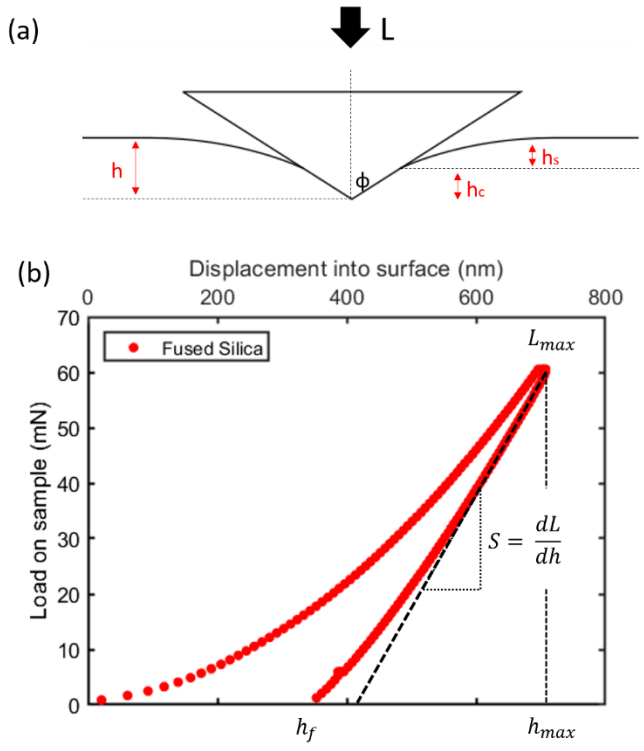

Figure 2.1.1 (a) Contact geometry for sharp tipped indentation into an elastic half-space. (b) Load displacement curve for fused silica via nanoindentation with a Berkovich indenter tip. Young's modulus is found to be 72 GPa and indentation hardness 9.8 GPa.

The essential points of nanoindentation instrumentation are shown in figure 2.1.2 (a), a schematic of an MTS Nanoindenter XP equipped with the dynamic contact module (DCM), the primary instrument used in this work. The sample is mechanically in parallel with a spring system supporting the load cell. These springs are designed to be compliant in the indentation axis, but very stiff in all other directions, ensuring that the system is one dimensional. The load cell consists on an electromagnetic coil actuator capable of generating loads of several 10's of mN with an accuracy on the order of 10's of nN. Displacements of the indenter shaft are tracked via a three-plate capacitance gauge, with the two outside plates fixed to the indenter head, and the middle plate moving with the shaft. To the shaft is attached the tip, which is typically made of diamond due to its high elastic modulus (~ 1TPa) minimising distortion during contact with the sample. The load frame supporting the sample and head is designed to be very stiff, so as to minimise flexure and parasitic strains, which will be registered by the capacitance gauge as true displacements of the tip into the surface, requiring post-indentation analysis to remove.

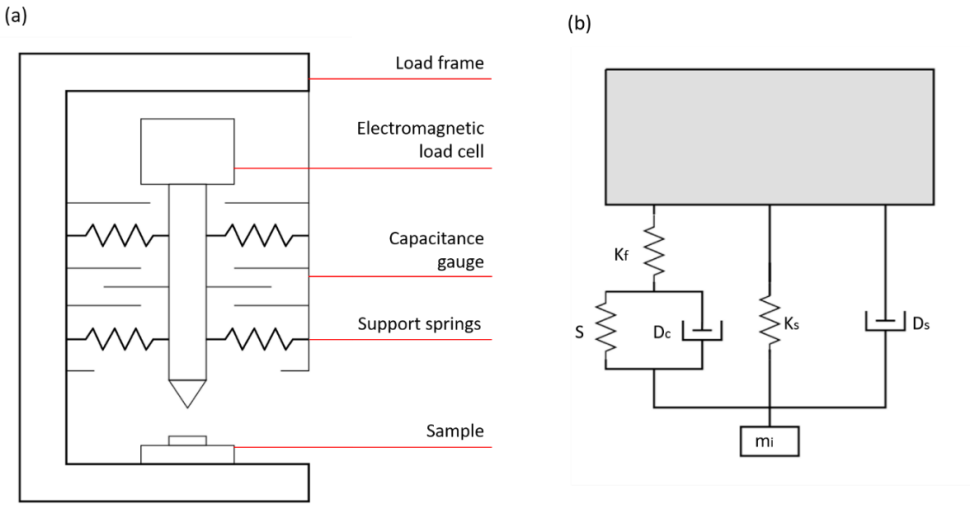

Figure 2.1.2 (a) Schematic of the MTS Nanoindenter XP head and supporting load frame. Force is generated by an electromagnetic coil load assembly. Vertical displacements are tracked through a capacitance gauge, essentially a parallel plate capacitor with one plate attached to the indenter shaft, meaning the capacitance varies as the tip moves. Leaf springs with high lateral stiffness, but minimal vertical stiffness support the load cell and effectively render motion one dimensional. (b) Representation of the nanoindenter as a one-dimensional damped simple harmonic oscillator. The relevant components of are the indenter mass m_i, the spring constants of the leaf springs K_s, the damping coefficient of the springs D_s, the stiffness of the load frame K_f, the contact stiffness S, and the contact damping coefficient D_c.

The quasi-static loading method described above provides one measure of hardness and Young's modulus per indent, at the point of initial unloading from maximum load. This means that several indents are required for a high level of statistical certainty. A significant advance in this respect was the development of the "continuous stiffness method" (CSM), in which a small oscillatory displacement typically on the order of 1 nm is applied on top of the general loading. This enables constant measurement of the contact stiffness, and as such continuous evaluation of hardness and Young's modulus, leading to higher accuracy and allowing for depth sensitive measurement[17]. By considering the indenter to be a one-dimensional damped harmonic oscillator as shown in figure 2.1.2 (b), we may write the contact stiffness S in terms of the total stiffness as:

$$S = \frac{K_f(K_{tot}\text{-}K_s)}{K_f\text{-}(K_{tot}\text{-}K_s)} \tag{2.1.7}$$

Where K_f and K_s are the stiffnesses of the frame and supporting springs respectively. The total damping of the system, D_{tot}, is similarly given by:

$$D_{tot} = D_c + D_s \tag{2.1.8}$$

Where D_c and D_s are the damping contributions of the contact and the support system respectively. The CSM operates via applying a small amplitude load of the form:

$$L(t) = L_0 e^{i\omega t} \tag{2.1.9}$$

Where ω is the frequency of oscillation. This leads to a vertical displacement $h(t)$:

$$h(t) = h_0 e^{i(\omega t\text{-}\phi)} \tag{2.1.10}$$

Where φ is the phase lag between the driving force and the displacement. These values may be inserted into the ordinary differential equation:

$$m\ddot{h}(t) + D\dot{h}(t) + Kh(t) = L(t) \tag{2.1.11}$$

The real and imaginary parts of the solution to equation 2.1.11 yield the damping and stiffness solutions respectively, and are of the form:

$$D_{tot}\omega = \frac{L_0}{h_0}\sin(\phi), \qquad K_{tot}\text{-}m\omega^2 = \frac{L_0}{h_0}\cos(\phi) \tag{2.1.12}$$

This allows equation 2.1.7 to be rewritten as:

$$S = \frac{K_f\left[\frac{L_0}{h_0}\cos(\phi) - \frac{L_0}{h_0}\cos(\phi)\,|_{free}\right]}{K_f - \left[\frac{L_0}{h_0}\cos(\phi) - \frac{L_0}{h_0}\cos(\phi)\,|_{free}\right]} \quad (2.1.13)$$

As well as enabling continuous depth-sensitive measurement of mechanical properties, the CSM technique has been heavily employed to study time dependent phenomena, with alterations in the frequency of oscillation allowing for the study of polymer viscoelastic phenomena on the nanoscale[18,19].

2.1.2 Specifics of flat punch indentation

Sharp tipped indenters have generally been preferred over the flat punch in nanoindentation for a variety of reasons. The fabrication of diamond flat punches with nanometre scale roughness and sharp side walls is often beyond the capabilities of traditional machining and require highly sophisticated techniques such as direct-write gallium masks[20] combined with plasma etching or focused ion beam milling, as shall be outlined in the next section. The large initial contact area necessitates high loads for significant deformation of stiff materials, and as such greater demands are places on the load frame for low compliance. There is also a significant risk of fracture in the punch itself. Most significantly for thin films is the challenge of co-alignment of the sample and punch normals. For high punch diameter to film thickness ratios, misalignments on the order of one degree cause significant alteration to the mechanics of the system, as full contact may not be established until the leading edge of the punch has penetrated the film to large strains. Overcoming this issue requires a specialised adjustable tilt stage and an external means of verifying alignment, most commonly through post-indentation AFM to judge the correction needed.

Despite these additional costs and experimental challenges, in many cases the flat punch geometry presents significant advantages. The contact mechanics are greatly simplified compared to those of a sharp tip and no assumptions are needed regarding contact area. In the absence of stress concentrators, the initial response is wholly elastic, allowing for the study yield phenomena in finer detail. Viscoelastic properties can be more easily studied through constant stress creep compliance experiments. With known film thickness and punch diameter, the extraction of stress and strain relations is trivial. The flat punch shall be the primary tool for the study of the non-linear stress-

strain response and non-equilibrium behaviour of polymer thin films in chapters three and four respectively.

The principal components of the indentation system used in this work are shown in figure 2.1.3. The system as a whole is shown in (a). Samples are mounted to a Physik Instrumente M-044 dual axis tilt stage with nominal sub µrad precision, shown in (b). Indents are preformed using the MTS Nanoindenter XP DCM module shown in (c), to which is mounted a flat FIB manufactured diamond flat punch, typically of 2-5 µm diameter. An example is shown in (d). Alignment is checked via a DME DS-95 AFM, visible in the top left corner of (a), operated in tapping mode and equipped with standard silicon tips.

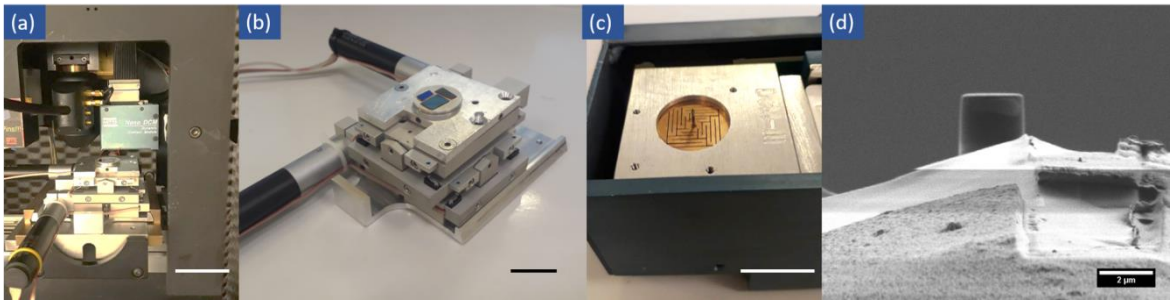

Figure 2.1.3 (a) The flat punch nanoindentation system used for the majority of this work. Scale bar is approximately 5 cm. (b) Physik Instrumente M-044 dual axis tilt stage, shown with three samples loaded. Scale bar is approximately 2 cm. (c) Nanoindenter XP DCM head. The indenter shaft is visible at the centre. Scale bar is 1.5 cm. (d) SEM image of a FIB manufactured diamond flat punch. Scale bar is 2 µm.

The process for sample alignment is shown in figure 2.1.4. An indent is made into the film in question (here a 200 nm polystyrene film on silicon) and a topography map taken via AFM, shown in (a). Height profiles are taken at various angles across the indent as shown in (b) to determine the magnitude and direction of maximum misalignment, shown here to be 0.52° at an angle of 150° with respect to the x-axis. The tilt stage is then adjusted to correct for this. The process is repeated until a satisfactory level of precision is achieved, typically less than 0.2° misalignment.

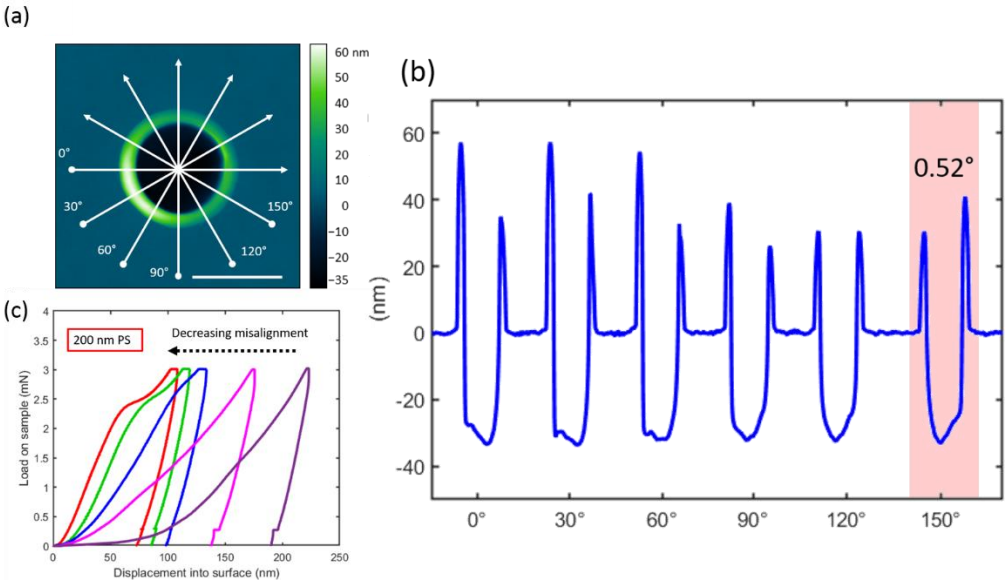

Figure 2.1.4 (a) AFM micrograph of an indent into 200 nm polystyrene with a 2.1 µm diameter flat punch. Scale bar is 2 microns. (b) Accompanying height profiles, used to calculate the angle of maximum misalignment, shown in red. The dual axis tilt-stage is then used to apply a correction of this magnitude in this direction (c) Load-displacement curves for 200 nm PS where punch to film misalignment is varied. For a well-aligned punch (red) the curve quickly linearises, as full contact occurs at low displacements, and remains fixed throughout the remainder of the test. For very poorly aligned samples (pink, purple) the response is non-linear to high displacements, as the contact area changes throughout testing. Further, the smaller contact area at low displacement leads to a less stiff response.

The effect of misalignment on the recorded the indentation load-displacement curves is shown in (c), where misalignment is decreased from greater than 1.5° (purple) to less than 0.2° (red) in a series of correction steps.

A load displacement curve for a standard indentation to 3.5 mN into a 300 nm polystyrene film on silicon is shown in figure 2.1.5 (a). The response is first linear in the elastic region, before plastic flow begins above the forming stress at approximately 2.5 mN. The loading process is shown in (b). Load is applied at a constant rate of 0.67 mN/s until the specified peak load of 3.5 mN is reached, whereupon it is maintained for 5 seconds. A 1 nm amplitude CSM oscillation is applied at 45 Hz during loading. The hold segment may be used to extract information about viscoelasticity at a given load if its duration is increased. Unloading then occurs at the same rate to 10% of the maximum load. At this point the punch is held on the surface and thermal drift is measured, which may then be subtracted from the load-displacement curve. (c) Shows the harmonic contact stiffness as measured via the CSM signal. The surface is easily distinguishable by the sharp increase from 0 to 10,000 N/m at 0 nm. Alternatively, the CSM phase angle may be used to detect the surface, which is marked by a sharp spike

in (d). This constitutes the standard methodology for indentation in this work. Section specific changes will be mentioned where relevant.

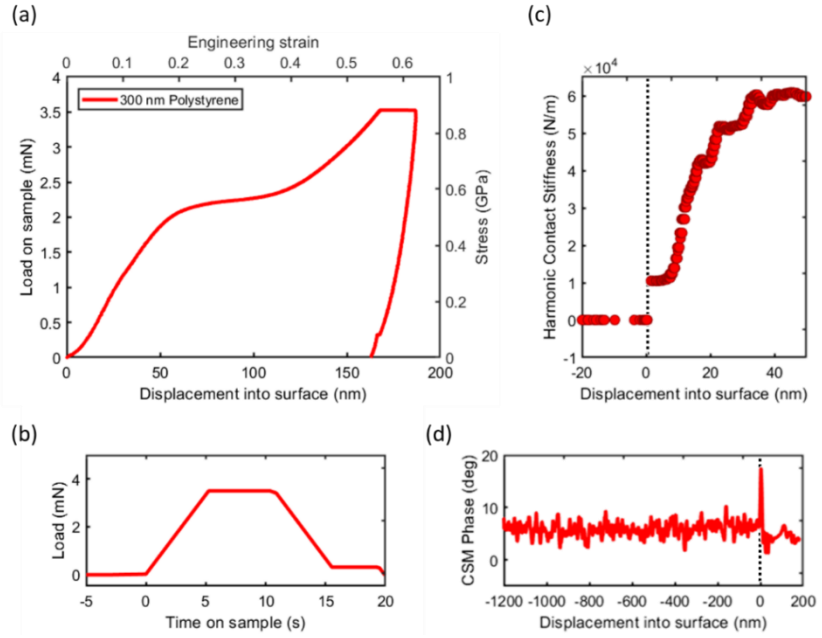

Figure 2.1.5 (a) Load displacement curve produced via flat punch indentation into 300 nm polystyrene. (b) General loading protocol. (c) Harmonics contact stiffness during indentation. (d) Phase inversion on contact with the surface.

2.2 Punch fabrication via focused ion beam milling

Precision flat punch indentation of thin films requires that any curvature or roughness of the punch face be minimal when compared to the initial thickness of the film. Extraction of stress and strain in a straightforward manner further necessitates that the punch area be known to a high degree of certainty and the side walls must be steep to maintain a constant contact area during indentation. Traditional fabrication techniques fail in these respects, due to the inherent challenges associated with micromachining extremely hard and anisotropic materials such as diamond. Focused ion beam (FIB) milling is a beam-based technique that allows for the fabrication of micro/nanostructures are of the required level of precision for nanomechanics.

Essentially, the FIB operates along the same principles as the scanning electron microscope (SEM), with a stream of massive charged particles, typically Ga^+ ions, being

focused by a series of lenses and apertures onto the sample, where they interact with surface atoms elastically and inelasticity, removing atoms and producing secondary electrons/ions. The use of a massive particle as opposed to electrons couples the high spatial accuracy which is a result of the particles short wavelength with momenta orders of magnitude higher than those achieved in SEM at the same accelerating voltage. This results in faster milling rates and shorter penetration depths. In this work two systems were used for punch fabrication: a Carl Zeiss Auriga FIB-SEM crossbeam system and an FEI Strata 235DB FIB-SEM system. In both systems the mode of operation is similar. Gallium is heated in a reservoir to near evaporation and flows to wet the point of a very sharp tungsten tip, typically of 1-5 μm diameter, drawn there by an electrode concentric to the tip, called the extractor. At the tip the liquid metal forms a sharp Taylor cone, with an apex of approximately 5 nm. An extraction voltage is then applied between the aperture and the tip, pulling Ga from the end of the Taylor cone and ionizing it. A series of electrostatic lenses then focuses the ion beam onto the target. Imaging is possible due to secondary electrons produced via inelastic collisions with the target, with the inclusion of a secondary electron detector. In-situ monitoring of the milling process is made possible by the inclusion of an electron beam at a 54° angle to the ion beam.

The fabrication process for flat punches consists of the following steps: first a thick film (600 – 800 nm) of silver or gold is deposited on a conventional indenter tip (in this case a boron-doped conductive diamond cube corner tip with r_{tip} < 50 nm, Micro Star Technologies, Inc) to reduce charging effects during milling. The indenter tip is then carefully aligned with the FIB beam axis, as shown in figure 2.2.1 (a). Increasingly fine concentric rings are then milled into the tip, with high beam currents (~2 nA, 30 kV) roughly milling away large amounts of material at the edge, and fine cuts (~20 pA, 30 kV) being used for precision milling towards the centre. A pillar with well defined, smooth sidewalls with the desired area is now left at the centre of this pattern. This can be seen in 2.2.1 (b). The tip is then rotated so that the pillar is at 90° to the beam and a low current polishing cut is made across the surface, shown in (c). Additional cuts are then made to remove any additional features/defects which may interfere with indentation. An example of a finished pillar with a 2.4 μm diameter is shown in (d).

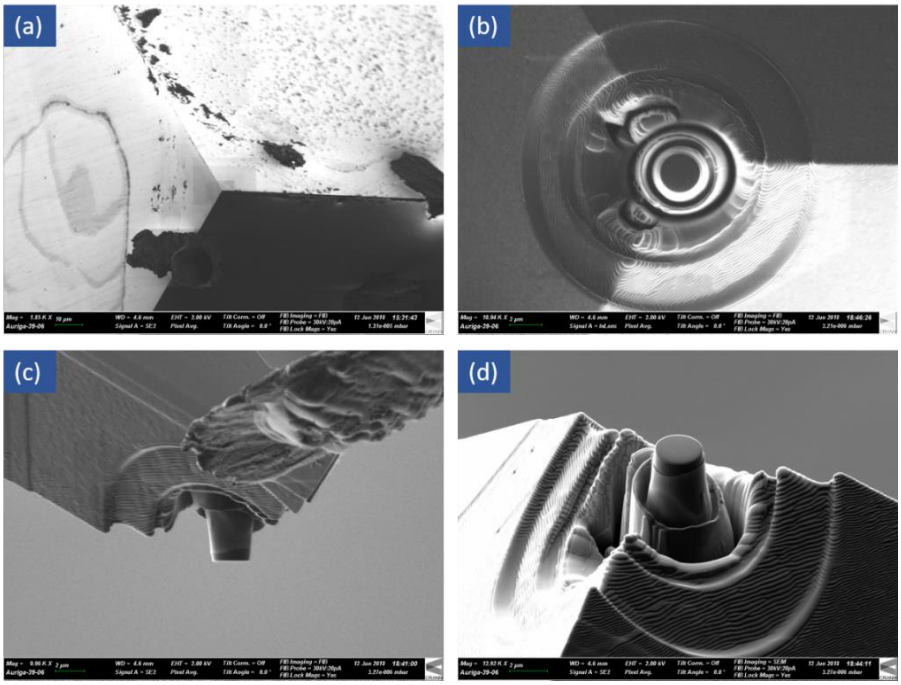

Figure 2.2.1 Fabrication of flat punches via FIB milling. (a) A previously used indenter tip is coated in a thick film of conductive metal and aligned with the beam (b) Concentric circles are milled, leaving a pillar of defined diameter. (c) The indenter is rotated and a polishing cut applied at 90°. (d) The final punch, with a 2.4 µm diameter.

2.3 Spin coating of polymer thin films

Spin coating is a technique used to produce uniform, low roughness polymer films on planar substrates. Typically, the film is spun from a dilute solution of the polymer and a well-matched solvent, as quantified by the Hildebrand solubility parameter, δ, the square root of the cohesive energy density of the polymer or solvent. Values are given in table 2.2.1 for PS, PMMA, and some common solvents. For optimal solutions $\delta_{solvent} \approx \delta_{polymer}$.

Table 2.3.1 Hildebrand solubility parameters of PMMA, PS, and some common solvents.

Polymer/solvent	δ (MPa)[21]
Polystyrene	17.6 – 19.8
PMMA	22.7
Toluene	18.2
Chloroform	19.0
Water	47.9

The spin coating processes can be considered to consist of four rough stages[22]: deposition spin-up, spin-off, and solvent evaporation. In the first step the polymer solution is deposited onto the stationary substrate, typically a highly polished silicon wafer. In the second step the substrate is accelerated to its peak rotational velocity and the solution spreads out radially to cover the surface due to the high centrifugal force. During the spin-off stage the substrate maintains peak rotational velocity and excess solution is ejected off the edges. The remaining liquid is now uniformly flat away from the edges and evaporation of the solvent commences, leaving a solid, uniform thin film in the absence of artefacts and contaminants. In the ideal case, the final film thickness h will be a function of initial viscosity (η_0), initial concentration (c_0), and rotational velocity (ω):

$$h = K\frac{\eta_0^{\gamma} c_0^{\beta}}{\omega^{\alpha}} \tag{2.3.13}$$

Where K is an empirical fitting constant, and α, ß, and γ are exponents less than 1.

While in solution the polymer is in a state of equilibrium. As solvent evaporates the mobility of the chains dramatically decreases, leading to a vitrification process where current chain configurations are effectively frozen in, similar to the thermal glass transition discussed in chapter one. This has been observed to occur at 15-20% approximate solvent content for polystyrene-toluene solutions at room temperature[23]. The out of equilibrium state of the film post spin coating has been shown to cause significant residual stresses on the order of 100's of MPa, and has been linked with increased physical aging, lower mechanical properties and negative thermal expansion in ultra-thin PS films[24]. The effects of residual stresses can be considerably lessened by the inclusion of a post spin-coating anneal at $T > T_g$, which has the additional benefit of removing any residual solvent content.

The standard process flow for polystyrene thin film preparation is shown schematically in figure 2.3.1. Silicon wafers are first cleaned in a succession of acetone, isopropanol and isopropanol ultrasonic baths. Carbon contaminants are then removed via mild oxygen plasma etching for 2 minutes in a Diener electronics Pico plasma asher. This step has the added benefit of increasing the wettability of the surface via oxygen activation. Dilute PS-toluene solutions with polystyrene weight percentages typically of 0.5 – 2.5% are then spun onto the substrates using a Speciality Coating Systems Inc.

model P6700, with the rotational velocity typically being within the 1000 - 4000 RPM range and a spinning time approximately 45 seconds. Samples are then heated to T_g + 30° for 30 minutes on a Torrey Pines Scientific hotplate, before being stored under vacuum overnight. Film thickness is then measured via profilometry using a Veeco Dektak 6M profilometer. A selection of spun films is shown in the bottom left image of the spin coating work-flow shown in figure 2.3.1.

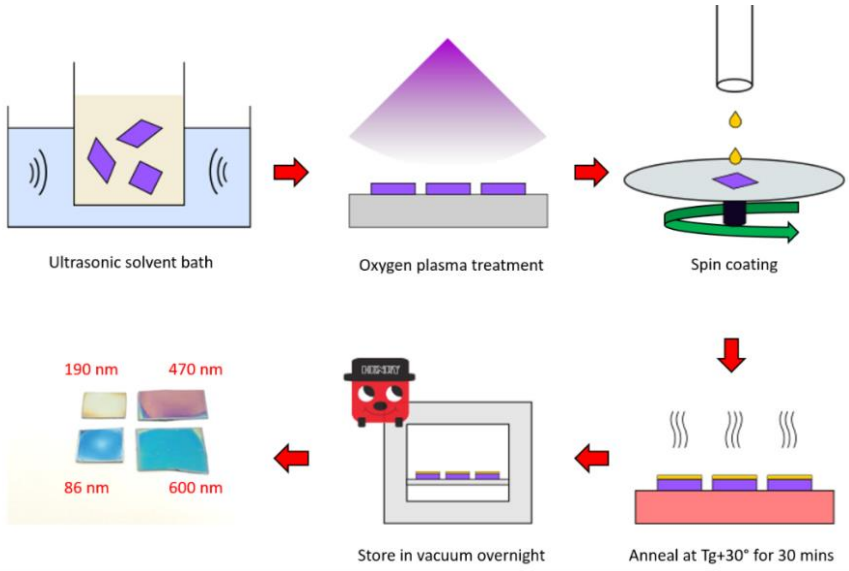

Figure 2.3.1 Graphical representation of the process flow for producing thin films via spin coating

A 5 x 5 micron AFM topography image of a 203 nm atactic polystyrene film (Mw = 1MDa) prepared in this fashion on a Si3N4 coated silicon wafer is shown in figure 2.3.2 (a). The arithmetic mean roughness R_a across the scan area is was measured as 0.55 nm, approximately 0.27% the thickness of the film. Roughnesses of films produced within the remainder of this these were generally found to be around this value. Figure 2.3.2 (b) shows a 3-D image of the height of the film, acquired by scratching a region of film with a plastic tweezers to expose the substrate. The average AFM height profile is shown in (c), as measured across a 5 micron wide region.

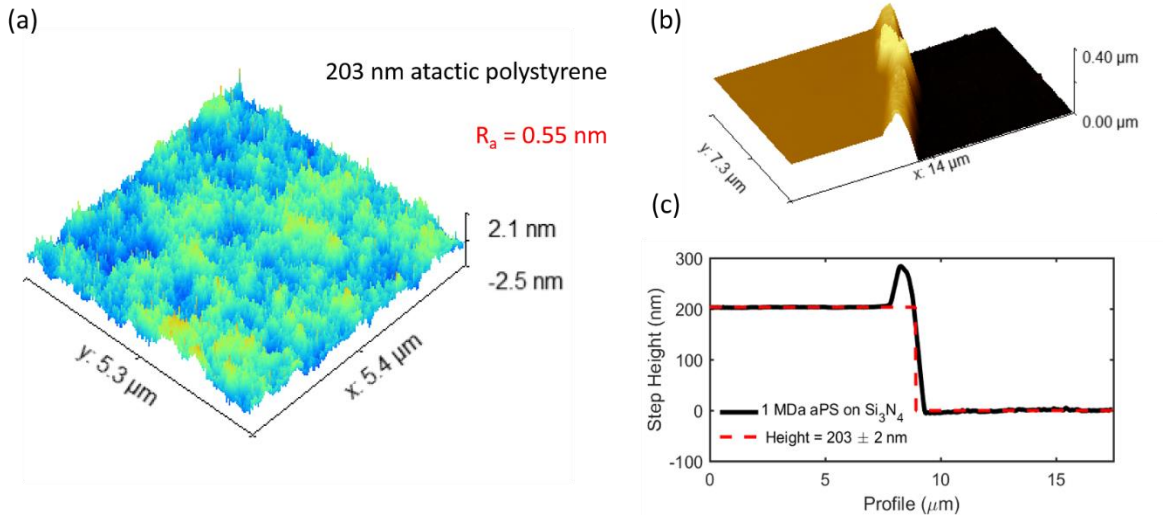

Figure 2.3.2 Roughness and height measurements of spin coated polystyrene films (a) 3-D AFM topography map of a spin coated PS film on 203 nm. The measured arithmetic mean roughness was 0.55 nm (b) Height of the film as measured near a scratch exposing the surface. (c) Fit of the step height, yielding a film thickness of 203 nm.

2.4 Atomic force microscopy

The atomic force microscope (AFM) was developed in the mid 1980's to measure extremely small forces (~10^{-18}N) between atomically sharp tips and surfaces[25], but has matured into the most common technique for three-dimensional characterization of sample topography at the micro and nanoscale. The essential points of AFM are shown in figure 2.4.1. A sharp tip (r_{tip} < 10 nm) affixed to a reflective cantilever, whose stiffness typically falls within the range $0.1 \leq k_{cantilever} \leq 40$ N/m, is rastered across the surface being studied. Onto the cantilever is shone a collimated laser, which is then reflected onto a position sensitive diode (PSD). The z-piezo moves the cantilever up and down in response to the PSD signal, so as to maintain a constant user-defined set point, typically either the peak-to-peak PSD oscillation amplitude in AC mode, or the deflection in contact mode. At each x-y point the z-piezo voltage is recorded, as well as several other useful quantities such as the error signal of the feedback loop maintaining the user setpoint, and the phase lead/lag in the PSD signal relative to the driving oscillation. From these quantities a height map may be extracted, and maps of other factors influencing surface-tip interaction, such as chemical composition, or amorphous and semi-crystalline regions.

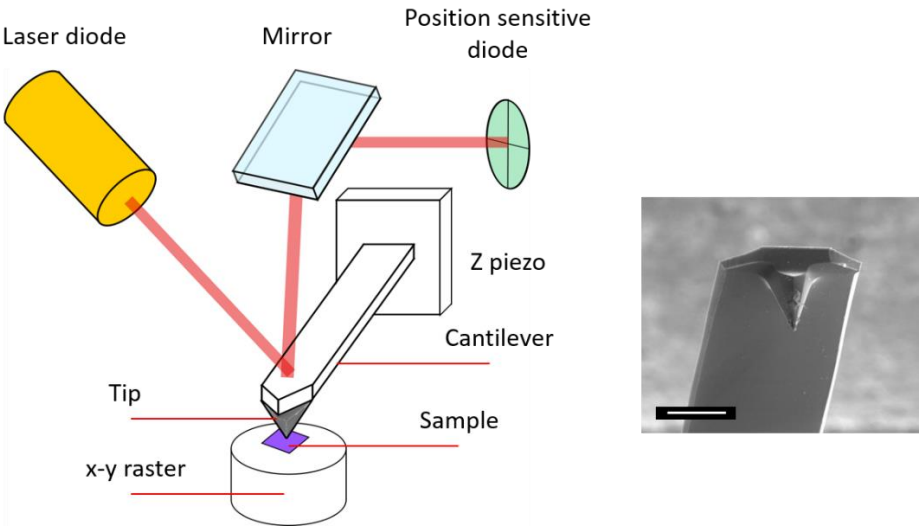

Figure 2.4.1 Schematic of basic AFM operation. A laser is shone onto the back of the AFM cantilever, after which it is reflected onto a position sensitive diode. Vertical deflections of the tip are translated into movement of the laser on the PSD. Internal electronics converts these to real displacements. A constant oscillation on the PSD (AC mode) is maintained by moving the vertical position of the sample via a piezo stack, whose signal is controlled via a feedback loop. The stage is rastered back and forth in x and y to trace out an image of the sample. SEM image on the right shows a typical used cantilever, equipped with a tip with nm scale radius. Scale bar is 20 µm.

The primary two modes imaging modes in AFM are contact mode and AC tapping mode. As the name implies, in contact mode the tip is brought directly into contact with sample to be scanned. As can be seen from the Lennard-Jones potential plotted in figure 2.4.2 (a), in this mode the dominant forces acting between tip and sample are repulsive. A positive set point deflection is defined and maintained by the feedback loop to keep the cantilever firmly in contact with the surface in the repulsive regime. This registers on the PSD as shown in (b). Contact mode is best suited to imaging very hard sample, as the interaction between tip and surface may damage soft materials. Contact mode has the added drawback of shorter tip lifetime due to wear. Somewhat counterintuitively, contact mode is also used for imaging very soft materials such as live biological tissue and cells, where tip oscillation in AC may disturb the surface. Such samples require very low deflection set points and soft cantilevers.

In tapping mode, the cantilever is driven at a frequency just off resonance at a set point amplitude of oscillation (450-750 mV typically in this work), which is maintained while scanning across the surface by the feedback loop. The tip experiences both attractive and repulsive forces, operating in the region denoted by the green lines in figure 2.4.2 (a). The z-piezo retracts the tip when repulsive forces corresponding to raised topography are encountered, and extends it over valleys/holes, keeping the amplitude

of oscillation of the laser on the PSD constant as shown in (c). The tip is therefore brought into contact with the surface far less frequently than in contact mode, minimizing wear and friction, preserving both tip and sample.

Under ambient conditions the force-distance plot shown in figure 2.4.2 (a) is not entirely representative of the interaction between tip and sample. Due to the presence of water on the sample surface, strong capillary forces arise between tip and sample, greatly extending the length of the attractive force regime. This may cause the tip to 'snap in' to contact as it approaches the surface.

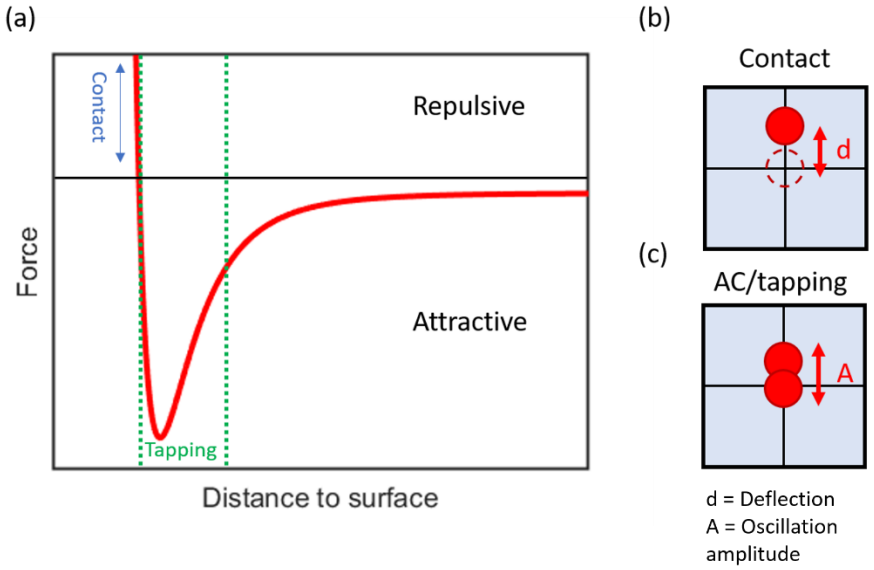

Figure 2.4.2 (a) Force range over which contact and intermediate contact/tapping mode AFM operates. (Note: Attractive capillary forces between tip and sample due to ambient humidity are not included. These tend to extend the attractive regime.) (b) Graphical representation of the PSD in contact mode. The deflection (marked as d) is maintained constant during scanning. (c) The PSD during tapping mode, where the amplitude (marked as A) of oscillation is held constant.

The primary instrument used in this work is an Asylum MFP-3D (Oxford Instruments) with a maximum scan size of 80 x 80 µm. A noteworthy feature of the MFP-3D system is the inclusion of a closed loop linear z sensor, which monitors motion of the optical lever detection assembly (laser, PSD, mirror) independently of the z-piezo, allowing for an additional measure of surface height free from the non-linearity, hysteresis, and creep associated with piezo scanners. As previously mentioned, a DME DS-95 system is also used in tandem with the tilt stage to correctly align the nanoindenter setup. Both systems were primarily operated in tapping mode.

2.5 Scanning transmission x-ray microspectroscopy

Scanning transmission x-ray microspectroscopy (STXM) is a technique that uses soft x-rays (50 – 2000 eV) to probe properties such as elemental composition[26], molecular orientation[27], mass density[28] and electronic and magnetic characteristics[29] of macromolecular samples such as polymer films. The technique relies on the fact that the interaction of x-rays with polymers over this photon energy range is dominated by absorption by inner shell electrons[30], in particular the carbon 1s edge (~290 eV), as well as the nitrogen (~405 eV) and oxygen 1s (535 eV) edges if present. Absorption leads to promotion of the core electrons to unoccupied molecular orbitals, whose energies are highly influenced by molecular structure. As such, the transmitted beam intensity across a spectrum of initial energies acts as a molecular fingerprint which when coupled with a sample rastering system, enables mapping of properties such as chemical composition or molecular orientation to spatial accuracies on the order of 30 nm[31]. Unlike scanning probe techniques which typically sample surface properties, STXM characterizes is a bulk characterisation technique.

The system used for this work was the PolLux beam line[32] at the Swiss light source (SLS) synchrotron at the Paul Scherrer Institut, Switzerland, and the technique is therefore explained with reference to that instrument. The SLS is a 2.4 GeV electron synchrotron capable of producing high intensity, stable synchrotron light over a wide wavelength spectrum. The system consists of linear accelerator (linac), a booster ring, a storage ring, and 21 individual beam lines, including PolLux. At the linac electrons are pulled from a cathode by application of a 90 kV voltage between anode and cathode before being sped up to 100 MeV over two accelerating sections. Electrons are then fed into the 270 m circumference booster consisting of 237 bending magnets, which accelerates them up to a final energy of 2.4 GeV via the Lorentz force. Electrons are then periodically injected into the storage ring, to keep the intensity of the circulating beam constant. The 288 m circumference storage ring is made up of 36 dipole magnets, each with a magnetic field of 1.4 T, combined into 12 groups of 3, producing achromatic deflections of the beam, as well as 177 quadrupole magnets for beam focusing and several other correction magnets. An overview of the SLS is shown in figure 2.5.1 (a).

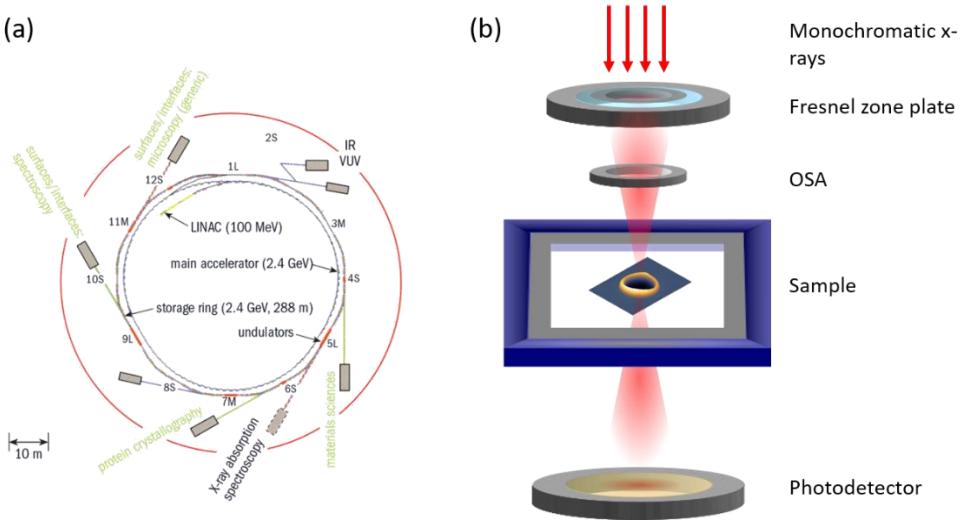

Figure 2.5.1 (a) Top down overview of the Swiss Light Source. (b) Schematic of the PolLux user end station.

The PolLux beam line uses as its x-ray source a bend magnet with a critical energy of 5.5 keV. A toroidal mirror deflects the photon beam into the entrance slit of the system, after which it is incident onto a monochromator consisting of two spherical gratings with line densities of 300 and 600 lines/mm respectively. The beam is then focused by a Fresnel zone plate to a diffraction limited spot. Higher order diffractions are supressed using an optical sorting aperture (OSA.) A 100 nm silicon nitride (Si_3N_4) membrane upstream of the zone plate separates the end station from the beam line and allows the system to be operated at a vacuum of ~ 10^{-6} mbar. The sample, typically supported on a TEM grid or an Si3N4 window, sits on a stage which may be rastered in x and y. The total energy range of the PolLux system is 250-1600 eV, while the maximum spatial resolution is < 40 nm. A schematic of the end station is shown in figure 2.5.1 (b), while 2.5.2 shows photographs of the exterior and interior of the end station.

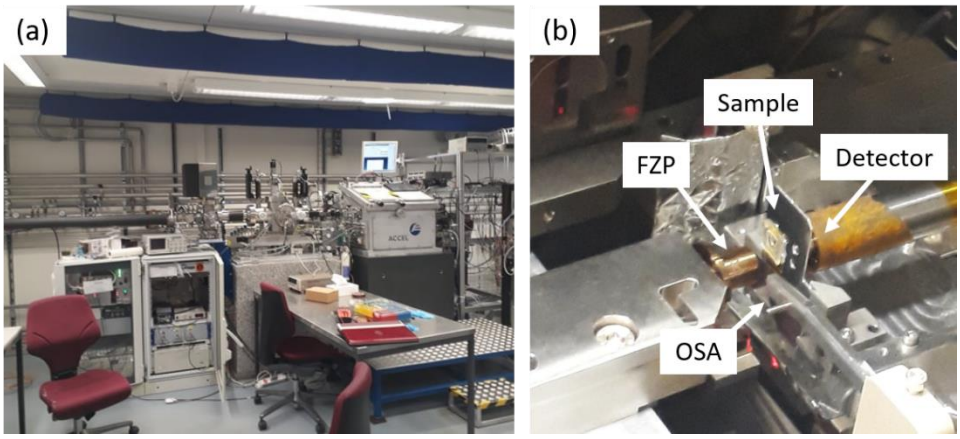

Figure 2.5.2 (a) The PolLux end station. (b) The main system components.

A typical STXM experiment conducted either at a fixed energy or over a spectrum consists of scanning a sample while monitoring the transmitted intensity, I_T. Chemical/molecular contrast is visible due to the different absorption probabilities as expressed in their x-ray spectra. With knowledge of the initial beam intensity incident on the sample, I_0, the optical density (OD) may be calculated via the Beer-Lambert formula:

$$\mathrm{OD} = -\log\left(\frac{\mathrm{I_T}}{\mathrm{I_0}}\right) = \mu(\lambda)\rho h_0 \qquad (2.5.1)$$

Where $\mu(\lambda)$ is the wavelength specific mass attenuation coefficient, and ρ is the mass density. Independent measurement of the sample thickness h_0 allows for accurate measurement of ρ, as shall be seen in chapter 4.

2.6 Thermal nanoimprint lithography

Large scale technological usage of nanopatterned matter requires fabrication techniques that can couple high quality production of features displaying sub 100 nm critical dimensions with industrial scale throughput. Traditionally this has been achieved via photolithography, with UV-lithography and its successor extreme UV-lithography being the current technologies of choice within the semiconductor industry. However, these techniques are both complex and prohibitively costly, typically requiring class 100 or greater cleanroom environments, advanced light sources, and

optical components that are non-absorbing at the operating wavelength. Further, these techniques are diffraction limited, prohibiting sub 10 nm feature fabrication. Beam based lithography methods such as FIB and electron beam lithography may achieve greater resolution, but at the cost of un-scalable throughput. Nanoimprint lithography (NIL)[33], presents an alternative approach, where a compliant resist material is mechanically patterned via a pre-formed stamp/mold of much greater stiffness, leading to replication of the mirror image of the mold features in the resist. NIL is scalable at a much lower cost than the methods outlined above, as single stamp may be reused several thousand times without loss of feature quality[34]. A NIL relies on mechanical pattern transfer there is no theoretical feature limit, and individual features as small as 2 nm have been realised[35]. The past two decades have seen NIL mature into a versatile, widely adopted technique that has been utilized in fields such as bioengineering[36], photonics[37], optoelectronics[38], and microfluidics[39].

Nanoimprint is broadly divided into two process categories: thermal imprint, where the resist is either a thermoplastic or thermoset polymer, and UV imprint, where the resist is photo-curable. This work is concerned only with thermal imprint and as such that shall be the focus here, however most of the considerations discussed below are broadly applicable to the UV case as well.

The basic thermal NIL process is shown in figure 2.6.1. A rigid mold, typically fabricated by conventional lithographic techniques, is pressed into a supported thermoplastic polymer film heated to above T_g. The polymer then flows to fill the cavities in the mold structure. The imprint stack is then cooled below T_g, and the mold is removed, leaving its mirror image imprinted into the resist.

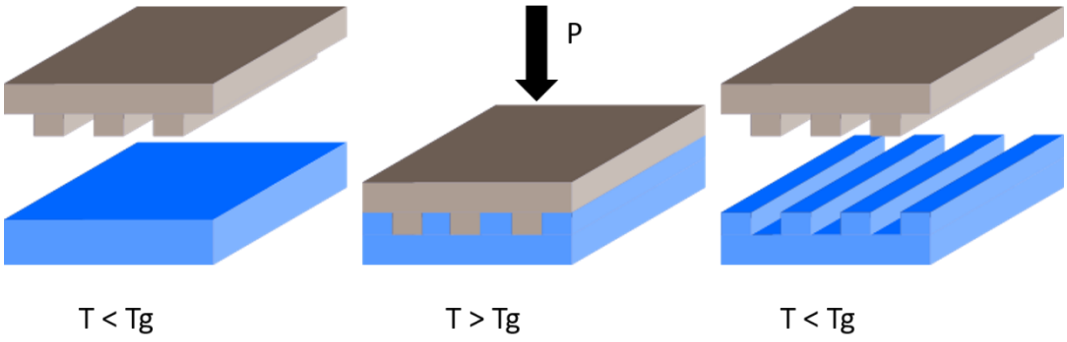

Figure 2.6.1 The thermal nanoimprint process

The parameters that must be considered in the design of thermal NIL processes can be broadly divided into three overlapping categories: geometry, rheological concerns such as molecular weight and imprint temperature, and interfacial conditions such as mold surface energy, heat flow, and thermal expansion. Considering geometry first, the user typically has control over the mold design and the initial thickness of resist to be patterned, h_0. The initial concern is that there be enough resist material to completely fill the mold cavities. A sketch of this problem is given in figure 2.6.2 for a single cavity surrounded by two asperities on a massively parallel line pattern mold. The width of the asperities are denoted s_i, while the width of the cavity is w_i. The height of the cavity is given by h_f. The long axis is not shown for simplicity. If the resist is assumed to be incompressible, the continuity equation across the width of the whole mold is:

$$h_0 \sum_{i=1}^{N} (s_i + w_i) + h_r \sum_{i=1}^{N} (s_i + w_i) + h_f \sum_{i=1}^{N} w_i \tag{2.6.1}$$

Where h_r is the thickness of the excess residual layer of resist beneath the mold features after imprint. Considering only a single cavity w, as in 2.6.2, where both mold features are the same size, $s_0 = s_i = s$, we may simply this relationship to:

$$w(h_f + h_r - h_0) = s(h_0 - h_r) \tag{2.6.2}$$

The final thickness of the residual layer may then be written as:

$$h_r = h_0 - \frac{wh_f}{\lambda} \tag{2.6.3}$$

Where $\lambda = w + s$. It is useful to further characterize the filling geometry through a dimensionless fill factor ζ, the ratio of the amount of material available to material required to fully fill the mold cavities:

$$\zeta = \frac{h_0 \lambda}{wh_f} \begin{cases} < 1, & \text{underfilling} \\ = 1, & \text{matched} \\ > 1, & \text{overfilling} \end{cases} \tag{2.6.4}$$

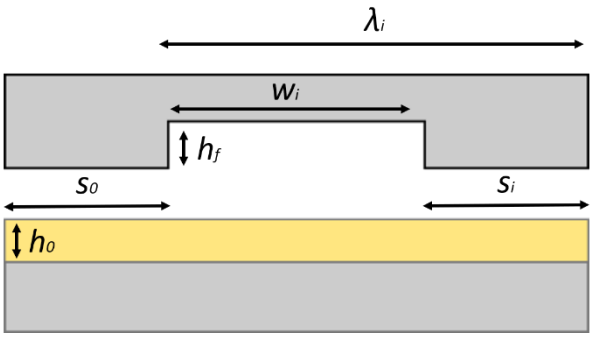

Figure 2.6.2 Imprint geometry for a single cavity in a massively parallel line pattern mold.

On first inspection it may be thought preferable to match $\zeta \approx 1$ to minimize the thickness of the residual layer thickness to ensure that any future processes steps such as a reactive ion etch (RIE) can proceed without having to remove so much material that the imprinted features are distorted, a situation graphically represented in figure 2.6.3. However, both experiment and theory have shown that it is not possible to displace all resist material from beneath the mold asperities[40,41]. From a fluid mechanics perspective this problem is often treated as one of "squeeze flow,"[42] in which a viscous liquid is sandwiched between two parallel plates, one of which is fixed and on the other is exerted a compressive force, *F,* causing the fluid to flow laterally. Operating under the assumption of a no-stick boundary condition at the fluid-plate interfaces, it is found that the remaining fluid thickness between the plates is inversely proportional to the square root of *F* and the allotted squeeze time, $t_{squeeze}$:

$$h(t) \propto \left(\frac{F}{\eta_0} t_{imprint}\right)^{-\frac{1}{2}} \tag{2.6.5}$$

Where η_0 is a constant shear viscosity. As this function asymptotically approaches zero, there will always be a residual layer present and in terms of nanoimprint this implies that a fill factor close to unity will result in poor cavity filling and long imprint times. A compromise therefore must be struck between providing sufficient material to allow for cavity filling over practical time scales and not supplying so much resist that it will make a subsequent RIE step challenging. Alternatively, new techniques must be found that can enhance squeeze flow in high aspect ratio geometries. This problem shall be reconsidered in chapter five of this work, when discussing the small amplitude oscillatory shear forming technique, which aims to do just that.

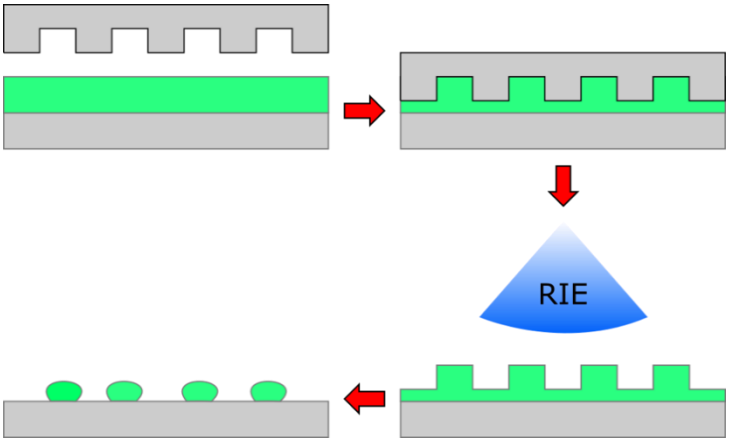

Figure 2.6.3 Nanoimprint process with a reactive ion etch step included to remove the residual layer. Excessive residual layer requires aggressive etching, which may lead to feature distortion.

As a final consideration on film thickness, it is worth mentioning the case of imprinting a free-standing film with macroscopic thickness, where $\zeta >> 1$. In this situation the issues of material supply and squeeze flow are irrelevant due to the effectively infinite supply of polymer to fill the mold cavities. In this simplified scenario nanoimprint represents a surface modification of a bulk system, which may be incorporated into as a single step in a larger device fabrication process. Examples of this process include the production of anti-wetting coatings[43], or tissue scaffolds with imprinted nanotopography[44]. This situation shall be revisited in chapter six.

As evidenced by equation 2.6.5, another important factor in squeeze flow is the rheological properties of the resist, expressed here through the zero-shear viscosity, η_0. As discussed in chapter one, permanent deformation in polymers, and as a consequence their viscosity, is a thermally activated process, and is often treated in the vicinity of T_g using the super-Arrhenian Vogel-Fulcher-Tammann (VFT) equation:

$$\eta_0 = \eta_c \exp\left(\frac{B}{T-T_0}\right) \tag{2.6.6}$$

Where T_A, η_c, and T_V are fitting parameters referred to as the activation temperature, the VFT viscosity, and the Vogel temperature respectively. T_v typically lies approximately 50 °C below T_g and corresponds to the divergence of viscosity from equation 2.6.5. This dependence of resistance to deformation of the resist is shown for PMMA in figure 2.6.4 where the storage modulus G' is plotted as a function temperature from the glassy state, through the supercooled viscoelastic region and into the viscous melt regime. Evidently, it is preferable to imprint at temperatures well

above T_g where resistance to flow is minimal. However, the high heat capacities of typical imprint modules may lead to long heating and cooling times, increasing the overall processing time. A balance is typically struck at approximately T_g + 80 °C, which from figure 2.6.4 is seen to lie past the "viscoelastic shoulder," there is optimal for forming[45].

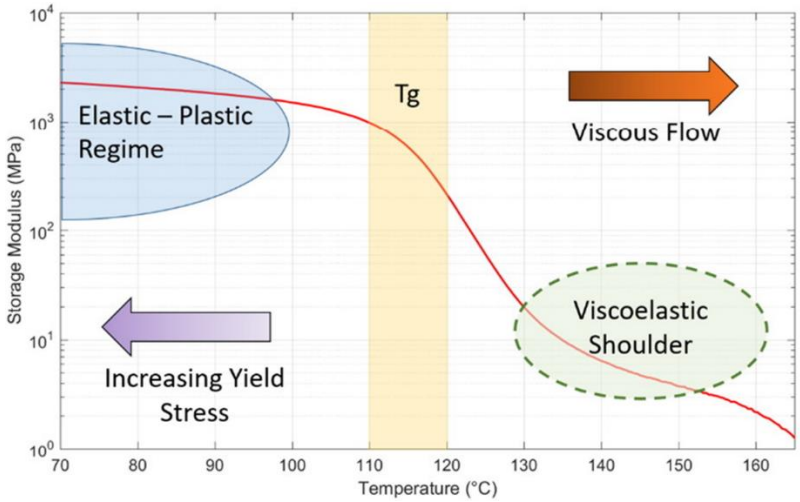

Figure 2.6.4 Elastic storage modulus *G'* of PMMA as a function of temperature, as measured by dynamic mechanical analysis at 1 Hz. At temperatures below the nominal glass transition, the material approximates an elastic-plastic solid with a modulus on the order of 1 GPa, and a yield stress of several 10's of MPa at this testing timescale. Above T_g resistance to deformation (modulus) decreases by several decades as the materials transitions to first a viscoelastic rubber and then a viscous melt.

The other primary factor controlling intrinsic viscosity is the molecular weight of the resist, M_w. As explained in chapter one, viscosity has been found to scale linearly with M_w below a critical entanglement weight, M_{wc}, whereupon chain entanglements form a network that constricts motion. Mathematically this is described by a transition from Rouse ideal chain statistics to an entangled reptation model:

$$\eta_0 \propto M_w^{\alpha}$$

$$\alpha \begin{cases} = 1, & M < M_c \\ = 3.4, & M > M_c \end{cases} \qquad (2.6.7)$$

Therefore, it is typically better to work with low molecular weight polymers where possible. The results of *Cross* et al.[46] in forming experiments in entangled polystyrene have shown that for well-confined polymers ($h(t) \sim r_g$) the reptation model fails and the expected viscosity behaviour inverts:

$$\eta_0 \propto M_w^{\alpha}, \qquad \alpha < 1 \tag{2.6.8}$$

This inversion is likely due to poor entanglement in the quasi-2D geometry, a phenomenon also observed at the free surface of thin films. As such, for low ζ imprint processes it may be preferable to use high molecular weight polymers.

Much of the initial research in nanoimprint was performed using PMMA as the resist material, most likely as it is one of the most commonly available and best profiled thermoplastic polymers. In recent years however several nanoimprint specific polymers have been developed, such as the micro rest technology mr-I 7000R series[47], the thermosetting mr-I 9000M[48] series which is thermally stable once imprinted and cured, and the mr-NIL 6000E[49] series, which may be used in both thermal and UV nanoimprint processes. Due to the relative simplicity of the technique however, most generic thermoplastics are compatible with thermal NIL.

Finally, when designing a thermal nanoimprint experiment, consideration must be given to the different thermal and energetic properties of the resist and mold. Differences in thermal expansion coefficient between resist and mold may lead to imperfect pattern transfer, while adhesion between the pair may lead to defects during demolding and eventual degradation of the mold through "clogging" of its features. To address the latter of these issues, it is common to apply a low surface energy self-assembled monolayer/anti-stick coating such as Trichloro(octadecyl)silane to ease separation during demolding[50]. Further, the demolding temperature can be selected to minimize temperature dependent adhesion forces. For a PMMA/silicon resist/mold system this minimum has been found to occur at approximately 85 °C.[51]

The instrument used in this work was a Nanoimprint Technologies CNI 1.0 thermal imprint unit with a maximum imprint temperature of 200 °C. Imprint pressures of up to 1 MPa are deliverable across a 100 mm (4 inch) area through an inflatable membrane. Increased pressures may be achieved by modification of the imprint stack to ensure the membrane contacts only the mold. Heat is supplied via Joule heating of a 100 mm ceramic wafer on which the sample/mold stack rests. An image of the instrument with a 20 x 20 cm mold placed at the centre of the heating plate is shown in figure 2.6.5 (a), while a wafer scale imprint performed with the CNI is shown in (b).

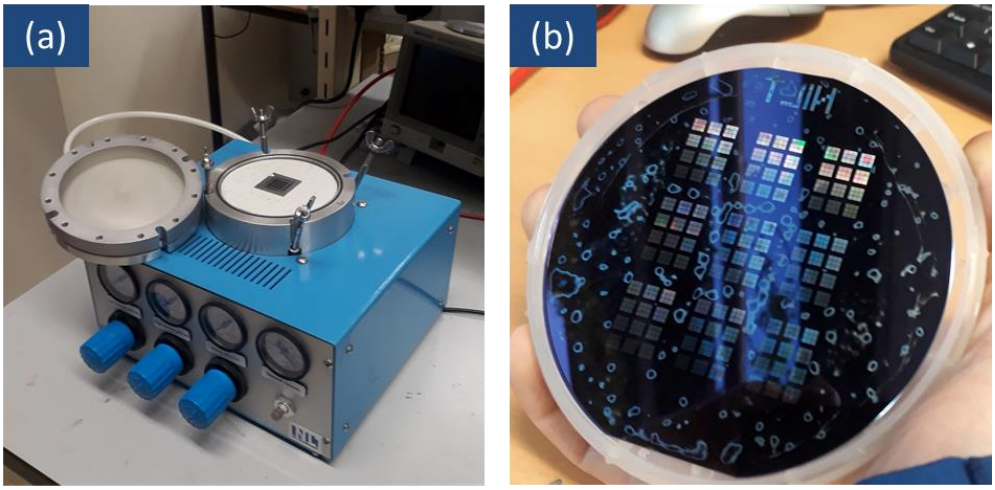

Figure 2.6.5 (a) The NILT CNI thermal nanoimprint unit. A 20 x 20 cm imprint mold is placed at the centre of the white ceramic heating wafer. The inflatable membrane is seen to the left. (b) A wafer scale imprint performed into a 300 nm PMMA film with the CNI.

2.7 Finite element analysis for mechanics problems

Many of the problems encountered in solid mechanics involve solving partial differential equations for which there exist no easily attainable analytic solution due to complex geometries, boundary conditions, and constitutive laws. For example, in the case of indentation of a compliant layer on a rigid substrate with a flat punch, the film bonded to the substrate is restricted in its vertical motion, while the top surface is free to deform. At the edge of the contact area there are flexible elastic-plastic walls allowing for lateral strains. Traditionally a full stick friction condition is applied at the film-substrate interface, while the film-punch interface is assumed to be frictionless. Even for this relatively straightforward geometry obtaining a solution in analytic form is extremely challenging. In such cases, numerical strategies such as finite element analysis (FEA) which yield approximate solutions can offer a great deal of insight into the problem.

2.7.1 Example problem: one dimensional Poisson's equation

FEA problem solving is typically divided into four steps: conversion of the relevant differential equation into its weak form, construction of a mesh on which the problem will be solved, representation of the approximate solution by a linear combination of

basis functions, and numerically solving the resultant matrix equations. To illustrate this, we consider Poisson's equation in one dimension:

$$-u''(x) = f(x), \qquad x \in (0,1)$$

$$u(0) = u(1) = 0 \tag{2.7.1}$$

The first step is to convert the differential equation into its weak formulation by multiplying both sides by a smooth trial function *v(x)*, which must satisfy the boundary conditions of the solution, and integrating over the domain:

$$\int_0^1 (-u''(x)v(x))dx = \int_0^1 f(x)v(x)dx$$

$$v(0) = v(1) = 0 \tag{2.7.2}$$

This may be reduced via integration by parts to:

$$\int_0^1 u'(x)v'(x)dx = \int_0^1 f(x)v(x)dx \tag{2.7.3}$$

This is referred to as the weak formulation, as equation 2.7.3 is merely required to be hold for all trial functions in trial function space, as opposed to all values of x as in equation 2.7.1. Following conversion into the weak form, the domain is discretised into *n* elements, divided by *n + 1 nodes* on which the problem will be solved, shown in figure 2.7.1 below

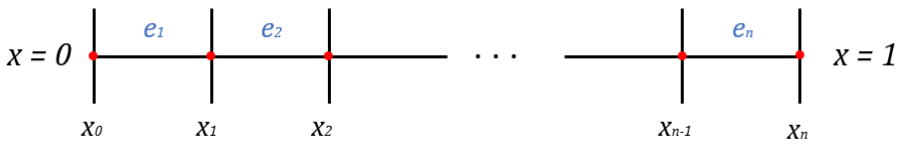

Figure 2.7.1 Discretisation of the problem domain into *n* elements with *n* + 1 nodes

The great strength of the FEA is that elements can be of arbitrary shape, allowing for nodes to be concentrated at areas of high gradients. To complete discretisation, a basis set φ must be selected for the domain. In this case, a piecewise linear function is a sensible choice:

$$\varphi_i(x) = \begin{cases} \left(\frac{x-x_{i-1}}{e_i}\right), & x_{i-1} \le x \le x_i \\ \left(\frac{x_{i+1}-x}{e_{i+1}}\right), & x_i \le x \le x_{i+1} \\ 0, & \text{else} \end{cases} \tag{2.7.4}$$

This scheme is represented in figure 2.7.2.

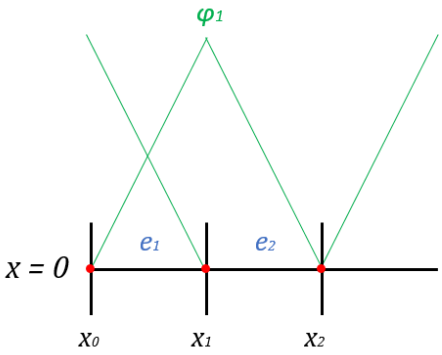

Figure 2.7.2 Representation of the basis function φ_i, as well as the nodes x_i and elements e_i.

The approximate numerical solution is then represented as a linear combination of the basis/shape functions:

$$u_h = \sum_1^n c_j \varphi(x) \tag{2.7.5}$$

The weak form solution then becomes:

$$\sum_{j=1}^{n-1} c_j \int_0^1 \varphi'(x)v'(x)dx = \int_0^1 f(x)v(x)dx \tag{2.7.6}$$

To solve this, we may use the Galerkin formulation, in which the trial function $v(x)$ and the basis function are the same. We then sum over φ for $v(x)$, leading to a system of linear equations:

$$\left(\int_0^1 \varphi_1'\varphi_1'dx\right)c_1 + \cdots + \left(\int_0^1 \varphi_1'\varphi_{n-1}'dx\right)c_{n-1} = \int_0^1 f\varphi_1 dx$$
$$\vdots \qquad\qquad \vdots \qquad\qquad \vdots$$

$$\left(\int_0^1 \varphi'_{n-1}\varphi'_1 dx\right)c_1 + \cdots + \left(\int_0^1 \varphi'_{n-1}\varphi'_{n-1} dx\right)c_{n-1} = \int_0^1 f\varphi_{n-1} dx \qquad (2.7.7)$$

These may be expressed more simply in matrix form:

$$\begin{bmatrix} a(\varphi_1,\varphi_1) & \cdots & a(\varphi_1,\varphi_{n-1}) \\ \vdots & \ddots & \vdots \\ a(\varphi_{n-1},\varphi_1) & \cdots & a(\varphi_{n-1},\varphi_{n-1}) \end{bmatrix} = \begin{bmatrix} c_1 \\ \vdots \\ c_{n-1} \end{bmatrix} \begin{bmatrix} (f,\varphi_1) \\ \vdots \\ (f,\varphi_{n-1}) \end{bmatrix} \qquad (2.7.8)$$

Where:

$$a(\varphi_i,\varphi_j) = \int_0^1 \varphi'_i\varphi'_j dx, \qquad (f,\varphi_i) = \int_0^1 f\varphi_i dx \qquad (2.7.9)$$

Therefore, with knowledge of f(x) and the basis function, 2.7.8 can be solved for the coefficients and an approximate solution to the problem may be obtained via 2.7.3.

Finite element simulations in this were carried out with commercial software suite Abaqus 2017 FEA (Dassault Systemes) on a 32 Gb PC equipped with 4 cores. Simulations were generally performed using the "explicit" analyser, employing an explicit integration scheme better suited to large strain deformations than the traditional scheme. Details regarding specific material models and boundary conditions may be found in the relevant chapters.

In summary, the methods outlined in this chapter allow for the mechanical characterisation and patterning of small volumes of materials. Indentation based experiments enable load-displacement curves with sub-nm spatial resolution and sub-mN load control to be obtained. FIB milling allows for precision tip geometries to be created, allowing access to intrinsic stress-strain data. Thermoplastic films can be deterministically patterned with high throughput via thermal nanoimprint lithography Through AFM the topography of patterned or indented films can be studied to high precision, while STXM supplies information on x-ray absorption, which in turn may be used to calculate mass density. While the work conducted in this thesis is primarily experimental, finite element analysis functions as an invaluable comparative tool, enabling access to variables and quantities which may not be easily measured. As a whole, these techniques enable high precision nanomechanical experiments to be performed with confidence.

Bibliography

1. Farges, G. & Degout, D. Interpretation of the indentation size effect in vickers microhardness measurements-absolute hardness of materials. *Thin Solid Films* **181**, 365–374 (1989).

2. Pethica, J. B., Hutchings, R. & Oliver, W. C. Composition and hardness profiles in ion implanted metals. *Nucl. Instruments Methods Phys. Res.* **209–210**, 995–1000 (1983).

3. Fischer-Cripps, A. C. Nanoindentation of Thin Films. in 132–143 (2004). doi:10.1007/978-1-4757-5943-3_8

4. Oliver, W., Hutchings, R. & Pethica, J. Measurement of Hardness at Indentation Depths as Low as 20 Nanometres. in *Microindentation Techniques in Materials Science and Engineering* 90-90–19 (ASTM International, 1985). doi:10.1520/STP32953S

5. Pethica, J. B., Hutchings, R. & Oliver, W. C. Hardness measurement at penetration depths as small as 20 nm. *Philos. Mag. A* **48**, 593–606 (1983).

6. Bulychev, S. I., Alekhin, V. P., Shorshorov, M. K. & Ternorskii, A. P. Determining Young's modulus from the indenter penetration diagram. *Zavod. Lab* **41**, 11137–11140 (1975).

7. Fröhlich, F., Grau, P. & Grellmann, W. Performance and analysis of recording microhardness tests. *Phys. Status Solidi* **42**, 79–89 (1977).

8. Newey, D., Wilkins, M. A. & Pollock, H. M. An ultra-low-load penetration hardness tester. *J. Phys. E.* **15**, 119–122 (1982).

9. Stilwell, N. A. & Tabor, D. Elastic Recovery of Conical Indentations. *Proc. Phys. Soc.* **78**, 169–179 (1961).

10. Doerner, M. F. & Nix, W. D. A method for interpreting the data from depth-sensing indentation instruments. *J. Mater. Res.* **1**, 601–609 (1986).

11. Lawn, B. R. & Howes, V. R. Elastic recovery at hardness indentations. *J. Mater. Sci.* **16**, 2745–2752 (1981).

12. Bhattacharya, A. K. & Nix, W. D. Finite element simulation of indentation experiments. *Int. J. Solids Struct.* **24**, 881–891 (1988).

13. Chiang, S. S., Marshall, D. B. & Evans, A. G. The response of solids to elastic/plastic indentation. I. Stresses and residual stresses. *J. Appl. Phys.* **53**, 298–311 (1982).

14. Pharr, G. M. & Oliver, W. C. Measurement of Thin Film Mechanical Properties Using Nanoindentation. *MRS Bull.* **17**, 28–33 (1992).

15. Oliver, W. C. & Pharr, G. M. Measurement of hardness and elastic modulus by instrumented indentation: Advances in understanding and refinements to methodology. *J. Mater. Res.* **19**, 3–20 (2004).

16. Sneddon, I. N. The relation between load and penetration in the axisymmetric boussinesq problem for a punch of arbitrary profile. *Int. J. Eng. Sci.* **3**, 47–57

(1965).

17. Hay, J., Agee, P. & Herbert, E. Continuous stiffness measurement during instrumented indentation testing. *Exp. Tech.* **34**, 86–94 (2010).

18. Herbert, E. G., Oliver, W. C., Lumsdaine, A. & Pharr, G. M. Measuring the constitutive behavior of viscoelastic solids in the time and frequency domain using flat punch nanoindentation. *J. Mater. Res.* **24**, 626–637 (2009).

19. Herbert, E. G., Oliver, W. C. & Pharr, G. M. Nanoindentation and the dynamic characterization of viscoelastic solids. *J. Phys. D. Appl. Phys.* **41**, 074021 (2008).

20. McKenzie, W., Pethica, J. & Cross, G. A direct-write, resistless hard mask for rapid nanoscale patterning of diamond. *Diam. Relat. Mater.* **20**, 707–710 (2011).

21. Brandrup, J., Immergut, E. H. & Grulke, E. A. *Polymer handbook*. (Wiley-Interscience, 1999).

22. Society of Photographic Scientists and Engineers., D. E., SPSE--the Society for Imaging Science and Technology., C. W. & Scriven, L. E. *Journal of imaging science. Journal of Imaging Technology* **13**, (Society of Photographic Scientists and Engineers, 1985).

23. Croll, S. G. The origin of residual internal stress in solvent-cast thermoplastic coatings. *J. Appl. Polym. Sci.* **23**, 847–858 (1979).

24. Raegen, A. *et al.* Aging of Thin Polymer Films Cast from a Near-Theta Solvent. *Phys. Rev. Lett.* **105**, 227801 (2010).

25. Binnig, G., Quate, C. F. & Gerber, C. Atomic Force Microscope. *Phys. Rev. Lett.* **56**, 930–933 (1986).

26. Dhez, O., Ade, H. & Urquhart, S. . Calibrated NEXAFS spectra of some common polymers. *J. Electron Spectros. Relat. Phenomena* **128**, 85–96 (2003).

27. Watts, B., Schuettfort, T. & McNeill, C. R. Mapping of Domain Orientation and Molecular Order in Polycrystalline Semiconducting Polymer Films with Soft X-Ray Microscopy. *Adv. Funct. Mater.* **21**, 1122–1131 (2011).

28. Watts, B., Warnicke, P., Pilet, N. & Raabe, J. Nanoscale measurement of the absolute mass density of polymers. *Phys. status solidi* **212**, 518–522 (2015).

29. Bernstein, D. P. *et al.* Nonuniform switching of the perpendicular magnetization in a spin-torque-driven magnetic nanopillar. *Phys. Rev. B* **83**, 180410 (2011).

30. Ade, H. & Hitchcock, A. P. NEXAFS microscopy and resonant scattering: Composition and orientation probed in real and reciprocal space. *Polymer (Guildf).* **49**, 643–675 (2008).

31. Winn, B. *et al.* Illumination for coherent soft X-ray applications: the new X1A beamline at the NSLS. *J. Synchrotron Radiat.* **7**, 395–404 (2000).

32. Raabe, J. *et al.* PolLux: A new facility for soft x-ray spectromicroscopy at the Swiss Light Source. *Rev. Sci. Instrum.* **79**, 113704 (2008).

33. Chou, S. Y., Krauss, P. R. & Renstrom, P. J. Nanoimprint Lithography. *J. Vac. Sci. Technol. B, Nanotechnol. Microelectron. Mater. Process. Meas. Phenom.* **14**, 4129–4133 (1996).

34. Guo, L. J. Nanoimprint Lithography: Methods and Material Requirements. *Adv. Mater.* **19**, 495–513 (2007).

35. Feng Hua *et al.* Polymer Imprint Lithography with Molecular-Scale Resolution. (2004). doi:10.1021/NL048355U

36. English, A. *et al.* Substrate topography: A valuable in vitro tool, but a clinical red herring for in vivo tenogenesis. *Acta Biomater.* **27**, 3–12 (2015).

37. Ok, J. G. *et al.* Continuous and scalable fabrication of flexible metamaterial films via roll-to-roll nanoimprint process for broadband plasmonic infrared filters. *Appl. Phys. Lett.* **101**, 223102 (2012).

38. GUO, L. J., CHENG, X. & CHAO, C. Y. Fabrication of photonic nanostructures in nonlinear optical polymers. *J. Mod. Opt.* **49**, 663–673 (2002).

39. Studer, V., Pépin, A., Chen, Y. & Ajdari, A. Fabrication of microfluidic devices for AC electrokinetic fluid pumping. *Microelectron. Eng.* **61–62**, 915–920 (2002).

40. Cross, G. L. W., O'Connell, B. S. & Pethica, J. B. Influence of elastic strains on the mask ratio in glassy polymer nanoimprint. *Appl. Phys. Lett.* **86**, 1–3 (2005).

41. Schift, H., Heyderman, L. J. & Sotomayor Torres, C. M. Nanorheology. in *Alternative Lithography* (2004).

42. Hoffmann, T. & Sotomayor Torres, C. M. Viscoelastic Properties of Polymers. in *Alternative Lithography* (2004).

43. Varagnolo, S. *et al.* Effect of hair morphology and elastic stiffness on the wetting properties of hairy surfaces. *Microelectron. Eng.* **161**, (2016).

44. Bettinger, C. J., Langer, R. & Borenstein, J. T. Engineering substrate topography at the micro- and nanoscale to control cell function. *Angew. Chem. Int. Ed. Engl.* **48**, 5406–15 (2009).

45. Sotomayor Torres, C. M. Alternative lithography. *Mater. Sci.* 446 (2002). doi:10.1007/978-1-4419-9204-8_1

46. Rowland, H. D., King, W. P., Pethica, J. B. & Cross, G. L. W. Molecular Confinement Accelerates Deformation of Entangled Polymers During Squeeze Flow. *Science* 720–724 (2008).

47. mr-I 7000R series | micro resist technology GmbH. Available at: https://www.microresist.de/en/products/nanoimprint-resists/thermal-nanoimprint-lithography/mr-i-7000r-series. (Accessed: 30th July 2018)

48. mr-I 9000M series | micro resist technology GmbH. Available at: https://www.microresist.de/en/products/nanoimprint-resists/thermal-nanoimprint-lithography/mr-i-9000m-series. (Accessed: 30th July 2018)

49. mr-NIL 6000E series | micro resist technology GmbH. Available at: https://www.microresist.de/en/products/nanoimprint-resists/combined-t-and-photo-nanoimprint-lithography/mr-nil-6000e-series. (Accessed: 30th July 2018)

50. Brazil, O., Usov, V., Pethica, J. B. & Cross, G. L. W. Large area thermal nanoimprint below the glass transition temperature via small amplitude oscillatory shear forming. *Microelectron. Eng.* **182**, (2017).

51. Trabadelo, V., Schift, H., Merino, S., Bellini, S. & Gobrecht, J. Measurement of

demolding forces in full wafer thermal nanoimprint. *Microelectron. Eng.* **85**, 907–909 (2008).

Chapter 3:

Confined Flat Punch Indentation of Polymer Thin Films

Abstract

The indentation of compliant thin films supported on stiffer substrates by a precisely aligned flat punch is studied over a punch diameter to initial film thickness range (aspect ratio, χ) of 11:1 to 4:1. It is shown that at large aspect ratio this geometry approximates to a state of uniaxial strain, wherein strains orthogonal to the applied axial load are suppressed by the surrounding film. This simplified geometry provides a new approach to mechanical characterization of small volumes of materials, including the observation of a distinct, singular yield event of the material beneath confined the punch in a pressure dominated stress environment. This phenomenon is studied via finite element simulation and nanoindentation experiments using high molecular weight atactic polystyrene films, as well as a variety of other glassy systems. The effects of initial film thickness, punch interface friction, and substrate compliance on the stress-strain response of the film are all examined. The method, called the confined layer compression test, allows for extraction of elastic modulus, bulk modulus, Poisson's ratio, and yield stress from a single load-up curve with minimal sample preparation.

3.1 Introduction

Due to their ever widening application in technology and fundamental scientific significance in materials science, the mechanical properties of supported thin films of thicknesses a few microns or less represents one the most active areas of interest within the nanomechanics community[1–3]. The development of depth-sensing indentation instrumentation and techniques[4–6] using sharp tips has allowed determination of material mechanical properties down to the nanometre scales[7,8], enabling the inference of elastic and plastic properties with no independent measurement of local sample

strain. The extraction of parameters such as elastic modulus and hardness within a supported thin film geometry presents a significant experimental challenge however. The complex stress and strain fields arising from sharp tipped indentation compel the use of empirical constants, correction terms, and thickness-dependent weighting functions[9–13] to calculate these quantities, thereby significantly increasing the complexity and uncertainty of the data analysis process. Furthermore, due to the comparatively small volume of material involved in testing, errors due to geometric effects such as tip-rounding are heightened when compared with conventional micro/nanoindentation[14].

As highlighted by *Nix*[15], the study of changes in material properties due to size effects at the nanoscale requires the development simplified testing geometries which allow for the minimization of imposed stress and strain gradients. The micropillar compression test[16], wherein the sample is micromachined into a single pillar and compressed axially via an indenting punch, is one such geometry, imposing a condition of uniaxial stress on much of the pillar. For supported thin films, the flat punch again provides the simplest geometric definition, however has been employed less than sharp tipped methods due to the precise alignment required between punch face and sample to realise accurate formation of contact[17]. The first detailed flat punch indentation studies were performed by Li in the 1970's who examined the mechanics who examined diffusion and dislocation creep in succinonitrile crystals in the so-called impression creep test[18,19]. Since then numerous refinements have been made. *Yang* developed an explicit expression for the contact stiffness of a compressible elastic film bonded to a rigid substrate for contact radii much larger than the film initial film thickness[20]. *Gao*[21] attempted to account for substrate effects following the approach of *Sneddon*[22], and arrived at a closed form solution for the contact compliance of a thin film supported on a substrate with film to substrate modulus ratios ranging from 0.5 to 2.0 for a range of punch radius to film thickness ratios. This was later extended by *Pharr*[23] to cover a range of 0.2 to 10. *Turner*[24] et al. further parameterised the small strain elastic regime for compliant films ($E_{film} > E_{sub}$) via finite element simulations incorporating variables such as punch diameter to initial film thickness ratio, friction at the punch film interface, film-substrate compliance ratios, and the bonding of the film to the substrate. A semi-analytic model was derived and applied with high accuracy to low density polyethylene films on a variety of substrates. In terms of scientific application, the flat punch geometry has been used to study the fundamental properties of polymers confined in gaps smaller than the size of the bulk macromolecule, with an inversion

conventional melt viscosity scaling with molecular weight being observed for confined films[25]. The geometry is also of technological importance, replicating the squeeze-flow conditions encountered in nanoimprint lithography[26,27].

This chapter will focus on the indentation of supported polymer thin films in the flat punch configuration. It shall be shown that at sufficiently high punch diameter to initial film thickness aspect ratio, the system enters a state of quasi-uniaxial strain deformation, in which the film surrounding the contact area acts to suppress lateral strains. A discrete yield event is observed at a stress higher than the conventional yield stress due to the confining film and represents the onset of highly uniform plasticity for material beneath the punch. This new test, called the confined layer compression test (CLCT) is studied via experimental indentation into high molecular weight polystyrene films and via finite element simulation. It will be shown that the CLCT can be used to extract the elastic modulus, yield stress, Poisson's ratio, and bulk modulus for simple isotropic elastic-plastic materials. For materials displaying more complex constitutive laws, the CLCT is used to study elastic and plastic response in a pressure dominated stress environment. Comparisons will be made between the CLCT and the analytic solutions for the true uniaxial strain geometry, as well as with experimental realisations of the latter. The effects of initial film thickness, friction at the punch-film interface, and finite substrate stiffness are all considered. The material parameters extracted from the CLCT for polystyrene are found to agree well with literature values.

3.2 Uniaxial Strain Deformation

The fundamental conjecture of the confined layer compression test is that at sufficiently high punch diameter to initial film thickness ratio $\chi = d/h_0$, the material beneath the punch is subject to a state of uniaxial strain, which is sustained to indentation strains well beyond the elastic limit. Uniaxial strain is a mode of deformation in which all strains save those parallel to the direction of applied load are supressed. Uniaxial strain deformation has been achieved at the macroscopic scale through two distinct approaches: lateral deformation may be supressed by a rigid confining jacket which tightly surrounds the compressed material[28], or the test may be rendered effectively one-dimensional if the sample diameter to thickness aspect ratio is extremely high, typically on the order of 60:1[29]. Both of these approaches are displayed in figure 3.2.1.

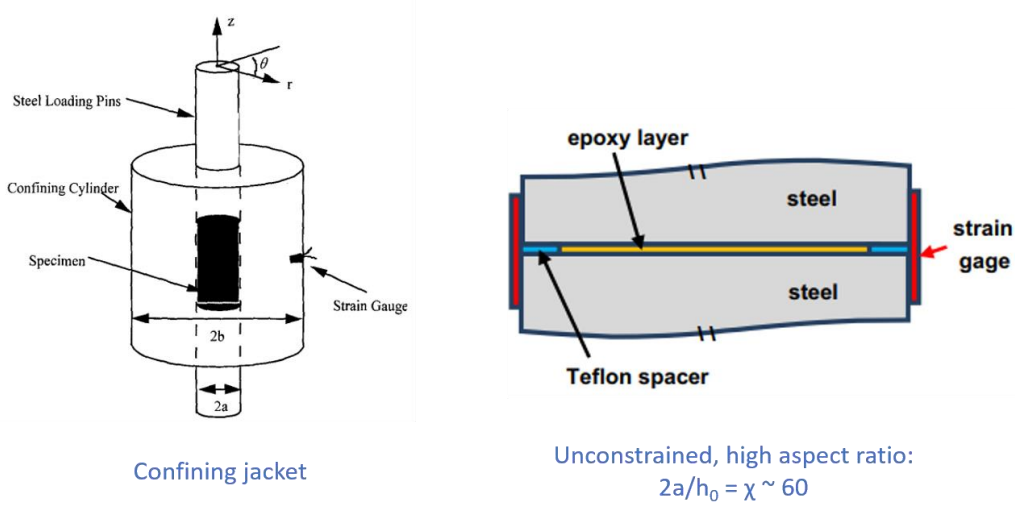

Figure 3.2.1 Conventional approaches to achieving uniaxial strain deformation with samples of macroscopic dimensions. Lateral strains may be supressed by a rigid confining jacket surrounding the sample (left), or may be neglected if the deformation is rendered effectively one-dimensional by compression of a sample with extremely high diameter to thickness aspect ratio (right.)

The degree to which microscopic flat punch indentation of a compliant film on a stiffer substrate will approximate a to uniaxial strain state will be dictated by geometric configuration factors such as film thickness, boundary conditions such as substrate stiffness, and intrinsic material properties such as Poisson's ratio. These shall be considered in due course; however, it is first instructive to consider the true uniaxial strain case, which shall form a reference mathematical framework for the remainder of this chapter. Comparison shall be made to the common case of frictionless uniaxial stress, in which no stresses are imposed orthogonal to the axial stress, allowing lateral strains via the Poisson effect and plastic flow. These geometries are shown in figure 3.2.1, where a mean axial stress σ_z is applied via a punch of diameter d to a layer of material of thickness h_0. In this two-dimensional radial cross-section representation, the jacket is shown as two infinitely stiff, frictionless blue blocks. The confined layer test is shown in (c).

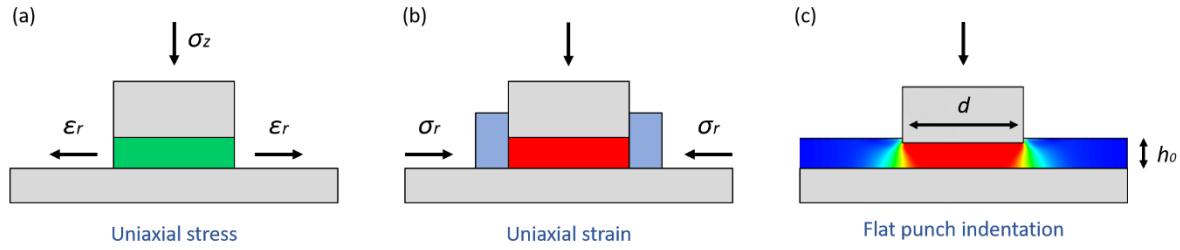

Figure 3.2.2 2D comparison of flat punch nanoindentation to uniaxial stress and uniaxial strain deformations (a) Uniaxial stress, in which an axial stress is applied and the material is free to deform laterally. (b) Uniaxial strain, where the material is laterally constrained and may only deform axially. (c) Flat punch indentation, in which the film surrounding the contact area plays a similar role to the jackets of (b), albeit with finite stiffness.

3.2.1 Elastic stresses

As outlined in chapter one, the principle stresses of an *isotropic linear elastic material* expressed in cylindrical coordinates are given by:

$$\sigma_{zz} = \frac{2G}{1\text{-}2\nu}[(1\text{-}\nu)\varepsilon_{zz} + \nu\varepsilon_{\theta\theta} + \nu\varepsilon_{rr}]$$

$$\sigma_{\theta\theta} = \frac{2G}{1\text{-}2\nu}[(1\text{-}\nu)\varepsilon_{\theta\theta} + \nu\varepsilon_{zz} + \nu\varepsilon_{rr}]$$

$$\sigma_{rr} = \frac{2G}{1\text{-}2\nu}[(1\text{-}\nu)\varepsilon_{rr} + \nu\varepsilon_{\theta\theta} + \nu\varepsilon_{zz}] \qquad (3.2.1)$$

The uniaxial strain condition mandates that all strains orthogonal to the applied axial stress be zero, i.e. $\varepsilon_{rr} = \varepsilon_{\theta\theta} = 0$. As such, equations 3.2.1 reduce to:

$$\sigma_{zz} = 2G\left(\frac{1\text{-}\nu}{1\text{-}2\nu}\right)\varepsilon_{zz} = C\varepsilon_{zz} \qquad (3.2.2\ a)$$

$$\sigma_{rr,\theta\theta} = 2G\frac{\nu}{1\text{-}2\nu}\varepsilon_{zz} = \left(K + \frac{2}{3}G\right)\varepsilon_{zz} = \lambda\varepsilon_{zz} \qquad (3.2.2\ b)$$

Where C is the constrained elastic modulus[30], and λ is Lame's second parameter. Alternatively, the in-plane stresses may be expressed in terms of the axial stress:

$$\sigma_{rr,\theta\theta} = \left(\frac{\nu}{1\text{-}\nu}\right)\sigma_{zz} \qquad (3.2.3)$$

In the elastic regime, stress vs. strain in the uniaxial strain test is linear, with a slope given by a confined elastic modulus C that is higher than Young's modulus for all values of Poisson's ratio ν, except materials showing no Poisson effect ($\nu = 0$) and is infinite for incompressible materials ($\nu = 0.5$). This is shown in figure 3.2.2 (a). Equation 3.2.3

highlights that the in-plane stresses exerted on the confining jacket walls are related to the applied stress through ν only, and this relationship is plotted in figure 3.2.2 (b). As materials with higher values of ν become more incompressible, the forces exerted on the walls increases dramatically, a fact of paramount importance for flat punch indentation where the surrounding material is identical to that being tested and is of finite stiffness and strength. As such, significant deviations can be expected in the stress response of the CLCT, particularly in the plastic limit where $\nu \rightarrow 0.5$ and the radial stresses become equal to the applied axial stress in accordance with equation 3.2.3.

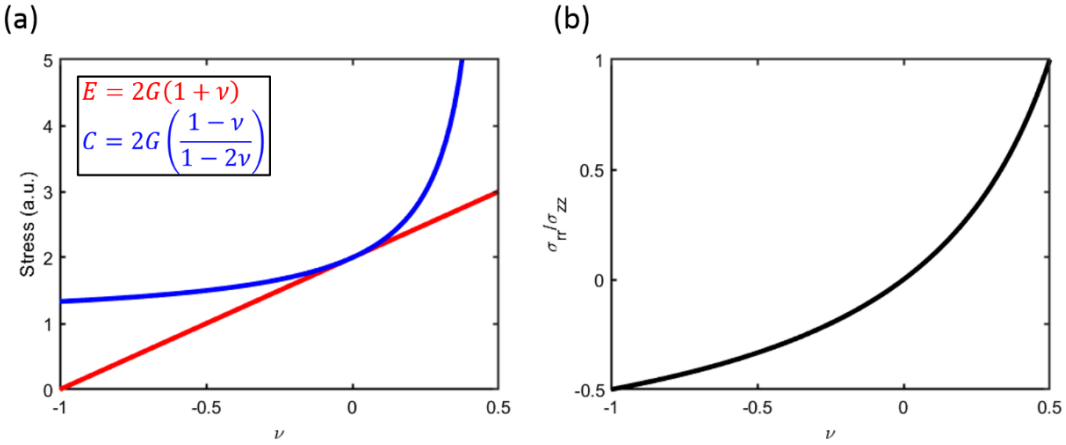

Figure 3.2.2 (a) Scaling of the uniaxial strain confined modulus *C* and Young's modulus with Poisson's ratio (including auxetic materials with negative *ν*). (b) Scaling of the ratio of radial stress to axial stress ratio with Poisson's ratio.

3.2.2 Hydrostatic and shear stress components

The geometric simplicity of the uniaxial strain configuration allows for the straightforward partitioning of the overall stress tensor into its hydrostatic and deviatoric components. As described in chapter one, these components can be represented in scalar form through the invariants I_1 and J_2 respectively. The hydrostatic pressure P is given by:

$$P = \frac{I_1}{3} = \frac{1}{3}(\sigma_{rr} + \sigma_{\theta\theta} + \sigma_{zz})$$

$$= \frac{1}{3}\left(\frac{1+\nu}{1-\nu}\right)\sigma_{zz} \qquad (3.2.4)$$

Shear stress is represented via the Von Mises equivalent stress, σ_{VM} a scalar function of the second deviatoric invariant, J_2:

$$\sigma_{VM} = \sqrt{3J_2} \tag{3.2.5}$$

This becomes:

$$\sigma_{VM} = \sqrt{\frac{1}{2}[(\sigma_{zz}-\sigma_{rr})^2 + (\sigma_{rr}-\sigma_{zz})^2]} = |\sigma_{zz}-\sigma_{rr}| = \frac{1-2\nu}{1-\nu}\sigma_{zz} \tag{3.2.6}$$

Equations 3.2.4 and 3.2.6 can be readily combined to give a functional relationship between P and σ_{VM}:

$$\sigma_{VM} = 3\frac{1-2\nu}{1+\nu}P = 2\frac{G}{K}P \tag{3.2.7}$$

Where G and K are the shear and bulk moduli respectively. For uniaxial tension/compression the equivalent expression is given as:

$$\sigma_{VM} = 3P \tag{3.2.8}$$

By contrast, the uniaxial strain state represents a pressure dominated stress state, as shown in the plots shear versus pressure stress of expressions 3.2.7 & 3.2.8 for various ν in figure 3.2.3. While the degree to which pressure dominates the relative composition is dictated by ν, it can be seen for most values the resultant stress environments will lie far to the right of the uniaxial stress case.

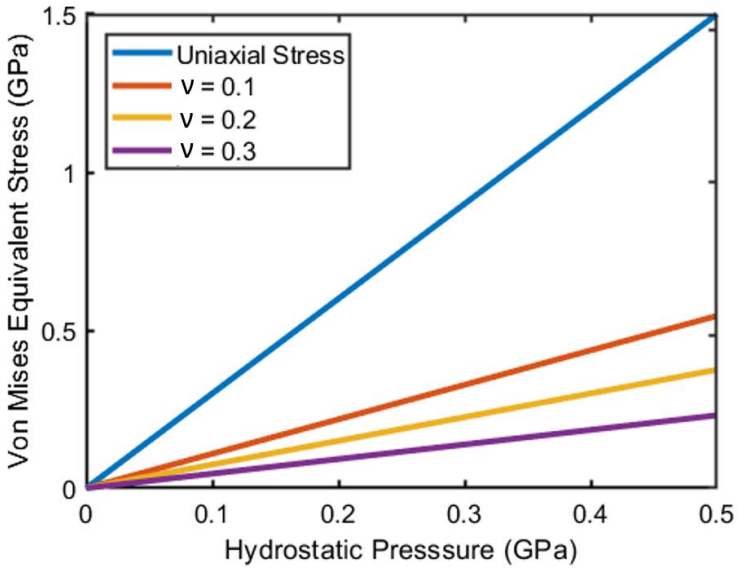

Figure 3.2.3 Von Mises equivalent shear stress as a function of hydrostatic pressure for uniaxial strain compression over a range of Poisson's ratio values, and for uniaxial stress compression (blue.)

3.2.3 Plastic yield conditions

For a perfectly plastic material, the onset of yield occurs when σ_{VM} intercepts the yield surface at a critical stress value Y, as developed in chapter one. For uniaxial strain, this is expressed as:

$$\sigma_{VM} = \sigma_{zz}\left(1-\frac{\nu}{1-\nu}\right) = Y \tag{3.2.9}$$

Rearranging, we find the system yields when the axial stress reaches:

$$\sigma_{zz} = \left(\frac{1-\nu}{1-2\nu}\right)Y = Y_c \tag{3.2.10}$$

As with the confined modulus C, this confined yield stress Y_c will exceeds the that yield stress in uniaxial tension/compression for all values of Poisson's ratio save $\nu = 0$ and will rise sharply towards infinity as $\nu \rightarrow 0.5$.

Realistically representing the physics of inelastic deformation in amorphous materials such as the of polymers, where yield is strongly related to molecular mobility[31,32], often requires the introduction of a pressure dependence into the yield criterion[33]. For pressure dominated stress states such as uniaxial strain and the confined layer compression test, the inclusion of this pressure term is vital. A modification to the Von Mises criterion is typically expressed through the octahedral shear stress[34]:

$$\tau_{oct} = \tau^0_{oct} + \alpha P, \qquad \tau_{oct} = \frac{1}{3}\sqrt{(\sigma_{zz}-\sigma_{rr})^2 + (\sigma_{rr}-\sigma_{\theta\theta})^2 + (\sigma_{\theta\theta}-\sigma_{zz})^2} \tag{3.2.11}$$

Where α is a constant characterizing the degree of pressure sensitivity, typically ranging from $0.05 - 0.25$ for amorphous polymers[34]. For consistency, we may express this modified criterion in terms of σ_{VM} as:

$$\sigma^P_{VM} = \sigma^0_{VM} + \left(\frac{3}{\sqrt{2}}\alpha\right)P = \sigma^0_{VM} + \alpha' P \tag{3.2.12}$$

This leads to the pressure dependent confined yield modulus, Y_c^P:

$$\sigma_{zz} = \left[\left(1-\frac{\nu}{1-\nu}\right) - \frac{\alpha'}{3}\left(1+\frac{2\nu}{1-\nu}\right)\right]^{-1} Y_0 = Y_c^P \tag{3.2.13}$$

In compression, $Y_c^P > Y_c$ for all cases; when $\alpha' \rightarrow 0$ the two values reduce to equivalence. The addition of this pressure term has the effect of introducing a range of ν for which

yielding is completely inaccessible in the uniaxial strain geometry. This is shown in figure 3.2.4 (a) which plots yield stress as a function of Poisson's ratio for a range of pressure coefficients. For the pressure independent case, yield is only forbidden in the incompressible case, ν = 0.5, where Y_c^P goes to infinity. As the pressure dependency of the yield surface increases, this singularity shifts left to lower values of Poisson's ratio, creating a parameter space for which yield is inaccessible governed by the dividing line:

$$Y_C^{max}(\nu, \alpha') = \alpha' - \frac{3(1-2\nu)}{1+\nu} \tag{3.2.14}$$

This is plotted in figure 3.2.3 (b). As glassy polymers typically sit in the range $0.25 < \nu < 0.45$ and $0.1 < \alpha' < 0.5$, this forbidden region may explain why previous uniaxial strain systems have failed to produce discrete yield events[28,35,36].The problem is further exacerbated by the fact that Poisson's ratio is generally found to increase with increasing pressure for free volume materials[37].

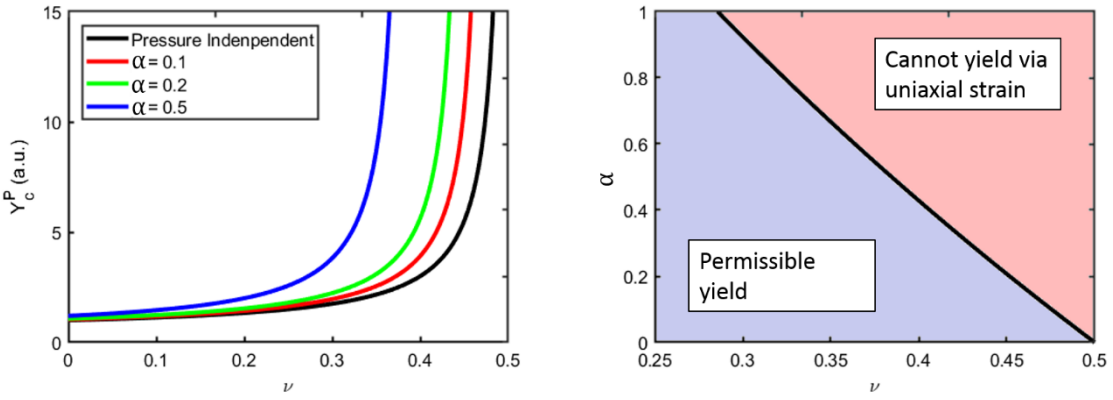

Figure 3.2.4 (a) Pressure dependent constrained yield point as a function of Poisson's ratio for a range of pressure sensitivity coefficients. (b) Constrained yield point parameterised in α' and ν. Materials lying to the right of the black line incapable of yield in a uniaxial strain geometry.

3.2.4 Plastic flow rules

As was shown in chapter one, the Prandtl-Reuss equations governing deformation in the plastic regime for associated flow may be written as:

$$d\varepsilon_{ij} = \frac{1+\nu}{E} d\sigma_{ij} - \frac{\nu}{E}\delta_{ij} d\sigma_{kk} + d\lambda s_{ij} \tag{3.2.14}$$

Where s_{ij} is the relevant deviatoric term and λ the scalar plastic multiplier. For uniaxial strain this becomes:

$$d\varepsilon_{zz} = \frac{1}{E}\left[d\sigma_{zz}\text{-}2\nu d\sigma_{rr,\theta\theta}\right] + \frac{2}{3}d\lambda\sigma_{zz}\left(\frac{2\nu\text{-}1}{\nu\text{-}1}\right) \quad (3.2.15\text{ a})$$

$$d\varepsilon_{rr} = \frac{1}{E}\left[d\sigma_{rr}\text{-}\nu(d\sigma_{\theta\theta} + d\sigma_{zz})\right] + \frac{1}{3}d\lambda\sigma_{zz}\left(\frac{2\nu\text{-}1}{1\text{-}\nu}\right) \quad (3.2.15\text{ b})$$

Where equation 3.2.3 is assumed valid at the point of first yield, and the appropriate substitutions performed. If perfect plasticity is assumed, at the yield point $\sigma_{zz} = Y_c$, therefore:

$$d\varepsilon_{zz} = \frac{1}{E}\left[d\sigma_{zz}\text{-}2\nu d\sigma_{rr,\theta\theta}\right] + \frac{2}{3}d\lambda Y_c\left(\frac{2\nu\text{-}1}{\nu\text{-}1}\right) \quad (3.2.16\text{ a})$$

$$d\varepsilon_{rr} = \frac{1}{E}\left[d\sigma_{rr}\text{-}\nu(d\sigma_{\theta\theta} + d\sigma_{zz})\right] + \frac{1}{3}d\lambda Y_c\left(\frac{2\nu\text{-}1}{1\text{-}\nu}\right) \quad (3.2.16\text{ b})$$

In the plastic regime the pure longitudinal strain condition still holds, therefore, all increments of in-plane strain will be zero. Furthermore, with the in-plane stresses being functions only of the applied axial stress and ν, which is assumed to be constant, all principle stress increments are equal: $d\sigma_{rr,\theta\theta} = d\sigma_{zz}$. This allows equations 3.2.16 to be rewritten as:

$$d\varepsilon_{zz} = \frac{1}{E}(1\text{-}2\nu)d\sigma_{zz} + \frac{2}{3}d\lambda Y_c\left(\frac{2\nu\text{-}1}{\nu\text{-}1}\right) \quad (3.2.17\text{ a})$$

$$d\varepsilon_{rr} = \frac{1}{E}(1\text{-}2\nu)d\sigma_{zz} + \frac{1}{3}d\lambda Y_c\left(\frac{2\nu\text{-}1}{1\text{-}\nu}\right) = 0 \quad (3.2.17\text{ b})$$

Equation 3.2.17 (b) now allows us to solve for the scalar plastic multiplier $d\lambda$:

$$d\lambda = \frac{3}{Y_c E}(1\text{-}\nu)d\sigma_z \quad (3.2.18)$$

Substituting this into 3.2.17 (a) and solving yields:

$$d\varepsilon_{zz} = \frac{3(1\text{-}2\nu)}{E}d\sigma_{zz} \quad (3.2.19)$$

Therefore, the slope of the axial stress strain curve in the post-yield regime is given by:

$$\frac{d\sigma_{zz}}{d\varepsilon_{zz}} = \frac{E}{3(1\text{-}2\nu)} = K \quad (3.2.20)$$

Where K is the bulk elastic modulus. In isotropic elastic systems, there are only two independent elastic constants, thus knowledge of any two allow for all other parameters to be determined. Within the uniaxial strain test, Poisson's ratio can be expressed as:

$$\nu = \frac{3 - K/C}{3 + K/C} \tag{3.2.21}$$

Therefore, it allows extraction of elastic and bulk moduli, Poisson's ratio, and yield stress in one measurement with each value of stress representative a unique strain point. This situation is summarized in figure 3.2.5 and contrasted with the uniaxial stress test. In the latter, only 2 parameters, the elastic modulus and yield stress, may be extracted as post-yield stresses are no longer single valued functions of strain and vice versa.

The non-idealised boundary conditions of the confined layer test lead to a convolution of jacket film plasticity with that of the puck beneath the punch and as such the slope of the plastic region is referred to as the effective confined plastic modulus, C^*. Deviations from the bulk modulus are studied as a function of aspect ratio, substrate stiffness, and frictional boundary conditions in the remainder of this chapter.

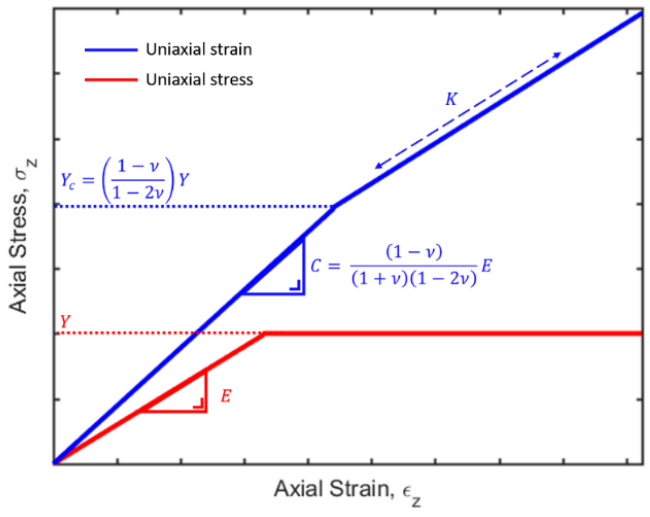

Figure 3.2.5 Axial stress-strain response of an isotropic linear elastic - simple plastic material in subjected to compressive/tensile loading in the uniaxial strain (blue) and uniaxial stress (red) geometries. In the uniaxial stress case, the slope of the curve is given by the material's Young's modulus E in the elastic limit, where it is subject to lateral Poisson strains. At the yield stress Y permanent deformation initiates, and the material flows laterally with no further resistance. In the case of uniaxial strain, Poisson strains are restricted in the elastic limit and the slope follows the confined modulus C. Plasticity begins at the elevated confined yield stress Y_c, and further loading in the plastic regime follows the bulk modulus K. This is as conventional plastic flow is not possible, leading to a purely compressive form of plasticity.

These relationships for yield and plasticity are derived for linear, isotropic media and as such deviation may be expected in real materials, where greater complexity can be expected. Separate internal relaxation mechanisms such as the α and ß transitions in glassy polymers show different pressure dependencies which may affect mechanical response[38]. Within semi-crystalline polymers, the failure mode may change based on the amount of crystallinity present[39], while at the nanoscale the properties of conventional engineering materials may deviate from their bulk values due to significant size effects[40,41]. Geometric complication is introduced in the CLCT by the imperfect rigidity of the confining side walls and the finite punch to film aspect ratio. Decoupling the material and geometric contributions to the non-ideal uniaxial strain response of thin film under confined compression requires systematic investigation with comparison between ideal and more complex materials. The distinct ductile yield transition between elastic and plastic behaviour produced via uniaxial strain has yet to be encountered within thin film form. As yield represents a fundamental change in the loaded material[42], the study of this failure mode is of high scientific value. This chapter shall focus primarily on the fundamental mechanics of the confined layer test geometry with reference to elastic-plastic material models. Polymer specific phenomena such as viscoelastic mechanical response, and non-equilibrium properties such as aging and mechanical rejuvenation shall be considered in chapter four, after the fundamental properties of the CLCT have been firmly established.

3.3 Experimental/Simulation Methods

3.3.1 Polymer Indentation Experiments

Polystyrene thin films (Polymer Source Inc.) of 1.13 MDa molecular weight and polydispersity ≈ 1 of thicknesses ranging from 190 to 470 nm were prepared via spin coating from a 2% wt. toluene solution on silicon <100> wafer pieces of approximately 1 cm^2 (University Wafer.) Films were then heated to 120 °C (T_g + 20°) for 20 minutes to remove any residual solvent content and stresses from the spin coating processes. PMMA (Mw = 0.35 MDa, Sigma Aldrich) films were prepared in a similar fashion from a 2% wt. chloroform solution. Samples were then mounted via crystal bond (Electron Microscopy Sciences) to the tilt stage (Physik Instrumente M-044) and alignment between sample and punch face being checked and corrected via a DME DS 95 AFM.

Indentations were performed using the Nanoindenter XP DME system equipped with a 2050 nm diameter FIB manufactured flat punch to a variety of peak loads at a constant load rate of 0.67 mN/s, corresponding to a stress rate of 0.20 GPa/s, except where explicitly stated. The residual strain imparted via indentation was studied via tapping mode AFM (Asylum MFP 3D) using standard tips.

Load displacement data was converted to engineering stress-strain data using the relations:

$$\sigma_{zz} = \frac{L}{A_{punch}}, \varepsilon_{zz} = \frac{d}{h_0} \tag{3.3.1}$$

Where A_{punch} is the area of the punch, which corresponds to a constant contact area between punch and film during testing. Finite instrument stiffness is subtracted from indentation data in post-indent analysis step which is detailed in section 3.4.2.

3.3.2 Finite Element Simulations

Axisymmetric simulations of the confined layer compression test geometry were performed using the Abaqus 2017 Explicit (Dassault Systemes) finite element package. The punch was modelled as a perfectly rigid body of 2 µm diameter with a radius of curvature of 50 nm at each corner. This value was chosen to reflect the finite sharpness of the punches edges produced experimentally via FIB milling and to aid in the simulation process by lessening the degree of stress concentration. The film was modelled as an elastic-perfectly plastic material with E = 3.0 GPa, ν = 0.33, Y = 0.1 GPa, and ρ = 1.04 g/cm^3. These values were chosen to reflect a typical glassy polymer well below T_g[43]. Film thicknesses ranged between 20 and 500 nm, covering an aspect ratio range of 100:1 to 4:1. The width of the film was set at 40 µm. 4-node bilinear axisymmetric quadrilateral (CAX4R) elements were utilized, with the initial element area set as 10 x 10 nm^2 for all film thicknesses. Indentation is simulated via prescribing a vertical displacement of the punch face. No other displacements of the punch are allowed. A full-slip condition is specified between film surface and film, except where otherwise stated. An encastre condition was applied to the bottom surface of the film such that $U_r = U_z = 0$, simulating a full-stick condition on a rigid substrate. This condition is relaxed in section 3.4.2, when studying the role of a compliant substrate. Load-displacement curves were produced via tracking the displacement and vertical reaction forces on a reference point at the centre of the punch. Reaction forces were

converted to stresses by dividing by the initial contact area corresponding to a diameter of 1900 nm when punch rounding was subtracted. Displacements to engineering strain by dividing by the initial film thickness.

For the pressure dependent yield surface outlined in equation 3.2.11 and studied in section 3.4.3 a Drucker-Prager plasticity model was employed. The appropriate values for internal friction and angle of dilation were chosen to reduce the model to the specified modified Von Mises yield criterion.

3.4 Results & Discussion

3.4.1 Stress-strain response of the confined layer compression test

Figure 3.4.1 shows the fundamental stress-strain response of a polymer thin film in the confined layer geometry indented at a constant stress rate. 3.4.1 (a) shows the experimental realisation of the test geometry for a 240 nm aPS film (χ = 8.5) loaded at a rate of 0.20 GPa/s, while (b) shows an approximately equivalent finite element (FEA) simulation of the test into a linear elastic-plastic material for χ = 8 (h_0 = 200 nm). The magenta dashed line represents the analytical uniaxial strain solution for the chosen elastic constants and test dimensions. The common features of both curves are:

- An initial linear elastic region, followed by an abrupt change of slope at yield at stresses of 0.32 (a) and 0.197 (b) GPa.
- A second linear region representing uniaxial strain plasticity, continuing until extrusional flow occurs at a stress of 0.65 (a) 0.4 (b) GPa, at which the uniaxial strain assumption breaks down.
- A plastic flow region in which the strain increases with little change in stress, followed by a geometrically induced quasi strain hardening regime at very high strains.

The experimental curve displays a short region of curvature upon initial contact of the punch with the film surface. As the CLCT acts as an approximation to the uniaxial strain state at intermediate strains, focus is given to the two primary features of the of the stress-strain curve occurring before the breakdown of this approximation at extrusion, namely the initial non-linear portion and the elastic-to-plastic transition. It is within this small to intermediate strain limit that a uniform state of deformation is achieved, allowing extraction of intrinsic stress versus strain data from load-

displacements curves. With the commencement of extrusion, the uniformity of deformation is lost, and strain values become less meaningful. As such, this portion of the curve shall be the focus of this section and the remainder of the chapter.

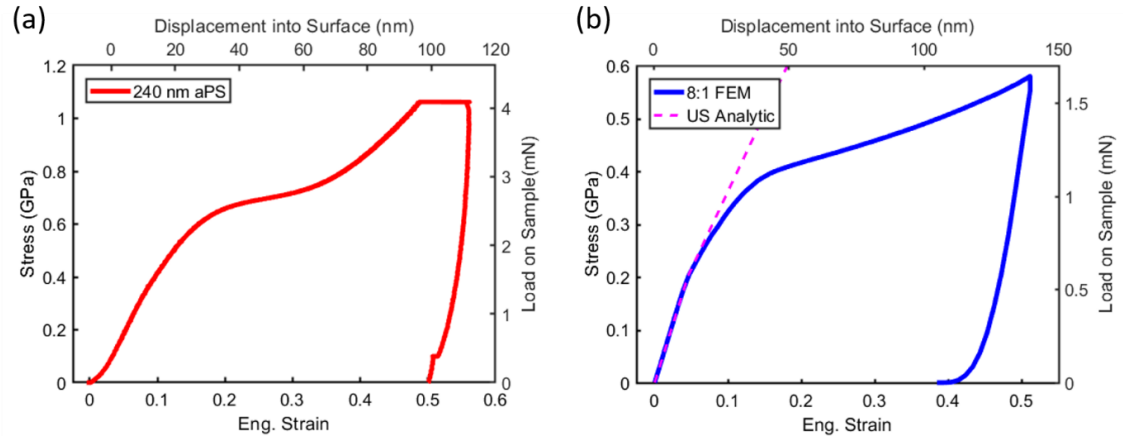

Figure 3.4.1 (a) Stress-strain curve for a 240 nm atactic polystyrene film indented with a 2050 nm flat punch in the CLCT geometry. (b) Approximately equivalent FEA simulation for an isotropic elastic-plastic material at an aspect ratio of **χ** = 8. The analytical uniaxial strain solution is shown in magenta.

Initial contact

The shape of the initial region of the load-displacement/stress-strain curve is controlled primarily by geometric deviations from the ideal case of a cylindrical punch incident to a compliant film supported on a rigid substrate[17,44]. In the case of a low roughness film as produced by spin-coating from a well-matched solvent, angular misalignment between punch face and film is the dominant factor. This is shown in figure 3.4.2 for a 190 nm PS film. (a) and (b) show AFM micrographs of two separate indents performed at misalignment angles of 3.5 and 5.9 mrad respectively, as determined by measuring their height profiles along the axis of greatest misalignment, shown here by dotted lines. These profiles are shown in (c). These angles correspond to a vertical misalignment distance of 7.2 and 12.1 nm, or 3.8% and 6.4% of the initial film thickness respectively.

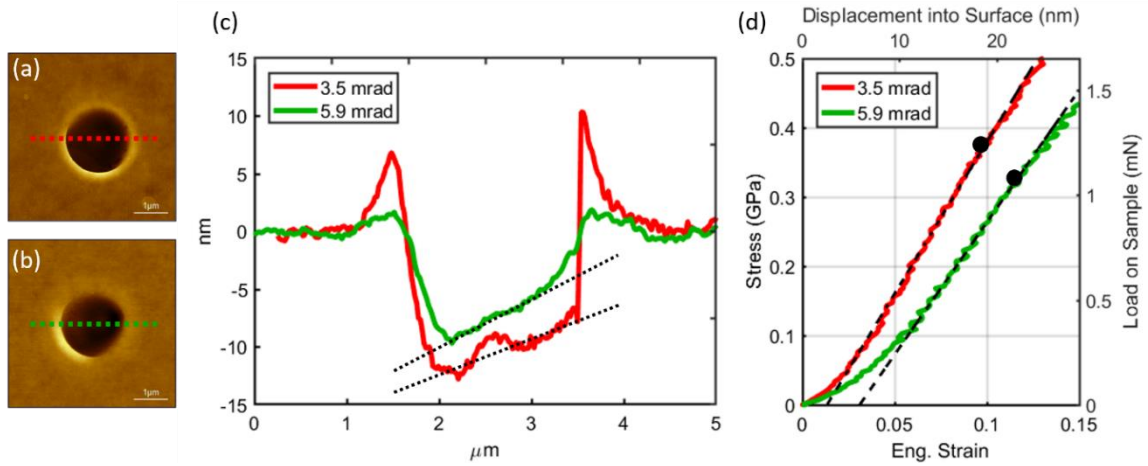

Figure 3.4.2 (a) AFM micrograph of flat punch indent with a punch to film misalignment angles of 3.5 mrad. (b) Equivalent image for a 5.9 mrad misalignment. (c) Corresponding height profiles. (d) Initial portion of the strain strain curves for the two indents. The confined yield points are shown as black circles.

The stress-strain curves in (d) show that these distances correspond well to the length of the initial non-linear regions at the start of the curves. The influence of this misalignment persists well beyond the non-linear region however, due to the increased shear stress and poorer lateral confinement resulting from the more wedge-like geometry. This manifests as a decrease of the confined elastic modulus from 4.38 to 3.82 GPa between the two indents, and a drop in yield stress from 0.36 to 0.32 GPa as highlighted by the black dots in (d). This section is not intended to serve as an exhaustive study of misalignment, but rather as a brief discussion of its experimental consequences. A fully study would take further take into account misalignment of the punch face and indenter load vector as well, which would require a detailed, fully three-dimensional FEA analysis.

Elastic to plastic yield

In this section it is shown that the inflection point in the curves of figure 3.4.1 represents a sharp yield transition from fully elastic to plastic behaviour. This transition is studied in greater detail in figure 3.4.3 for both for a 190 nm PS film and the FEA case at χ = 10. 3.4.3. (a) shows stress-strain curves for three separate indentation simulations; one loaded within the elastic limit $\sigma_{peak} < Y_c$ (green), one loaded into the confined plastic zone $Y_c < \sigma_{peak} < Y_{flow}$ (red), and one loaded past the extrusion point into the conventional plastic flow region $\sigma_{peak} < Y_{flow}$ (blue). Of principle interest is the emergence of a 2.3 nm residual strain following unloading within the confined

plastic region, demonstrating that the inflection point at 0.2 GPa represents a true yield event.

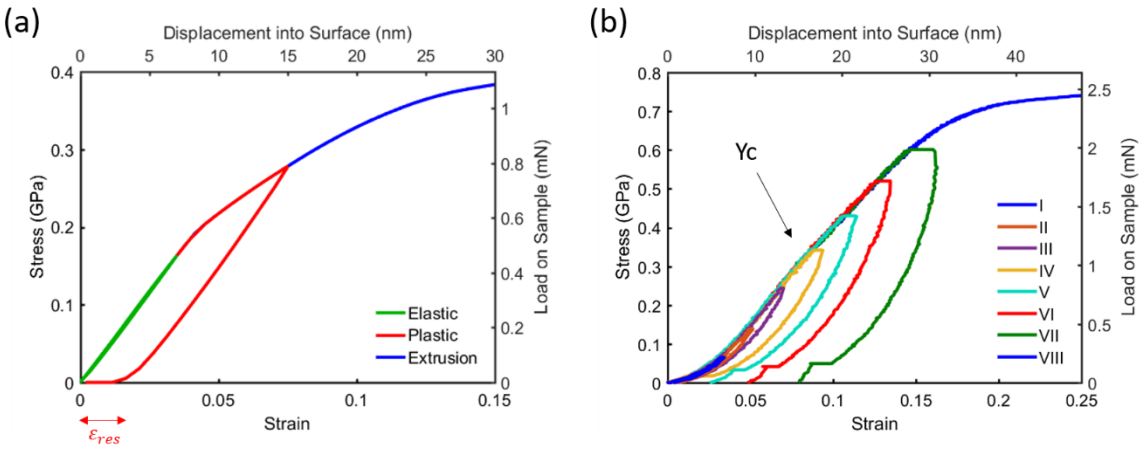

Figure 3.4.3 (a) FEA stress-strain curves for an isotropic elastic-plastic material in the CLCT for χ = 10. (b) Stress-strain curves for independent indents into a 190 nm PS film (χ = 10.8) in the CLCT geometry, with increasing peak displacement.

A similar behaviour is exhibited in the experimental data of (b), where the peak displacement into the surface is incremented by 4 nm with successive independent indents. Curves I - III lie in the elastic regime, and curves IV – VII within the confined plastic zone. The yield point is observable at 0.32 GPa, between curves iii and iv. Above this peak stress a residual strain is observable upon full unload along the x-axis, at which point the punch leaves the film surface. The magnitude of this residual strain increases with further peak loading into the confined plastic zone, before confinement failure at 0.7 GPa. To study further the development of plasticity, tapping mode AFM was performed on the residual impressions of indents iii-viii approximately one week after indentation and are shown in figure 3.4.4 (a).

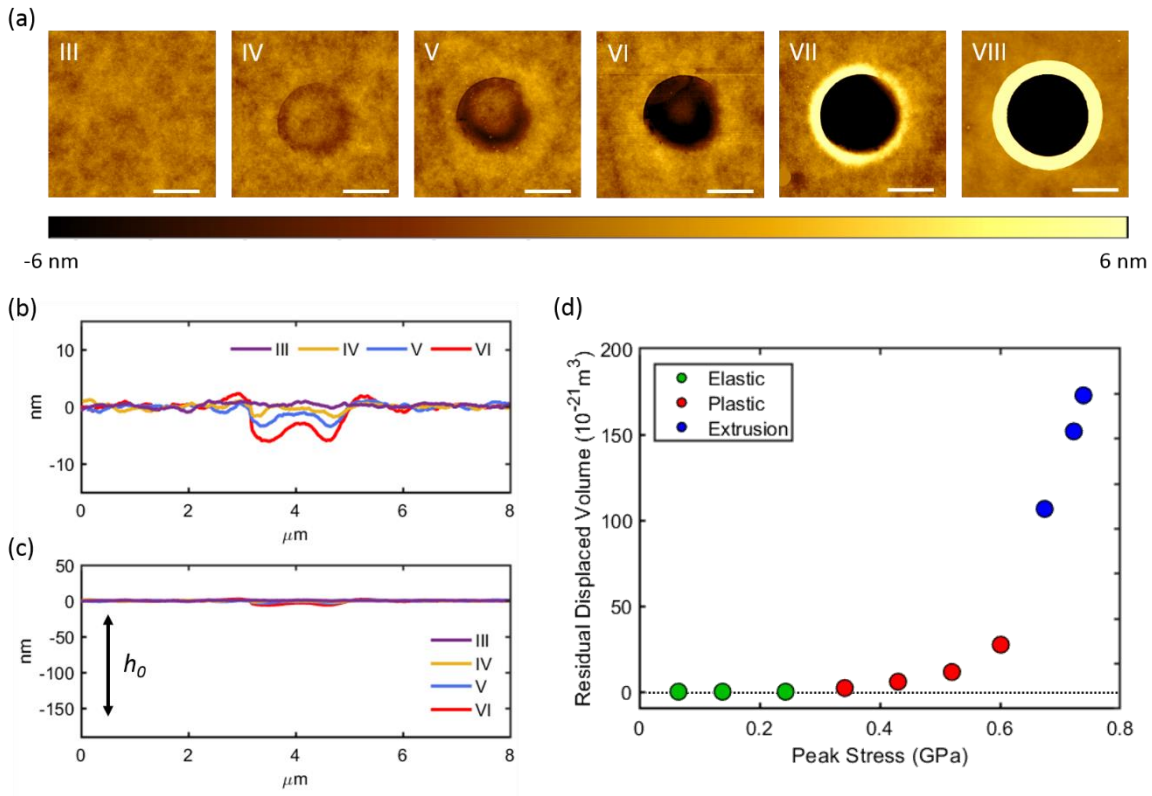

Figure 3.4.4 (a) Tapping mode afm micrographs of indents iii-viii, covering a peak stress range of 0.24-0.70 GPa. Scale bar is 2 micron (b) Height profiles of indents iv-vi. (c) Profiles scaled in terms of the initial film thickness, h_0 (d) Plot of peak stress vs residual displaced volume from the indented region.

As can be clearly seen, indent IV marks the onset of permanent plasticity, with the magnitude of the residual impression increasing until confinement ends at indent viii, where a largo halo of extruded material can be observed surrounding the contact area. This permanent plastic deformation is shown to be truly uniaxial in the height profiles of indents III – VI plotted in (b), where it can be observed the amount of material extruded to the surrounding region is minimal in the low-stress limit. These profiles are plotted again in (c) where they are scaled to the initial thickness of the film h_0, demonstrating the amount of residual strain is minimal. The total volume displaced from the indented regions is plotted as a function of peak applied stress in (d), where the confined plastic region is distinguished by a gradual increase in displaced volume before a rapid acceleration as the material surrounding the contact area yields, allowing extrusional flow. As can be observed from (a) and (d), indent VII represents a mixed stated of uniaxial strain deformation and incipient shear flow, evidenced by the greater quantity of material extruded to the area surrounding the indent and the increased displaced volume.

Of crucial interest is how closely the CLCT corresponds to true uniaxial strain, where deformation is uniform throughout the tested material. The height profiles in figure 3.4.4 (b) demonstrate that a degree of non-uniformity across the residual impression exists, with a distinct elevated region present at the centre of all indents. This non-uniformity is the result of residual stress pinned by local plasticity at the contact periphery which is generated by stress concentration at the punch edge. Schapery[45] addressed a somewhat similar problem for the case of a macroscopic "poker-chip" experiment, wherein a high aspect ratio sample ($\chi = 20$) is subjected to a longitudinal tensile deformation in the absence of any surrounding confining material. Treating the sample as a thin elastic disk, the variance of the mean principle shear stress τ_{rz} across the sample at a given strain within was a found to be a function of the sample properties and χ:

$$\tau_{rz} = \frac{3E\nu}{1+\nu}\sqrt{\frac{K}{E}}\frac{I_1\left(r\sqrt{\frac{K}{E}}\right)}{I_0\left(\chi\sqrt{\frac{K}{E}}\right)} \tag{3.4.1}$$

Where I_1 and I_0 are modified Bessel functions of the first kind and second kind respectively. This is plotted as a function of radial position for a range of aspect ratios in figure 3.4.5 (a), where it can be seen that the magnitude of shear stress at the punch/sample edge increases dramatically with decreasing χ. The relation of this equation to the CLCT geometry is demonstrated in 3.4.5 (b), which shows the normalised residual height profiles for a series of simulated indents to 0.075 peak indentation strain into films over the same aspect ratio range as (a). It can be observed that the residual impression deviates most from the ideal case at low aspect ratio, where at $\chi = 5$ there is significant curvature at the centre in comparison to the $\chi = 20$ case, and the greater residual impression at the punch edges. Despite some non-uniformity in shear stress, yield is reached for all material beneath the punch over a narrow range of applied axial stress even at modest aspect ratios. This is shown by considering simulation elements over a range $0 < r < 0.75$, highlighted in 3.4.5 (c) for the four χ's used here. We consider an element to be actively yielding when its equivalent plastic strain, a scalar quantity analogous to Von Mises equivalent stress, is greater than zero[46].

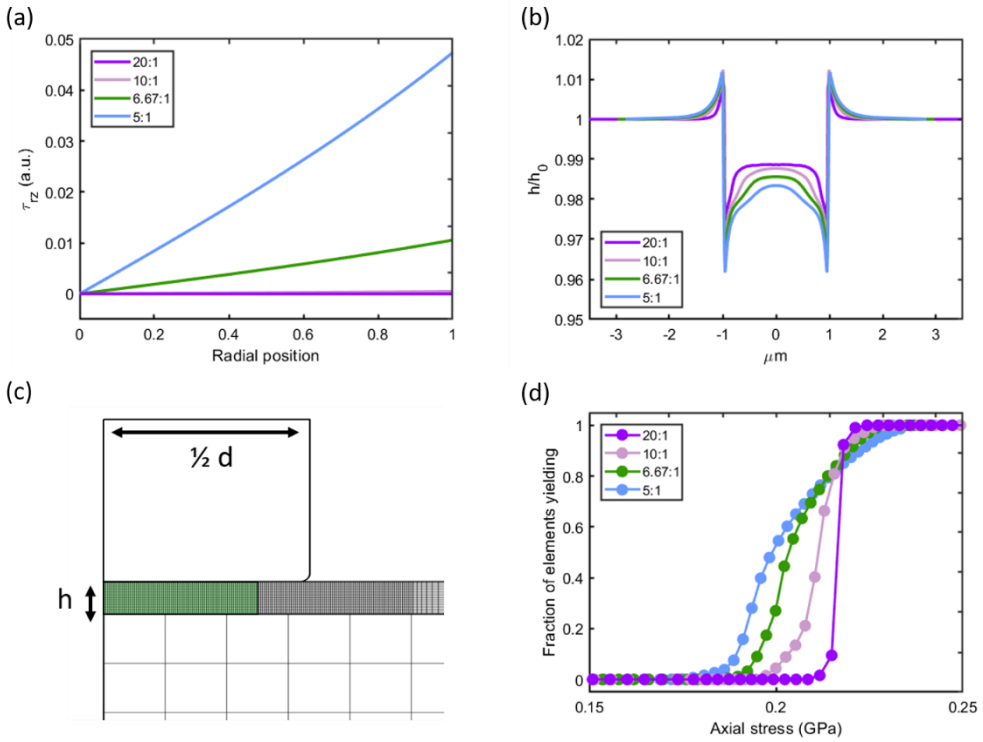

Figure 3.4.5 (a) Plot of principal shear stress as a function of radial position beneath the punch for a range of aspect ratios within Schapery's poker chip geometry. (b) Residual impression profiles for FEA simulations of indents to 0.075 strain into films of the same aspect ratios as (a). (c) Elements in which yielding status is measured highlighted in green. Edge elements are not included as they are contained within a different meshing region. (d) Fraction of elements beneath the punch actively yielding as a function of applied axial stress.

The normalized number of elements yielding within the volume considered is plotted as a function of applied axial stress in 3.4.5 (d). It is observed that as χ is increased, yielding becomes more uniform, becoming a discrete event across the volume at $\chi = 20$. At lower χ, the yield event is more gradual, occurring over an axial stress range of approximately 0.05 GPa, with material closer to the punch edge yielding earlier due to the heightened shear stress. It should also be noted that yield appears to occur at a higher axial stress value than the prescribed confined yield stress of 0.197 GPa for the $\chi = 10$ and $\chi = 20$ systems. This is due to the way in which stress is calculated: plasticised material at the punch edge contacting the rounded punch corners and sidewalls, increasing the total contact area and the load required to reach a stress of 0.197 GPa at the central region. Examination of the σ_{zz} components of the elements highlighted reveal they do indeed yield when this value reaches Y_c.

Further evidence that the change in slope represents a yield event is the dependence of the observed yield stress on the applied strain rate. In many amorphous polymers, yield stress is known to scale linearly with the natural logarithm of the applied strain rate within ranges typically achievable in the laboratory[47,48]. A straightforward model to explain this phenomenon is an Eyring rate activated kinetic process, in which macroscopic deformation is achieved by structural rearrangement at the molecular level associated with a single energy barrier ΔH. The effect of an applied stress is to tilt the potential energy landscape such that molecular motion in the direction of the stress is preferable:

$$\dot{\varepsilon} = \dot{\varepsilon_0} \exp\left[-\frac{\Delta H}{k_B T}\right] \sinh\left[\frac{V\sigma}{k_B T}\right] \tag{3.4.2}$$

Where $\dot{\varepsilon_0}$ is a fitting parameter and V is an activation volume associated with the molecular mechanism in question[49]. At stresses sufficiently high enough to induce yield $\sinh(x) \cong \frac{1}{2}\exp(x)$, therefore:

$$Y = \frac{k_B T}{V} \ln\left(\frac{2\dot{\varepsilon}}{\dot{\varepsilon_0}}\right) + \frac{\Delta H}{V} \tag{3.4.3}$$

To demonstrate the applicability of equation 3.4.3 to the confined yield event, a series of constant strain rate indents covering a range of 0.002 to 0.023 s^{-1} were performed into a 285 nm amorphous selenium film on a diamond substrate at room temperature (T_g-10°). The initial portion of the stress-strain curves for these tests is shown in figure 3.4.6 (a), while the dependence of the yield stress on strain rate is plotted in (b) and is shown to be approximately linear with respect to the logarithm of strain rate. A fit of equation 3.4.3 to the data yields an activation volume of 0.042 nm^3. This volume corresponds to a spherical radius of 0.46 nm, approximately twice the average bond length of amorphous selenium at 30 K as measured by *Kolobov* via extended x-ray absorption fine structure measurements[50]. Physical interpretation of this value is beyond the scope of this chapter however. Of concern here is the fact that a linear relationship between Y_c and $\ln(\dot{\varepsilon})$ is observed. This, serves as further proof that the point of inflection in the early strain portion of the CLCT stress-strain curve truly corresponds to an elastic to plastic yield transition.

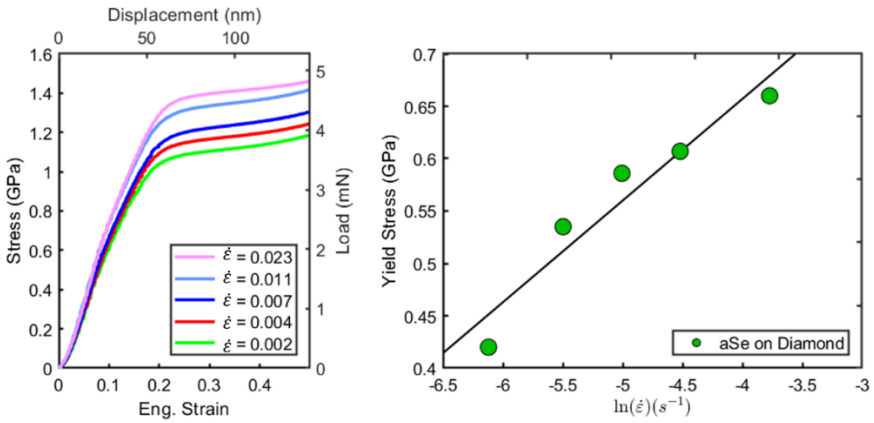

Figure 3.4.6 (a) Stress-strain curves for a 285 nm amorphous selenium film supported on a diamond substrate loaded at a range of constant strain rates. (b) Dependence of the confined yield stress on strain rate.

3.4.2 Aspect ratio scaling & boundary condition sensitivity

In this section, the role of the various boundary conditions affecting the CLCT are individually considered. This begins with treatment of the effect of film thickness to punch aspect ratio χ on the mechanics of the test, as well as the role of the surrounding confining film in general. Friction at the probe-film boundary is then treated, before the finite stiffness of real substrates is studied and a correction proceedure devised to accurately extract stress versus strain curves.

The effect of changing χ by varying initial thickness of the film is shown for both experiment (atactic polystyerene) and FEA simulation (simple elastic-plastic) in figure 3.4.7. (a) Shows the confined portion of the load-dispalcement curves for aPS thicknesses of 190, 240, 300, and 470 nm, corresponding to aspect ratios of 10.8, 8.5, 6.8, and 4.4 respectively, loaded at a constant stress rate of 0.2 GPa/s or 0.67 mN/s. This data is converted to stress-strain response in (b). An identical process is carried out on the FEA data in figures (c) and (d), covering an χ range of 13 to 4. The analytic uniaxial strain solution is shown as a dashed black line in (d). In both (b) and (d) a number of common trends may be observed. The two moduli, C and C^* are seen to increase with increasing χ, however while the change in the confined elastic modlus is relatively slight, the effective plastic modulus increases dramatically. Similarly, both the confined yield stress and extrusional flow stress increase with increase χ, with the extrusion stress being more affected. These trends are plotted for the experimental aPS data in (e) and (f).

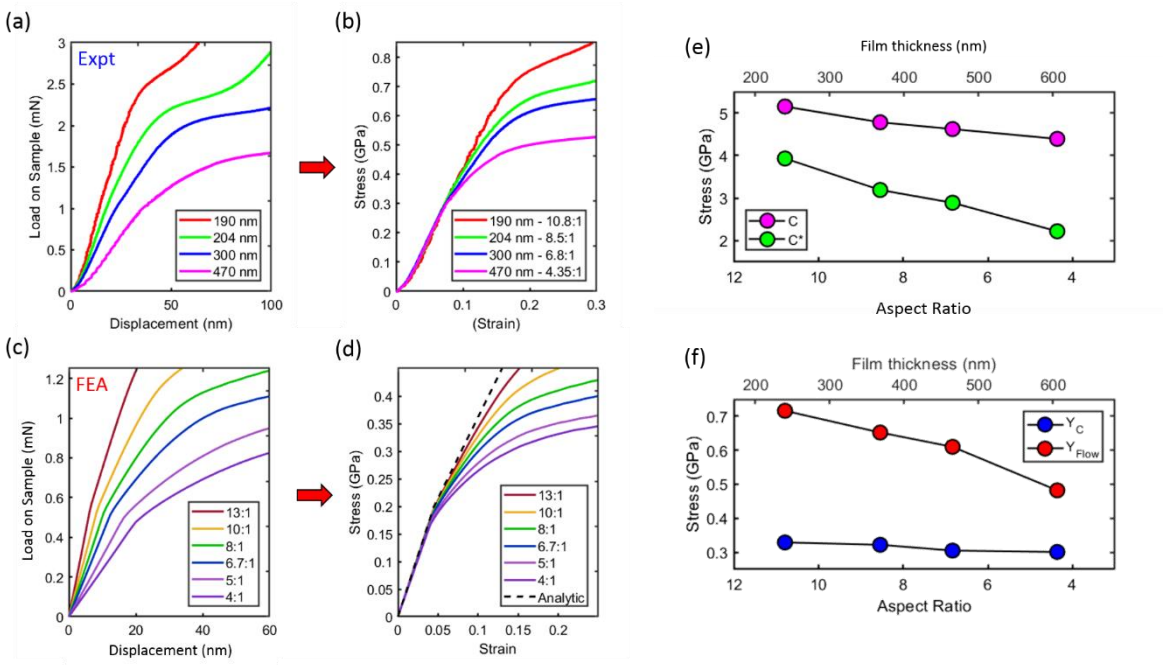

Figure 3.4.7 (a) Load-displacement curves for a range of aPS film thicknesses loaded at a stress rate of 0.2 GPa/s. (b) Equivalent stress-strain curves. (c) FEA load-displacement curves for a perfectly elastic-plastic material at a range of film to punch aspect ratios. (d) Equivalent stress strain curves. (e) Scaling of confined moduli with χ for aPS. (f) Scaling of yield stresses with χ for aPS data.

To understand this behaviour, it is useful to consider the role of the lateral confinement offered by the surrounding film in the CLCT. For a laterally unconstrained system such as that shown in figure 3.4.8 (a), deformation beneath the punch will asymptotically approach uniaxial strain as χ goes to infinity, even in the absence of a confining jacket. This can be seen in 3.4.8 (b), where an FEA unconstrained curve for $\chi = 200$ shows the typical behaviour of a uniaxial strain system. Essentially, this can be understood as the 'edge' regions contributing less to the total deformation of the body. At lower aspect ratios, such as the χ = 4, 10, and 20 curves plotted in (b), the unconstrained system adheres much more closely to a uniaxial compressive stress geometry, yielding in the vicinity of Y_0. The role of the surrounding film in the CLCT is therefore to greatly accelerate how quickly the stress-strain behaviour of the system approaches one of uniaxial strain by supressing lateral displacement. This can again be seen in (b), where the CLCT curves for χ = 20 and χ = 10 are much closer to uniaxial strain than their unconfined equivalents, and even the χ = 200 case. However, because the confining jacket is of finite rigidity, increasing the aspect ratio in the CLCT will still lead to a system closer to true uniaxial strain, for the same reasons as in the unconfined case. As such, the effect of increasing/deceasing χ in the stress-strain curves of figure 3.4.7 (b) and (d) is to be expected.

That the plastic C^* region is more affected by increasing χ can be understood in terms of equation 3.2.3, $\sigma_{zz} = \left(\frac{\nu}{1-\nu}\right)\sigma_{rr}$. As the material yields, $\nu \rightarrow 0.5$ and as such the radial stress on the surrounding confining film greatly increases, equalling that of the applied axial stress. As thinner films have greater flexural strength than thicker ones, they are better equipped to resist this increased stress, providing greater confinement and pushing the volume under the punch closer to a uniaxial strain state, therefore explaining the aspect ratio behaviour seen in figure 3.4.7.

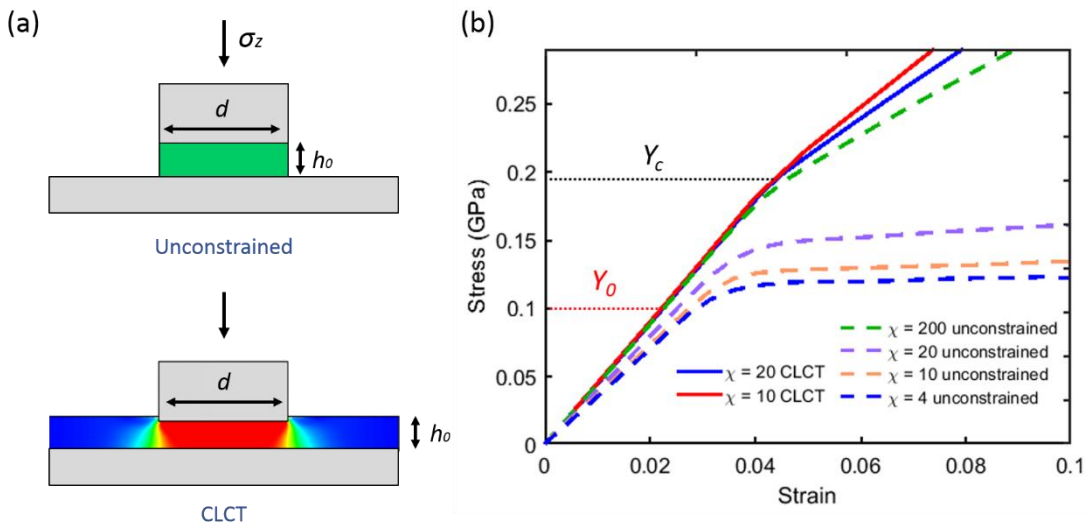

Figure 3.4.8 (a) Comparison of an unconstrained compressive deformation with the CLCT. As very high χ, the uncompressed system will tend towards a state of uniaxial strain. (b) FEA stress-strain curves comparing the response of an unconstrained compressive deformation with the CLCT at a range of aspect ratios. Lateral confinement in the CLCT pushes the system closer to uniaxial strain.

Probe-Film Friction

The effect of friction at the film-punch interface has been studied via finite element simulation. A straightforward Coulomb model[51,52] was employed, with static and kinetic friction coefficients being equal: $\mu_{stat} = \mu_{kin} = \mu$. Figure 3.4.9 (a) shows stress-strain curves for a $\chi = 10$ film on a rigid substrate where friction is varied from full-slip ($\mu = 0$) to $\mu = 1$, as well as for several intermediate partial slip states. The elastic response of the film is found to be invariant with respect to μ. This is in line with previous FEA studies of flat punch indentation into elastic-plastic half-spaces. In particular, separate studies conducted *Yang*[53] and *Montanari*[54] showed that the elastic contact modulus is friction invariant. This is likely that this is due to the minimal lateral strain present

during elastic loading of the half-space due to the confinement effect. As the yield point represents the terminus of elastic behaviour it is therefore unsurprising that it too is unaffected by changes in interfacial boundary conditions, particularly as the confined yield event is a non-localized transition affecting all material within the contact volume. This behaviour was also observed in the two previously mentioned FEA studies, albeit in their case yield corresponded to an extrusion event. This friction invariant elastic behaviour marks an important distinction between the CLCT and sharp tip indentation: In the latter, lateral plastic flow occurs close to the tip-material interface even at low strain, and parameters such as hardness and pile-up are strongly coupled to friction conditions[55,56].

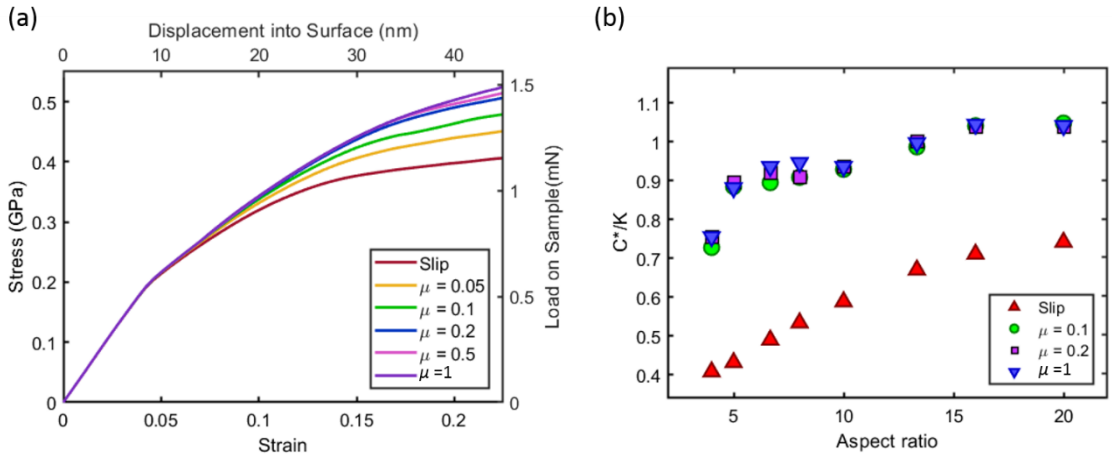

Figure 3.4.9 (a) Effect of interfacial friction on the stress-strain response of a χ = 10 elastic-plastic supported film. (b) Scaling of the normalized plastic modulus with aspect ratio at several Coulomb friction coefficients.

The confined plastic modulus C^* is found to increase with increasing stick at the punch interface as the surface traction opposes the radial force of equation 3.2.3, improving confinement and leading to a stiffer response. Figure 3.4.9 (b) explores the impact of friction at aspect ratios ranging from χ = 4 to χ = 20, where C^* is measured between strains of 0.05 and 0.065 and is normalized by the bulk modulus, the ideal value of C^* in pure uniaxial strain. For the case of full slip, C^* shows a strong dependence on χ, with radial plastic flow ensuring that C^*/K only reaches a value of 0.7 at χ = 20, and decays to 0.4 at χ = 4. The introduction of modest friction of μ = 0.1 at the punch-film interface shifts C^*/K to values of 0.9 at intermediate aspect ratios and to unity for aspect ratios of greater than 10. Further increases in the friction coefficient to 0.2 and greater are shown to have minimal effect. Nanotribology studies conducted via lateral

force microscopy[57] and scratch testing[58] with Si_3N_4 tips indicate that PS films generally have a static friction coefficient ranging from $0.2 \leq \mu \leq 0.45$, with a slight molecular weight dependency. Based on the findings of figure 3.4.9 (b) this would indicate that at high χ a very good adherence of C^* to K can be expected for the experimental PS samples considered in this chapter. To remove ambiguity around the intrinsic friction of the sample in future, modifications may be made to the punch surface either through a well-characterised roughness/patterning or through chemical modification to boost friction. This is an important experimental design consideration and a radical departure from conventional material testing, where efforts are generally made to minimise friction.

Instrument stiffness correction and high aspect ratio limit

A critical element in characterising the mechanical response of a system through depth sensing indentation is the decoupling of the true displacement of the tip into the surface from any background displacements of the supporting frame during loading. The depth measuring systems used by most nanoindenters will register these frame displacements as true displacements of the tip, and as such they must be removed in a post indentation analysis step[4,59]. Deflections in the support frame are the result of its finite stiffness, defined as the ratio of applied load to resultant frame deflection. For our purposes we consider the supporting frame to consist of the sample substrate, the punch and indenter shaft, the sample mount and stage, and the load frame. These elements may be treated as springs in series[60], as shown in figure 3.4.10.

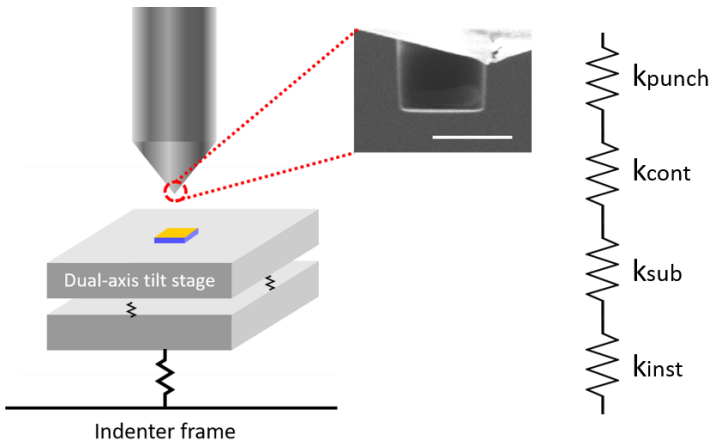

Figure 3.4.10 Schematic of the confined layer test support frame and spring representation. An SEM image of the flat punch is shown with 2 micron scale bar.

The total local stiffness as measured during indentation may be written as:

$$k_{tot}^{-1} = \left(\frac{dL}{dh}\right)^{-1} = k_{contact}^{-1} + k_{sub}^{-1} + k_{punch}^{-1} + k_{inst}^{-1}$$

$$= k_{contact}^{-1} + k_{frame}^{-1} \quad (3.4.4)$$

The contact stiffness is a function of contact area, meaning for self-similar geometries such as Berkovich or conical tips, it will be a function of elastic penetration depth h_c and will be sensitive to deviations from ideal tip shape. To determine the frame stiffness, a series of indentations into an elastic-plastic material must be made to differing peak displacements, with the intercept of a plot of $1/h_c$ versus dh/dL giving the compliance[61]. For the CLCT geometry, the contact area is fixed, and as such all compliances external to the sample itself may be ascertained to a good approximation by simply indenting a portion of the sample where the film has been removed and the substrate is exposed. This background stiffness will only have contributions from the support frame and should achieve a constant value once full contact is established. The true displacement of the tip into the film in subsequent tests may then be calculated as:

$$d_{true} = d_{total} - d_{frame}$$

$$d_{total} - \frac{L}{k_{frame}} \quad (3.4.5)$$

This correction process has been performed for a 240 nm aPS film on a silicon substrate in figure 3.4.11. (a) Shows the measured harmonic contact stiffness from an indent into an uncovered region of the substrate supporting the film to a peak load of 6 mN, obtained by superposition of a small oscillatory displacement of 1 nm at 45 Hz on to the main load during indentation via the CSM method. A constant frame stiffness of 115,000 N/m is measured upon establishment of a total contact at loads greater than 1 mN. This correction is then applied to the aPS indent in (b) through equation 3.4.5, with the raw data shown in blue and the stiffness corrected data shown in green. With the deflection of the frame removed, the data is shifted to the left. The load-displacement curve for the bare silicon indent is also shown in grey. The correction has the effect of increasing C and C^*, driving them closer to the intrinsic value of the film

by factoring out parasitic strains. The yield stress *Yc* is unaffected, as the load across each spring for a set of springs in series is equal[62].

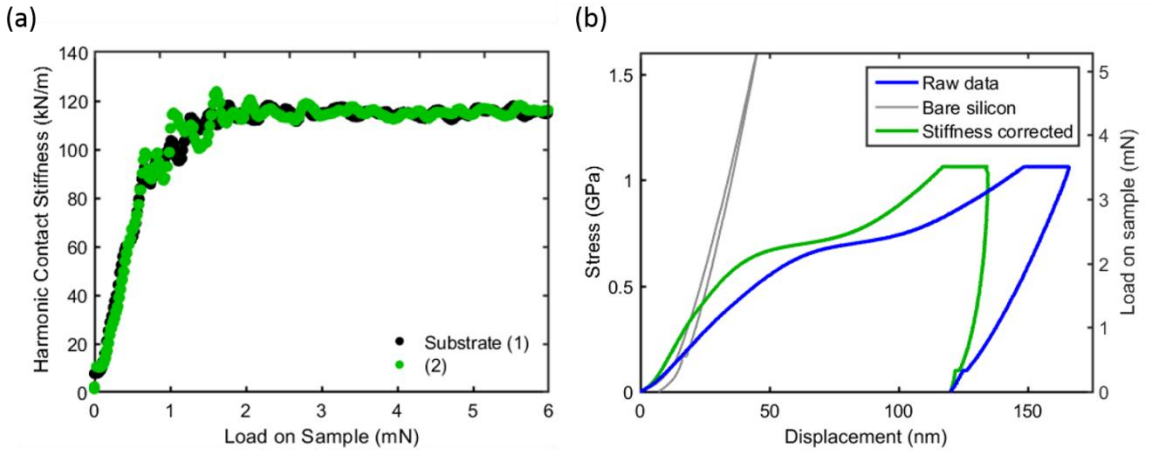

Figure 3.4.11 (a) Harmonic contact stiffness of bare silicon measured by flat punch indentation to a peak load of 6 mN. (b) Stress-strain curve for a 240 nm aPS film before and after stiffness correction is applied.

The underlying assumption of this correction process is that the geometry supporting the contact area does not change during loading. In other words, the correction assumes a simple one-dimensional model of a lumped spring for the boundary stiffness. This is only true if the stiffness of the film is low enough that there is not significant elastic strain transmitted to the substrate. An upper estimate of the stiffness of the film beneath the punch in the elastic regime is given by[1]:

$$k_{film} = \frac{C\pi a^2}{h_0} = \frac{C\pi a\chi}{2} \tag{3.4.6}$$

Where a is the contact radius, in this case equal to the punch radius r. The stiffness of the substrate is approximated by[63,64]:

$$k_{sub} = maE_{sub} \tag{3.4.7}$$

Where m is a fitting parameter, dependent on the aspect ratio χ, the Poisson's ratio of the substrate, and frictional boundary conditions. The value of m can also be expected differ slightly from the typical pre-factor of 2 for the contact stiffness of an elastic half-space indented by a flat punch:

$$k_{sub} = 2aE_{sub} \tag{3.4.8}$$

This is because equation 3.4.8 is arrived at under the assumption that the surface of the half-space beneath the punch is uniformly vertically displaced, with a non-uniform contact pressure. In our case the situation is reversed, with a uniform pressure being transmitted from the film to the substrate. Further, as it is the displacement of the punch that is measured, which is located away from the deforming substrate-film interface, close adherence to an analytic expression cannot be expected.

Equation 3.4.6 shows that the stiffness of the thin film increases with increasing χ. Together with equation 3.4.7 this implies that there is an limited parameter space in terms of χ and the ratio of substrate elastic modulus to film modulus $S = E_{sub}/E_{film}$ for which the idea of a one-dimensional correction procedure will be valid. For high χ and low S, a situation corresponding to a thin film of material whose modulus is approximately that of the substrate (e.g. a metal on silicon), significant distortion of the contact geometry can be expected due to stress concentration at the punch edges leading to substrate bending. As such, the one-dimensional nature of the problem is lost and equation 3.4.5 can no longer accurately correct for the substrate. This situation graphically illustrated in figure 3.4.12 (a).

To study the effect of substrate deformation on the accuracy of the stiffness correction procedure, a 50 µm thick perfectly elastic substrate was introduced to the FEA model. A series of simulations were carried at various combinations of χ and S. The same elastic-plastic material was used for the film as in previous simulations. The Poisson's ratio of the substrate was fixed at $\nu = 0.2$ for all simulations, while five values of substrate elastic modulus, E_{sub}, were studied: 15, 30, 60, 150, and 300 GPa, corresponding to $S = 5$, 10, 20, 50, and 100, respectively. Simulated indents were performed over an initial thickness range of 20 nm ($\chi = 100$) to 400 nm ($\chi = 5$), covering a film stiffness range of 27,900 N/m to 699,000 N/m, in accordance with equation 3.4.6. The substrate and film were tied such that all vertical displacements at the film-substrate interface would be equal. Figure 3.4.12 (b) shows a Von Mises stress map of this configuration for a $\chi = 5$, $S = 50$ simulation at the point of yield.

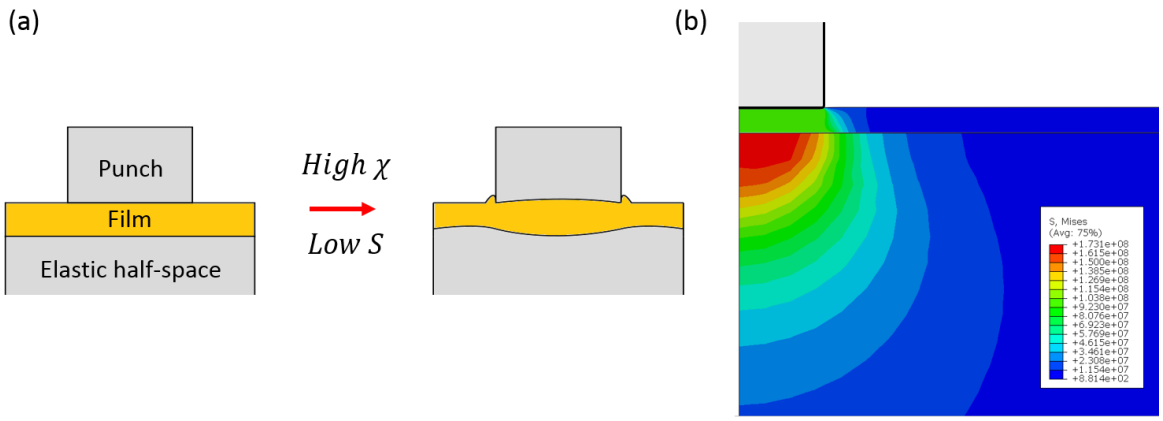

Figure 3.4.12 (a) Distortion of the contact area at high aspect ratio and low relative substrate stiffness. Bending of the substrate leads to the punch edges 'digging in' and a loss of uniaxial strain deformation (b) Schematic of the FEA model used to study the influence of substrate stiffness and aspect ratio. Von Mises stress map taken at $\chi = 5$, $S = 50$.

Substrate stiffness corrected stress-strain curves are shown for the range of S values studied at $\chi = 5$ in figure 3.4.13 (a). A value of $m = 3.1$ for the pre-factor in equation 3.4.7 was found to give the best correction of simulated stress-strain curves onto the analytic confined modulus C. This value was used in all subsequent corrections. At this low aspect ratio, the film is relatively compliant, and the correction accurately moves all curves onto the analytical elastic solution for C, shown here as a dashed black line. Furthermore, the yield point is clearly visible in all cases. The same family of curves is plotted in (b) for $\chi = 20$. In this case however only the $S = 100$ curve, corresponding to a very stiff substrate, adheres to the analytic solution. Distortion of the contact area due to the increased stiffness of the film causes the other curves to fall to the right. In the extreme case of $S = 5$ the typical sharp yield point is no longer distinguishable. Figure 3.4.13 (c) plots the stiffness corrected confined modulus C_{stiff} for all simulations carried out. In the ideal case $C_{stiff} = C$, the analytic confined elastic modulus. Some overestimation of the modulus is encountered at low χ due to which the way in stress is calculated. The contact area is treated as fixed through testing, when in fact is slightly increases due to the rounded tip corners.

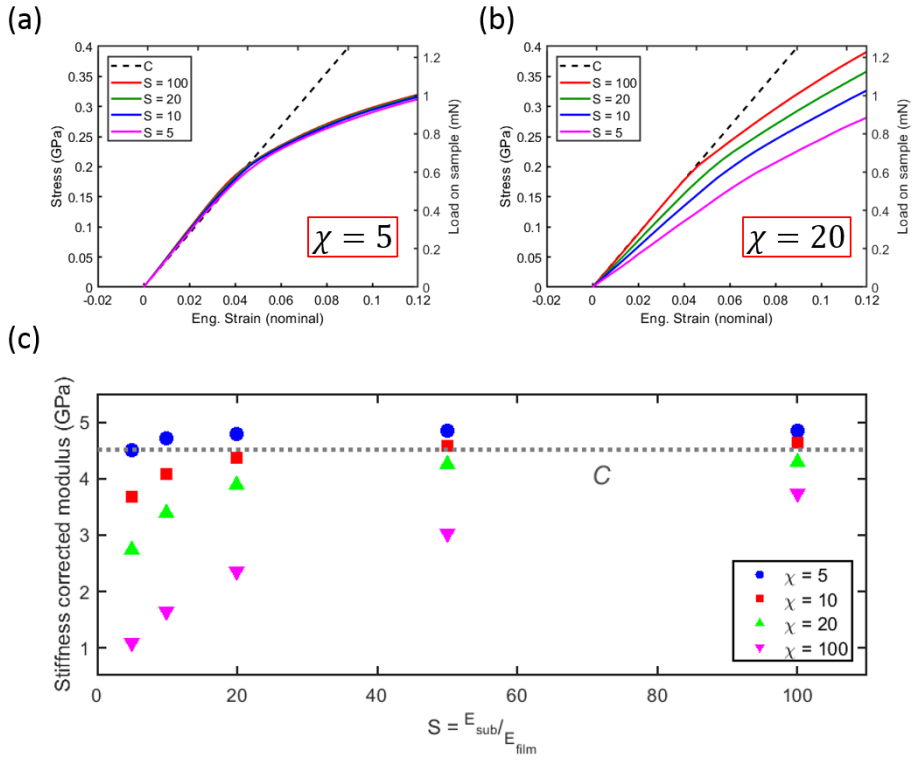

Figure 3.4.13 (a) Corrected stress-strain curves for a range of substrate to film elastic modulus ratio S at a fixed aspect ratio of χ = 5. (b) The same set of curves for χ = 20. (c) Scatter plot of the measured stiffness corrected confined elastic modulus C_{stiff} for all simulations. The analytic solution is shown as a grey line.

The 'levelling off' of the scatter plots to zero slope moving from left to right in (c) indicates the combinations of S and χ where the CLCT can be reliably used for parameter extraction. For the case of glassy polymers supported on silicon, S ≈ 50. Therefore, aspect ratios of up to approximately χ = 20 are testable. For future testing of stiff materials such metals however, the range will be far more limited. With the maximum substrate modulus being limited by nature to about 1 TPa (diamond) S will generally be limited to between 5 and 10, indicating low aspect ratios must be used. Therefore, in real systems a trade-off must be made between the uniformity of deformation within the film that comes with high χ and choosing a low enough aspect ratio that the contact isn't so distorted that the uniaxial strain approximation breaks down.

In summary, the roles of finite substrate stiffness and aspect ratio have been characterised. It has been shown that higher χ systems will generally require stiffer substrates to prevent contact distortion, while the testing of very stiff materials will require low χ for the same reason.

3.4.3 Stress decomposition & pressure sensitive yield

In this section, FEA is used to study the uniformity of stress beneath the punch during loading. It is also used to study the partitioning of stress into shear and pressure terms, as was developed in section 3.2.2. This process is then extended to treat materials with pressure dependent yield surfaces and to show how the CLCT can be used to cause yield in systems where pure uniaxial strain deformation has been able to do so, such as PMMA.

Within the elastic limit, the principal stress fields generated by the confined layer compression test are highly uniform for the volume directly beneath the punch. This is shown in figure 3.4.14 for a 200 nm ($\chi = 10$) elastic-plastic simulation at an applied of stress $\sigma_{zz} = 0.65$ GPa, well below yield. The axial stress (a) is effectively limited to the volume directly beneath the contact area, while radial stresses extend out well into the confining wall (b). In both cases stress concentrations can be observed at the point of contact with the punch edge.

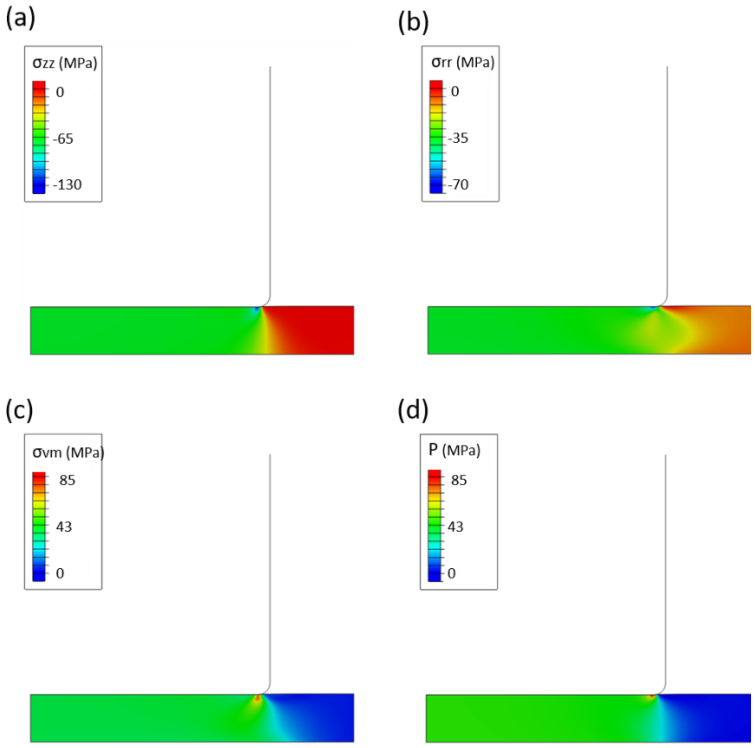

Figure 3.4.14 Stress fields in the compression test in the elastic zone. (a) σ_{zz} (b) σ_{rr} (c) Von Mises equivalent shear stress (d) Equivalent hydrostatic pressure stress

Coupled to these principal stresses are the scalar equivalent shear and hydrostatic pressure fields, defined by eqns. 3.2.4 and 3.2.6, which are shown in (c) and (d) respectively. The finite element method allows for evaluation of these fields for all cells

within the compressed volume at each time step, enabling the validity of eqn. 3.2.7 to be tested explicitly for the confined layer geometry. Von Mises shear stress during loading is plotted as a function of pressure in figure 3.4.15 (a) for χ = 20, 10 and 4 respectively, with the analytic solution plotted in black. Individual time steps within the simulation may be identified by the clustering of data points. Within the elastic zone the well confined systems are tightly distributed to the along the true uniaxial strain solution, however at lower aspect ratios the system shifts left to a more shear-oriented stress state. Further, within each time step there is greater variance in both pressure and shear, due to the loss of geometric definition. The net result of this increase in shear within the system is a decrease in the mean hydrostatic pressure across the volume at yield, as plotted for aspect ratios between $\chi = 5$ and $\chi = 20$ in 3.4.15 (b). For $20 \geq \chi \geq 10$ deviation from the predicted uniaxial strain pressure of 0.129 GPa is slight, however this then falls off rapidly.

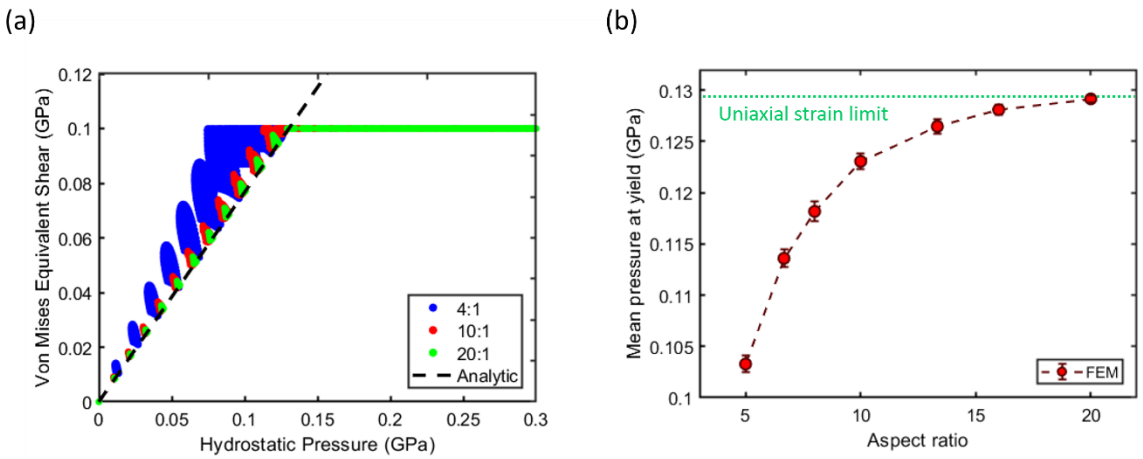

Figure 3.4.15 (a) Hydrostatic pressure vs Von Mises shear stress for FEA simulations of χ = 20,10 and 4. Analytic uniaxial strain solution shown in black. (b) χ vs mean pressure at yield for the volume beneath the punch.

When a pressure dependent term is incorporated into the yield criterion, as in equation 3.2.11, the radial variation in pressure and shear across the test volume has meaningful consequences. As equation 3.2.14 showed, for certain combinations of α', ν, and Y_0 a material may never yield within a strict uniaxial strain geometry, as the pressure-shear path never intersects the yield surface. An example of such a material is shown in figure 3.4.16 (a), with $\alpha' = 0.49$, $\nu = 0.37$, and $Y_0 = 0.125$ GPa. These constants were chosen to accurately reflect the pressure dependent properties of PMMA and are in line with

literature values[65–67]. The pressure-dependent yield surface is shown in red and the uniaxial strain path of the material in pressure-shear space as a dashed black line, following equation 3.2.7. Within the confined layer compression test the radial stress variation causes elements nearer to the punch edge to deviate from the uniaxial strain condition and intersect the yield surface, leading to the yield, albeit in a more gradual manner than for pressure invariant materials. The yield point becomes more pronounced at lower aspect ratio as more elements are shifted left of the analytical line. This is shown for χ = 20, 10, and 5 in (a). The resultant stress-strain curves are shown in (b). As expected, the true uniaxial strain case (black) shows no inflection point, and the magnitude of the slope change grows with decreasing χ for the CLCT geometry.

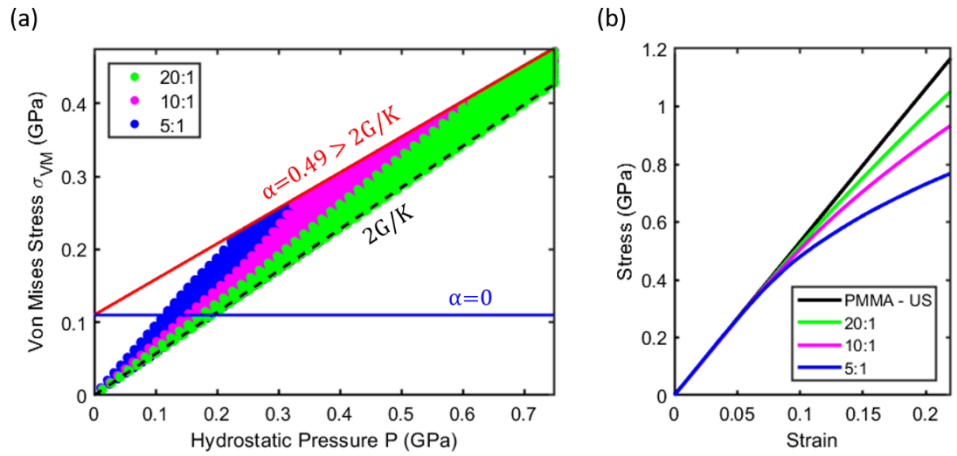

Figure 3.4.16 (a) Simulated pressure-stress distribution for an α' = 0.49, ν = 0.37 pressure dependent yield surface representing PMMA for the uniaxial strain case (black) and three confined layer aspect ratios. The yield surface is shown in red. (b) Accompanying stress-strain curves.

Experimental realisation of this system is shown in figure 3.4.17. for a 270 nm (χ = 7.6) PMMA film. (a) Demonstrates that a yield point exists at approximately 0.40 GPa, as evidenced by the change in slope. This is verified in (b) where residual plasticity is observed only after Y_c as shown by loading to three different peak stresses. Previous attempts to yield PMMA in uniaxial strains by *Ravi-Chandar*[35] proved unsuccessful, with the confining steel jacket failing before the confined polymer. The added shear stress in the CLCT therefore is something of a positive, as it enables yield of pressure-sensitive materials to be studied in a controlled manner.

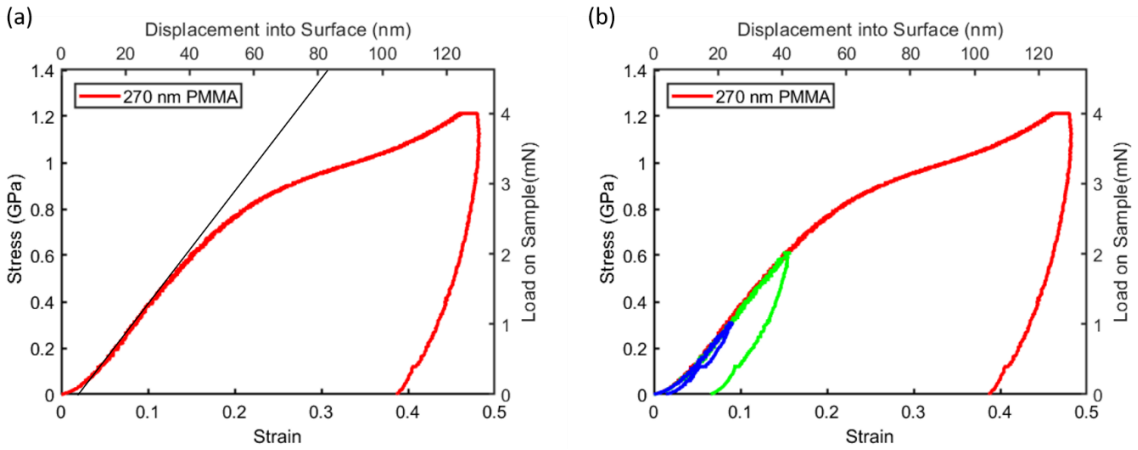

Figure 3.4.17 (a) Stress-strain curve for a 270 nm PMMA film in the confined layer geometry. (b) Development of residual plasticity after Y_c.

3.4.4 First order parameter extraction

The previous sections have outlined some of the difficulties associated with parameter extraction in the CLCT. The plastic modulus has been shown to have a strong dependence on both aspect ratio and friction boundary conditions, while deformation of the substrate invalidates the global stiffness correction at high χ and low S. However, these difficulties may be alleviated by intelligent design of experiment. An aspect ratio should be selected on the basis of being large enough to ensure deviation of C^* from K is minimal, while being small enough so as to ensure its stiffness is not so great when compared to that of the substrate. The results of section 3.4.2 indicate that a range of $12 \geq \chi \geq 7.5$ satisfy these conditions for $S \approx 50$, typical of a glassy polymer supported on silicon. Use of higher aspect ratios may be preferable in some situations but requires added precision in punch-film alignment.

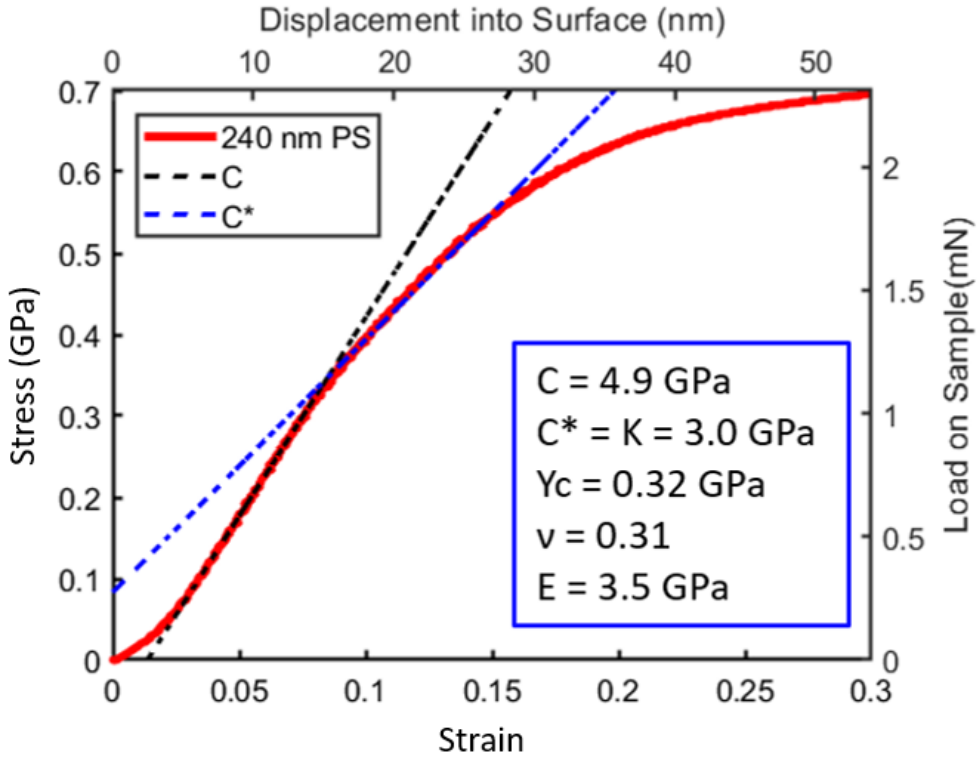

Figure 3.4.18 Parameter extraction in the confined layer test for a 240 nm ($\chi = 8.5$) aPS film boned to a silicon <100> substrate. Values for *C* and *C** were obtained by linear fits of the first and second linear regions of the stress-strain curve over ranges of 0.04 – 0.08 and 0.11 – 0.14 respectively. These values were chosen to avoid inclusion on the non-linear initial pre-full contact post confinement extrusion regions of the curve. The confined yield stress Y_c was taken as the intercept of these two lines.

Table 3.4.1 Extracted mechanical properties from figure 3.4.18 with measured and literature ν.

240 nm aPS	C (GPa)	K (GPa)	Yc (GPa)	E (GPa)	Y (GPa)	*ν*
Measured *ν*	4.9	3.0	0.32	3.5	0.18	0.31
Literature *ν*				3.2	0.15	0.34[67]
Literature values	-	3.0[73]	-	3.3 – 3.9[74]	0.095[73]	0.34[67]

Parameter extraction is performed for a 240 nm ($\chi = 8.5$) atactic polystyrene film on silicon <100>, as shown in figure 3.4.18. The extracted moduli and Poisson's ratio are shown in the blue inset. Values for ν, K, and E are found to be broadly in line with literature figures[43,65,68–70], with some underestimation. Alternatively, a reference value may be used for ν, as is common in *Oliver-Pharr* calculations for elastic modulus and hardness in stiff materials[4,61] to improve accuracy in E and Y. Taking a value of ν =

0.34[65] for polystyrene yields an elastic modulus of 3.2 GPa and a yield stress of 0.155 GPa. These values are compared in table 3.4.1. as well as reference values from literature.

The above analysis assumes that the material being tested can be adequately described by isotropic linear elasticity and perfect plasticity. For polymers this is simply a first approximation. Due to the critical role of free volume in polymer deformation, the elastic modulus, bulk modulus, and yield stress will all display significant pressure dependencies[71,72]. The assumption of perfect plasticity implies a single molecular mechanism for yield which is full activated at the yield stress. For polymers it has been shown that several mechanisms such as the α and β relaxations may contribute to yield[73], and it is logical to suppose that higher energy mechanisms may become accessible at greater stresses. Inclusion of a pressure dependency in Y_c renders the plastic flow rule analysis of section 3.2.4 invalid, and C^* does not correspond to bulk modulus even in pure uniaxial strain. The values for E, K, Y, and ν derived above must therefore be treated first order approximations, useful in the design of nanoscale systems and devices, but not fully characterising the total elasto-plastic behaviour of polystyrene. The key point however is that under optimal conditions of high S and χ true stress-stain data to well past the elastic limit may be accessed, enabling study of constitutive behaviour regardless of the material model used and allowing for investigation of thin film phenomena such as finite size effects.

3.5 Conclusions

The mechanics of flat punch indentation into a compliant layer supported on a stiffer substrate has been investigated. It has been shown that at sufficiently punch diameter to initial film thickness with a rigid substrate a state of uniaxial strain is achieved for the material directly beneath the punch. At small strains the response of the material is wholly elastic, before a discrete, confined yield event occurs across the entirety of the contact volume. Following this, confined, longitudinal plasticity occurs in the absence of conventional lateral flow. This geometry and the associated yield event have not been encountered previously in thin film systems.

The confined layer compression test has been studied experimentally via indentation into polystyrene films covering an initial thickness range of 190 – 470 nm and via finite element simulations covering an aspect ratio range of 100:1 to 4:1. The yield event has

been studied by examination of the residual strain imparted to the film, both via analysis of the stress-strain curves and via ex-situ AFM. The strain rate dependence of this yield point has been studied for a 285 nm amorphous selenium film and has been shown to obey a typical Eyring relationship. Above the yield stress, the stress-strain response of the material follows the bulk modulus in the ideal case. Deviations from this behaviour were studied in the context of initial film thickness and punch-film friction. It is found that higher aspect ratios lead to a more uniform response across the volume, while friction at the punch face lead to traction opposing outward flow thereby improving confinement.

It was shown that the background compliance of the indenter support frame could be treated as set of springs in series and could be calculated and subtracted via an indent an uncovered area of substrate. The validity of this simplified model was found to break down at $\chi > 10$ for a $E_{sub}/E_{film} = 50$ system, due to bending of the substrate distorting the contact volume. Overcoming this problem at high χ will require use of stiffer substrates such as diamond.

The behaviour of a material with a highly pressure sensitive yield surface was studied via simulation and indentation of PMMA. It was shown that the confined layer geometry produced a yield event which cannot be achieved in a true uniaxial strain set up, however this comes at the cost of material beneath the punch intersecting the yield surface at different values of pressure and shear stress.

Finally, it was shown that the confined layer test can be used to accurately extract material properties such as Young's modulus and Poisson's ratio for compliant films, with values of $E = 3.5$ and $\nu = 0.31$ measured for a 240 nm polystyrene film.

Bibliography

1. Wald, M. J., Considine, J. M. & Turner, K. T. Determining the Elastic Modulus of Compliant Thin Films Supported on Substrates from Flat Punch Indentation Measurements. *Exp. Mech.* **53**, 931–941 (2013).
2. Li, H. & Vlassak, J. J. Determining the elastic modulus and hardness of an ultra-thin film on a substrate using nanoindentation. *J. Mater. Res.* **24**, 1114–1126 (2009).
3. Zeilinger, A. *et al.* In-situ Observation of Cross-Sectional Microstructural Changes and Stress Distributions in Fracturing TiN Thin Film during Nanoindentation. *Sci. Rep.* **6**, 22670 (2016).
4. Oliver, W. C. & Pharr, G. M. An improved technique for determining hardness and elastic modulus using load and displacement sensing indentation experiments. *J. Mater. Res.* **7**, 1564–1583 (1992).
5. Pethica, J. B., Hutchings, R. & Oliver, W. C. Hardness measurement at penetration depths as small as 20 nm. *Philos. Mag. A* **48**, 593–606 (1983).
6. Doerner, M. F. & Nix, W. D. A method for interpreting the data from depth-sensing indentation instruments. *J. Mater. Res.* **1**, 601–609 (1986).
7. Carrasco, E., Rodríguez de la Fuente, O., González, M. A. & Rojo, J. M. Dislocation cross slip and formation of terraces around nanoindentations in Au(001). *Phys. Rev. B* **68**, 180102 (2003).
8. Cross, G. L. W., Schirmeisen, A., Grütter, P. & Dürig, U. T. Plasticity, healing and shakedown in sharp-asperity nanoindentation. *Nat. Mater.* **5**, 370–376 (2006).
9. Jung, Y.-G., Lawn, B. R., Martyniuk, M., Huang, H. & Hu, X. Z. Evaluation of elastic modulus and hardness of thin films by nanoindentation. *J. Mater. Res.* **19**, 3076–3080 (2004).
10. King, R. B. Elastic analysis of some punch problems for a layered medium. *Int. J. Solids Struct.* **23**, 1657–1664 (1987).
11. Jönsson, B. & Hogmark, S. Hardness measurements of thin films. *Thin Solid Films* **114**, 257–269 (1984).
12. Bhattacharya, A. K. & Nix, W. D. Finite element simulation of indentation experiments. *Int. J. Solids Struct.* **24**, 881–891 (1988).
13. Chicot, D. & Lesage, J. Absolute hardness of films and coatings. *Thin Solid Films* **254**, 123–130 (1995).

14. Pharr, G. M. & Oliver, W. C. Measurement of Thin Film Mechanical Properties Using Nanoindentation. *MRS Bull.* **17**, 28–33 (1992).
15. Uchic, M. D., Dimiduk, D. M., Florando, J. N. & Nix, W. D. Sample dimensions influence strength and crystal plasticity. *Science* **305**, 986–9 (2004).
16. Lee, S.-W., Han, S. M. & Nix, W. D. Uniaxial compression of fcc Au nanopillars on an MgO substrate: The effects of prestraining and annealing. *Acta Mater.* **57**, 4404–4415 (2009).
17. Cross, G. L. W., O'Connell, B. S., Pethica, J. B., Rowland, H. & King, W. P. Variable temperature thin film indentation with a flat punch. *Rev. Sci. Instrum.* **79**, 013904 (2008).
18. Chu, S. N. G. & Li, J. C. M. Impression creep; a new creep test. *J. Mater. Sci.* **12**, 2200–2208 (1977).
19. Yang, F., Chen, J., Seidmann, I. & Li, J. C. M. Punch tip effects in diffusional impression creep. *Mater. Sci. Eng. A* **207**, 30–35 (1996).
20. Yang, F. Asymptotic solution to axisymmetric indentation of a compressible elastic thin film. *Thin Solid Films* **515**, 2274–2283 (2006).
21. Huajian, G., Cheng-Hsin, C. & Jin, L. Elastic contact versus indentation modeling of multi-layered materials. *Int. J. Solids Struct.* **29**, 2471–2492 (1992).
22. Sneddon, I. N. The relation between load and penetration in the axisymmetric boussinesq problem for a punch of arbitrary profile. *Int. J. Eng. Sci.* **3**, 47–57 (1965).
23. Rar, A., Song, H. & Pharr, G. M. Assessment of New Relation for the Elastic Compliance of a Film-Substrate System. *MRS Proc.* **695**, L10.10.1 (2001).
24. Wald, M. J., Considine, J. M. & Turner, K. T. Determining the Elastic Modulus of Compliant Thin Films Supported on Substrates from Flat Punch Indentation Measurements. *Exp. Mech.* **53**, 931–941 (2013).
25. Rowland, H. D., King, W. P., Pethica, J. B. & Cross, G. L. W. Molecular Confinement Accelerates Deformation of Entangled Polymers During Squeeze Flow. *Science* 720–724 (2008).
26. Cross, G. L. W., O'Connell, B. S. & Pethica, J. B. Influence of elastic strains on the mask ratio in glassy polymer nanoimprint. *Appl. Phys. Lett.* **86**, 081902 (2005).
27. Cross, G. L. W. The production of nanostructures by mechanical forming. *J. Phys. D. Appl. Phys.* **39**, R363–R386 (2006).
28. Ma, Z. & Ravi-Chandar, K. Confined compression: A stable homogeneous

deformation for constitutive characterization. *Exp. Mech.* **40**, 38–45 (2000).

29. Kim, J. W., Medvedev, G. A. & Caruthers, J. M. Observation of yield in triaxial deformation of glassy polymers. *Polymer (Guildf).* **54**, 2821–2833 (2013).
30. Mavko, G., Mukerji, T. & Dvorkin, J. *The Rock Physics Handbook*. (Cambridge University Press, 2009). doi:10.1017/CBO9780511626753
31. Lee, H.-N., Paeng, K., Swallen, S. F. & Ediger, M. D. Direct measurement of molecular mobility in actively deformed polymer glasses. *Science* **323**, 231–4 (2009).
32. Ediger, M. D., Lee, H. N., Paeng, K. & Swallen, S. F. Dye reorientation as a probe of stress-induced mobility in polymer glasses. *J. Chem. Phys.* **128**, (2008).
33. Seltzer, R., Cisilino, A. P., Frontini, P. M. & Mai, Y.-W. Determination of the Drucker–Prager parameters of polymers exhibiting pressure-sensitive plastic behaviour by depth-sensing indentation. *Int. J. Mech. Sci.* **53**, 471–478 (2011).
34. Quinson, R., Perez, J., Rink, M. & Pavan, A. Yield criteria for amorphous glassy polymers. *J. Mater. Sci.* **32**, 1371–1379 (1997).
35. Ravi-Chandar, K. & Ma, Z. Inelastic Deformation in Polymers under Multiaxial Compression. *Mech. Time-Dependent Mater.* **4**, 333–357 (2000).
36. Qvale, D. & Ravi-Chandar, K. Viscoelastic characterization of polymers under multiaxial compression. *Mech. Time-Dependent Mater.* **8**, 193–214 (2004).
37. Zha, C., Hemley, R. J., Mao, H., Duffy, T. S. & Meade, C. Acoustic velocities and refractive index of SiO 2 glass to 57.5 GPa by Brillouin scattering. *Phys. Rev. B* **50**, 13105–13112 (1994).
38. Simha, R. & Quach, A. The effect of pressure on the ß-relaxation of polystyrene. *Macromolecules* **4**, 268–270 (1971).
39. Jones, M. A., Carriere, C. J., Dineen, M. T. & Balwinski, K. M. Failure and deformation studies of syndiotactic polystyrene. *J. Appl. Polym. Sci.* **64**, 673–681 (1997).
40. Arzt, E. Size effects in materials due to microstructural and dimensional constraints: a comparative review. *Acta Mater.* **46**, 5611–5626 (1998).
41. Espinosa, H. D. & Prorok, B. C. Size effects on the mechanical behavior of gold thin films. *J. Mater. Sci.* **38**, 4125–4128 (2003).
42. Ortiz, M. Plastic Yielding as a Phase Transition. *J. Appl. Mech.* **66**, 289 (1999).
43. Brandrup, J., Immergut, E. H. & Grulke, E. A. *Polymer handbook*. (Wiley-Interscience, 1999).
44. Pelletier, C. G. N., Dekkers, E. C. A., Govaert, L. E., den Toonder, J. M. J. &

Meijer, H. E. H. The influence of indenter-surface misalignment on the results of instrumented indentation tests. *Polym. Test.* **26**, 949–959 (2007).

45. Lindsey, G., Schapery, R. A., Williams, M. L. & Zak, A. R. *The triaxial tension failure of viscoelastic materials*. (1963).
46. Bao, Y. & Wierzbicki, T. On fracture locus in the equivalent strain and stress triaxiality space. *Int. J. Mech. Sci.* **46**, 81–98 (2004).
47. Rottler, J. & Robbins, M. O. Shear yielding of amorphous glassy solids: Effect of temperature and strain rate. *Phys. Rev. E - Stat. Physics, Plasmas, Fluids, Relat. Interdiscip. Top.* **68**, 10 (2003).
48. Bending, B., Christison, K., Ricci, J. & Ediger, M. D. Measurement of segmental mobility during constant strain rate deformation of a poly(methyl methacrylate) glass. *Macromolecules* **47**, 800–806 (2014).
49. Ward, I. M. & Hadley, D. W. *An Introduction to the Mechanical Properties of Solid Polymers*. (John Wiley & Sons, 1993).
50. Kolobov, A. V., Oyanagi, H., Tanaka, K. & Tanaka, K. Structural study of amorphous selenium by in situ EXAFS: Observation of photoinduced bond alternation. *Phys. Rev. B* **55**, 726–734 (1997).
51. Barber, J. . & Ciavarella, M. Contact mechanics. *Int. J. Solids Struct.* **37**, 29–43 (2000).
52. Spence, D. A. The hertz contact problem with finite friction. *J. Elast.* **5**, 297–319 (1975).
53. Lu, Y. C., Kurapati, S. N. V. R. K. & Yang, F. Finite element analysis of cylindrical indentation for determining plastic properties of materials in small volumes. *J. Phys. D. Appl. Phys.* **41**, 115415 (2008).
54. Riccardi, B. & Montanari, R. Indentation of metals by a flat-ended cylindrical punch. *Mater. Sci. Eng. A* **381**, 281–291 (2004).
55. Mata, M. & Alcalá, J. The role of friction on sharp indentation. *J. Mech. Phys. Solids* **52**, 145–165 (2004).
56. Adam, C. J. & Swain, M. V. The effect of friction on indenter force and pile-up in numerical simulations of bone nanoindentation. *J. Mech. Behav. Biomed. Mater.* **4**, 1554–1558 (2011).
57. Michel, D., Kopp-Marsaudon, S. & Aimé, J. P. Tribology of a polystyrene polymer film investigated with an AFM. *Tribol. Lett.* **4**, 75–80 (1998).
58. Taku Aoike, *, Hiroki Uehara, Takeshi Yamanobe, and & Komoto, T. Comparison of Macro- and Nanotribological Behavior with Surface Plastic

Deformation of Polystyrene. (2001). doi:10.1021/LA001326O

59. Herbert, E. ., Pharr, G. ., Oliver, W. ., Lucas, B. . & Hay, J. . On the measurement of stress–strain curves by spherical indentation. *Thin Solid Films* **398–399**, 331–335 (2001).
60. Fischer-Cripps, A. C. Nanoindentation of Thin Films. in 132–143 (2004). doi:10.1007/978-1-4757-5943-3_8
61. Oliver, W. C. & Pharr, G. M. Measurement of hardness and elastic modulus by instrumented indentation: Advances in understanding and refinements to methodology. *J. Mater. Res.* **19**, 3–20 (2004).
62. Symon, K. R. *Mechanics*. (Addison-Wesley Pub. Co, 1971).
63. Wald, M. J., Considine, J. M. & Turner, K. T. Measuring the elastic modulus of soft thin films on substrates. *Exp. Appl. Mech. Vol 6* 741–747 (2011). doi:10.1007/978-1-4419-9792-0
64. Johnson, K. L. *Contact Mechanics*. (Cambridge University Press, 1985). doi:10.1017/CBO9781139171731
65. Mott, P. H., Dorgan, J. R. & Roland, C. M. The bulk modulus and Poisson's ratio of "incompressible" materials. *J. Sound Vib.* **312**, 572–575 (2008).
66. Caddell, R. M., Raghava, R. S. & Atkins, A. G. Pressure dependent yield criteria for polymers. *Mater. Sci. Eng.* **13**, 113–120 (1974).
67. Swallowe, G. M. & Lee, S. F. Quasi-static and dynamic compressive behaviour of poly(methyl methacrylate) and polystyrene at temperatures from 293 K to 363 K. *J. Mater. Sci.* **41**, 6280–6289 (2006).
68. Tao, R. & Simon, S. L. Bulk and shear rheology of silica/polystyrene nanocomposite: Reinforcement and dynamics. *J. Polym. Sci. Part B Polym. Phys.* **53**, 621–632 (2015).
69. Krevelen, D. W. van (Dirk W. & Nijenhuis, K. te. *Properties of polymers : their correlation with chemical structure ; their numerical estimation and prediction from additive group contributions*. (Elsevier, 2009).
70. Torres, J. M., Stafford, C. M. & Vogt, B. D. Impact of molecular mass on the elastic modulus of thin polystyrene films. *Polymer (Guildf).* **51**, 4211–4217 (2010).
71. Bowden, P. B. & Jukes, J. A. The plastic flow of isotropic polymers. *J. Mater. Sci.* **7**, 52–63 (1972).
72. Rottler, J. & Robbins, M. O. Yield conditions for deformation of amorphous polymer glasses. *Phys. Rev. E* **64**, 051801 (2001).

73. van Breemen, L. C. A., Engels, T. A. P., Klompen, E. T. J., Senden, D. J. A. & Govaert, L. E. Rate- and temperature-dependent strain softening in solid polymers. *J. Polym. Sci. Part B Polym. Phys.* **50**, 1757–1771 (2012).

Chapter 4:
Thermo-mechanical Signatures of Yield and Densification in Polystyrene Films

Abstract

In this chapter the confined layer compression test is used to probe and manipulate the thermomechanical state of supported glassy polystyrene films. The effect of structural recovery on the characteristic stress-strain curve is explored, with well annealed films exhibiting stiffer and stronger responses than freshly quenched samples. The effect of confined yield on the subsequent mechanical properties of the sample is studied through creep compliance testing and complex loading histories. It is shown that yield is accompanied by a significant increase in molecular mobility despite no lateral flow occurring. Cyclic loading experiments reveal a significant hardening effect, resulting in an increased yield stress upon subsequent loading. Through indentation of polystyrene films and finite element simulations, this is revealed to be primarily due to residual shear stresses imparted to the sample during plastic loading. This combination of a strongly constrained geometry and classical plasticity amounts to a confinement induced stress memory effect. This memory effect is also found to result in significant densification of the sample, which is probed via scanning transmission x-ray microscopy. A peak density increase of 3.4% is achieved by indention to 0.84 GPa, approximately equal to the density increase achieved by physically ageing the sample by several millions of years, albeit by a significantly different physical mechanism.

4.1 Introduction

The influence of mechanical stimuli on the thermodynamic evolution of the glassy state has long been a topic of practical concern. While changes in volume and enthalpy brought about by structural recovery are modest, typically less than 1% of the total volume over testing periods[1], the resultant changes in mechanical properties through

physical ageing may be considerable. Yield stress increases on the order of 100% have been reported[2], as well as changes in the failure mode from ductile to brittle in many polymers through ageing[3,4]. Structural recovery must also be considered in the design of systems such as batteries, supercapacitors, and fuel cells, where free volume strongly influences charge transport[5]. Conventional theories of structural recovery/physical ageing state that in unstressed conditions free volume is gradually reduced as the glassy system moves toward equilibrium, with accompanying decreases in segmental mobility and specific volume. In his 1978 thesis, *Leendert Struik* proposed his mechanical erasure hypothesis[6]. In Struik's model, segmental mobility and free volume were mutually dependent. Macroscopic deformation of the sample required increased mobility, and therefore an increase in the free volume content of the system, regardless of the deformation mode. Deformation induced free volume creation was thought to have the effect of erasing previous structural recovery and to rejuvenate the sample to an unaged state. This is idea is represented in temperature-volume space in figure 4.1.1 (a), where the stress applied σ undoes the spontaneous evolution of the system at T_a.

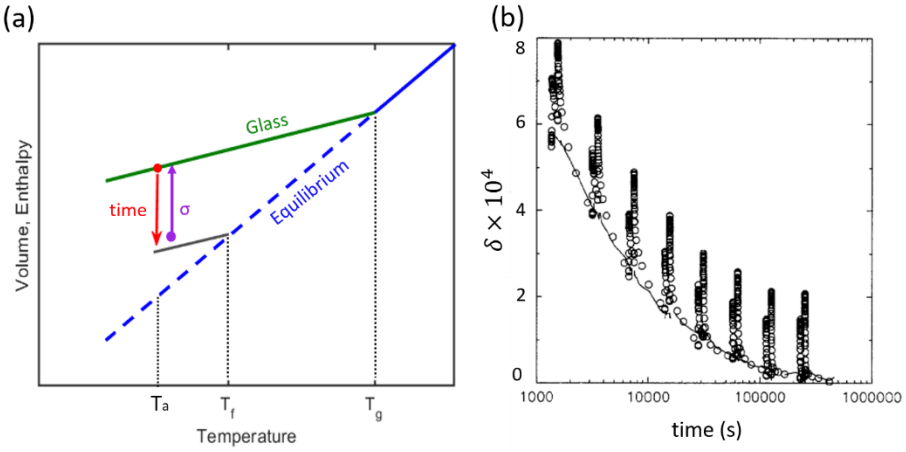

Figure 4.1.1 (a) The mechanical erasure hypothesis. The application of a stress σ reverses the effect of structural recovery, deageing the sample. (b) Structural recovery of an epoxy sample exposed to periodic torsional strains. While causing a temporary increase in departure from equilibrium (δ), the mechanical signals are decoupled from the underlying ageing process. Reproduced with permission from [7].

The mechanical erasure hypothesis has since fallen out of favour. Torsional dilatometry experiments by *McKenna* et al. have revealed recovery from mechanical deformation to be effectively decoupled from the volumetric structural recovery process. These results

are presented in figure 4.1.1 (b). An epoxy sample was quenched to below the glass transition temperature T_g and allowed to age. During the ageing process large, but sub-yield torsional stresses were periodically applied[7]. While mechanical straining did temporarily increase the departure from equilibrium δ, defined as the normalised current volume of the sample minus the volume at equilibrium, the underlying recovery process was unaffected. Molecular dynamics simulations conducted by *Riggleman*[8] have further shown that molecular mobility increases during uniaxial compression testing, where the total free volume content of the sample decreases. Recent stress relaxation and creep experiments in compression by *Caruthers* et al.[9] appear to validate these results.

This leaves the matter of how free volume, mobility, and applied stress interreact within the context of structural recovery of glasses as something of an open question. Under certain conditions, pre-yield stresses appear to increase the structural recovery rates of both polymers[10] and metallic glasses[11] in a phenomenon known as accelerated ageing. Post-yield deformation appears to lead to the generation of a thermodynamic state that possess some properties suggestive of a rejuvenated state such as quicker dynamics, but differs significantly in terms of spatial and temporal heterogeneity of relaxation times[12,13]. An analogous "overageing" phenomenon that leaves the system in a lower energy state with longer relaxation times has also been reported[14–16]. The confined layer compression test (CLCT) introduced in the previous chapter represents an effective new tool with which to explore these problems. Due to the constant contact area maintained during the test, extraction of ageing-dependent mechanical properties from the stress-strain curve is straightforward. The effect of the uniform, confined yield event on segmental mobility may be qualitatively monitored via creep compliance testing at multiple pre and post-yield stresses, while more complex loading patterns may be used to study changes in mechanics upon yield. As this yield event occurs within a hydrostatically dominated stress environment with confinement preventing conventional volume preserving shear flow, the question arises as to its effect on free volume. In the converse case of high shear in a dilatational background during deep notch extension, bulk metallic glasses have been found to be left in a densified state upon the removal of load[11]. The compressive CLCT case is studied through careful volumetric analysis using the STXM and AFM techniques outlined in chapter two. The possibility of using such a densification event for free volume engineering is considered. These topics shall form the focus of this chapter.

Before proceeding, a brief summary of recent experimental and simulation studies concerning the role deformation and stress on relaxation dynamics is included to provide context for the subsequent results.

4.2 The influence of deformation on polymer dynamics

Structural recovery in the absence of external stresses consists of molecules lowering their configurational energy through thermally assisted barrier hopping, in a manner that optimizes local packing and therefore reduces free volume and free energy. The glassy system therefore evolves towards a state of lower energy. A useful framework in which to consider this process is the multidimensional potential energy landscape (PEL) picture[17]. The PEL represents the potential energy of the system in configurational space. Formally, the PEL is a 3N-dimensional surface for an N-body system[18]. This is conceptually represented by a 2-dimensional schematic as in figure 4.2.1.

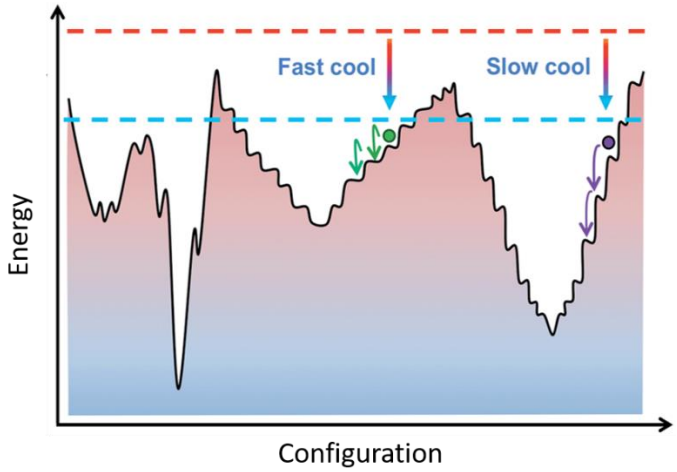

Figure 4.2.1 Two-dimensional representation of the potential energy landscape. As the system ages/recovers it moves deeper into the PEL, where energy barriers are larger and therefore dynamics are slower. This leads to trapping of the system in these basins, particularly at fast cooling rates Reproduced with permission from [17].

At high temperatures the system is ergodic and may explore all possible configurations. As temperature is reduced the path of the system within the PEL becomes obstructed by a rugged landscape of energy barriers which are overcome by thermally activated

hopping. The various minima of the PEL are termed intrinsic states, while groups of such states are called metabasins. Slow cooling rates keep the sample in equilibrium longer and allow the system to enter deeper metabasins, while fast cooling rates leave the system trapped in shallow, high energy basins, as shown in figure 4.2.1. As the system ages it proceeds down these metabasins, minimizing its configurational energy. Local energy barriers increase in size deeper into the metabasins due to the denser glass having fewer configurational degrees of freedom, manifesting as the commonly observed reduction in molecular mobility with ageing. These higher energy barriers help to explain other features of physical ageing such as increased yield stress, as the barriers to local rearrangement required for flow are greater.

The PEL is a particularly useful model with which to view the role of deformation on the energetic state of glasses, as shown by Lacks et al.[19] in a set of important simulations regarding athermal molecular glasses exposed to shear. Cyclic shear deformations of 30%, 15%, and 5% strain were imposed on quenched and annealed systems, with the quenched system further from equilibrium in a higher energy state. Following the large 30% strain, both annealed and quenched systems were found in a higher energy state than prior to deformation. Further, the new state was found to be thermal history independent. This represented a mechanical rejuvenation event. For the 5% strain, both systems were found in lower energy states, indicating overageing had occurred. At the intermediate 15% strain, the energy of the annealed sample was found to increase and the quenched to decrease, indicating that they had been rejuvenated and overaged respectively. Within the PEL model these results may be interpreted as follows: All strains cause a distortion of the local PEL in a manner similar to the Eyring mechanism[20], where the barriers between energy states are lowered and eventually destroyed, at which point the system moves to a state that is lower in energy *at the applied strain*. This phenomenon is often called landscape tilting[21,22]. When strain is reversed, the new energy minimum remains lower than the original for small applied strains and the sample is overaged. At larger strains the probability that the new minimum remain at a lower energy reduces, eventually going to zero in the limit of large plastic deformations, where rejuvenation occurs. At intermediate strains either rejuvenation or overageing may occur based on the pre-deformation position of the system within the PEL. These mechanisms are shown in figure 4.2.2. It is important to emphasise that while mechanical rejuvenation/overageing are reminiscent of structural recovery and thermal quenching, they are physically distinct processes corresponding to different pathways in the PEL.

This results in quantitative differences that have been shown in both simulations[23–27] and experiment[7,28,29].

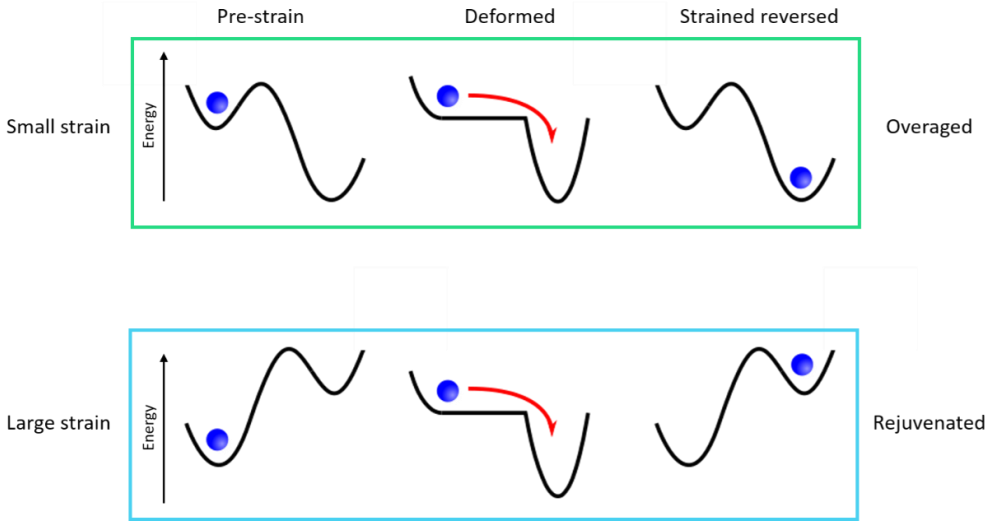

Figure 4.2.2 Landscape tilting within the potential energy landscape. Strains both small and large destroy the local minimum within which the system resides, resulting in it moving to a lower minimum at that strain. When the strain is reversed the new minimum may be lower or higher than the initial, depending on the magnitude of the strain and thermal history of the system.

Simulation techniques provide a valuable insight into the dynamics of glasses in an athermal (0 K temperature) environment, as in the *Lacks* study described above. However, in a more realistic, thermally active system where temperature is sufficient to activate relaxation processes, molecular dynamics are less successful due to the long timescales associated with thermally assisted relaxation. As such, experimental techniques must be relied upon to obtain a picture of dynamics under complex loading histories. Recently, a new technique developed by *Ediger* and *Lee* has enabled direct measurement of relaxation times in macroscopic tensile tests[30–33]. Segmental dynamics are monitored via inclusion of a fluorescent probe molecule within a PMMA matrix, whose reorientation time when exposed to laser light is proportional to the relaxation times of the surrounding polymer. It was found that during constant strain rate loading experiments in tension relaxation times steadily decreased by up to three orders of magnitude in the pre-yield regime. At and above yield, relaxation times were observed to plateau, with no further decrease with loading. These results are consistent with the PEL interpretation outlined above. Prior to yield, strain tilts the local landscape resulting in faster dynamics. Strains sufficient to induce yield move the system further

up the PEL where relaxation times are short due to the relatively small energy barriers. These results are further supported by the work of *Caruthers* who performed stress relaxation experiments on an epoxy glass, finding the same relaxation behaviour[34]. Crucially, *Caruthers* performed his experiments in both tension and compression, with both geometries showing the same behaviour. As such, the increase in mobility cannot be tied to changes in free volume, as was also shown in the previously mentioned simulations of *Riggleman*[8].

In summary, molecular mobility typically increases greatly during deformation. Large scale plastic deformations mechanically rejuvenate the sample, moving it to a higher position in the PEL. While similar to a thermal quench, rejuvenation is a distinct phenomenon and leaves the sample in a thermal history independent state in the plastic limit. Under certain testing geometries, such as tension and torsional deformations, sample volume and therefore free volume may increase, however this is not required for yield or the observed increase in mobility. Indeed, mobility has been found to increase even in cases where sample volume is reduced.

These ideas are central to the remainder of this chapter. The CLCT is a unique geometry in terms of polymer testing. While other uniaxial strain setups have been studied[35–38], the stresses and pressures achievable in compression have been well below what is required to achieve yield. An exception is the pressure-temperature studies of *Kimmel* and *Uhlmann* where a high aspect ratio Bridgman anvil cell allowed the density of a PMMA sample to be measured during deformation up to pressures of 5 GPa both above and below T_g. No attempt was made to monitor stain in their tests however, and as such the mechanical response of their samples during compression was poorly defined[39]. The CLCT allows for more complete study of yielding phenomena in amorphous matter in a uniquely pressure oriented environment, where the hydrostatic background may be expected to inhibit mobility. The confined layer compression test is first used to characterise the mechanical response of atactic polystyrene films exposed to different thermal histories, showing the effects of ageing on the stress-strain curve and validating the rejuvenation hypothesis at high strains. The confined yield phenomenon reported in the last chapter is studied from a thermomechanical perspective, with molecular mobility tracked via creep compliance in the confined pre and post yield regions, and volumetric changes characterized as a function of applied stress. After the applied load is removed, a permanent reduction in the total volume of material compressed by the punch is observed, which must be accompanied by a

reduction of free volume, as no lateral, volume preserving flow occurs. This phenomenon is understood in terms of residual shear stresses imparted to the sample during loading. These are studied experimentally and via finite element simulation.

4.3 Experimental Methods

4.3.1 Thermal history and creep compliance experiments

Polystyrene thin films (Polymer Source Inc.) of 1.13 MDa molecular weight and polydispersity ≈ 1 of thicknesses 550 and 670 nm were prepared via spin coating from a 4% wt. toluene solution on silicon <100> wafer pieces of approximately 1 cm^2 (University Wafer.) Samples were then heated to 120°C for 2 minutes to remove residual solvent.

The films were then heated and held at 130°C for 30 minutes, before the temperature was ramped down to 75°C ($T_g - 25^{\circ}$) at a rate of 8°/hr. They were then annealed for 5 hours at 75°C before being abruptly cooled to room temperature. This represents the 'annealed' thermal history path. The samples were then aligned via the procedure discussed in section 2.1.2 and indented using a 4.8 µm diameter flat punch prepared via FIB milling, yielding aspect ratios of $\chi = 8.7$ and $\chi = 7.2$ for the 550 nm and 670 nm films, respectively. Indentation was performed using the MTS Nanoindenter XP system as opposed to the DCM module, due to its higher load capacity.

Following indentation, the films were removed from the indenter and again heated to 130°C and held for 30 minutes in order to thermally rejuvenate them and erase their previous ageing history. They were then rapidly cooled from this melt state to room temperature, representing the thermal 'quench' path. The samples were then re-inserted in the indenter and indented following the same procedure as for the annealed sample group. Alignment was assessed via AFM and corrected until the difference between the two runs was minimal. The two thermal history paths discussed here are shown in figure 4.3.1 (a), with an idealised representation of their structural evolution shown in (b). By using the same samples for both the annealed and quenched thermal histories and ensuring that indentation conditions were as similar as was practical for both sets of experiments, differences in the results can be ascribed to the influence of thermal history alone.

To ensure that mechanical conditions (alignment, background stiffness) could be reliably reproduced for the same film following different thermal treatments, a special sample mounting procedure was employed. Samples were mounted to a microscopy stub via high temperature cement (Omega CC.) This stub was then screwed into the tilt stage. Alignment marks were made on both stub and stage, which could be matched together when the stub was removed for heating and then then replaced. This ensured minimal rotation of the samples with respect to the aligned punch due to the heating process. An 'X' was scratched into the surface of both samples via tweezers, removing the film in this location and providing an optical landmark which could be identified via the indenter optics. This enabled the second set of indentation experiments to be carried out on the samples near the locations of the first, but not so close as to risk indents 'overlapping.' By placing the indents from each set of experiments close together it was ensured that the background frame stiffness wouldn't not be significantly altered between each run. Finally, the degree of misalignment for both the 'annealed' and 'quenched' experiments (i.e. Before sample removal and after its replacements) was assessed via AFM and found to be within error. This data is available in appendix 2.

By using the same samples for both the annealed and quenched thermal histories and ensuring that indentation conditions were as similar as was practical for both sets of experiments, differences in the results can be ascribed to the influence of thermal history alone.

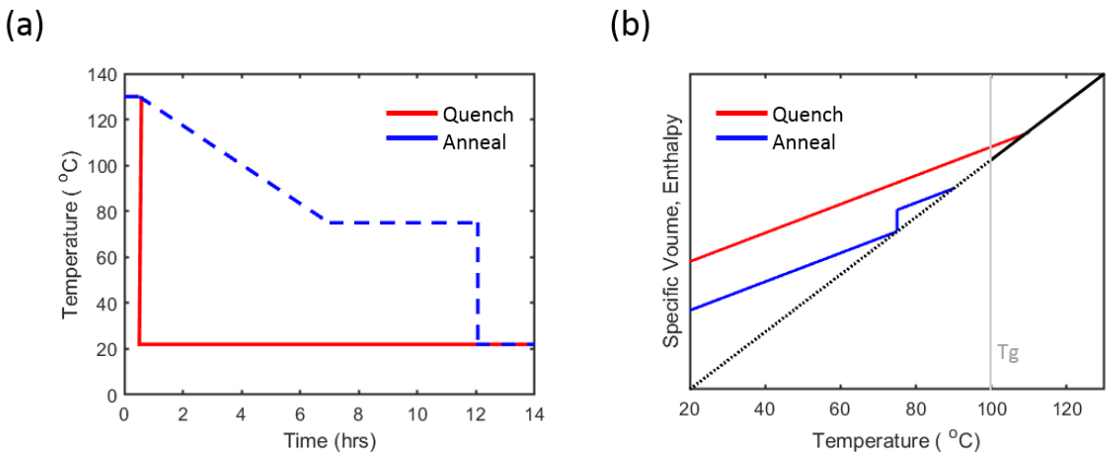

Figure 4.3.1 (a) Thermal histories of the quenched and annealed sample groups prior to indenting. (b) Idealised representation of the structural evolution of these samples during the heating/cooling process. Further ageing at room temperature is expected to be minimal, due to the extremely low segmental mobility of the system deep in the glassy state.

4.3.2 Finite element simulations

Axisymmetric simulations were performed using the Abaqus 2017 Explicit (Dassault Systemes) finite element package in order to study residual stresses and sample densification. In contrast to the previous chapter where the CLCT geometry was directly studied, simulations in this chapter used a 'pure' uniaxial strain geometry with the test volume confined by rigid sidewalls. This was done to allow for easier comparison between experimental results and the predictions of elastic-plastic constitutive models. Further, this made measurement of radial stresses exerted on the sidewall more accessible. The punch was modelled as a perfectly rigid body of 1 µm radius with sharp corners. The same elastic-perfectly plastic material with $E = 3.0$ GPa, $\nu = 0.33$, $Y = 0.1$ GPa, and $\rho = 1.04$ g/cm^3 used in chapter three was employed again. No constitutive laws allowing for strain hardening were included. The test volume consisted of a cylinder of 1 µm height and radius. 4-node bilinear axisymmetric quadrilateral (CAX4R) elements were utilized, with the initial element area set as 50 x 50 nm. Indentation was simulated via prescribing a vertical displacement of the punch face. No other displacements of the punch are allowed. A full-slip condition was specified between punch surface and sample. An encastre condition was applied to the bottom surface of the sample such that $U_r = U_z = 0$, simulating a full-stick condition on a rigid substrate. A boundary condition setting radial displacements to zero was imposed at the sample wall throughout to enforce the uniaxial strain condition. Stresses and strains were extracted using the same procedure as in chapter three.

4.3.3 Scanning transmission x-ray microscopy experiments

STXM experiments were conducted at the PolLux beamline of the Swiss Light Source at the Paul Scherrer Institute, Switzerland, with the purpose of probing densification in polystyrene films due to the confined layer test. Polystyrene films of 203 nm thickness were prepared from a 2% wt. toluene sample. STXM requires that the polymer film be supported on a thin, x-ray transparent substrate. To facilitate this, the film was spun onto a 1 x 1 cm silicon wafer piece with a 190 nm Si_3N_4 layer on either side. The Si_3N_4 was grown onto silicon via a low stress LPCVD recipe at 820oC in an ammonia/dichlorosilane environment at Rogue Valley Microelectronics, California. An array of 25 indents as produced using a 2140 nm diameter punch, corresponding to an aspect ratio of 10.5:1 and covered a peak axial stress range of 0.10 – 1.6 GPa, however

only the first 20 indents to 0.84 GPa were studied in detail as past this point uniaxial strain confinement no longer applied. No hold time was included at peak stress. Sample topography maps were then taken via AFM using the Asylum MFP 3D system.

A novel back-etching technique was developed to remove silicon beneath the indented area. Following indentation, the back layer of Si_3N_4 was removed by mechanical scratching, exposing the silicon. The front side of the sample was then protected, and the silicon beneath the indent array wet etched with a 20% wt. aqueous NaOH solution at 55˚C for approximately two days. NaOH was chosen over the more commonly used KOH due to its relative x-ray transparency. This sample preparation process is shown in figure 4.3.2 (a). An AFM image of the indentation array is shown in (b), with the order in which the indents were made indicated by the white line (starting at 1, going to 25.) An optical image of the final sample is shown in (c). The film/window is the yellow region, while the surrounding pink area is unetched silicon. Some NaOH residue is visible on the window but did not interfere with measurements.

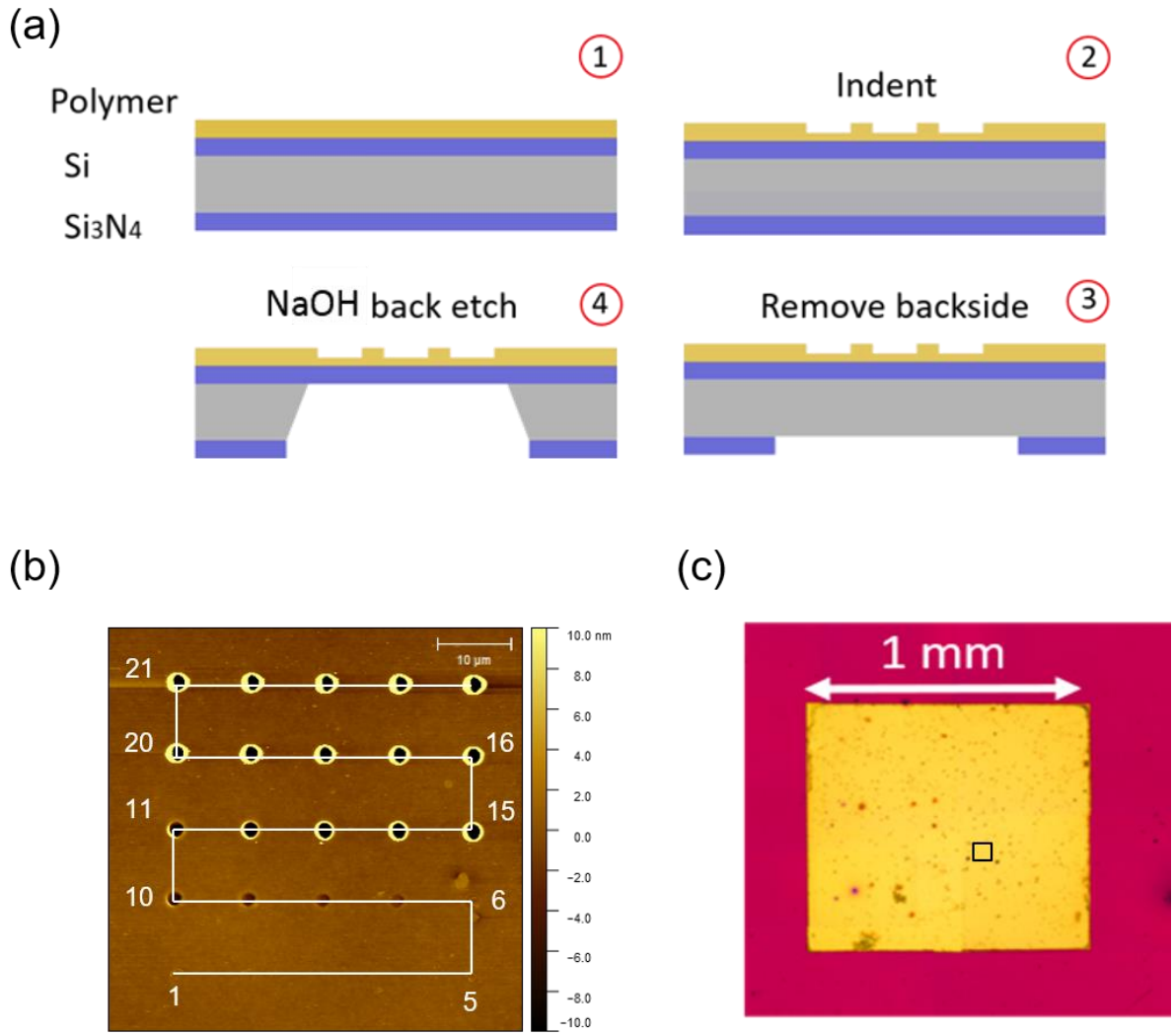

Figure 4.3.2 (a) Sample fabrication process for STXM density studies at the PolLux beamline. The 203 nm PS film is first spun onto the Si/Si_3N_4 wafer. The film is then indented, the back layer of Si_3N_4 removed, and the sample wet etched with NaOH at 55˚C for two days. (b) AFM map of the indent array. Indents 1-5 fall in the elastic regime and therefore no residual impression is visible. Indents were made in the snake pattern indicated by the white line, starting at #1 (low stress, elastic) and finishing at #25 (high stress, post extrusion limit.) (c) Optical image of the wafer sample following the etching procedure. The yellow box is the successfully etched window. The approximate area of the indent array is shown as a black square.

STXM measurements were primarily made at the 384.8 eV polystyrene absorption peak, corresponding to the 1s → C=C 1π* orbital transition. Secondary measurements were performed for selected indents at other absorption peaks corresponding to other transitions (see figure 4.4.12 (b)). The sample was loaded into a holder and optically imaged to locate the indent array, before being transferred to STXM vacuum chamber, where the sample holder was mounted to a piezo positioning system. The optical image of the sample was then fed into a custom program which allowed the beam to be positioned approximately over the indented region. Indents were scanned individually,

with a typical scan consisting of a 5 x 4 μm rectangular region around each individual indent, with a dwell time of 50 ms. The pixel resolution of each image was 250 x 200, yielding a lateral spatial resolution of approximately 40 nm and with scans taking approximately 5 minutes each. Prior to the main scan, each indent was located and centred in the field of view via with low resolution, 2 ms dwell time scan. Live raster images of the scanned regions were generated, similar to the operation of most commercial AFMs, meaning beam position A normalisation process was required to remove the influence of the Si_3N_4 window, which is detailed in appendix 1. Post experiment data analysis was performed using the freely available aXis 2000 STXM[40] software developed at McMaster University and a custom AFM-STXM image mapping program written in MATLAB.

4.4 Results & Discussion

4.4.1 Influence of thermal history on the confined mechanical response of polystyrene films

The influence of thermal history on the CLCT stress-strain curve is shown for the quenched and annealed 550 nm polystyrene films in figure 4.4.1 (a) for a stress-rate controlled load sequence at 0.05 GPa/s. Changes in the initial film thicknesses due to the annealing process were less than 0.5% and as such both annealed and quenched samples are plotted on the same set of axes. A close-up of the low strain region where confinement is well maintained is shown in figure 4.4.1 (b). The features typical[41] of physical ageing are evident: The confined yield stress Y_c, confined plastic modulus C^*, and the flow stress Y_{flow} are higher for the annealed sample than for the quenched. By contrast the confined elastic modulus C is relatively unaffected. We note that in our stress-controlled experiment there is no strain softening or yield drop in the post Y_{flow} region as normally. An increase in the size of the flat flow region ($d\sigma/d\varepsilon \approx 0$) with annealing is present however. Finally, an upturn in the stress-strain slope is seen at very high strain, which is often attributed to chain alignment[42] (biaxial in this case), which has associated with it an entropic cost. In the flat punch geometry a squeeze-flow[43] effect will also increase resistance at very high strain.

The changes in C^* and yield stresses are summarised in table 4.4.1 for both the 670 nm and 550 nm films.

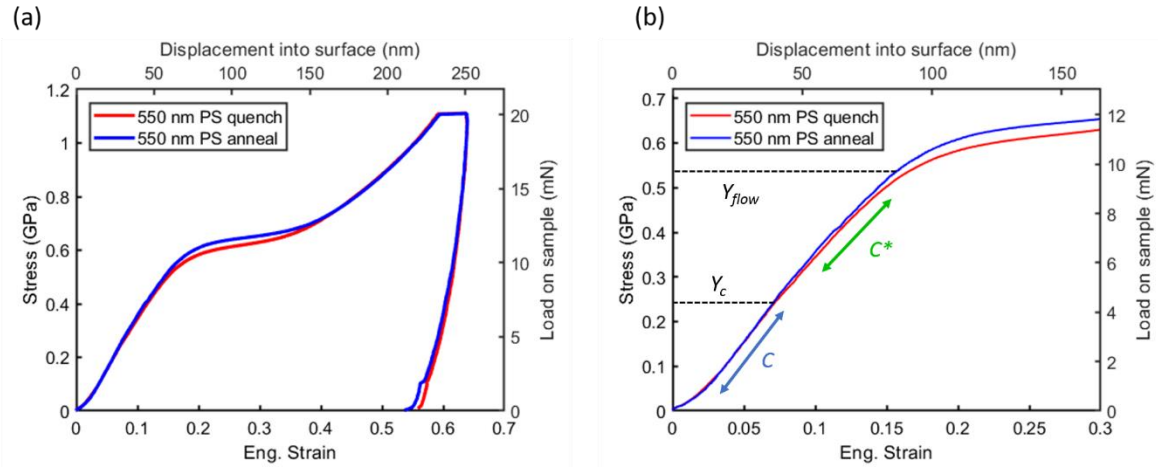

Figure 4.4.1 (a) Characteristic stress-strain curves for the annealed (blue) and quenched (red) 550 nm polystyrene films. (b) Close-up view of the confined region. In the elastic limit, the two films respond identically, with their curves lying directly on top of each other. The different thermal histories of the two samples leads to a divergence of response in the confined plastic limit, with the annealed sample showing larger confined yield and flow stresses, as well as a lightly higher confined plastic modulus C^*, in line with conventional polymer ageing theory. At large strains of 0.4, well into the extrusion limit, the two curves again converge, suggestive of a mechanical erasure of previous thermal history.

Table 4.4.1 Confined plastic modulus and yield stresses for 550, 670 nm quenched and annealed films.

	C* (GPa)	Y_c (GPa)	Y_{flow} (GPa)
550 nm anneal	3.80	0.273	0.577
550 nm quench	3.54	0.252	0.530
670 nm anneal	3.50	0.259	0.545
670 nm quench	3.36	0.244	0.505

At an engineering strain of approximately 0.4, the quenched and annealed curves converge and follow the same path in stress-strain space, viewable in (a). This suggests mechanical rejuvenation of the previous thermal history of the glass, pushing the system into a state that is independent of previous thermal cycling, in line with the arguments made in section 4.2. This rejuvenation event is indicative of the manner in which the ageing process may be manipulated by the application of stress. This may be contrasted with the stress-strain response of a 300 nm film of the thermoset imprint polymer MR-I 9000M before and after thermal cross-linking at 150 °C, shown in figure 4.4.2. Structural recovery and cross-linking are processes which share some similar features, such the increase in entanglements due to denser segmental packing

resembling the increased connectivity of the thermoset brought about by covalent bond formation[6]. The confined regions of figures 4.4.1 (a) and 4.4.2 do indeed show a strong resemblance. The confined elastic modulus C is essentially unchanged in each case, while Y_c and C^* are increased by the ageing and cross-linking processes. The extrusion regime behaviour is qualitatively different however, due to the irreversibility of the cross-linking process, in contrast to densification introduced by structural recovery.

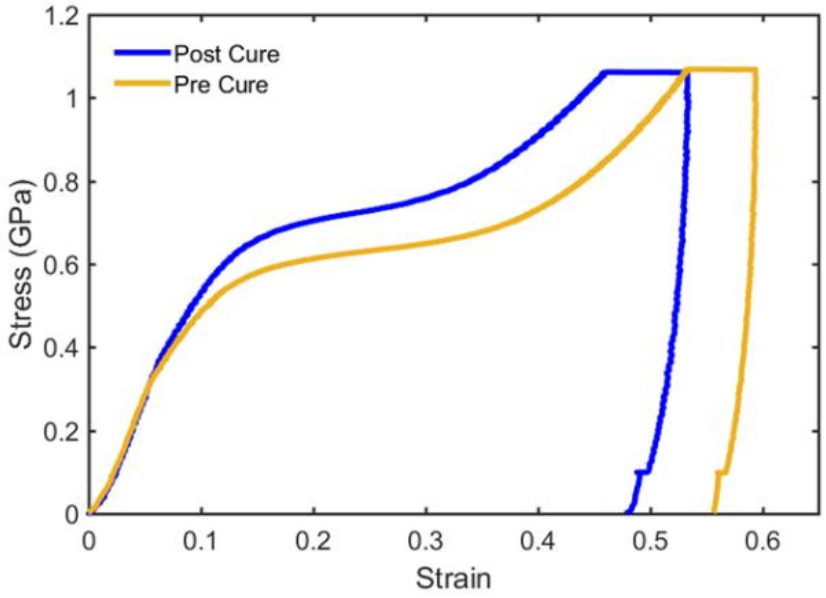

Figure 4.4.2 Stress-strain curves for a 300 nm mr-I 9000E cross-linkable thermoset polymer before and after a curing treatment at 150°C for 5 mins.

4.4.2 Influence of deformation and yield on polystyrene mechanical properties

Yield is associated with dramatic changes in the mechanical behaviour of the material in question and in the past has been likened to both a phase transition[44] or a polymorphic transition, similar to that seen in amorphous ice[45]. In terms of mechanics, these changes may express themselves as changes in the yield stress[46,47] upon further cycling or changes in the viscoelastic properties such as stress relaxation modulus or creep compliance. Changes in these latter properties are often linked to changes in underlying segmental mobility, and while less sensitive than the optical dye method

mentioned in section 4.2[48], mechanical measurements of compliance may yield qualitative information about mobility under different stress conditions[9,49].

4.4.2.1 Creep Compliance Testing

Creep compliance is measured within the confined layer compression test using the protocol shown in figure 4.4.3. The loading procedure is shown for a 550 nm quenched aPS film in (a), where the sample is loaded at a rate of 0.05 GPa/s until the desired creep stress σ_c is achieved. This stress is then held for 100 s, after which it is increased by 1.1 GPa and then decreased to 0.05 GPa, where thermal drift is measured. A standard load-up procedure with no creep step is shown as a dashed blue line for comparison. The purpose of the large final increase in load is to extrude as much polymer from beneath the punch as possible before measuring drift, in order to remove sample viscoelastic effects and measure only instrument drift[50]. This method yielded relatively constant drift values falling typically between -0.04 and 0.04 nm/s, independent of the applied creep stress (A plot of creep stress vs thermal drift is included in appendix 2). Further, the measured displacement during the creep step would typically be much larger than an extrapolated drift displacement over the same time frame (see appendix 2), indicating the procedure is relatively robust.

The resultant stress-strain curves obtained from this procedure are shown in (b), where three values of σ_c are shown corresponding to three distinct regions of material response. Creep tests carried out at stresses lower than Y_c are called elastic, as the short-term material response is primarily elastic (or anelastic, with fully reversible time dependent strain[42].) Following similar logic, tests taking place at σ_c's slightly above Y_c are called confined plastic, while tests occurring near Y_{flow} are dominated by confinement failure and wall extrusion and are called flow tests. The development of strain during the creep step is shown for the three σ_c's in (c), where it can be observed that the flow region has associated with it the largest deformations. Extrusion can be observed in the blue 'no creep' control curve by the rapid increase in strain at approximately 12 seconds.

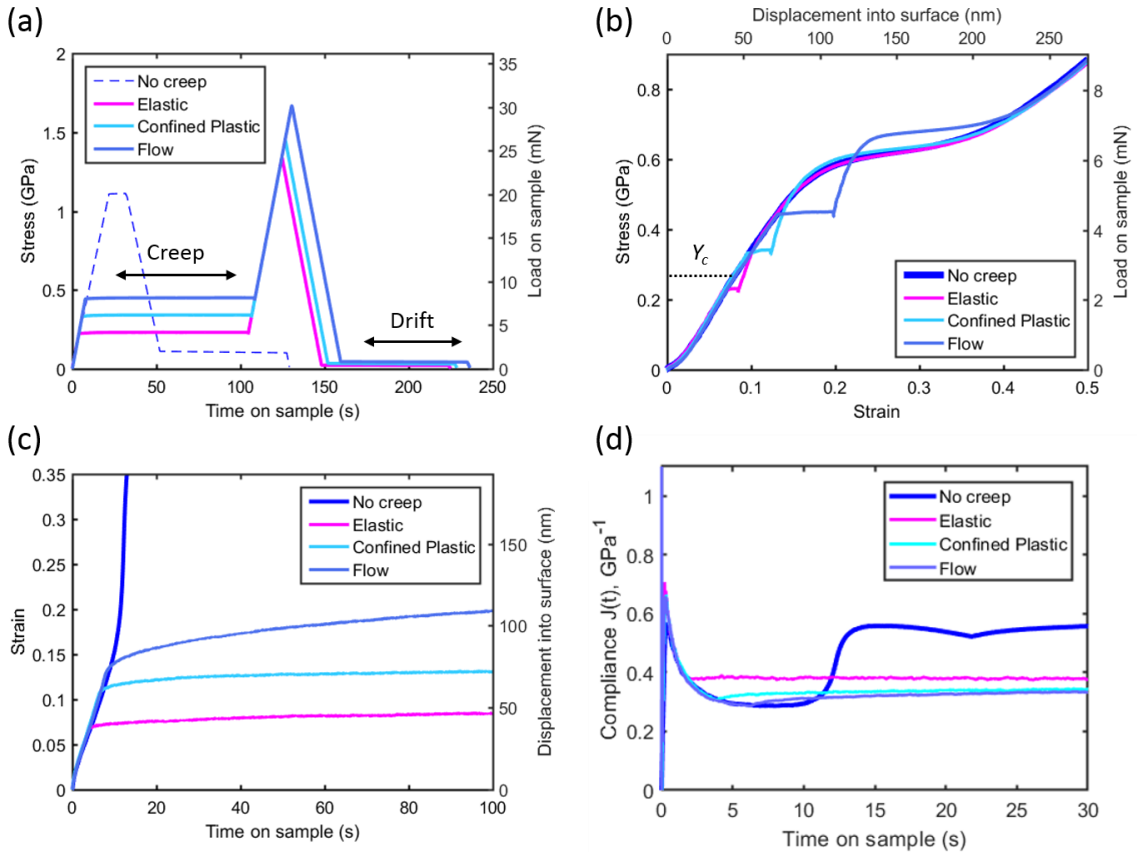

Figure 4.4.3 Creep compliance testing via the confined layer test for a 550 nm quenched aPS film. (a) Loading protocol. Stress is ramped up to a set creep stress, where it held for 100s to measure viscoelastic properties. Three creep stresses are shown here: one in the confined elastic regime (pink σ_c = 0.25 GPa), one in the confined plastic regime (cyan σ_c = 0.35 GPa) and one in the flow regime (blue σ_c = 0.45 GPa). Following creep, the load is again increased to over 20 mN in order to extrude as much polymeric material as possible before drift measurement. A loading procedure with no creep step is also included for comparison. (b) Resultant load displacement curves at three stresses. As σ_c is increased, the amount of creep strain that occurs during the holding phase increases, in accordance with non-linear viscoelasticity. (c) Evolution of engineering strain during creep, again confirming greater strain development at larger creep stresses. Extrusion in the 'no creep' curve (dark blue) is identified by the slope change (d). Creep compliance for the three creep stresses. A non-linear experimental compliance background must be removed to normalize the measurements, shown here as the dark blue line. This background compliance is largely the result of sample-punch misalignment, and appears as a decreasing compliance with increasing creep stress if not properly treated.

Creep compliance may be defined experimentally as $J(t) = \varepsilon(t)/\sigma(t)$[51,52]. This is plotted for the three stress levels in (d). In (d) it appears that *J(t)* decreases as the applied creep stress is increased, contrary to the typical behaviour of materials within the non-linear viscoelastic regime[52] as discussed in section 1.4.3. This however, is an experimental artefact. *J(t)* is effectively a measure of the inverse stiffness of the contact, being proportional to the displacement of the punch over the load. As such, non-linearities resulting from experimental considerations such as imperfect punch alignment or indenter settle time may appear as material response. To highlight this, *J(t)* for the

stress-strain curve with no creep hold is included in (d) as the blue line. It may be seen that compliance spikes upon initial contact to approximately 0.6 GPa^{-1}, before decreasing throughout the elastic regime (0 – 5 s) and plateauing in the confined plastic regime (5 – 10 s), before increasing again at extrusion. The ideal response of the elastic region should be a compliance value inversely proportional to C, with constant zero slope with respect to time. This experimental artefact is subtracted by setting the initial compliance of each creep test to zero when σ_c is reached at $t_c = 0$. This is equivalent to removing the instantaneous elastic element from the generalised Kelvin-Voigt model discussed in section 1.4.3. This renders comparison of the compliances obtained via the CLCT and other methods challenging, as other testing methods will include this portion of the curve. However, as the purpose of this section is only to observe changes in material response around the confined yield point it is sufficient for the CLCT curves to be comparable with each other at different creep stresses.

To study the dependence of background-corrected compliance on stress around the yield point, individual creep tests were performed into the 550 nm quenched aPS film at load increments of 0.5 mN, corresponding roughly to stress increments of 0.025 GPa with the 4.8 µm diameter punch. These results are plotted in figure 4.4.4, where the time scale in (a) in linear and logarithmic in (b). A distinct increase in compliance may be observed between 0.20 and 0.225 GPa, and 0.4 and 0.5 GPa, which separate the three families of curves indicated by the green, purple/blue, and red colour hues. The first distinction is due to the confined yield event. While the jump in $J(t)$ occurs slightly below $Y_c = 0.25$ GPa, this is most likely due to the initiation of plasticity locally at the punch edges due to the finite aspect ratio of the layer compression test, as was discussed in section 3.4.2. This results in the yield point being somewhat smeared out.

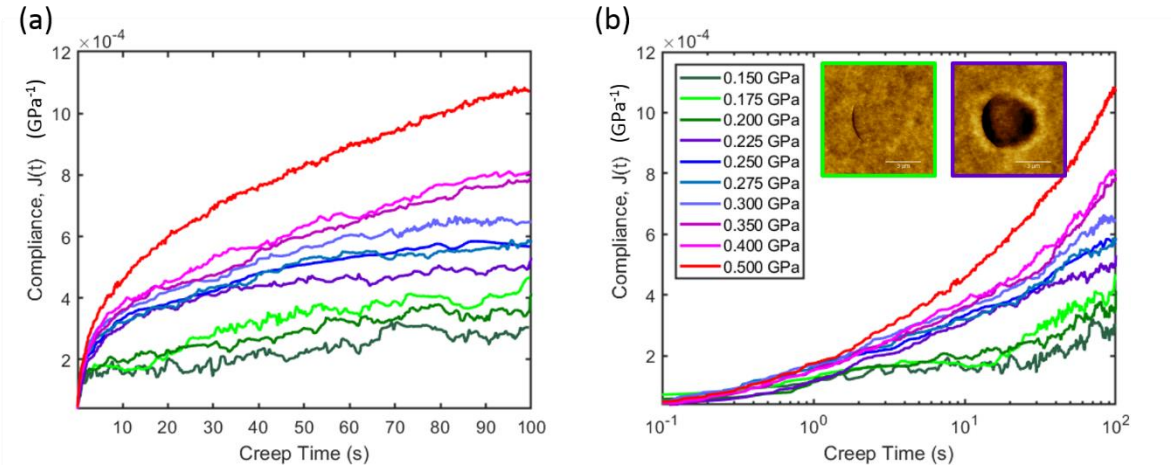

Figure 4.4.4 Corrected creep compliance curves for a 550 nm quenched aPS film. (a) Linear time scale. (b) Logarithmic time scale. AFM inserts show residual deformation for pre-yield (0.175 GPa) and post-yield (0.225 GPa) stresses. Outline colours correspond to the compliance curve in question.

In a one-dimensional creep compliance test, increases in *J(t)* with increasing stress are ascribed to a stress induced increase in segmental mobility. This was described in section 1.4.3 using an Eyring stress activated dashpot in a Kelvin-Voigt (KV) viscoelastic model. Such models are extended to include multiple relaxation modes via the inclusion of several individual KV elements in series, each with a unique associated retardation time. Application of such a model to the data presented in figure 4.4.4 enables quantitative study of the change in segmental dynamics due to yield. A two element KV model is employed in the form:

$$J(t) = C_0\text{-}C_1\left(e^{-\frac{t}{\tau_1}}\right)\text{-}C_2\left(e^{-\frac{t}{\tau_2}}\right) \qquad (4.4.1)$$

Where τ_1 and τ_2 are retardation times. In a conventional creep test C_0 would be related to the instantaneous elastic modulus and C_1 and C_2 to the long-time relaxed modulus, however due to the difficulties separating instantaneous response from misalignment artefacts discussed in figure 4.4.3 these quantities are here simply treated as fitting parameters. Plots of τ_1 and τ_2 determined via equation 4.4.1 from the compliance data of figure 4.4.4 are shown in figure 4.4.5 (a) and (b), respectively. In 4.4.5 (a) it can be seen that the shorter retardation time τ_1 increases approximately linearly with the applied creep stress σ_c, indicative of a slowing down of this particular mechanism. This effect may be due to the influence of the significant hydrostatic pressure imposed on the volume within CLCT. As pressure is increased, less free volume is available for motion and a slowdown in dynamics may be expected. Pressure is known to also cause

a linear increase in T_g for polystyrene, again associated with the suppression of segmental dynamics[53]. More dramatic behaviour is seen in (b), where the longer retardation time τ_2 falls from 118 s to 48 s. This is strongly indicative of a large increase in segmental mobility associated with yield. While τ_2 increases as σ_c is increased within the confined plastic limit ($0.225 < \sigma_c < 0.5$ GPa) it is always significantly lower than the pre-yield values, indicating that the yield process is associated with faster and easier molecular/segmental rearrangements in spite of the increasing pressure and a lack of traditional volume preserving shear flow.

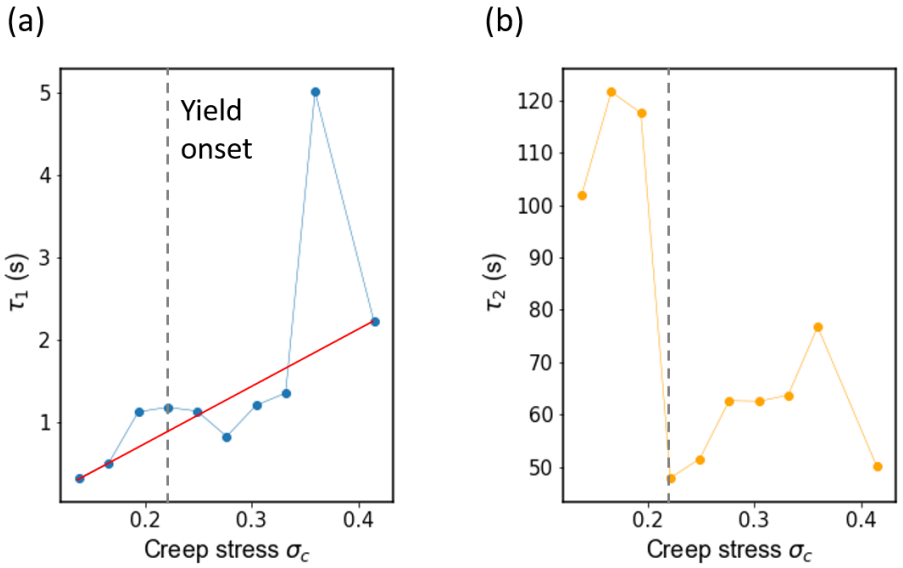

Figure 4.4.5 Retardation times for the 550 nm quenched polystyrene indenation data presented in figure 4.4.4 obtained via fitting to a 2 element Kelvin-Voigt viscoelastic model. (a) Short retardation time τ_1 as a function of applied creep stress σ_c. τ_1 increases approximately linearly with increasing stress, indicating a slowing down of this mechanism. This is likely due to the influence of increased hydrostatic pressure. No significant change in behaviour is observed at confined yield, denoted by the dashed grey line. (b) Longer retardation time τ_2 as a function of applied creep stress σ_c. A dramatic decrease is observed following confined yield, indicative of a molecular/segmental motion becoming significantly easier above the yield stress.

4.4.2.1 Post creep mechanical response

An added benefit of the loading program used to obtain *J(t)* is that it allows the mechanical response of the polymer to be studied during the post-creep step, when the load is increased to aid drift correction. Thus, the effect of creep strains and sustained stresses above and below the yield stress on the subsequent mechanics may be studied in a geometrically controlled manner. Sustained stresses have been previously shown to influence both microscopic properties such as chain alignment[54] and macroscopic phenomena including yield stress[55] and are therefore worthy of examination. Stress-

strain behaviour under resumed loading after creep tests in the elastic, confined plastic, and flow regions are presented in figures 4.4.6 (a), (b), and (c) respectively. The creep test phase of the curves are distinguishable as large increases in strain with a virtually unchanging stress. In each graph the grey curve represents the virgin stress-strain curve with no creep step applied.

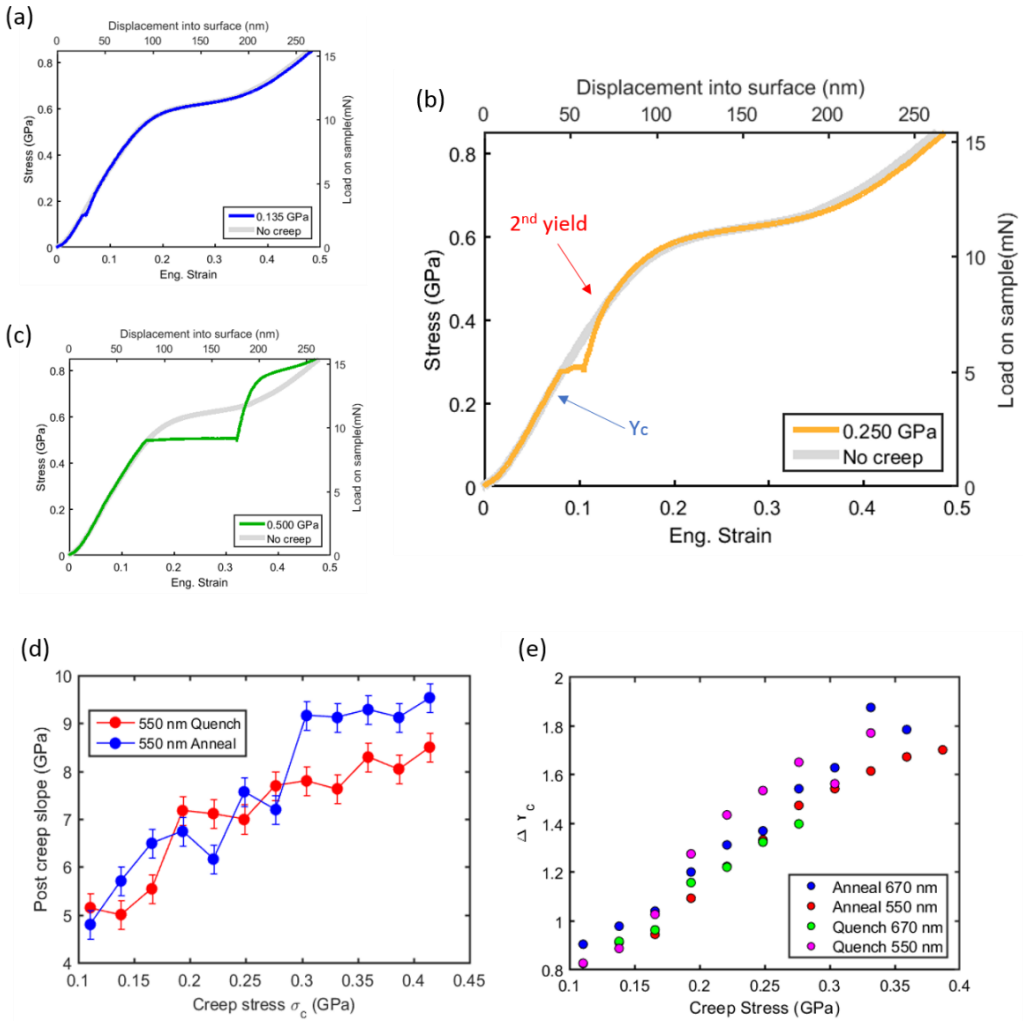

Figure 4.4.6 Post creep stress-strain response (a) Stress-strain curve for creep tests in the elastic regime, σ_c = 0.135 GPa. Following creep, the curve follows a steeper slope and yield at a higher stress. (b) Same curve for confined plastic creep, σ_c = 0.250 GPa. A second confined yield event is observed at approximately 0.4 GPa. (c) Flow region curve for σ_c = 0.500 GPa. (d) Slope of post creep loading region as a function of σ_c for annealed and quenched 550 nm samples. (e) Relative increase in yield stress as a function of σ_c for all samples.

Several features of (a-c) are worth of comment. Firstly, in all cases the post-creep slope is found to be dramatically stiffer/steeper than either the confined elastic modulus C or plastic modulus C^*. Second, in the cases of (a) and (b) the yield stress appears to be

substantially raised. For experiments conducted in the confined plastic region such as (b), a second confined yield event is visible, here at approximately 0.42 GPa. These increases in modulus and yield stress are suggestive of a stress induced densification event, similar to how glasses that have densified through physical ageing are stiffer and stronger[56]. The post-creep slope is plotted as a function of creep stress for the 550 nm annealed and quenched films in (d), while the relative increase in yield strength is plotted for the 670 nm and 550 nm films in (e). Both quantities increase steadily when creep stress is increased within the confined region.

When considering stress induced densification, it is important to distinguish any permanent material change from temporary stiffening of the volume due to elastic compactification of the polymer matrix, which may relax out once the load is removed. To study this, a loading protocol was designed in which the applied stress is dropped to 0.015 GPa following the creep step and maintained for 100 s, allowing relaxation to occur over the same timescale for which σ_c was applied. This protocol is plotted as a function of time in figure 4.4.7 (a). Experiments were performed on the quenched sample at the same increments of σ_c used to measure compliance. The post relaxation reload portion of the stress-strain curves are plotted in 4.4.7 (b), with the virgin curve again plotted in grey. Curves have been horizontally shifted for clarity. The yield stress for each curve is indicated by a black dot.

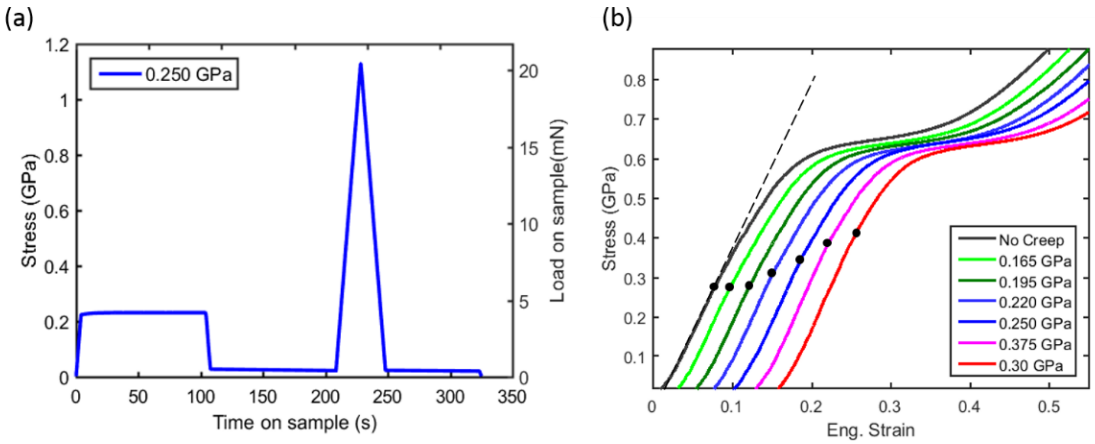

Figure 4.4.7 (a) Loading protocol utilised to measure effect of sustained creep load on mechanical properties. A 100 s low stress step at 0.015 GPa is included from 100 – 200 s to allow for relaxation of elastic compactification before reloading. (b) Stress-strain curves for the reloading portion of the protocol. The confined modulus returns to its pre-deformation value, however yield stress is substantial increased for curves where $\sigma_c > Y_c$.

Notably, the apparent stiffening of the stress-strain curves encountered in figure 4.4.6 disappears upon unloading to a lower stress. This suggests that this is either due to an elastic compactification of the polymer as discussed above, or an increased contact area during creep testing due to material contacting the rounded edges and side wall of the punch. The latter would be similar to the pile-up phenomenon encountered in spherical and sharp tipped indentation, which lead to dramatic overestimation of elastic modulus and hardness[57–59]. In either case, the effect appears to be transient, with both C and C^* reverting to their pre-deformation values after unloading. For tests where creep was performed in the elastic limit, i.e. $\sigma_c < Y_c$ it is found that the yield stress also reverts to its pre-deformation value, as shown by the 0.165 and 0.195 GPa curves in (b) These tests therefore show that creep deformation below the yield stress for periods up to 100 s appears to have no measurable effect on the subsequent mechanical response of the polymer in the CLCT. For creep tests conducted above Y_c, the reloaded yield stress appears to grow steadily with the applied creep stress. It shall be shown in the next section however that this phenomenon primarily results from the unique stress environment of uniaxial strain deformation in the plastic domain that is independent of material properties such as free volume, strain hardening, viscoelastic time dependencies. While these may also be present to some degree, they appear to be of secondary effects. Observing that the other plastic properties C^* and Y_{flow} are unaffected by creep upon reloading, it appears that creep deformation in the confined plastic regime also has no substantial, mechanically measurable effect on the subsequent response of the material, once the intrinsic increase of Y_c by time independent plastic deformation is explained.

In summary, the confined layer compression test may be extended to study the viscoelastic properties of glassy films through creep compliance testing. It is found that plastic yield results in a notable increase in compliance in polystyrene, indicating an increase in segmental mobility. This is in line with previous studies of mobility through yield in various geometries. The sustained creep stress causes a temporary stiffening of the test volume, possibly due to either reversible elastic compactification or viscoelastic pile-up. No permanent change in the subsequent mechanical response is induced by the creep stress, except for an increase in the yield stress after the sample has been previously loaded above Y_c. This however is not a polymer specific phenomenon and is explained in the next section.

4.4.3 Cyclic loading and strengthening through imparted residual stress

Figure 4.4.8 shows the result of a cyclic loading pattern into the 550 nm (χ = 8.7) quenched polystyrene film. The sample was first loaded at a rate of 0.05 GPa/s to 0.30 GPa, approximately 0.06 GPa above Y_c, well into the plastic zone. The sample was then unloaded back into the elastic regime, before being reloaded twice past yield to 0.385 and 0.470 GPa. For each reload cycle it can be seen that yield occurs at a higher stress than on the previous cycle, with the volume yielding when the stress-strain curve intersects the confined plastic slope C^*. This behaviour is suggestive of two phenomena generally associated with non-equilibrium aspects of glassy mechanics; physical ageing, in which the mechanical strength of the sample increases as it approaches equilibrium, and a mechanical memory effect where the sample remembers its deformation history[60]. The sample yielding at its loading path's intersection with C^* is indeed a memory effect, however it arises as a consequence of the approximate uniaxial strain geometry of the CLCT and time-independent classical plasticity rather than being a non-equilibrium glassy phenomenon. Residual shear stress imparted to the sample during plastic loading has the effect of lengthening the path the sample must follow in stress space to yield on subsequent reloading cycles. By reproducing the effect in FEA simulations of an isotropic linear elastic-plastic material with no internal structure, time dependent properties or strain hardening constitutive laws it is can be shown that the effect is not of non-equilibrium or polymer-specific origin.

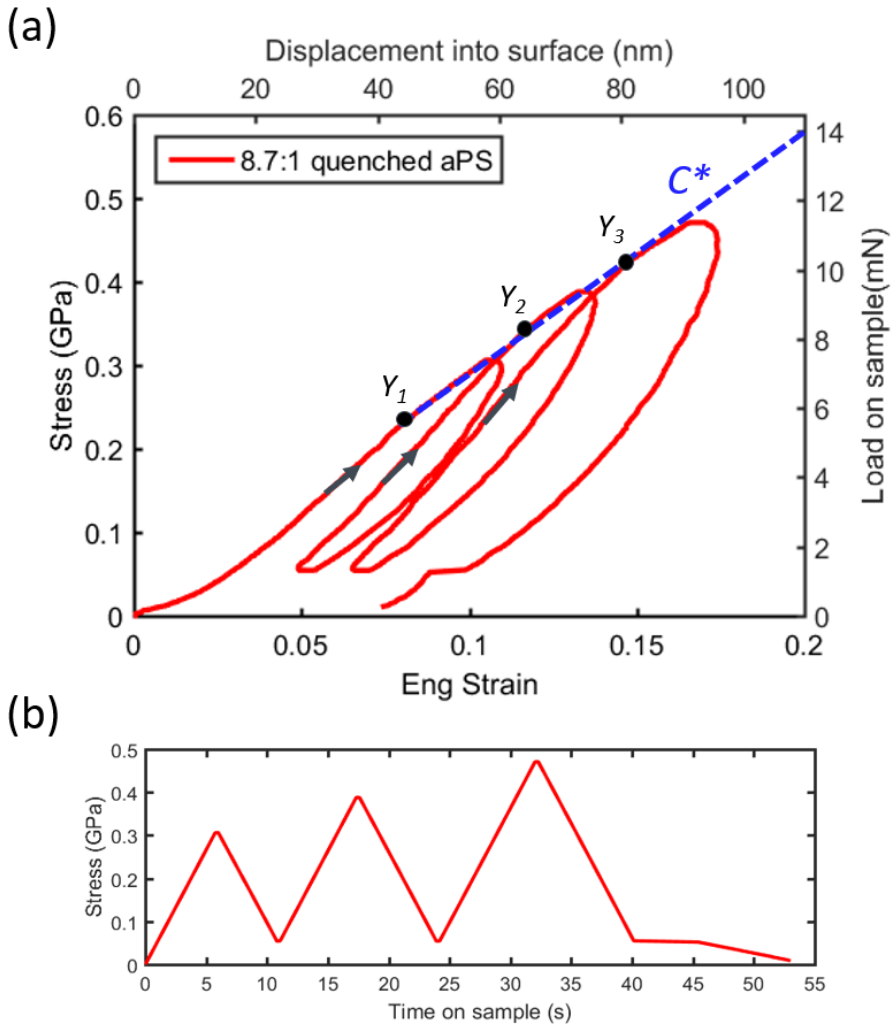

Figure 4.4.8 (a) Cyclic stress-strain curve for the 550 nm quenched polystyrene film. The sample is loaded into the confined plastic zone, before being unloaded and reloaded again. With each loading cycle Y_c is increased, with yield occurring when the curve intersects C^*. Grey arrows highlight loading sections. (b) Loading procedure used to produce the stress-strain curve shown in (a).

Finite element simulations of a cyclic loading pattern in a uniaxial strain geometry with rigid side walls and substrate are presented in figure 4.4.9. The material tested was the same elastic-plastic material as used in chapter three, with E = 3.0 GPa, Y_0 = 0.1 GPa, and ν = 0.33. No strain hardening parameter is included. The test geometry is shown in (a). The stress-strain response to a cyclic loading procedure equivalent to that employed in the experimental PS data of figure 4.4.8 is shown in (b). As (b) clearly shows, repeated loading into the confined plastic zone results in an increased yield stress, mimicking the behaviour of figure 4.4.8, aside from the lack of viscoelastic deformation during unload, which is responsible for the hysteresis loops in that figure.

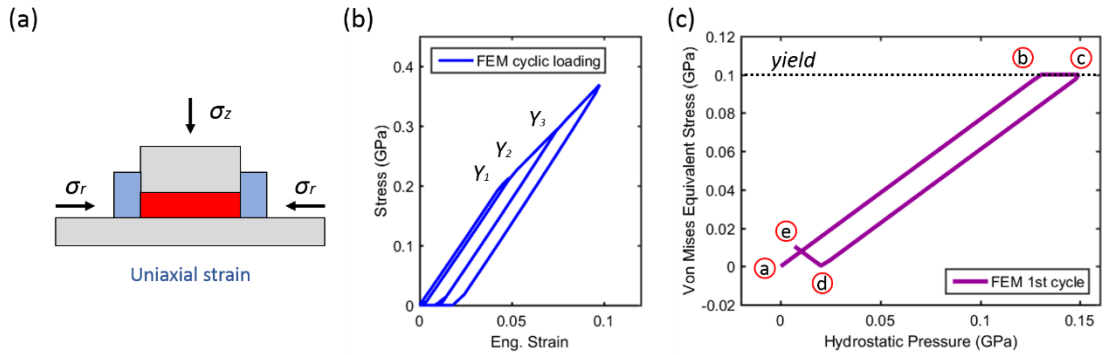

Figure 4.4.9 Finite element simulations of cyclic uniaxial strain loading of an elastic-perfectly plastic material. (a) Two-dimensional cross-sectional representation of the ideal (rigid confining sidewalls) uniaxial strain geometry simulated. (b) FEA simulated stress-strain curve for a loading cycle similar to that produced experimentally in figure 4.4.7 with three peak loads. Three yield distinct yield points are observed at Y_1, Y_2, and Y_3, when the stress-strain curve intersects the C^* slope. (c) Path of the material in pressure- shear stress space during the first load-unload cycle. During elastic loading/unloading the slope of the curve is described by the analytic solution given in equation 4.4.1 (c). Following yield at point b, the material is bound to the Von Mises yield surface and no further increase in shear is permitted, with further loading resulting in an increase in hydrostatic pressure. Stresses generated in this regime will be converted to stored residual shear stress upon the removal of load (point e).

The origin of the increase in Y_c can be understood by considering the material's path in pressure – shear stress space during the first loading cycle of 4.4.9 (b), where the material is loaded to $Y_c + 0.019$ GPa, before being unloaded to zero axial stress. This path is shown in (c). It is useful to restate the uniaxial strain elastic relationships between axial stress σ_{zz}, hydrostatic pressure P, and Von Mises equivalent stress σ_{VM} obtained in chapter three:

$$P = \frac{1}{3}\left(\frac{1+\nu}{1-\nu}\right)\sigma_{zz}, \qquad \sigma_{VM} = \left|\left(\frac{1-2\nu}{1-\nu}\right)\sigma_{zz}\right|, \qquad \sigma_{VM} = 2\frac{G}{K}P \qquad (4.4.2\ a, b, c)$$

Where ν, G, and K are Poisson's ratio, the shear modulus, and the bulk modulus respectively. The initial loading of the sample is elastic, following the path $a \rightarrow b$ in figure 4.4.9 (c), whose slope is given by equation 4.4.2 (c). This proceeds until yield, which occurs at $\sigma_{VM} = Y_0$ and $\sigma_{zz} = Y_c$. Further loading into the plastic regime by an additional applied stress $\Delta\sigma_{zz}$ results only in an increase of hydrostatic pressure P, as the shear stress σ_{VM} is fixed at the yield surface, in accordance with the Von Mises yield criterion[61]. This results in the path $b \rightarrow c$, leading the axial stress to increase to $\sigma_{zz} = Y_c + \Delta\sigma_{zz_{b\rightarrow c}}$ at point c. When the sample is then unloaded it responds elastically again

as it leaves the yield surface, following the path $c \rightarrow d$. At d, the shear stress in the material has been reduced to zero, however there is still an applied axial load of $\Delta\sigma_{zz_{b\rightarrow c}}$ and associated hydrostatic pressure. Further unloading to $\sigma_{zz} = 0$ therefore rather unintuitively results in an increase in shear stress, as σ_{VM} must always be positive. This leads to the path $d \rightarrow e$, where $\sigma_{zz} = 0$ at e, while P decreases and σ_{VM} increases, leaving significant residual stress within the sample. This loading pattern is more succinctly summarised in table 4.4.1.

Table 4.4.1 Evolution of the applied axial stress, hydrostratic pressure and Von Mises equivalent shear stress along the path a → b → c → d → e sketched out in figure 4.4.8 (c). Residual pressures and shear stress remain when the axial load is removed due to plastic loading. The analytical predictions for these residual stresses match well with the FEM results, as shown by the lower part of the table.

	σ_{zz}	P	σ_{VM}
a → b	Y_C	$\frac{1}{3}\left(\frac{1+\nu}{1-\nu}\right)Y_c$	Y_0
b → c	$Y_c + \Delta\sigma_{zz_{b\rightarrow c}}$	$\frac{1}{3}\left(\frac{1+\nu}{1-\nu}\right)Y_c + \Delta\sigma_{zz_{b\rightarrow c}}$	Y_0
c → d	$\Delta\sigma_{zz_{b\rightarrow c}}$	$\Delta\sigma_{zz_{b\rightarrow c}}$	0
d → e	0	$\left[1-\frac{1}{3}\left(\frac{1+\nu}{1-\nu}\right)\right]\Delta\sigma_{zz_{b\rightarrow c}}$	$\left(\frac{1-2\nu}{1-\nu}\right)\Delta\sigma_{zz_{b\rightarrow c}}$

FEM: $\Delta\sigma_{zz_{b\rightarrow c}} = 0.019\ GPa$

	Theory	FEM
P_{res} (GPa)	0.0066	0.0069
$\sigma_{VM_{res}}$ (GPa)	0.0096	0.0104

The magnitude of plastic loading $\Delta\sigma_{zz_{b\rightarrow c}}$ was 0.019 GPa for the first FEA load-unload cycle. This value was inserted into the derived equations for P and σ_{VM} in the last line of table 4.4.1 and used to calculate the expected residual hydrostatic and equivalent shear stresses in the system, which are shown in the blue insert of table 4.4.1. To test this interpretation, FEA mean values for P and σ_{VM} were extracted from each element of the compressed volume at point e of the loading cycle and are compared to the analytical solution value in the insert. The two solutions show good agreement., justifying the validity of this interpretation.

The crucial point is that when the material is reloaded from point e it must follow the path $e \rightarrow d \rightarrow c$ in figure 4.4.9 (c) to intersect the yield surface. This path is longer than the initial path $a \rightarrow b$ by $\Delta\sigma_{zz_{b\rightarrow c}}$, leading to the yield stress increasing by this amount.

This can be seen in 4.4.9 (b) where the second yield stress is $Y_2 = Y_1 + \Delta\sigma_{zz_{b\to c}}$. The residual stress imparted due to plastic loading therefore acts to effectively strengthen the material.

This residual stress arises from a change in the rate at which the radial stress σ_{rr} changes with the applied axial σ_{zz} when going from elastic to plastic deformation. When the material is elastically deformed, the rate at which σ_{rr} changes is given by:

$$\frac{d\sigma_{rr}}{d\sigma_{zz}} = \frac{\nu}{1\text{-}\nu} \tag{4.4.3}$$

In accordance with the relationships derived in chapter three. When loaded plastically however, the Von Mises yield criterion requires that:

$$\sigma_{VM} = \sqrt{\frac{1}{2}[(\sigma_{zz}\text{-}\sigma_{rr})^2 + (\sigma_{rr}\text{-}\sigma_{zz})^2 + (\sigma_{\theta\theta}\text{-}\sigma_{rr})^2]} = |\sigma_{zz}\text{-}\sigma_{rr}| \equiv Y_0 \tag{4.4.4}$$

To maintain σ_{VM} at Y_0 as the material travels along the path $b \rightarrow c$, the radial stress must scale exactly with the axial stress as the latter is increased, meaning:

$$\frac{d\sigma_{rr}}{d\sigma_{zz}} = 1 \tag{4.4.5}$$

This change is mathematically equivalent to Poisson's ratio becoming 0.5 once the material yields, as can be seen from equation 4.4.3. Figure 4.4.10 (a) plots σ_{rr} as a function of σ_{zz} during the FEA cyclic loading program, as evaluated by measuring the reaction forces on the punch and sidewalls respectively. It can be seen in the elastic region the slope is given by equation 4.4.3, where $\nu = 0.33$. In the plastic region the slope is given by equation 4.4.5. As the sample is unloaded elastically, σ_{rr} can only decrease in accordance with equation 4.4.3, meaning that there is an excess radial stress at $\sigma_{zz} = 0$, visible again in figure 4.4.10 (b) where the curve intersects the y-axis. This residual stress on the y-axis here is exactly equal to the residual Von Mises stress calculated in table 4.4.1 for the first load-unload cycle.

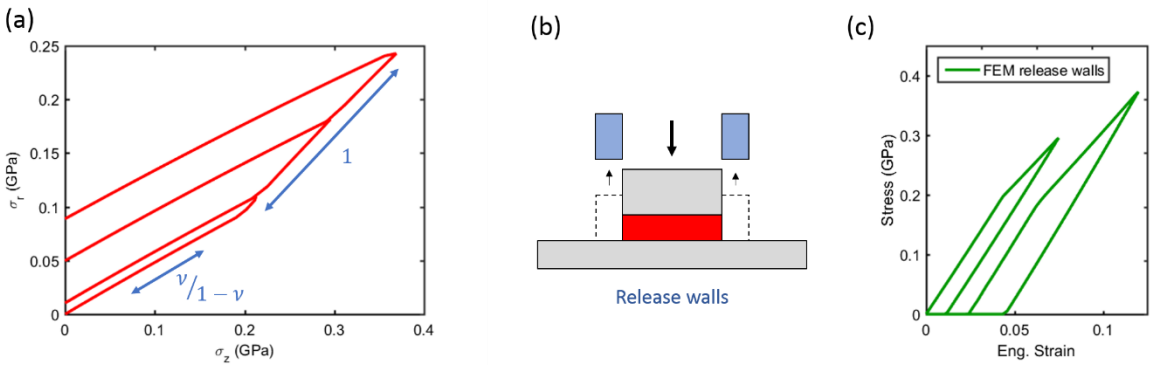

Figure 4.4.10 (a) Radial stress σ_{rr} as a function of applied axial stress σ_{zz} during the cyclic loading program of 4.4.8. Below yield, the slope is given by equation 4.4.2, while above yield it is one. After each loading cycle a residual strain Is imparted to the side wall. (b) Removal of the confining jacket to allow radial stress relaxation, before it is replaced, and the sample reloaded. (c) Stress-strain curves when the jacket is removed and replaced before reloading. Y_c reverts to its original value as the radial stress relaxes.

Effectively, this means that the residual radial stress exerted by the volume on the confining jacket acts to increase the yield stress of the material during subsequent loading cycles, despite there being no alteration of the material's intrinsic properties. In this sense, the increase in yield stress is a memory effect, as it determined by the previous deformation history of the sample. This memory effect is solely the result of plastic loading within the unique stress environment provided by the uniaxial strain geometry and closely approximated by the CLCT. To demonstrate that it is indeed the residual radial stress exerted on the confining jacket that increases Y_c, an FEA simulation was designed in which the sample was loaded past Y_c and then unloaded to $\sigma_{zz} = 0$. The jacket was then removed, as shown in 4.4.10 (b) to allow radial stress relaxation. The jacket was then effectively put back in place by introducing a boundary condition allowing for no radial motion at the sample's edge. The sample was then reloaded above Y_c. The stress-strain curve for this procedure is presented in 4.4.10 (c). It can be observed that the increase in Y_c has been erased by allowing the radial stress to relax, and the sample yields at the initial confined yield stress when loaded again.

The CLCT does not provide the perfect lateral confinement of a true uniaxial strain geometry. The surrounding film is non-rigid and the geometric aspect ratio is not infinite. Moreover, in the case of polymers it is viscoelastic and may relax under the stress imposed on it by the test volume. The close adherence of figure 4.4.8 to the behaviour of the elastic-plastic model of 4.4.9 (b) does indicate that at short timescales these imperfections do not greatly affect the stress memory effect, even at the relatively

modest aspect ratio of χ = 8.7. Regarding viscoelastic relaxation of the wall, it should be noted that the residual stresses imparted during plasticity are small in the context of inducing flow in polymers deep in the glassy state. For example, the first loading cycle of figure 4.4.8 results in a theoretical residual radial stress of 0.03 GPa, in accordance with equation 4.4.2 (b). This is comparable to the stresses imparted to polymer thin films during spin coating[62,63]. As such, significant relaxation over experimentally accessible timescales is likely to be small. This is highlighted in figure 4.4.11, which shows AFM profiles and images of an indent into a 203 nm polystyrene film with a 2140 nm punch to a stress of 0.494 GPa, taken one year apart. No significant change to topography is observed, indicating minimal stress relaxation. As such, the memory effect appears to be persistent over long time periods. To truly confirm this would require the material to be re-indented following a lengthy interval (days to weeks), however this had proven experimentally challenging due to a lack of adequate precision in lateral position and stage/sample drift.

In summary, an increase in the confined yield stress of a material loaded in the CLCT has been observed upon reloading. This is attributable to residual stresses imparted during plastic loading. While structural changes to the material may be present, these do not appear to be the dominant factor. In the next section, changes in relative mass density as a result of these residual stresses are studied via finite element and indentation experiments into PS.

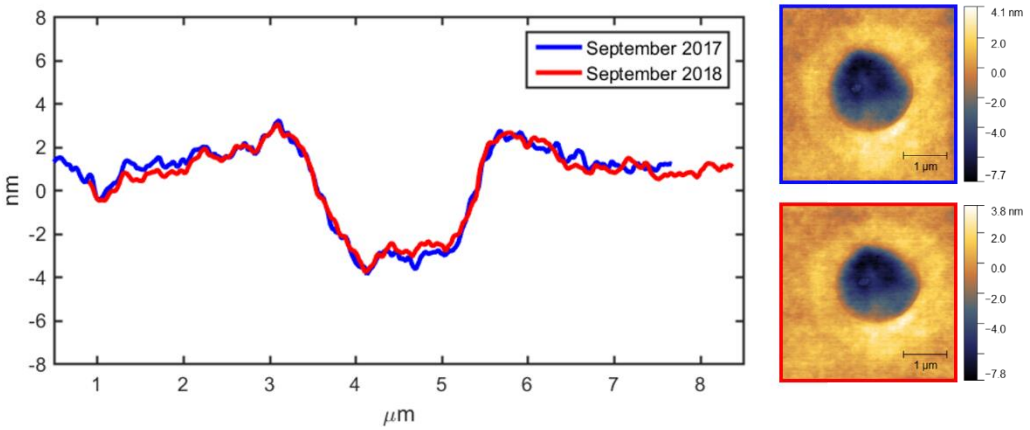

Figure 4.4.11 AFM profiles and images of an indent into 203 nm polystyrene with a 2140 nm diameter punch to a peak stress of 0.494 GPa. The blue curve/image was taken approximately one week after indentation, while the red curve was taken approximately one year later. No significant relaxation with time observed.

4.4.4 Densification of polystyrene films through confined yield

Implicit in the idea of compressive plastic deformation in the absence of volume preserving flow is a densification process wherein sample volume is reduced. In a uniaxial strain geometry, and by extension the confined compression layer test, this densification is enabled by the residual radial stress preventing the sample from returning to its initial volume. In this sense densification is elastic for simple materials; should the residual stress be removed, as in the FEA simulations of figure 4.4.10, the sample would return to its undeformed volume. As non-equilibrium materials however, polymers show a more nuanced response to stress and deformation. As section 4.2 outlined, stress and deformation can greatly influence polymer dynamics, including molecular mobility[19], free volume content[8], and ageing rates[54] in a non-straightforward manner. Previous studies have shown that deformation can lead to 'overageing' and an increase in density due to alterations of the potential energy landscape by the imposed stress[16]. In longitudinal tensile tests into a notched bulk metallic glass sample, *Schuh* was able to demonstrate densification through a diffusional free volume annihilation mechanism, resulting in a reduction in total sample volume[11]. In other geometries, post-yield deformation has been shown to result in sample volume increases through a mechanical rejuvenation process[45]. As such, for polymer films subjected to plastic deformation in the CLCT two competing non-volume preserving processes may be at work: The elastic densification mechanism, and a dynamic response of the non-equilibrium glass to yield.

Whether these two processes can be separated and quantified experimentally is a challenging question. The simplest means to do so it to treat their contributions to the overall density change of the volume beneath the punch as independent and additive:

$$\Delta\rho_{total} = \Delta\rho_{elastic} + \Delta\rho_{dynamic} \tag{4.4.6}$$

Where $\Delta\rho$ is the total density change, $\Delta\rho_{elastic}$ is the elastic contribution, and $\Delta\rho_{dynamic}$ is the change through dynamic response of the polymer to yield. This is obviously a simplification, as the residual elastic stress field will interact with polymer dynamics within the tested volume. The benefit of this approach is that it allows comparison of FEA simulations which can predict $\Delta\rho_{elastic}$ for simple elastic-plastic materials with experimental techniques such as STXM which can measure $\Delta\rho_{total}$ directly. Should $\Delta\rho_{total} \approx \Delta\rho_{total}$, it can be inferred that the elastic densification mechanism is the

dominant process. If a large discrepancy exists between the two quantities, then a more dynamic material response is at play.

In polymers, density may be controlled to a degree by the thermal history of the sample as outlined in section 4.4.2. Glasses formed from the melt state under high pressures may also have densities higher than those formed at ambient[17], however for both processes the change in volume is small, typically on the order of 1%[39]. Neither process is well suited to a directed patterning process, particularly at small scales where controlling thermal gradients is challenging. Regardless of the exact mechanism, the ability to selectively densify glassy thin films is an attractive prospect as it would enable tuning of density dependent properties such as mechanical strength, ion or gas permeability (batteries and containers), solubility and stability (pharmacetuicals) and conductivity (organic electronics) over microscale dimensions while maintaining chemical homogeneity. In this section mechanical densification of a 203 nm atactic polystyrene film on a Si_3N_4/Si substrate is achieved via the confined layer test and studied by AFM and STXM. First densification of an elastic-plastic material in a true uniaxial strain geometry is considered via FEA.

To study densification in a uniaxial strain geometry, FEA were performed with the same model as was used in the previous section. The material is again elastic-plastic with no internal mechanism for non-volume-persevering plasticity. As such, any permanent volume change can be attributed to the geometric stress memory effect outlined in the previous section. Simulations were performed in which the sample was loaded to a peak axial stress and then unloaded to zero. The volume of each element was tracked and summed to give the total volume change during loading/unloading. The initial volume was then divided by the final volume to give the relative densification. Peak stress was incremented to cover a range spanning both elastic and plastic behaviour. An example stress-strain curve loaded to above $2Y_c$, well into the plastic regime, is shown in figure 4.4.12 (a). Figure 4.4.12 (b) shows the relative final density as a function of peak stress, with the top axis being normalised to Y_c. As expected, below Y_c there is no volume change. For peak stresses covering the range $Y_c \leq \sigma \leq 2Y_c$ density increases linearly with increasing stress, achieving a maximum densification of 2.23% before plateauing at $2Y_c$.

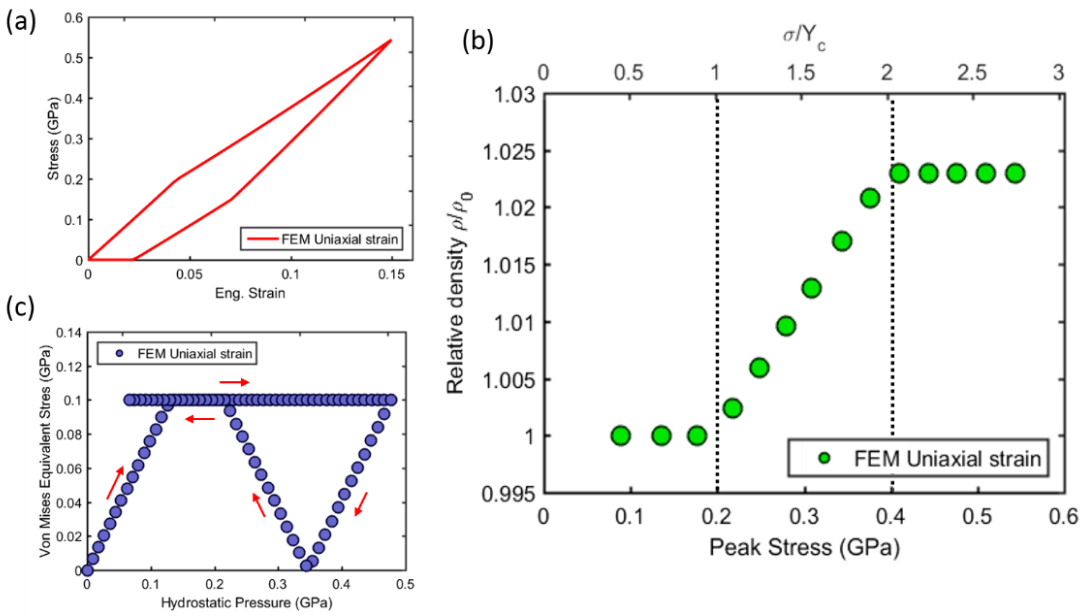

Figure 4.4.12 Densification of an elastic-plastic material in uniaxial strain. (a) Stress-strain curve for a FEA test to $2Y_c$ in the uniaxial strain geometry. (b) Final density as a function of peak strain via FEA simulations. A maximum density increase of 2.23% is achieved. (c) Pressure-stress path for the test considered in (a) Loading past $2Y_c$ results in the sample re-yielding on unload, limiting the amount degree of densification.

In understanding why the density plateaus at $2Y_c$ it is again useful to consider the loading path in pressure-shear stress space, plotted in (c) for the stress-strain curve shown in (b). Again, the curve follows the slope given by equation 4.4.2 (c) during elastic loading until it yields at $\sigma_{VM} = Y_0$ or $\sigma_{zz} = Y_c$. In the plastic zone σ_{rr} must increase by the same amount as σ_{zz} to keep the Von Mises stress constant at the yield surface. Therefore, when the sample is loaded to a total axial stress of $\sigma_{zz} = 2Y_c$ an excess radial stress of Y_c is generated during plastic loading, meaning the sample's pressure-shear path can re-intersect the yield surface during unload to $\sigma_{zz} = 0$. As this residual shear stress is responsible for elastically densifying the material, it follows that the density can no longer increase once σ_{VM} becomes fixed on the yield surface during unload. It should be stated however that the elastic-plastic model used in these simulations serves only as a first-order approximation to glassy mechanics and as such the existence of this second yield during unloading has not been encountered in the systems considered here experimentally. For example, the pressure sensitivity of polymer yield surfaces discussed in sections 3.2.3 and 3.4.3 would allow σ_{VM} to increase after yield and change the length of the elastic path during unload. As such $\sigma_{zz} = 2Y_c$ should not be treated as a limiting stress for densification via elastic residual stresses in more complex materials.

In the context of glassy systems, the 2.23% increase in density achieved above would represent an extreme alteration of the system. As a comparison, recent experiments performed in 20 million year old glassy amber (Tg = 136.2˚C) revealed a density increase of only 2.1% over the lifetime of the sample when compared to its density when heated above Tg and quenched[64]. This example serves only to highlight the degree of densification achieved via residual stress and not as a direct comparison between the two methods, which are very distinct from each other.

To determine if the residual stress induced densification effect is realisable and dominant in a real glassy material in the CLCT, an array of peak stress indents covering a range of 0.1 – 0.84 GPa was made into a 203 nm polystyrene film with a 2140 nm diameter flat punch ($\chi = 10.5$) for density measurements via scanning transmission x-ray microscopy (STXM). Indents were performed at a stress rate of 0.20 GPa/s, with yield occurring at approximately 0.32 GPa. As described in chapter two, STXM can determine relative material density based on simple Beer-Lambert absorption laws[65]. For a single component system, knowledge of the initial beam intensity I_0 and the sample thickness h_0, allows the absorption coefficient to be determined via the relation:

$$OD = -\log\left(\frac{I_T}{I_0}\right) = Ah_0 = \mu(E)\rho h_0 \qquad (4.4.7)$$

Where *OD* is the optical density, I_T is the transmitted x-ray intensity, and $\mu(E)$ mass attenuation coefficient. For the sample used here the silicon nitride substrate introduces a second component which must be removed prior to density measurement. This normalisation process is detailed in appendix 1. STXM scans were performed on the individual indents at a photon energy of 284.4 eV, corresponding to the primary 1s → C=C 1π* molecular orbital transition for carbon atoms in the polystyrene phenyl ring[66]. Secondary scans were also performed at higher energy peaks to check for energy specific effects. The polystyrene *OD* spectrum is shown in figure 4.4.13 (a), with the measurement peaks identified and the corresponding orbital transitions listed in (b). The polystyrene *OD* spectrum is converted to an absorption spectrum via normalisation by the known mean film thickness, which is obtained by AFM.

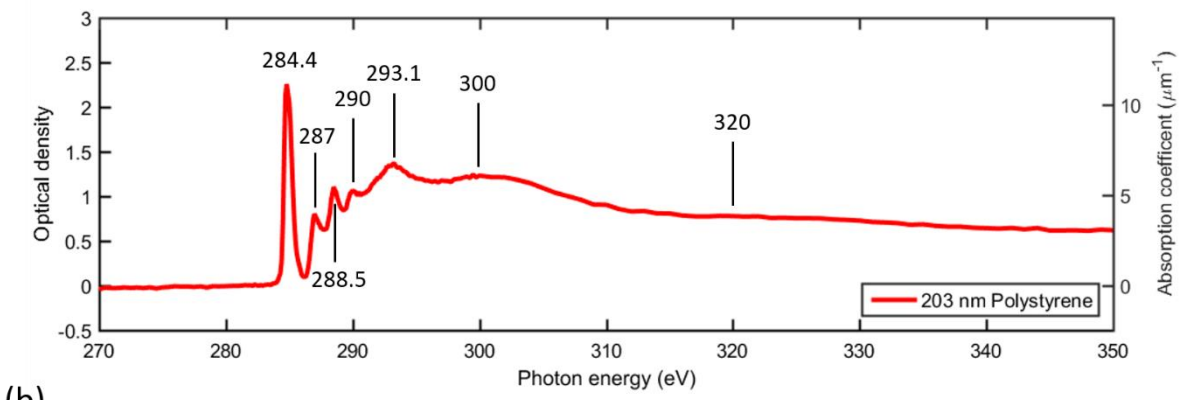

(b)

Excitation energy (eV)	Assigned final orbital (1s → x)
284.4	C=C $1\pi^*$
287	C-H*
288.5	C=C $2\pi^*$
290	Ionisation threshold
293.1	C-C σ^*
300	C=C σ^*
320	N/A

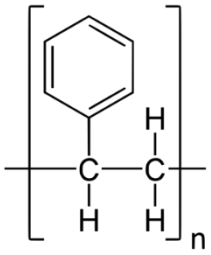

(c)

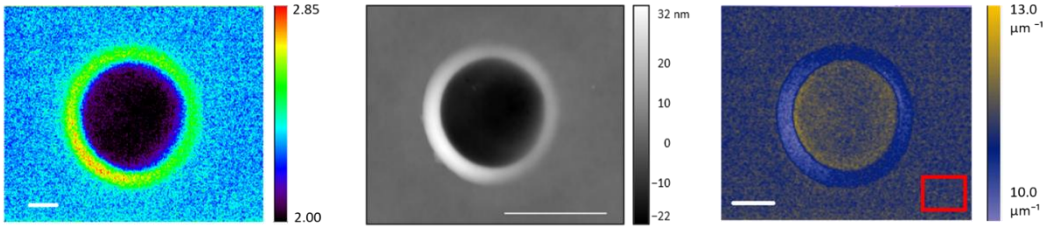

Figure 4.4.13 (a) Background corrected optical density and absorption coefficient spectra in the soft x-ray regime for the 203 nm polystyrene film studied by STXM. The effect of the Si3N4 supporting window was subtracted through nuclear scattering calculations (Appendix 1). STXM measurements on indented film were primarily performed out at the 284.4 eV absorption peak, however secondary measurements were performed on some indents at the other highlighted values. (b) Molecular orbital destination of the promoted 1s electron for the peaks identified in (a). The E = 320 eV corresponds to an off-resonance measurement. Values are reported from [65]. A representation of the polystyrene base unit accompanies the table. (c) Processes for obtaining relative density maps. An optical density map is obtained via STXM rastering of the indented region (left). This is then divided by a previously obtained AFM height map (centre) to produce an absorption coefficient map (right). By diving this image by the mean absorption value away from the indent, highlighted by the red box, a density map is produced in accordance with equation 4.4.6.

The process for obtaining relative density maps is shown in figure 4.4.13 (c) The first image shows an OD map of an indent at σ = 0.61 GPa, which is obtained via the normalisation process of appendix 1. This is converted to an absorption map by dividing it by an AFM thickness profile in accordance with equation 4.4.6. The mean absorption

over a 0.5 x 0.5 μm area away from the indent (highlighted in red) is then measured and the image normalised to this value. This yields a density map as:

$$\frac{A}{A_0} = \frac{\mu(E)\rho}{\mu(E)\rho_0} = \frac{\rho}{\rho_0} \tag{4.4.8}$$

Figure 4.4.14 (a) plots the mean relative density within the indented volume as a function of peak stress. The locations of the indents on the characteristic stress-strain curve are shown in (b). No readings were possible before approximately 0.42 GPa due to the low contrast in the STXM images. A peak density increase of 3.42% is recorded at a stress of 0.84 GPa. Interestingly, densification appears to proceed even after extrusion, where conventional flow resumes. To better understand this process a loading procedure was designed to decouple extrusion from any remaining uniaxial strain behaviour which may be masked by the large flow strains. The previously used 550 nm $\chi = 8.7$ system was loaded at a rate of 0.027 GPa/s under the stopping condition:

$$\frac{d\sigma}{dt} = \begin{cases} 0.027\ \text{GPa/s}, & \frac{dh}{dt} < 5\ \text{nm/s} \\ 0, & \frac{dh}{dt} > 5\ \text{nm/s} \end{cases} \tag{4.4.9}$$

As such, flow is allowed to fully proceed before loading is resumed. The results of this test are compared with the standard loading procedure in figure 4.4.14 (c). In the case of the modified protocol a second linear region emerges after extrusion, which is hidden in the standard loading case. This indicates that densification via the uniaxial strain mechanism may continue after flow as at least a portion of the volume beneath the punch is subjected to uniaxial strain conditions, therefore explaining the high stress results of 4.4.14 (a).

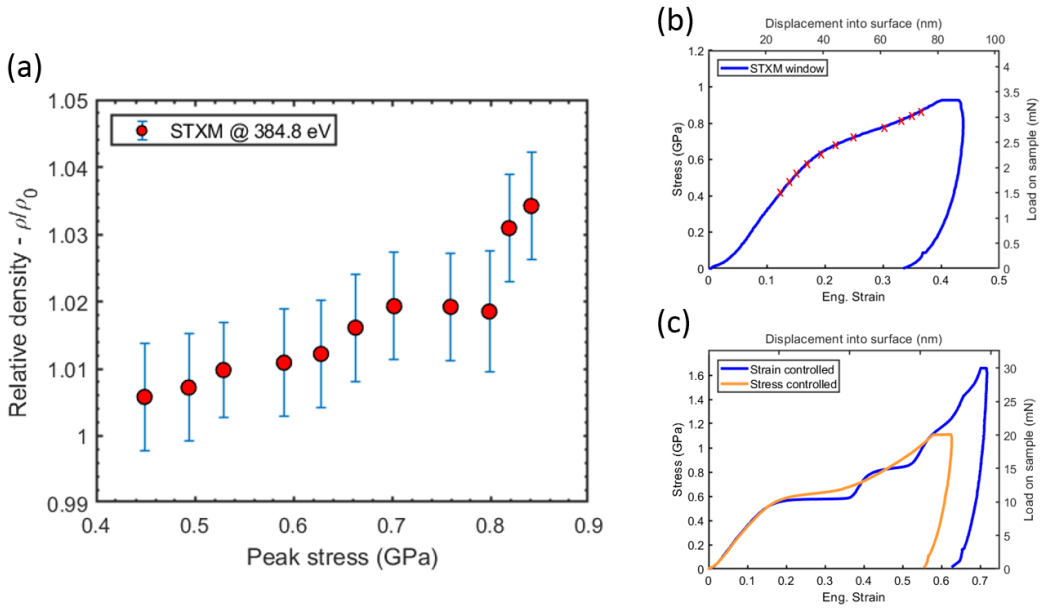

Figure 4.4.14 (a) Relative density as a function of peak indentation stress as measured via STXM at *E* = 384.8 eV. A peak density increase of 3.42% is achieved at 0.84 GPa. (b) Location of the peak stress density measurements of (a) on the characteristic confined layer stress-strain curve. (c) Comparison of the standard confined layer stress-strain curve (stress controlled) with the decoupled flow curve. Further linear behaviour is masked in the standard case by extrusion.

Figure 4.4.15 examines the beam energy dependence of the STXM measurements for a single indent to 0.53 GPa. (a) Shows *OD* maps at the 7 peaks identified in figure 4.4.14 (a), as well as a pre-absorption edge scan at 283 eV. Unsurprisingly, there are few detectable features in this image. For higher energies the degree of contract is dependent on the height of the absorption peak. Low contrast images at small peaks such as at 300 and 320 eV lead to high standard deviations when converted to relative densities as in figure 4.4.15 (b). Density values recorded at these higher energy peaks match closely to the primary 284.8 eV measurement, indicating no strong energy specific effects, therefore validating the general method. Further, as the different absorption peaks correspond to core electron jumps to different molecular orbitals, sampling at several peaks can indicate where there are any chain alignment or orientation effects induced. For example, if a markedly different signal was observed when electron are promoted to a main chain orbital as opposed to a side group orbital this could indicate potential phenyl ring interactions between side groups on different chains[67]. In this case no such phenomenon is reported, indicating the material remains amorphous.

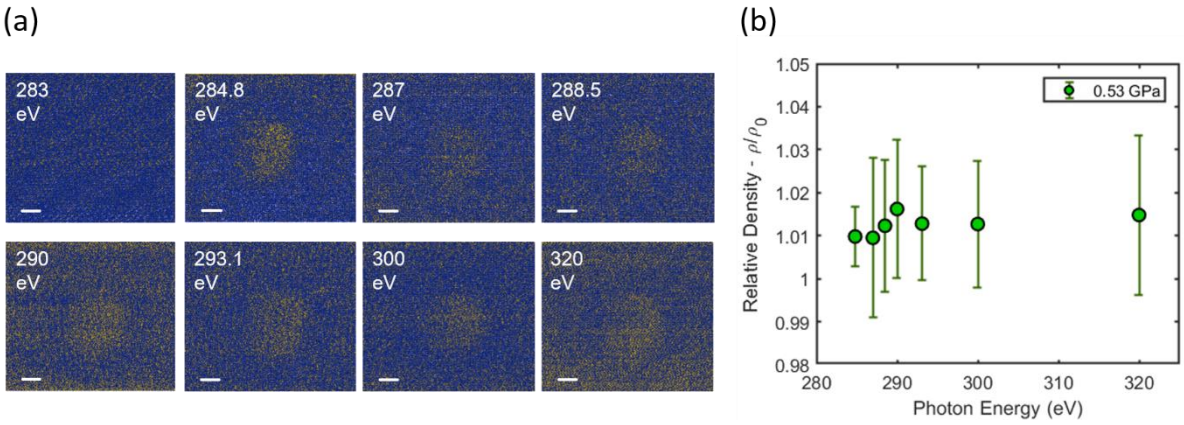

Figure 4.4.15 (a) Energy dependency of STXM readings. The images show the optical density (OD) signal for a single indent to 0.53 GPa. The indented region is clearly visible as the yellow region in the centre, save for the *E* = 283 eV image. This is as this energy corresponds to the pre-absorption peak region, where the sample is effectively x-ray transparent and there is minimal interaction between beam and sample(OD ≈ 0, as can be seen in figure 4.4.12) No energy-specific structures/patterns or anisotropy are visible, indicating that the indented region remains amorphous following densification. Image contrast is dependent on the relative strength of the specific absorption peak, and as such greatest contrast is observed for the 284.8 eV image. (b) Relative density plotted as a function of STXM scan energy for the 0.53 GPa indent. No significant energy dependency is observed, with all measured densities falling within a 1 – 1.7% range. Low contrast (poor absorption) images yield larger errors as the measurement compares relative density of material within and without the indented region. For reference, the 283 – 320 eV energy range utilised here corresponds to a wavelength range of 4.38 – 3.87 nm.

In summary, it has been demonstrated that the confined layer test can used to achieve densities far greater than those encountered in glasses by physical ageing. The effect of this densification process on free volume sensitive properties such as conductivity and gas permeability remains to be investigated, however there is the potential for a deterministic free volume engineering process that would be compatible with already mature technologies such as roll-to-roll imprint.

4.5 Conclusions

In this chapter the confined layer compression test introduced in chapter three was used to study specific aspects of the non-equilibrium thermomechanical response of glassy polystyrene films. Attention was given to the effect of structural recovery and yield on subsequent mechanical response, and the impact of residual stresses due to plastic loading on the yield stress and density of the material.

First, the influence of thermal history on the characteristic confined layer stress-strain curve was studied. 550 nm (χ = 8.7) and 670 nm χ = (7.2) polystyrene films were

prepared via two thermal pathways: A rapid "quench" to room temperature from above T_g, and a slow ramp to 75˚C, following by an "annealing" step. For both thicknesses the annealed samples displayed higher confined yield and flow stresses as well as a higher plastic modulus, in accordance with standard physical ageing behaviour. A mechanical rejuvenation event was observed at high stresses in the extrusion limit, where the stress-strain curves of all samples became history independent.

The influence of confined yield on the viscoelastic properties of the films was studied via creep compliance tests at constant stresses. It was found that yield corresponded to a significant increase in the compliance of the 550 nm films, indicative of an increase in segmental mobility despite the lack of lateral flow. This was quantified via analysis using a two element Kelvin-Voigt material model. It was determined that the short retardation time τ_1 increased gradually with increasing creep load, most likely due to increased hydrostatic pressure inhibiting molecular rearrangement. The longer retardation time τ_2 fell dramatically at the confined yield stress however, indicating that this yield event is associated with significantly easier segmental motion despite the lack of volume preserving shear flow. This is indicative of a free volume annihilation process.

Cyclic loading tests into the 550 nm quenched film revealed that loading the sample to within the plastic regime raised Y_c on the next cycle. Further, the sample would yield when the stress-strain curve intersected the confined plastic slope C^*. Finite element simulations of true uniaxial strain deformation into an elastic perfectly plastic material showed that this was not the result of strain hardening, but rather a geometrically induced stress memory effect. Due to excess radial stresses produced during plastic loading the sample must follow a longer stress path to intersect the yield surface on reloading, which manifests as an effective hardening of the material. It is believed that this is the first demonstration of a stress memory phenomenon with precision geometry in elastic-plastic films.

Finally, it was shown via finite element simulation that the residual stresses introduced during plastic deformation lead to a significant densification effect. STXM studies of flat punch indentation into a 203 nm polystyrene film with a 2140 nm diameter punch revealed that this densification phenomenon is experimentally achievable via the confined layer test. A maximum density increase of 3.42% was achieved at an applied stress of 0.84 GPa, greatly surpassing increases brought about by structural recovery in other glassy systems aged over millions of years. This

potentially opens the way for a new form of mechanical lithography in free volume materials.

Bibliography

1. McKenna, G. B. Mechanical rejuvenation in polymer glasses: factor fallacy ? *J. Phys. Condens. Matter* **15**, S737 (2003).

2. Tant, M. R. & Wilkes, G. L. Physical aging studies of semicrystalline poly(ethylene terephthalate). *J. Appl. Polym. Sci.* **26**, 2813–2825 (1981).

3. Legrand, D. G. Crazing, yielding, and fracture of polymers. I. Ductile brittle transition in polycarbonate. *J. Appl. Polym. Sci.* **13**, 2129–2147 (1969).

4. Golden, J. H., Hammant, B. L. & Hazell, E. A. The effect of thermal pretreatment on the strength of polycarbonate. *J. Appl. Polym. Sci.* **11**, 1571–1579 (1967).

5. Wohlfahrt-Mehrens, M. *et al.* New materials for supercapacitors. *J. Power Sources* **105**, 182–188 (2002).

6. Struik, L. C. E. *Physical aging in amorphous polymers and other materials*. (1977).

7. Santore, M. M., Duran, R. S. & McKenna, G. B. Volume recovery in epoxy glasses subjected to torsional deformations: the question of rejuvenation. *Polymer (Guildf).* **32**, 2377–2381 (1991).

8. Riggleman, R. A., Lee, H. N., Ediger, M. D. & De Pablo, J. J. Free volume and finite-size effects in a polymer glass under stress. *Phys. Rev. Lett.* **99**, 1–4 (2007).

9. Kim, J. W., Medvedev, G. A. & Caruthers, J. M. Nonlinear stress relaxation in an epoxy glass and its relationship to deformation induced mobility. *Polymer (Guildf).* **54**, 3949–3960 (2013).

10. Kokou D. Dorkenoo, K. D. & Pfromm, P. H. Accelerated Physical Aging of Thin Poly[1-(trimethylsilyl)-1-propyne] Films. (2000). doi:10.1021/MA9921145

11. Wang, Z. T., Pan, J., Li, Y. & Schuh, C. A. Densification and Strain Hardening of a Metallic Glass under Tension at Room Temperature. *Phys. Rev. Lett.* **111**, 135504 (2013).

12. Rottler, J. & Robbins, M. O. Unified description of aging and rate effects in yield of glassy solids. *Phys. Rev. Lett.* **95**, 2–5 (2005).

13. Bending, B., Christison, K., Ricci, J. & Ediger, M. D. Measurement of segmental mobility during constant strain rate deformation of a poly(methyl methacrylate) glass. *Macromolecules* **47**, 800–806 (2014).

14. Wallace, M. L. & Joós, B. Shear-Induced Overaging in a Polymer Glass. *Phys. Rev. Lett.* **96**, 025501 (2006).

15. Viasnoff, V. & Lequeux, F. Rejuvenation and Overaging in a Colloidal Glass under Shear. *Phys. Rev. Lett.* **89**, 065701 (2002).

16. Colucci, D. M., O'Connell, P. A. & McKenna, G. B. Stress relaxation experiments in polycarbonate: A comparison of volume changes for two commercial grades. *Polym. Eng. Sci.* **37**, 1469–1474 (1997).

17. Gray, L. A. G. & Roth, C. B. Stability of polymer glasses vitrified under stress. *Soft Matter* **10**, 1572 (2014).

18. Roth, C. B. *Polymer glasses*. (CRC Press, 2016).

19. Lacks, D. J. & Osborne, M. J. Energy landscape picture of overaging and rejuvenation in a sheared glass. *Phys. Rev. Lett.* **93**, 1–4 (2004).

20. Eyring, H. Viscosity, Plasticity, and Diffusion as Examples of Absolute Reaction Rates. *J. Chem. Phys.* **4**, 283–291 (1936).

21. Chen, K. & Schweizer, K. S. Theory of aging, rejuvenation, and the nonequilibrium steady state in deformed polymer glasses. *Phys. Rev. E - Stat. Nonlinear, Soft Matter Phys.* **82**, (2010).

22. Chen, K. & Schweizer, K. S. Theory of yielding, strain softening, and steady plastic flow in polymer glasses under constant strain rate deformation. *Macromolecules* **44**, 3988–4000 (2011).

23. Lyulin, A. V. & Michels, M. A. J. Time Scales and Mechanisms of Relaxation in the Energy Landscape of Polymer Glass under Deformation: Direct Atomistic Modeling. *Phys. Rev. Lett.* **99**, 085504 (2007).

24. Warren, M. & Rottler, J. Mechanical rejuvenation and overaging in the soft glassy rheology model. *Phys. Rev. E* **78**, 041502 (2008).

25. Warren, M. & Rottler, J. Deformation-induced accelerated dynamics in polymer glasses. *J. Chem. Phys.* **133**, 164513 (2010).

26. Smessaert, A. & Rottler, J. Recovery of Polymer Glasses from Mechanical Perturbation. *Macromolecules* **45**, 2928–2935 (2012).

27. Chung, Y. G. & Lacks, D. J. Atomic Mobility in a Polymer Glass after Shear and Thermal Cycles. *J. Phys. Chem. B* **116**, 14201–14205 (2012).

28. Lee, A. & McKenna, G. B. The physical ageing response of an epoxy glass subjected to large stresses. *Polymer (Guildf).* **31**, 423–430 (1990).

29. Xie, L. *et al.* Positronium Formation as a Probe of Polymer Surfaces and Thin Films. *Phys. Rev. Lett.* **74**, 4947–4950 (1995).

30. Ediger, M. D., Lee, H. N., Paeng, K. & Swallen, S. F. Dye reorientation as a probe of stress-induced mobility in polymer glasses. *J. Chem. Phys.* **128**, (2008).

31. Lee, H.-N., Paeng, K., Swallen, S. F. & Ediger, M. D. Direct measurement of molecular mobility in actively deformed polymer glasses. *Science* **323**, 231–4 (2009).

32. Lee, H. N. & Ediger, M. D. Interaction between physical aging, deformation, and segmental mobility in poly(methyl methacrylate) glasses. *J. Chem. Phys.* **133**, (2010).

33. Paeng, K., Swallen, S. F. & Ediger, M. D. Direct measurement of molecular motion in freestanding polystyrene thin films. *J. Am. Chem. Soc.* **133**, 8444–8447 (2011).

34. Kim, J. W., Medvedev, G. A. & Caruthers, J. M. Nonlinear stress relaxation in an epoxy glass and its relationship to deformation induced mobility. *Polymer (Guildf).* **54**, 3949–3960 (2013).

35. Ma, Z. & Ravi-Chandar, K. Confined compression: A stable homogeneous deformation for constitutive characterization. *Exp. Mech.* **40**, 38–45 (2000).

36. Ravi-Chandar, K. & Ma, Z. Inelastic Deformation in Polymers under Multiaxial Compression. *Mech. Time-Dependent Mater.* **4**, 333–357 (2000).

37. Kim, J. W., Medvedev, G. A. & Caruthers, J. M. Mobility evolution during tri-axial deformation of a glassy polymer. *Polymer (Guildf).* **55**, 1570–1573 (2014).

38. Kim, J. W., Medvedev, G. A. & Caruthers, J. M. Observation of yield in triaxial deformation of glassy polymers. *Polymer (Guildf).* **54**, 2821–2833 (2013).

39. Kimmel, R. M. & Uhlmann, D. R. Effects of High Pressure on Amorphous Polymers: Densification of Polymethyl Methacrylate. *J. Appl. Phys.* **41**, 2917–2927 (1970).

40. Hitchcock, A. P. aXis2000 - Analysis of X-ray Images and Spectra. (2018). Available at: http://unicorn.mcmaster.ca/axis/aXis2000-windows-pre-IDL8.3.html.

41. Hutchinson, J. M. Physical aging of polymers. *Prog. Polym. Sci.* **20**, 703–760 (1995).

42. Argon, A. S. *The physics of deformation and fracture of polymers*. (Cambridge University Press, 2013).

43. Schift, H., Heyderman, L. J. & Sotomayor Torres, C. M. Nanorheology. in *Alternative Lithography* (2004).

44. Ortiz, M. Plastic Yielding as a Phase Transition. *J. Appl. Mech.* **66**, 289 (1999).

45. McKenna, G. B. Mechanical rejuvenation in polymer glasses: fact or fallacy? *J. Phys. Condens. Matter* **15**, S737–S763 (2003).

46. Senden, D. J. A., van Dommelen, J. A. W. & Govaert, L. E. Strain hardening and its relation to Bauschinger effects in oriented polymers. *J. Polym. Sci. Part B Polym. Phys.* **48**, 1483–1494 (2010).

47. Van Melick, H. G. H., Govaert, L. E. & Meijer, H. E. H. On the origin of strain hardening in glassy polymers. *Polymer (Guildf).* **44**, 2493–2502 (2003).

48. Ricci, J., Bennin, T. & Ediger, M. Aging in Polymer Glasses: A Comparison of Optical and Mechanical Measurements of Segmental Dynamics. *APS March Meet. 2017, Abstr. id. B18.012* (2017).

49. Medvedev, G. A., Kim, J. W. & Caruthers, J. M. Prediction of the relationship between the rate of deformation and the rate of stress relaxation in glassy polymers. *Polymer (Guildf).* **54**, 6599–6607 (2013).

50. Rowland, H. D., King, W. P., Pethica, J. B. & Cross, G. L. W. Molecular Confinement Accelerates Deformation of Entangled Polymers During Squeeze Flow. *Science* 720–724 (2008).

51. Ferry, J. D. *Viscoelastic properties of polymers*. (Wiley, 1980).

52. Struik, L. C. E. Some problems in the non-linear viscoelasticity of amorphous glassy polymers. *J. Non-Cryst. Sol.* **131–133**, 395–407 (1991).

53. van Breemen, L. C. A., Engels, T. A. P., Klompen, E. T. J., Senden, D. J. A. & Govaert, L. E. Rate- and temperature-dependent strain softening in solid polymers. *J. Polym. Sci. Part B Polym. Phys.* **50**, 1757–1771 (2012).

54. Liu, A. Y.-H. & Rottler, J. Aging under stress in polymer glasses. *Soft Matter* **6**, 4858 (2010).

55. Caddell, R. M., Raghava, R. S. & Atkins, A. G. A yield criterion for anisotropic and pressure dependent solids such as oriented polymers. *J. Mater. Sci.* **8**, 1641–1646 (1973).

56. Hutchinson, J. M. Relaxation processes and physical aging. in *The Physics of Glassy Polymers* 85–153 (Springer Netherlands, 1997). doi:10.1007/978-94-011-5850-3_3

57. Taljat, B. & Pharr, G. M. Development of pile-up during spherical indentation of elastic–plastic solids. *Int. J. Solids Struct.* **41**, 3891–3904 (2004).

58. Bolshakov, A. & Pharr, G. M. Influences of pileup on the measurement of mechanical properties by load and depth sensing indentation techniques. *J. Mater. Res.* **13**, 1049–1058 (1998).

59. Herbert, E. ., Pharr, G. ., Oliver, W. ., Lucas, B. . & Hay, J. . On the measurement of stress–strain curves by spherical indentation. *Thin Solid Films* **398–399**, 331–335 (2001).

60. Dreistadt, C., Bonnet, A.-S., Chevrier, P. & Lipinski, P. Experimental study of the polycarbonate behaviour during complex loadings and comparison with the Boyce, Parks and Argon model predictions. *Mater. Des.* **30**, 3126–3140 (2009).

61. Shames, I. H. & Cozzarelli, F. A. *Elastic and inelastic stress analysis*. (Taylor and Francis, 1997).

62. Chung, J. Y., Chastek, T. Q., Fasolka, M. J., Ro, H. W. & Stafford, C. M. Quantifying Residual Stress in Nanoscale Thin Polymer Films *via* Surface Wrinkling. *ACS Nano* **3**, 844–852 (2009).

63. Thomas, K. R. & Steiner, U. Direct stress measurements in thin polymer films. *Soft Matter* **7**, 7839 (2011).

64. McKenna, G. B. & Simon, S. L. *50th Anniversary Perspective* : Challenges in the Dynamics and Kinetics of Glass-Forming Polymers. *Macromolecules* **50**, 6333–6361 (2017).

65. Watts, B., Warnicke, P., Pilet, N. & Raabe, J. Nanoscale measurement of the absolute mass density of polymers. *Phys. status solidi* **212**, 518–522 (2015).

66. Kikuma, J. & Tonner, B. P. XANES spectra of a variety of widely used organic polymers at the C K-edge. *J. Electron Spectros. Relat. Phenomena* **82**, 53–60 (1996).

67. Watts, B., Schuettfort, T. & McNeill, C. R. Mapping of Domain Orientation and Molecular Order in Polycrystalline Semiconducting Polymer Films with Soft X-Ray Microscopy. *Adv. Funct. Mater.* **21**, 1122–1131 (2011).

Chapter 5:
Large Area sub-T_g Thermal Nanoimprint via Small Amplitude Oscillatory Shear Forming

Abstract

Small amplitude oscillatory shear forming is a technique that improves the performance of nanoimprint lithography by amplifying shear flow in narrow, squeezed geometries created during melt molding or glass forming of supported polymer films. To date, the technique has only been demonstrated for single micron-scale contacts, representative of single features on wafer-scale nanoimprint stamps. In this chapter, scaling up of small amplitude shear forming to realize micro and nanometre feature patterning of thermoplastic polymer films over macroscopic centimetre square areas at temperatures in the vicinity of, and below the glass transition is achieved. By the use of a small amplitude (typically 5-10% the smallest pattern feature dimension) lateral oscillatory shear strain superposed during the normal motion of a nanoimprint mold, high fidelity pattern replication in PMMA is achieved at temperatures as low as 35° C below its glass transition temperature. It is shown that the technique is effective for both bulk polymer samples and supported thin films, with samples as thick as 50 µm and as films as thin as 40 nm being successfully patterned. In 800 nm PMMA films, a 61.5% reduction in the residual layer thickness at 100° C was achieved by the addition of shear strain. Enhanced pattern fidelity is demonstrated using line-pattern imprint molds of 4 µm pitch and 35 nm relief, as well as an assortment of other geometries. No feature distortion is observed due to the oscillatory motion of the mold. The technique is shown to be particularly advantageous for large scale features and cavities, as well as high aspect ratio geometries, as the lateral motion of the mold features acts to pump material into areas where stresses generated by the normal motion of the mold will not suffice.

5.1 Introduction

Since its development in the late 1990's, nanoimprint lithography (NIL) has established itself as an effective technology for the fabrication of micro and nanoscale patterns at the surface of bulk polymers and supported thin films[1–4]. The advent of roll to roll technologies has enabled the production of patterned surfaces at rates of up to several m^2/s, allowing for industrial scaling of the technology[5–7]. Applications of nanoimprint can be found in a diverse range of fields, including tissue engineering[8,9], memory applications[10], tailored hydrophobic surfaces[11], and organic solar cells[12]. Despite considerable refinement of imprint technology[13–15] and advancements in theoretical understanding[16–19], several key limitations have slowed nanoimprint's adoption as a truly ubiquitous patterning technique. Current NIL processes are limited to thermoplastic or UV-curable resists. In the case of thermal nanoimprint, the resist material must be heated to well above T_g, exploiting the orders of magnitude decreases in shear modulus and forming stress when the polymer transitions from the glassy to rubbery and liquid-like states[20,21]. As was outlined in chapter 2, thermal nanoimprint places rather strenuous demands on both the resist and mold, most of which are result from thermal cycling. Thermal expansion mismatch between mold, resist, and supporting material (approximately one order of magnitude for a thermoplastic polymer and silicon mold), pressure and heat gradients, and frictional wear at feature side walls during unloading may all lead to imperfect pattern replication. Adhesion forces between mold and resist have been shown to increase above T_g[22] and eventually lead to pattern degradation as the mold features become clogged or distorted. This is typically combatted by deposition of a low surface energy anti-stick coating[13], whose lifetime may be limited.

Thermal nanoimprint is typically carried out at temperatures exceeding T_g + 80 °C[23], for which the shear strength and viscosity of a typical thermoplastic will be sufficiently diminished to allow rapid forming. This is demonstrated in figure 5.1.1 (a), which shows the storage modulus as a function of temperature above and below the glass transitions for PMMA and PLGA. In both cases the modulus is observed to drop by approximately 3 orders of magnitude over a 30° range. Further decrease occurs once the rubbery regime is passed through at approximately T_g + 50°. A similar trend in yield stress was observed by *Cross* and *Rowland*[24] in their variable temperature flat punch experiments into polystyrene, presented in 5.1.1 (b). At T_g + 25° the forming stress is no longer detectable and resistance to deformation is minimal up to very large strains. Both phenomena derive from the rapid increase in segmental mobility as the polymer transitions from a non-

equilibrium glass, through the supercooled melt state, and into the equilibrium liquid phase[25].

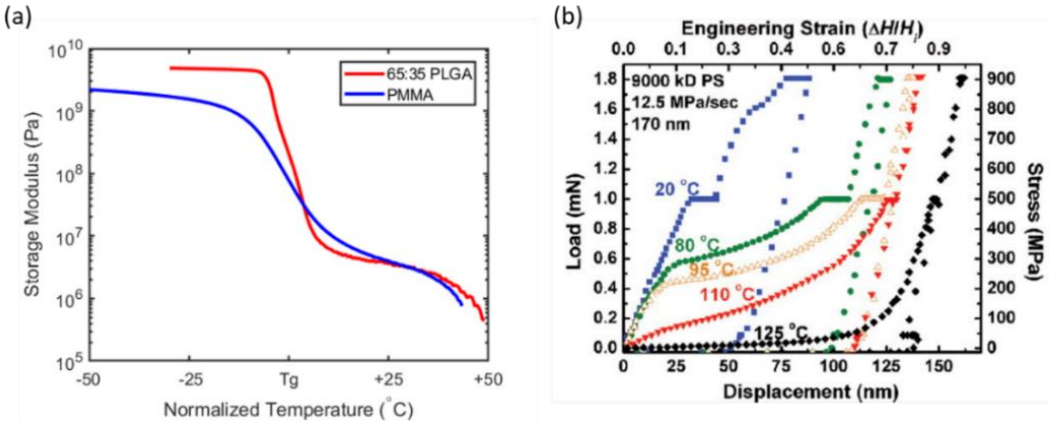

Figure 5.1.1 (a) Dynamic mechanical analysis scans of storage modulus (*G'*) versus normalized temperature for two thermoplastics PMMA & PLGA. Both show a three order of magnitude decrease in in *G'* after T_g. (b) Nanoimprint forming stress as a function of temperature for 170 nm PS. Reproduced with permission from [17].

To avoid thermal cycling, and the accompanying drawbacks outlined above, conventional forming techniques below T_g such as embossing must rely on extreme normal loads on the order of several hundred MPa to generate stresses exceeding the forming stress[26]. Such loads will generate significant distortion of the imprint mold and support frame[27], particularly in high aspect ratio geometries commonly encountered in thermal nanoimprint, where minimization of the residual layer thickness is often highly sought. This will necessitate greater tool integrity and high stiffness mold materials such as diamond or diamond-like carbon, which may be incompatible with traditional lithographic fabrication techniques[28]. An alternative approach is to augment the normal load with a small lateral oscillatory motion applied to the mold, a technique termed small amplitude oscillatory shear forming[29] (SAOSF), originally realised by *Cross* and *Pethica*. Within their experiments, a rigid mold was mounted to a nanoindenter and brought into contact with a supported 950 nm glassy polystyrene film. A normal load was applied, and inelastic deformation proceeded until constraint by material surrounding the contact area, friction at the substrate and punch boundaries, and the intrinsic strength of the residual layer prevented further plasticity. Shear strain oscillation was then injected into this system via a shear piezo element on which the sample was mounted. The addition of shear displacements on the order of 0.5-5% of the imprint feature size was found to initiate the resumption of plastic flow and allow for imprinting to greater depths and significant

residual layer thinning, with minimal feature distortion due to the lateral motion. This was demonstrated for several imprint feature geometries and was found to be largely independent of feature size.

In this chapter it will be shown that the SAOSF technique can be scaled up to massively parallel plate to plate nanoimprint architectures at much lower pressures, while still achieving significant improvements in feature replication and fidelity both above and below T_g. Using a 1 cm x 1 cm area imprint mold consisting of a 4 μm full pitch line pattern of 35 nm relief it will be shown that the SAOSF is effective in the glass transition region for both thin film and bulk PMMA samples. The influence of the shearing process on feature quality is explored, as well the role of feature geometry. First the mechanics of the SAOSF process are considered for single features and cavities, with illustrative finite element simulations into an elastic-plastic material similar to those used in chapter 3 serving as a reference.

5.2 Small amplitude oscillatory shear forming

The essential points of the SAOSF process are shown in figure 5.2.1, which details a 2-dimensional FEA simulation of an imprint into an elastic-plastic material of E = 3.0 GPa, Y = 0.1 GPa, and ν = 0.33, representative of a thermoplastic polymer deep in the glassy state. The initial film thickness is 5 μm. The mold consists of symmetric rectangular features centred around a single rectangular cavity, all of 3.5 μm width and height, i.e. $w = s = h_f$ = 3.5 μm. The 2D simulation is representative of a 3D state of plane strain, commonly encountered in the fabrication of massively parallel line patterns and used in the derivation of the nanoimprint fill factor ζ in section 2.6. In such a state, strains in the long axis of the feature are zero, and therefore all displacements are captured in the x-z plane of the 2D model. A Coulomb friction coefficient of μ = 0.5 is enforced at the film-mold interface.

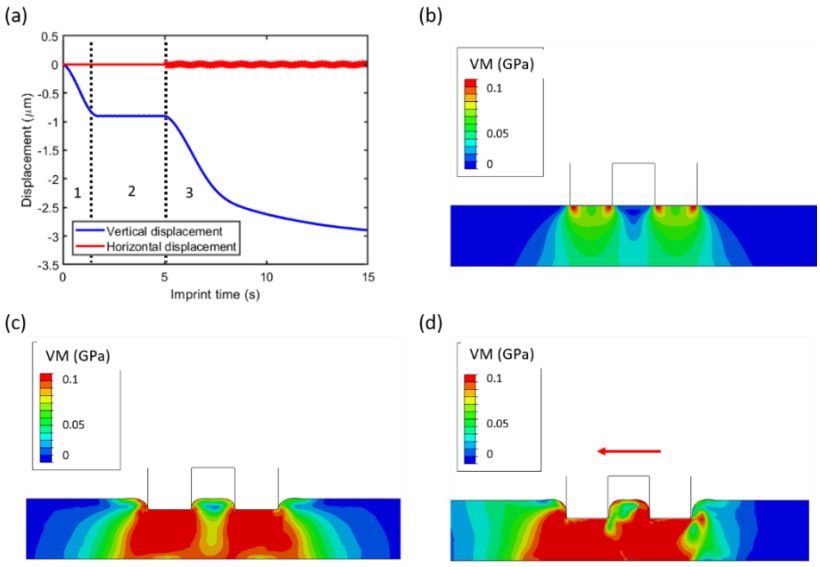

Figure 5.2.1. FEA simulation of a SAOSF imprint into a 5 μm elastic-plastic film. (a) Imprint time vs vertical and horizontal displacement of the mold. The SAOSF step begins at $t_{imprint}$ = 5s. (b)-(d) stress states and mold positions corresponding to regions 1,2, and 3 on (a) respectively.

Figure 5.2.1 (a) plots the displacement of the mold both vertically and horizontally as a function of imprint time. At $t_{imprint}$ = 0 an imprint load $F_{imprint}$ sufficient to induce plasticity beneath the mold feature is applied and the mold moves downwards into the film. This is marked as region 1 on the curve, and the corresponding Von Mises stress state is shown in (b), with plasticity localised near the feature edges. At a depth of approximately 1 μm $F_{imprint}$ is no longer sufficient to induce further plasticity due to confinement by the surrounding elastic film, and the mold ceases to move downward. This stress state is shown in (c). At $t_{imprint}$ = 5 s the SAOSF step is applied in the form of a 0.07 μm amplitude horizontal displacement, corresponding to 2% of the width of each individual feature, sinusoidally imposed at a frequency of 400 Hz. This results in greater plasticity within the imprinted volume as shown in (d) where the direction of shearing in this snapshot is marked by the arrow. The mold proceeds to move vertically again, achieving a final depth of imprint approximately 3 times greater than the standard imprint depth by $t_{imprint}$ = 15s.

Along with the increase in total plasticity due to the increased surface tractions brought about by the introduction of a lateral shear strain, several other characteristics of the SAOSF process are useful in elucidating the underlaying mechanism. Previous SAOSF studies have revealed the following:

- Material displaced in the SAOSF process during a cycle flows in a circular pattern centred around a point beneath the mold feature edge. Breaking of this circular

flow pattern by the edge wall results in pumping of material into the cavity. This process is shown in figure 5.2.2 (a-c), reproduced from [29].

- Friction between mold and film tends to enhance the SAOSF process. This is shown in figure 5.2.2 (d) where it may be seen that a full stick condition between mold and film results in greater vertical displacement per cycle than the partial stick condition.

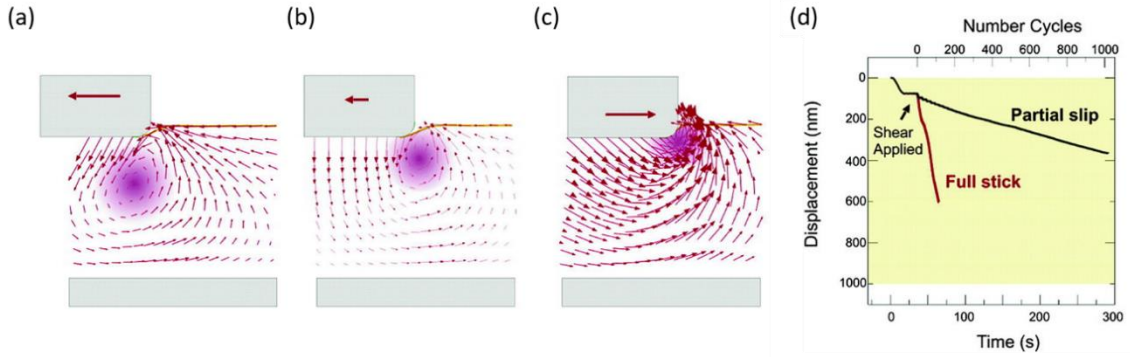

Figure 5.2.2 (a-c) Resist material flow patterns in a SAOSF process. Flow is centred around a point lying beneath e punch edge. Pumping into the cavity occurs as the presence of the feature side wall breaks the circular flow. (d) Displacement of imprint mold into the resist as a function time for different frictional boundary conditions. Increased friction is seen to enhance the SAOSF. Reproduced with author's permission from [29].

These behaviours can be explained by considering the stress distribution caused by a rigid rectangle of width $2a$ loaded with a uniform tangential traction q on an elastic half-space in a plane strain configuration, as depicted in figure 5.2.3 (a). The principal stresses σ_x and σ_z are given by[30]:

$$\sigma_x = -\frac{q}{2\pi}\left[4\ln\left(\frac{r_1}{r_2}\right) - (cos2\theta_1 - cos2\theta_2)\right] \qquad (5.2.1\ a)$$

$$\sigma_z = \frac{q}{2\pi}[(cos2\theta_1 - cos2\theta_2)] \qquad (5.2.1\ b)$$

Where $\theta_{1,2}$ and $r_{1,2}$ are reduced coordinates:

$$\theta_{1,2} = \arctan\left(\frac{z}{x \mp a}\right) \qquad (5.2.2\ a)$$

$$r_{1,2} = [(x \mp a)^2 + z^2]^{\frac{1}{2}} \qquad (5.2.2\ b)$$

Of greatest significance is the log term in equation 5.2.1.a, which leads to the generation of stress singularities at $x = a$, the feature edge. Equation 5.2.1.a is plotted at the surface of the half-space ($z = 0$) in figure 5.2.3 (b) to illustrate this. These stress singularities are thought to play a prominent role in fretting fatigue/wear of machine parts under

oscillating frictional loads[31]. The same effect is the underlying mechanism for the SAOSF process, however due to the orders of magnitude difference between the stiffnesses of the mold and resist, perceptible wear is only observable in the resist, appearing as an enhancement of the forming process. Stress concentration at the punch edge via tangential traction can explain the characteristics of the SAOSF process mentioned above. Firstly, the centre of the circular flow patterns seen in figure 5.2.2 (a-c) correspond approximately to the location of the stress singularities at the punch edge, indicating that plastic flow is greatest in the region where equation 5.1 indicates the Von Mises stress would be highest. Secondly, the increase in the effectiveness of SAOSF observed in figure 5.2.2 (d) can be explained by a Amonton's law relationship between the tangential traction q and an applied normal load p:

$$\sigma_x \propto q = \mu p \tag{5.2.3}$$

As such, increased friction will lead to increased lateral stress across the entire contact region, enhancing plasticity and forming fidelity in a nanoimprint process.

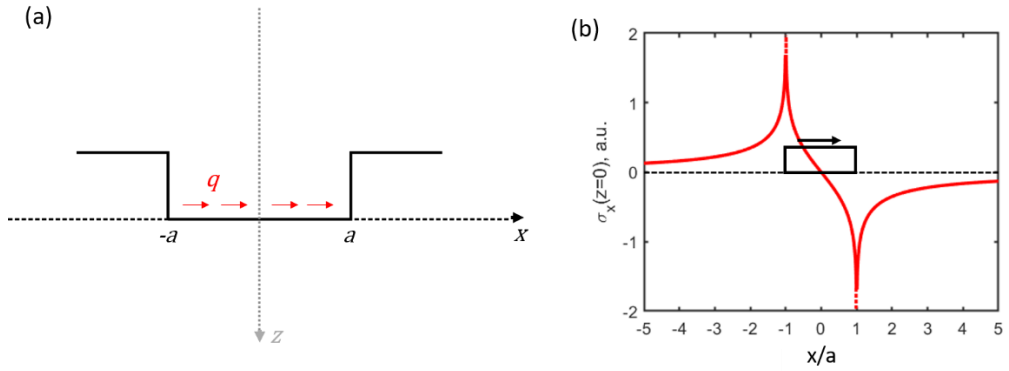

Figure 5.2.3 (a) Line loading of an elastic half-space with a tangential traction q across a length $2a$ in a plane strain geometry typical of nanoimprint of line patterns. (b) Resultant σ_x profile at the half-space surface (z = 0.) Stress singularities occur at the feature edge.

While not believed to be the primary mechanisms through which SAOSF enhancement occurs, two other phenomena related to the oscillatory motion of the mold that are not captured by the isothermal elastic-plastic FEM model above should be considered: shear thinning and heating of the resist through thermal dissipation. Shear thinning is a property of some viscoelastic liquids including many thermoplastic polymers such PMMA. An increase in the rate of shear applied to the material results in a drop in its viscosity. From a microstructure perspective, the origins of shear thinning in polymer melts are thought to arise from reorganization of the polymer chains into poorly entangled bands

aligned in the plane of shear, which may flow more easily[32] than strongly entangled chains. This phenomenon is particularly strong at the mold-resist interface, where entanglement is already weaker due to sample geometry[33]. Shear thinning typically emerges in polymer melts at rates on the order of $10^{-2} – 10^{0}$ s^{-1} and may manifest as a drop in viscosity of several orders of magnitude[3]. While in most conventional NIL setups the lateral flow rates are typically too low to cause significant thinning[34], in SAOSF experiments the added motion of the mold may induce a viscosity drop, particularly at feature edges where squeeze flow velocities are highest[23]. This is treated as a second order background effect however and will, if anything, serve to further enhance the SAOSF process.

As well as shear thinning, there exists the possibility that thermal dissipation of strain energy into the film may result in heating of the resist, leading to decreased viscosity due to the high sensitivity of the mechanical properties of polymers to changes in temperature, especially near T_g where the majority of work in this chapter is carried out. However, the local temperature increase for a single feature in a SAOSF process has been estimated to be negligible (less than 1°C) for shearing frequencies and displacement amplitude combinations of less than 1 MHz and 100 nm respectively[29]. Frequencies used in this work are on the order of several kHz while amplitudes are estimated to be at most approximately 70 nm, and as such local heating due to SAOSF is assumed to be negligible is comparison to the enhancement of plasticity due to increased stress brought about by tangential loading of the contact area.

The purpose of this chapter is to demonstrate that the small amplitude shear oscillation forming technique can be scaled up from molds consisting of one or few features on the micro/nano scale to massively parallel imprint schemes over several mm, while retaining local feature fidelity and enhancing imprint times. For the first time the SAOSF technique is incorporated into a conventional thermal nanoimprint process in a plate-to-plate geometry, with molds typically having areas of 1 cm^2. The work conducted focuses less on the fundamental physics of SAOSF, but rather on the engineering technicalities associated with scale-up, and characterization of the parameter space in which shear assisted imprint takes place, with respect to imprint temperature, mold geometry, number of shear cycles, and the thickness of the resist. The problem is first considered for the case of imprint into a bulk PMMA film, for which there exists a near infinite amount of available resist material to fill mold cavities, before examining SAOSF for films with material volumes closer to the fill factor ζ. It shall be shown in both cases that SAOSF

leads to increased pattern quality can be achieved at lower imprint temperatures in both for both cases and is invariant with respect to local feature geometry.

5.3 Experimental Methods

Imprint experiments were preformed using a modified NILT CNI 1.0 thermal imprint unit. Shear strains were supplied via a 1.5 x 1.5 x 0.05 cm monolithic shear plate actuator (Noliac instruments, CSAP04) with an unloaded resonance of 1,750 kHz, to which the imprint mold was mounted using high temperature, electrically insulating epoxy (Epo-Tek 920.) A sinusoidal voltage was supplied to the shear piezo via a Tektronix AFG3022 signal generator, fed through a Krohn Hite 7602M wideband amplifier. An image of this setup with the mold in place is shown in figure 5.3.1 (a), while a side view of the stack is shown in (b).

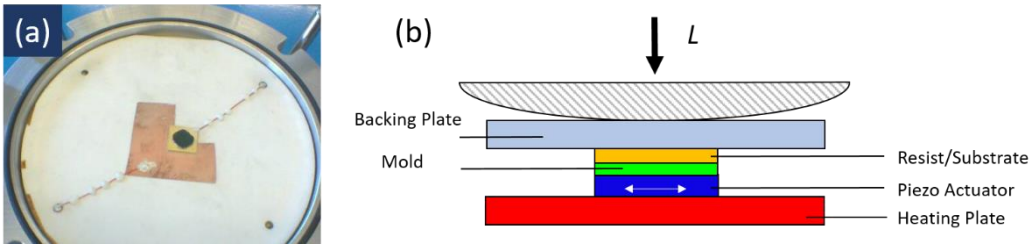

Figure 5.3.1 (a) Image of the custom SAOSF setup. The conventional NILT thermal nanoimprint unit has been modified to allow for nanoscale lateral oscillations of a mounted imprint mold. 4 holes have been precision drilled into the ceramic heating plate, allowing for an external voltage input to the top of the plate. A 500 nm copper film has been deposited at the centre of the plate, forming the back contact with the piezo shear actuator (yellow square). The second contact is applied to the top of the plate. The imprint mold (Silicon, 4 µm full pitch line pattern, fabricated via photolith) is secured to the piezo actuator via electrically insulating, high temperature epoxy. During imprint, the sample is mounted atop the mold, the backing plate put in place, and the system closed. (b) Side-on schematic of the SAOSF imprint stack during imprint. Normal load is applied via an inflatable membrane in contact with the backing plate.

The general SAOSF imprint process is shown in figure 5.3.2. The shearing step is designed to coincide with the entirety of the peak temperature/load phase. Typically, the shearing processes consists of a 150 V driving voltage applied at 10 kHz to the piezo for 120 seconds. Due to the enclosed nature of the NILT imprint system, no external verification of the magnitude of oscillation was possible. As such, only an upper bound could be placed on the lateral motion of the mold features with respect to the sample/resist. Considering friction, mechanical damping, and potential tool resonance effects, it is unlikely that this magnitude was reached during any of the shearing experiments. All temperatures

reached in this work were far from the piezo's Curie temperature of 360 °C. The literature relationship between displacement and voltage is given as:

$$\delta_{peak} = 2.88 \times 10^{-15} \frac{V^2}{t_p} + 5 \times 10^{-10} V \tag{5.3.1}$$

Where V is the applied peak voltage and t_p is the thickness of the actuator. Inserting values of 75 V and 0.5 mm respectively yields a of δ_{peak} 70 nm, meaning the maximum total motion of the mold per cycle is 140 nm.

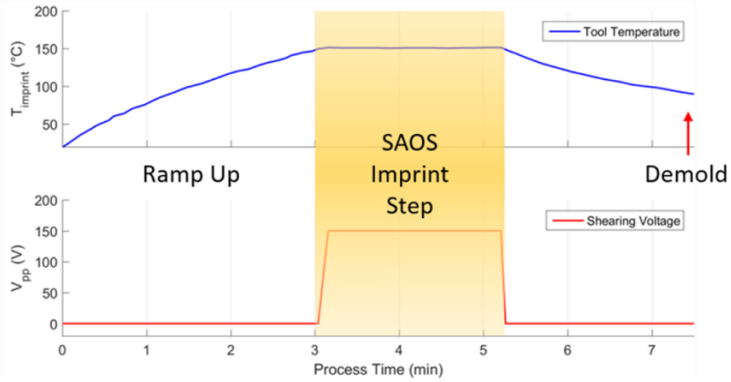

Figure 5.3.2 Time vs temperature and shearing voltage for the SAOSF process. The shearing step is designed to coincide with the peak temperature/pressure step of a standard imprint process.

5.3.1 Bulk film temperature dependence

A 1 cm x 1 cm imprint mold consisting of a 4 µm full pitch line pattern with feature heights of 35 ± 2 nm was fabricated via photolithography and coated in a trichloro(octadecyl)silane anti-stick self-assembled monolayer. This geometry imposes a state of plane strain on the sample during imprint. The mold was mounted to the imprint stack in such a fashion as to ensure the direction of oscillation was perpendicular to the long axis of the line pattern. Conventional and SAOSF imprinting processes were preformed into 50 µm thick free standing PMMA films (Goodfellow Inc.) with T_g of 110°C, as verified via dynamic mechanical analysis at 1 Hz. Individual imprints were carried out over a temperature range of 70 - 150°C. An imprint pressure of 4 MPa was applied for all imprints, and the peak hold time was 2 mins. Demolding was performed at 85°C, except in cases were $T_{imprint}$ < 85°C, for which samples were demolded at the same temperature as imprint. 85°C was chosen as it has been shown to correspond to an adhesion minimum between PMMA and silicon[22]. Both conventional and SAOSF imprint processes were carried out with the shear

assembly in place, so as to keep tool compliance consistent across all experiments. Imprint fidelity was inspected via tapping mode AFM using standard tips performed at the centre of the imprint pattern. Large scale verification was performed via optical microscopy using a Zeiss Axio imager. An AFM image of the imprint mold is shown in figure 5.3.3.

5.3.2 Geometric effects

The role of feature geometry with respect to the direction of shear was investigated using a checkerboard mold consisting of 32 x 32 µm raised squares, separated by 3 µm wide, 250 nm deep channel, fabricated via photolithography. Imprints were performed at 100°C into 50 µm thick PMMA sheets for 5 minutes, allowing for complete cavity filling in both the SAOSF and standard nanoimprint cases. The axis of shearing was aligned to the vertical axis of the channels, and perpendicular to the horizontal. Feature quality was assessed via AFM.

5.3.3 Thin film implementation

PMMA films (Sigma Aldrich, Mw = 93 kDa, Mw/Mn = 2.17) of 40 and 150 nm thicknesses were prepared via spin coating from a 2.5% wt. toluene solution on 1.2 x 1.2 cm silicon <100> wafer pieces (University Wafer.) These thicknesses correspond to fill factors of 2.3ζ and 8.6ζ respectively. Imprints were again carried out for 2 mins in the presence and absence of shear over a range of temperatures. For the 40 nm film, imprints were performed for 5 mins at 150°C, below which no pattern transfer was achieved either by conventional imprint of SAOSF.

To investigate material extrusion from beneath isolated features in a squeeze flow geometry imprints were made performed into 800 nm PMMA films with a mold consisting of squat, concave pillars of 6 µm height and 10 µm diameter, with a 50 µm centre to centre spacing. Imprints were carried out at 100°C with the number of oscillations varied over a range of 10^3 – 10^6, with the results compared to conventional imprint runs.

5.4 Results & Discussion

5.4.1 SAOSF into bulk PMMA

Figure 5.4.1 shows the key results of the effect of the introduction of shear strain oscillation on the temperature at which high fidelity imprint can be performed. (a) shows normalized imprint feature height (average imprint feature height/mold cavity depth) as a function of imprint temperature in the cases of SAOSF and conventional nanoimprint. In the conventional case, a sharp drop in imprinted feature height/depth is observed as temperature peak imprint temperature is lowered through the glass transition regime from 110 to 100°C as the polymer begins to stiffen due to decreased segmental mobility. Features only achieve approximately 0.5 times the prescribed height, and all traces of pattern replication disappearing at $T_{imprint}$ = 85°C. In contrast, the SAOSF technique shows full pattern replication at temperatures as low as 95°C, well below T_g = 110°C. Significant pattern transfer is observed at temperatures down to 75°C, at which point the yield stress of the material increases to such a point that the amplitude of shear strain is no longer sufficient to induce plasticity. (b) Compares the feature profiles of the conventional NIL and SAOSF patterns produced over a 90 - 100°C temperature range, averaged over a length of 25 µm. The added shear deformation appears to cause no significant pattern distortion either in the direction of shear or orthogonally, while pattern fidelity is much improved at lower temperatures.

Figures 5.4.1 (c) and (d) show a 25 x 25 µm 3D rendering imprinted surfaces produced by the two forming techniques at $T_{imprint}$ = 95°C. As well as achieving greater relief, SAOSF results in a lower defect concentration and a more uniform surface at low temperature. To demonstrate that this effect is non-local, images (f) and (g) show 80 x 80 µm AFM micrographs taken at the centre of the samples for SAOSF and nanoimprint surfaces respectively, both produced at 90°C. While pattern fidelity is reasonably consistent across the sheared surface, a large area in the bottom right quadrant of (g) remains totally unpatterned.

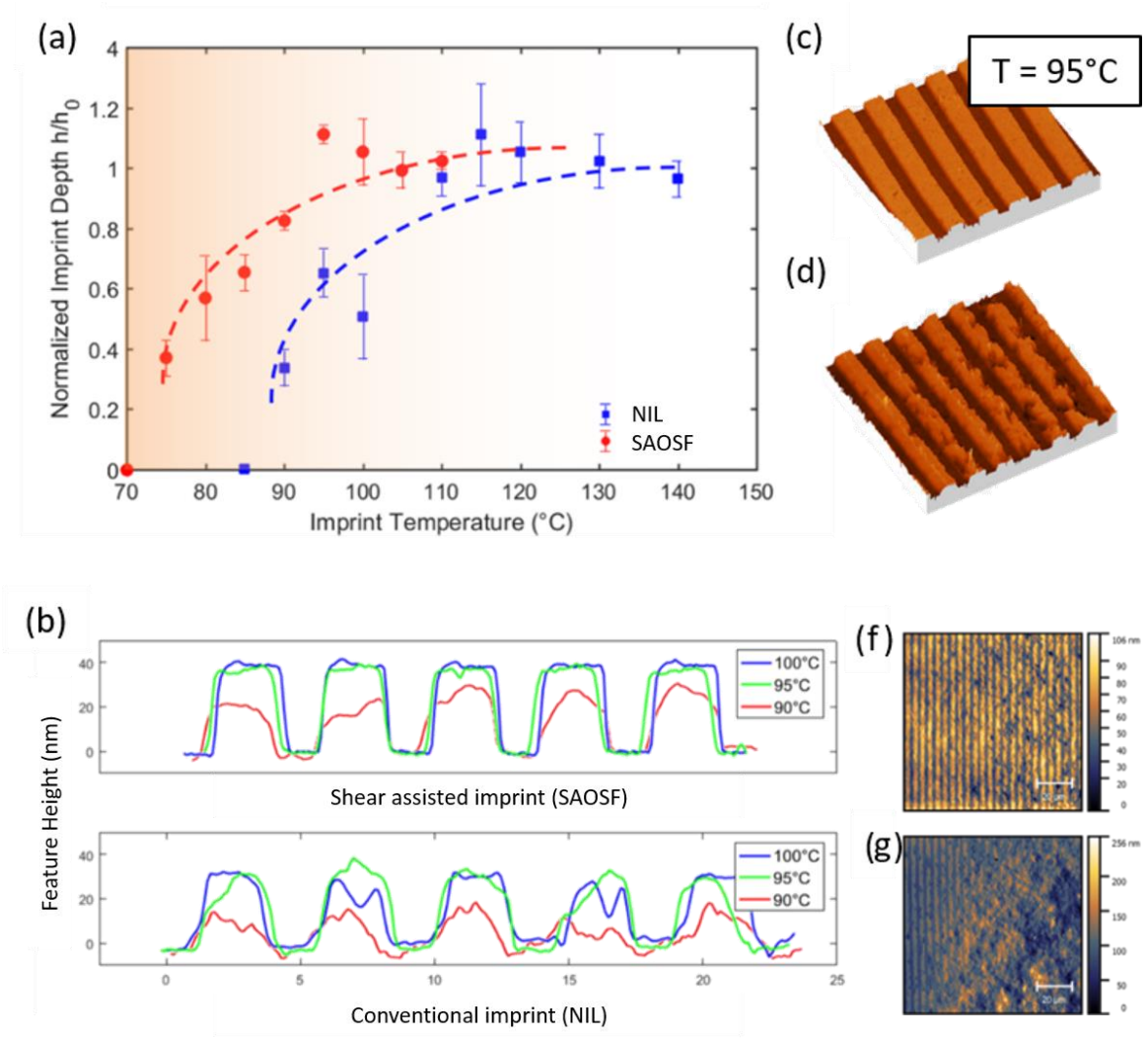

Figure 5.4.1 (a) Normalized imprint depth of the SAOSF process (red) and a conventional imprint process (blue) as a function of imprint. (b) Averaged feature height profiles for the two processes at three temperatures. (c), (d) 25 x 25 µm 3D AFM rendering of the SAOSF and NIL replicated surfaces at 95°C. (f), (g) 80 x 80 µm surface scans of imprints at 90°C.

In total, the addition of lateral oscillation of the mold during imprint into bulk PMMA has led to a decrease in the minimum temperature required for pattern replication of approximately 20°C.

5.4.3 Geometric effects

To demonstrate that the introduction of an additional shear motion causes minimal distortion to the produced pattern, imprints were carried out into the 50 µm PMMA sheets using the checkerboard mold described in section 5.4.2, with the direction of shearing aligned to the vertical axis. Figure 5.4.2 (a) shows an optical image of the resultant SAOSF

imprint at 100°C. Macroscopically no distortion of the pattern is evident. This is confirmed at the individual feature scale via AFM, with (b) showing an AFM image of one of the joints of the pattern. Line profiles were taken in the vertical and horizontal directions as indicated by the magenta and cyan lines and are plotted in (c). No significant difference is observed between the two directions. These can be compared to the features produced via conventional imprint at the same temperature in (d). It can be observed that the final imprint height of the features produced via SAOSF is approximately 25 nm greater than the NIL process, while there is no meaningful change in shape.

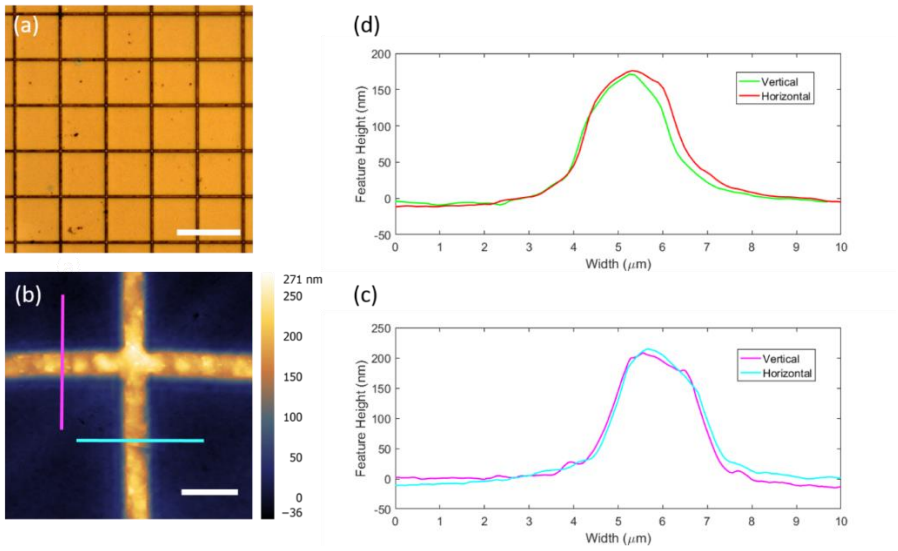

Figure 5.4.2 (a) Optical micrograph of a checkboard SAOSF imprint produced at 100°C. 50 µm scale bar. (b) AFM image of the same pattern, scale bar is 5 µm. (c) Vertical and horizontal feature line profiles taken from (b). (d) Comparable line profiles taken from a conventional imprint.

5.4.2 Thin film implementation

Figure 5.4.3 shows AFM images of the resultant imprints into 150 nm PMMA film on silicon over a peak temperature range of $120 \geq T_{imprint} \geq 105$°C with the 4 µm full-pitch line pattern mold. Each row contrasts the SAOSF (left) and nanoimprint (centre) processes at a given $T_{imprint}$, with a representative line profile shown on the right. As can be seen from the top row, full relief imprint at T_g + 10° is achieved via shear injection, while the nanoimprint processes yields features of approximately 5 nm height for the same cycle conditions. As in the bulk sample, a rapid decline in imprint quality follows as

$T_{imprint}$ intersects with the T_g region, eventually resulting in minimal pattern transfer for both NIL and SAOSF processes at T_g + 5°.

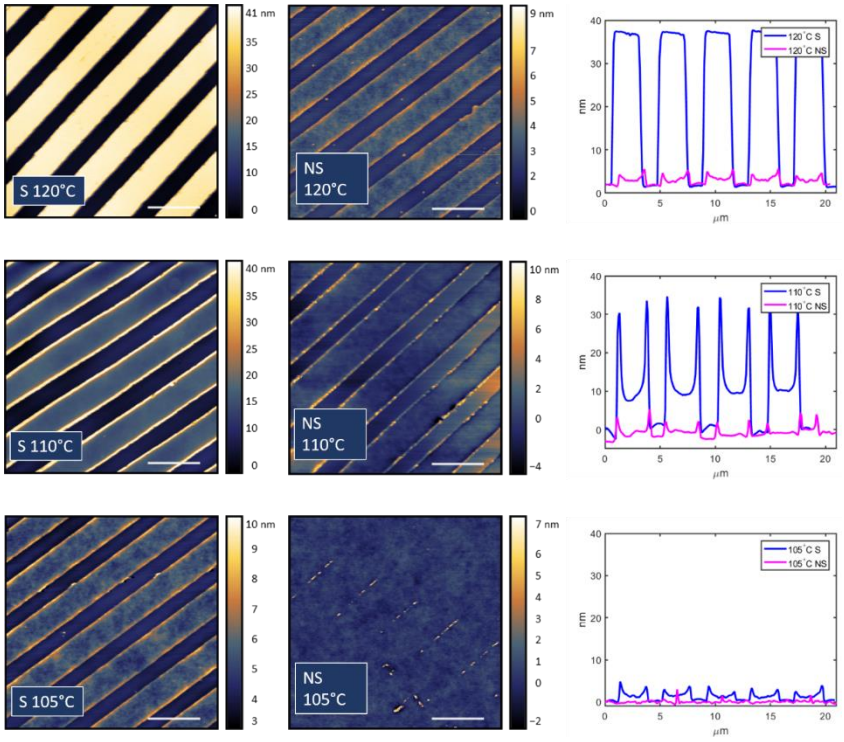

Figure 5.4.3 AFM micrographs of SAOSF (left) and NIL (centre) imprints and accompanying height profiles (right) for three temperatures: 120° (top), 110° (middle), and 105°C (bottom.) Scale bars are 5 μm

A fundamental difference between imprint into bulk samples and supported thin films is that in the latter material from beneath the mold features must be pumped into the adjacent unoccupied cavity, whereas for the former case all that is required is that material beneath the mold features be plasticized sufficiently to leave the required permanent deformation. Essentially, there exists beneath the cavity an infinite reservoir of in the bulk sample case, which only needs conform to the mold shape, and lateral material transport distances are minimal. This difference is outlined in figure 5.4.4, where the thin film case is shown in (a) and the bulk in (b) for an elastic-plastic material with a yield stress of 100 MPa. For each geometry there is associated a distinct mode of failure at low $T_{imprint}$; for thin films a failure to pump sufficient material into the centre of the cavity, and an inability to yield the material beneath features so as to penetrate to the full depth of relief in the bulk case. This is reflected in figure 5.4.4 (c – e) which show AFM scans and accompanying line profiles of nanoimprints into the 150 nm PMMA thin film and 50 μm bulk sample at $T_{imprint}$ of 150°C and 70°C respectively. The line profiles reveal

that for the film the majority of material is concentrated around the edge of the mold feature, with only minimal raised material (~ 5nm) towards the centre. In contrast, filling in the bulk geometry is somewhat uniform across the cavity, yet fails to reach full relief.

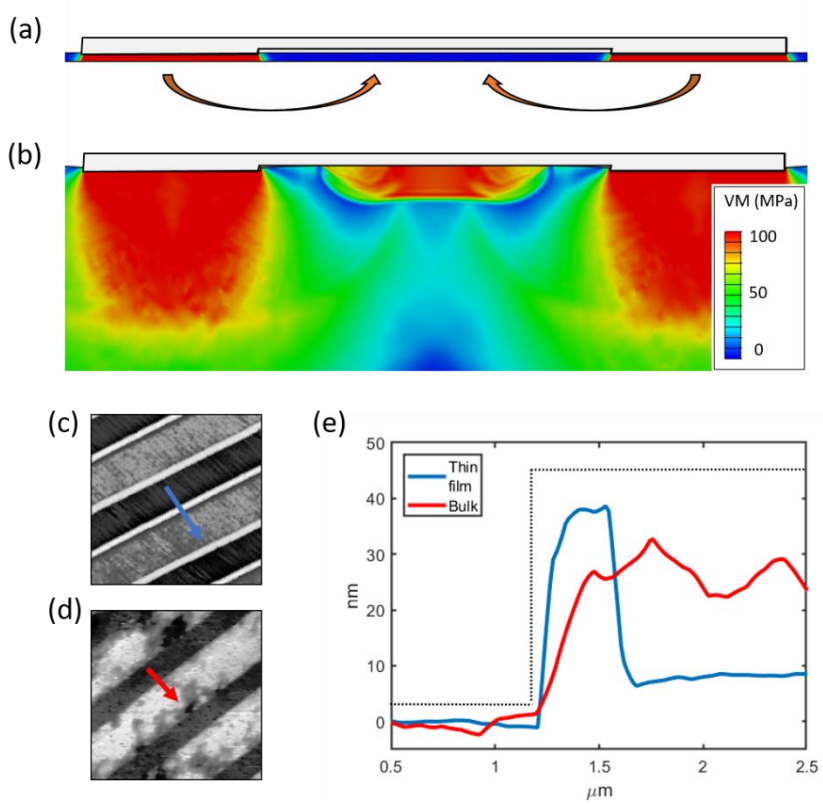

Figure 5.4.4 Imprint failure modes for thin films and bulk samples in nanoimprint. (a) Von Mises stress in a thin film geometry, where no stress is generated in the cavity. (b) VM stress in a bulk sample case, where the roof of the cavity contacts the resist, inducing plasticity. (c) AFM image of an imprint into 150 nm PMMA at 150° C. (d) Imprint into 50 µm bulk sample at 70° C. (c) Respective line scans indicating separate failure modes.

As was discussed in section 5.2, SAOSF mitigates against both failure modes by both increasing stress beneath the mold feature, and pumping material into the cavity. To quantify the latter in a manner comparable to the original shear forming experiments of Cross & Pethica on a macroscopic scale, a 1 x 1 cm mold consisting of an array of 6 µm tall, 10 diameter µm concave pillars were fabricated via photolithography, with a centre to centre spacing of 50 µm leaving each pillar relatively isolated from its nearest neighbour. An scanning electron micrograph of this mold is shown in figure 5.4.5 (a), and an imprint in (b). With f_{SAOSF} and $T_{imprint}$ held constant, imprints were performed into an 800 nm PMMA film ($\zeta >> h_{film}$), with the length of the shearing step varied across a range of 0.1 – 100s, corresponding to 10^3 – 10^6 oscillations. The AFM profiles plotted in (c)

demonstrate that as the number shear cycles is increased not only the amount of material extruded increases, but also the lateral distance over which material is transported. The inverted 3D surface plots of the standard NIL and the SAOSF 100s cycle processes plotted in (d) and (e) respectively show the massive increase in volume removed from beneath the feature by the shear strain oscillation, while (f) plots the thickness of the resist film beneath the feature edges as a function of number of shear oscillations/strokes. It is striking that even a 1 s SAOSF in a minute imprint cycle decreases the residual layer thickness by 20% over the standard NIL process. This suggests that the SAOSF process could be successfully implemented in roll to roll setups where the contact time between mold and resist is relatively short. Again, no distortion of the features due to the shear action was observed for this geometry.

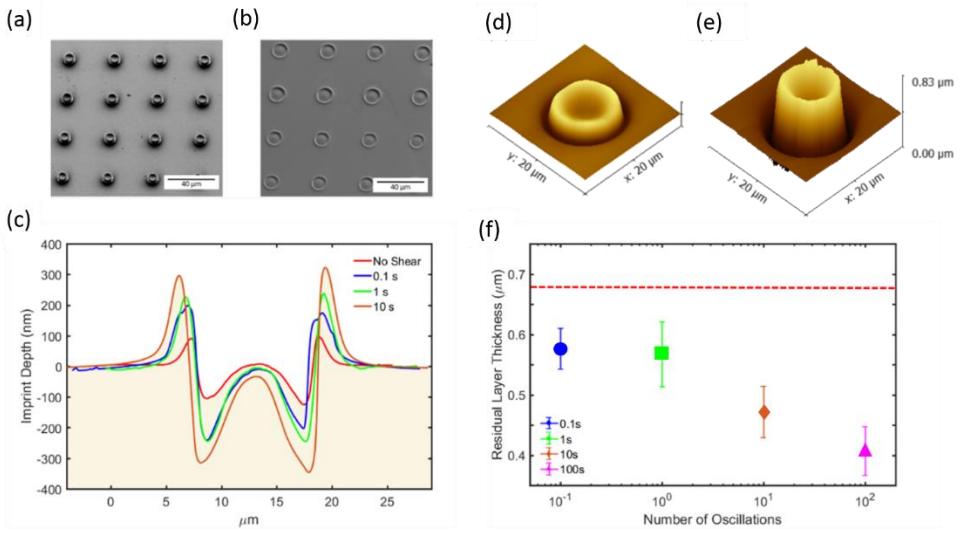

Figure 5.4.5 (a) Squat pillar mold used for material pumping study. (b) Resultant imprint in 800 nm PMMA. (c) Height profiles of imprints with shear applied at 10 kHz for 0.1-100s. (d) Inverse AFM 3D map of standard NIL imprint feature. (e) The same image, but for the SAOSF 100s cycle. (f) Residual layer thickness in features as a function of the number of shear cycles. The dashed red line shows the NIL depth.

As a final piece, SAOSF imprint was attempted using the 35 nm relief 4 µm full pitch line pattern mold into a 40 nm thick PMMA film, corresponding to a fill factor of 2.3ζ at 150 °C. Low fill factor has the potential to be a diffraction limit free technology for IC fabrication via reactive ion etching and as such demonstration of the SAOSF technique in this experimental space is highly attractive. AFM micrographs of the SAOSF and NIL imprints are shown in figure 5.4.6 (a) and (b) respectively. While full relief was not achieved in either case, significant enhancement is observed in the SAOSF case in

comparison to the standard nanoimprint, for which the pattern is poorly defined and the features sparse. While additional refinement of the SAOSF technique may be required to achieve full relief in high aspect ratio geometries for massively parallel features (including an imprint apparatus with greater lateral stiffness than the inflatable membrane system employed by the NILT CNI instrument used here) this result shows the potential of the shear forming when coupled to a standard imprint process.

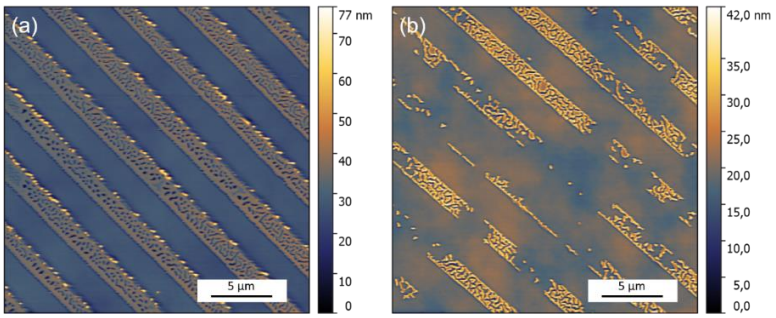

Figure 5.4.6 *(a) SAOSF imprint with a 4 µm full pitch mold of 35 nm relief into a 40 nm PMMA film at 150°C (b) Corresponding conventional NIL image.*

5.5 Conclusions

In conclusion, the small amplitude oscillatory shear technique has been successfully scaled up to imprint molds with macroscopic lateral dimensions in a conventional, commercially available imprint apparatus while retaining nanoscale feature accuracy. In bulk PMMA samples, it was shown that SAOSF could drop the lower temperature bound for imprint by 20° and enabled pattern transfer well into the glassy state. This has the potential to allow for more rapid processing and more energy efficient imprint processes due to less thermal cycling. The technique has been shown to be effective regardless of mold geometry. Imprints with a checkerboard pattered showed that lines formed parallel and perpendicular to the direction of shear were identical, both in terms of height and shape. This indicates that SAOSF can be used for complex mold geometries without fear of feature distortion.

In thin films SAOSF was also found to significantly enhance the forming processes over conventional NIL. Imprints of a 150 nm PMMA film with a 4 µm full pitch line pattern mild with 35 nm relief were found to be successful down to 120°C (T_g +10°), whereas failure occurred at 150°C for the conventional NIL case. It was shown that this improvement is the result of enhanced plasticity beneath the mold features and greater

lateral transport of resist material into the adjoining cavity. Even very short SAOSF times of 0.1 s in a 2 minute total imprint cycle were found to lead to significant enhancement of the pattern transfer process via this mechanism, indicating SAOSF can be incorporated into high speed techniques such as roll to roll imprint. Finally, enhancement of the imprint process was demonstrated via application of SAOSF in a $\zeta = 2.3$ system with minimal material available for cavity filling. While full pattern replication was not achieved, initial results suggest that small amplitude oscillatory shear forming could be a valuable tool for etch mask fabrication in microfabrication processes.

Bibliography

1. Chou, S. Y., Krauss, P. R. & Renstrom, P. J. Nanoimprint Lithography. *J. Vac. Sci. Technol. B, Nanotechnol. Microelectron. Mater. Process. Meas. Phenom.* **14,** 4129–4133 (1996).
2. Austin, M. D. *et al.* Fabrication of 5nm linewidth and 14nm pitch features by nanoimprint lithography. *Appl. Phys. Lett.* **84,** 5299–5301 (2004).
3. Tan, H., Gilbertson, A. & Chou, S. Y. Roller nanoimprint lithography. *J. Vac. Sci. Technol. B Microelectron. Nanom. Struct. Process. Meas. Phenom.* **16,** 3926 (1998).
4. Ahn, S. H. & Guo, L. J. High-Speed Roll-to-Roll Nanoimprint Lithography on Flexible Plastic Substrates. *Adv. Mater.* **20,** 2044–2049 (2008).
5. Ok, J. G. *et al.* Continuous and scalable fabrication of flexible metamaterial films via roll-to-roll nanoimprint process for broadband plasmonic infrared filters. *Appl. Phys. Lett.* **101,** 223102 (2012).
6. Ahn, S. H. & Guo, L. J. Large-Area Roll-to-Roll and Roll-to-Plate Nanoimprint Lithography: A Step toward High-Throughput Application of Continuous Nanoimprinting. *ACS Nano* **3,** 2304–2310 (2009).
7. Kooy, N., Mohamed, K., Pin, L. T. & Guan, O. S. A review of roll-to-roll nanoimprint lithography. *Nanoscale Res. Lett.* **9,** 320 (2014).
8. Hu, W., Crouch, A. S., Miller, D., Aryal, M. & Luebke, K. J. Inhibited cell spreading on polystyrene nanopillars fabricated by nanoimprinting and in situ elongation. *Nanotechnology* **21,** 385301 (2010).
9. Wu, Y. N. *et al.* Substrate topography determines the fate of chondrogenesis from human mesenchymal stem cells resulting in specific cartilage phenotype formation. *Nanomedicine Nanotechnology, Biol. Med.* **10,** 1507–1516 (2014).
10. Austin, M. D. *et al.* 6 nm half-pitch lines and 0.04 μm ^{2} static random access memory patterns by nanoimprint lithography. *Nanotechnology* **16,** 1058–1061 (2005).
11. Varagnolo, S. *et al.* Effect of hair morphology and elastic stiffness on the wetting properties of hairy surfaces. *Microelectron. Eng.* **161,** (2016).
12. Kang, M.-G., Kim, M.-S., Kim, J. & Guo, L. J. Organic Solar Cells Using Nanoimprinted Transparent Metal Electrodes. *Adv. Mater.* **20,** 4408–4413 (2008).
13. Beck, M. *et al.* Improving stamps for 10 nm level wafer scale nanoimprint lithography. *Microelectron. Eng.* **61–62,** 441–448 (2002).
14. Dahl-Young Khang, Hyewon Kang, Tae-Il Kim, and & Lee*, H. H. Low-Pressure Nanoimprint Lithography. (2004). doi:10.1021/NL049887D

15. Heidari, B., Maximov, I., Sarwe, E.-L. & Montelius, L. Large scale nanolithography using nanoimprint lithography. *J. Vac. Sci. Technol. B Microelectron. Nanom. Struct. Process. Meas. Phenom.* **17,** 2961 (1999).
16. Cross, G. L. W., O'Connell, B. S. & Pethica, J. B. Influence of elastic strains on the mask ratio in glassy polymer nanoimprint. *Appl. Phys. Lett.* **86,** 081902 (2005).
17. Rowland, H. D., Sun, A. C., Schunk, P. R. & King, W. P. Impact of polymer film thickness and cavity size on polymer flow during embossing: toward process design rules for nanoimprint lithography. *J. Micromechanics Microengineering* **15,** 2414–2425 (2005).
18. Hirai, Y., Konishi, T., Yoshikawa, T. & Yoshida, S. Simulation and experimental study of polymer deformation in nanoimprint lithography. *J. Vac. Sci. Technol. B Microelectron. Nanom. Struct.* **22,** 3288 (2004).
19. Hirai, Y. *et al.* Study of the resist deformation in nanoimprint lithography. *J. Vac. Sci. Technol. B Microelectron. Nanom. Struct.* **19,** 2811 (2001).
20. Cross, G. L. W. The production of nanostructures by mechanical forming. *J. Phys. D. Appl. Phys.* **39,** R363–R386 (2006).
21. Rowland, H. D., King, W. P., Pethica, J. B. & Cross, G. L. W. Molecular Confinement Accelerates Deformation of Entangled Polymers During Squeeze Flow. *Science* 720–724 (2008).
22. Trabadelo, V., Schift, H., Merino, S., Bellini, S. & Gobrecht, J. Measurement of demolding forces in full wafer thermal nanoimprint. 2–5 (2008). doi:10.1016/j.mee.2008.01.086
23. Schift, H., Heyderman, L. J. & Sotomayor Torres, C. M. in *Alternative Lithography* (2004).
24. Rowland, H. D., King, W. P., Cross, G. L. W. & Pethica, J. B. Measuring Glassy and Viscoelastic Polymer Flow in Molecular-Scale Gaps Using a Flat Punch Mechanical Probe. *ACS Nano* **2,** 419–428 (2008).
25. Roth, C. B. Mobility and stability of glasses. *J. Polym. Sci. Part B Polym. Phys.* **48,** 2558–2560 (2010).
26. Lister, K. A. *et al.* Direct imprint of sub-10 nm features into metal using diamond and SiC stamps. *J. Vac. Sci. Technol. B Microelectron. Nanom. Struct.* **22,** 3257 (2004).
27. Cross, G. L. W., O'Connell, B. S. & Pethica, J. B. Influence of elastic strains on the mask ratio in glassy polymer nanoimprint. *Appl. Phys. Lett.* **86,** 1–3 (2005).
28. McKenzie, W., Pethica, J. & Cross, G. A direct-write, resistless hard mask for rapid

nanoscale patterning of diamond. *Diam. Relat. Mater.* **20,** 707–710 (2011).

29. Cross, G. L. W., O'Connell, B. S., Özer, H. O. & Pethica, J. B. Room temperature mechanical thinning and imprinting of solid films. *Nano Lett.* **7,** 357–362 (2007).
30. Johnson, K. L. (Kenneth L. *Contact mechanics*.
31. McColl, I. ., Ding, J. & Leen, S. . Finite element simulation and experimental validation of fretting wear. *Wear* **256,** 1114–1127 (2004).
32. Tapadia, P., Ravindranath, S. & Wang, S.-Q. Banding in Entangled Polymer Fluids under Oscillatory Shearing. *Phys. Rev. Lett.* **96,** 196001 (2006).
33. Manias, E., Bitsanis, I., Hadziioannou, G. & Brinke, G. ten. On the nature of shear thinning in nanoscopically confined films. *Europhys. Lett.* **33,** 371–376 (1996).
34. Hoffmann, T. & Sotomayor Torres, C. M. in *Alternative Lithography* (2004).

Chapter 6:
Overall Conclusions and Outlook

The central theme of this work was the development of new techniques to mechanically characterise and pattern small volumes of material at the nanoscale. This has been accomplished through indentation of supported polymer thin films with a flat punch indenter and thermal nanoimprint experiments in a plate-to-plate geometry. The first of these techniques offers a wealth of fundamental insight into forming processes and mechanical response at the nanoscale. The large number of controllable variables such as stress, strain, and stress rate enable the complex constitutive response of glassy films to be well characterised and enable high precision forming to exact stress levels. The latter technique is an industrial scale technology, capable of mass production of high fidelity nanopatterned surfaces. This thesis therefore considers the topic of polymer forming at the nanoscale both from a local, fundamental physics level and a process orientated fabrication perspective. This final section shall briefly recap the findings of the previous chapters, as well as commenting on the future potential of the techniques developed and potential hurdles which must be overcome for their implementation.

In **chapter three** a new method for the extraction of the mechanical properties of supported thin films was developed called the confined layer compression test. Indentation of the film with a cylindrical diamond flat punch whose diameter is many times the initial film thickness was found to result in a state of uniaxial strain, where strains orthogonal to the indentation axis were minimal. While unconstrained one-dimensional deformation tends towards a state uniaxial strain at very high aspect ratio[1,2], the film surrounding the contact area in the confined layer compression test was found to greatly enhance this natural tendency by acting as a confining jacket[3,4], supressing lateral strain. In this geometry Young's modulus, Poisson's ratio, yield stress, and the bulk modulus could be extracted in a single loading step for simple materials with minimal sample preparation, even at modest punch diameter to film thickness ratios. The test was studied primarily through finite element simulations of an elastic-plastic material and indentation of high molecular weight polystyrene films over a thickness range of 190 – 470 nm with a 2050 nm diameter punch. PMMA and

amorphous selenium systems were also studied. It was shown that as the punch to film aspect ratio was increased the level of lateral confinement improved, more closely resembling a true uniaxial strain geometry and allowing for direct parameter extraction. A distinct kink in the indentation load versus displacement curve was also observed, corresponding to a discrete, confined yield event throughout the material under the contact area, an effect previously reported for any film system. The effects of aspect ratio, substrate compliance, and frictional boundary conditions were all considered.

In **chapter four,** confined yield was studied from the perspective of non-equilibrium polymer-specific thermomechanical effects. The yielded volume represents a highly exotic system, with a confined plastic state trapped directly beneath the punch and therefore open to mechanical study. It was shown via indentation of 550 and 670 nm polystyrene films with a 4800 nm diameter punch that both the confined yield stress and confined plastic modulus are sensitive to physical ageing in the conventional manner, increasing with thermal annealing. Yield was demonstrated to be associated with an increase in segmental mobility via creep compliance[5,6], with a decrease in the long term retardation time τ_2 from 118 s to 48 s directly following yield. A unique stress memory effect was discovered that resulted in significant raising of the confined yield stress and densification of the indented volume by up to 3.4%. This effect was found to arise from residual stresses imparted to the sample during plastic loading. In the plastic domain radial stresses were found to increase more quickly than in the elastic, balancing the applied axial stresses to keep the material on the yield surface. This phenomenon was studied both through finite element and experimental indentation, with both systems behaving in a similar fashion and matching well with analytic calculations.

In **chapter five**, confinement during deformation was studied from a different perspective. While in the previous two chapters, a confined state proved beneficial, in the context of mechanical forming processes such as thermal nanoimprint, it presents an impediment to cavity filling via shear flow of material from beneath the mold features. To aid lateral flow via a pumping action, a technique was implemented to introduce shear strains directly to the mold features. The small amplitude oscillatory shear forming (SAOSF) technique, previously demonstrated only for micron scale contacts, was applied to imprint molds with areas on the order of 1 cm². Imprints into 50 µm thick PMMA sheets with a line pattern mold of 35 nm relief and 4 µm full pitch

showed that the application of oscillatory shear during imprint can lead to full fidelity pattern replication at temperatures below the glass transition over modest imprint cycle times and at relatively low pressures (4 MPa). Similar results were achieved in supported PMMA films of 150 nm and 40 nm initial thicknesses with the same mold, corresponding to imprint fill factors of 8.6 and 2.3 respectively. While in the latter case full relief pattern replication was not achieved, the SAOSF sample showed significantly better pattern transfer than the standard imprint process. The mechanism of SAOSF was studied and improvement in forming quality was found to result from an increase in plasticity beneath the mold features and a pumping motion into surrounding cavities. The technique was studied for a variety of geometries with features aligned both perpendicular and parallel to the axis of shearing. No pattern distortion was reported due to shear loading.

6.1 Future perspectives

The confined layer compression test has the potential to become an extremely valuable technique for mechanical characterisation on nanostructured matter. The ability to measure intrinsic stress-strain behaviour well past the point of yield in a single test is extremely attractive prospect. That the test requires minimal sample preparation and is compatible with supported thin films further highlights this point, particularly when contrasted to preparation-intensive techniques such as micropillar compression. The discovery that an unambiguous, sharply defined yield event can be observed means that all parameters governing isotropic elasticity can be simultaneously extracted for the first time. The results enable full characterisation of the mechanical response of thin films with no assumptions well past the elastic limit. This is in contrast to the well-established Oliver-Pharr method where constitutive assumptions must be made about the sample's Poisson's ratio in order to extract elastic modulus[7] and Tabor's parameter must be assumed to get yield from hardness measurements[8].

The test still requires significant refinement to become a widely utilized testing method however. Firstly, supported film reference materials must be found that can fulfil the same function as fused silica in sharp tipped indentation. A thin film material with well-known isotropic elastic behaviour and yield stress is required to enable the user to calibrate artefacts in the measurement: geometric imperfections of the punch, alignment of the load and surface normal, and elastic compliance of the punch, film

support, and nanoindenter positioning system. Polymers may not be best suited to this task as parameter pressure dependence and physical ageing introduce complexity and uncertainty in both moduli and yield stress. Thin metallic films offer a potential solution, providing that all calibration samples are prepared in the same fashion to avoid changes in yield stress due to granularity or other size effects[9]. Secondly, the indentation of stiffer materials such as metals and ceramics requires that the overall stiffness of the substrate and indenter frame be sufficient and well understood to prevent excessive distortion of the contact area and allow reliable numerical corrections to the raw data to be made. Polished diamond is the obvious choice for a substrate material, with a Young's modulus on the order of 1 TPa, while modern tilt stages such as the Physik Instrumente Hexapod systems offer vertical stiffnesses orders of magnitudes higher the system employed here. Finally, a more user-friendly system of alignment would deem to be necessary for wide spread adoption of the confined compression layer test. This could be accomplished via an automated routine wherein the stage tilt-angle is incremented until the maximum initial contact stiffness is achieved. The latest generation of nanoindenters, which may perform several indents per second when optimised, should make this possible. With these developments in mind, the potential exists for the confined layer test to become an integral component in the testing of material properties at the nanoscale.

The question of yield in glassy systems is still one of fundamental scientific interest, despite decades of research. From this perspective the techniques developed in this work to study yield in a stress controlled, pressure dominated environment should prove invaluable over the coming years. While the mechanical measurements presented here are of great value by themselves, modifications to the confined layer compression test could allow for direct measurement of the primary alpha relaxation times during deformation. Through use of a conductive tip and substrate, in-situ dielectric spectroscopy[10,11] could be performed, enable the effects of creep, yield and stress/strain on segmental mobility to be studied in a manner similar to the previous optical dye[12] and NMR[13] experiments in tension. This could greatly expand our knowledge on the subject of dense glass yield, particularly in compression, which remains and active, controversial topic[14–16].

The densification effect resulting from residual stresses in chapter four suggests the possibility of a new form of mechanical lithography. Up to now, thermal nanoimprint and most other mechanical forming techniques have focused on changing the

topography of the film in question, but not the local materials (a notable exception being the photocuring SFIL technique through a metalized transparent imprint die[17].) For properties sensitive to density and free volume content such as electrical conductivity in fluoropolymers, the stress memory effect explored here may allow for deterministic tuning at very small length scales. This work is currently ongoing and may bear fruition in the coming years.

The SAOSF technique refined in chapter five may considerable improve the thermal nanoimprint process. By reducing the degree of thermal cycling required, thermoelastic strains during demoulding are reduced, less wear occurs on the mold, and process times are decreased. The ideal implementation of SAOSF is not the plate-to-plate geometry used here, but rather in a roll-to-roll system. In such systems the mold is mounted to a roller and the contact times between substrate and mold are greatly reduced. The ability to improve pattern transfer over such short times via SAOSF would represent a great step forward in this respect. Future work on SAOSF should therefore focus on the engineering challenges associated with application of the technique to roller geometry.

Bibliography

1. Kim, J. W., Medvedev, G. A. & Caruthers, J. M. Observation of yield in triaxial deformation of glassy polymers. *Polymer (Guildf).* **54,** 2821–2833 (2013).

2. Lindsey, G., Schapery, R. A., Williams, M. L. & Zak, A. R. *The triaxial tension failure of viscoelastic materials*. (1963).

3. Ravi-Chandar, K. & Ma, Z. Inelastic Deformation in Polymers under Multiaxial Compression. *Mech. Time-Dependent Mater.* **4,** 333–357 (2000).

4. Qvale, D. & Ravi-Chandar, K. Viscoelastic characterization of polymers under multiaxial compression. *Mech. Time-Dependent Mater.* **8,** 193–214 (2004).

5. Ward, I. M. & Hadley, D. W. *An Introduction to the Mechanical Properties of Solid Polymers*. (John Wiley & Sons, 1993).

6. Lee, H. N., Riggleman, R. A., De Pablo, J. J. & Ediger, M. D. Deformation-induced mobility in polymer glasses during multistep creep experiments and simulations. *Macromolecules* **42,** 4328–4336 (2009).

7. Oliver, W. C. & Pharr, G. M. An improved technique for determining hardness and elastic modulus using load and displacement sensing indentation experiments. *J. Mater. Res.* **7,** 1564–1583 (1992).

8. Oliver, W. C. & Pharr, G. M. Measurement of hardness and elastic modulus by instrumented indentation: Advances in understanding and refinements to methodology. *J. Mater. Res.* **19,** 3–20 (2004).

9. Uchic, M. D., Dimiduk, D. M., Florando, J. N. & Nix, W. D. Sample dimensions influence strength and crystal plasticity. *Science* **305,** 986–9 (2004).

10. Kummali, M. M. *et al.* Local mechanical and dielectric behavior of the interacting polymer layer in silica nano-particles filled SBR by means of AFM-based methods. *Polymer (Guildf).* **54,** 4980–4986 (2013).

11. Schwartz, G. A. *et al.* Broadband nanodielectric spectroscopy by means of amplitude modulation electrostatic force microscopy (AM-EFM). *Ultramicroscopy* **111,** 1366–1369 (2011).

12. Lee, H.-N., Paeng, K., Swallen, S. F. & Ediger, M. D. Dye reorientation as a probe of stress-induced mobility in polymer glasses. *J. Chem. Phys.* **128,** 134902 (2008).

13. Loo, L. S., Cohen, R. E. & Gleason, K. K. Chain mobility in the amorphous region of nylon 6 observed under active uniaxial deformation. *Science* **288,** 116–9 (2000).

14. Roth, C. B. Mobility and stability of glasses. *J. Polym. Sci. Part B Polym. Phys.* **48,** 2558–2560 (2010).

15. Argon, A. S. *The physics of deformation and fracture of polymers*. (Cambridge University Press, 2013).

16. Roth, C. B. *Polymer glasses*. (CRC Press, 2016).

17. Colburn, M. *et al.* Step and flash imprint lithography: a new approach to high-resolution patterning. in (ed. Vladimirsky, Y.) **3676,** 379 (International Society for Optics and Photonics, 1999).

Appendix 1:
Background subtraction and density measurement in scanning transmission x-ray microscopy

In chapter four scanning transmission x-ray microscopy was used in conjunction with AFM to determine the relative density increase in polystyrene films due to flat punch indentation. Largely following the methodology of *Watts* et al[1]., a complication is introduced due to the presence of the Si_3N_4 supporting window. This brief appendix will show how the effect of this window is removed and shall provide a more detailed description of how relative density is calculated.

For a single component system, the optical density *OD(E)* is calculated using the initial intensity $I_0(E)$ and the transmitted intensity I_T via the Beer-Lambert law. With knowledge of the sample thickness *h,* the absorption coefficient *A(E)* may be determined:

$$OD(E) = -\log\left(\frac{I_T}{I_0}\right) = Ah \qquad (A1.1)$$

Where E is the photon energy. For the two-component system considered here, consisting of the 203 nm polystyrene film and the Si_3N_4 window, an effective one-component optical density OD_{eff} may be determined by measuring the beam with the sample absent and in place over a spectrum of energies. These intensities are plotted as functions of photon energy in figure A1.1 (a) and (b) respectively. OD_{eff} is computed using equation A1.1 and is plotted in red in (c).

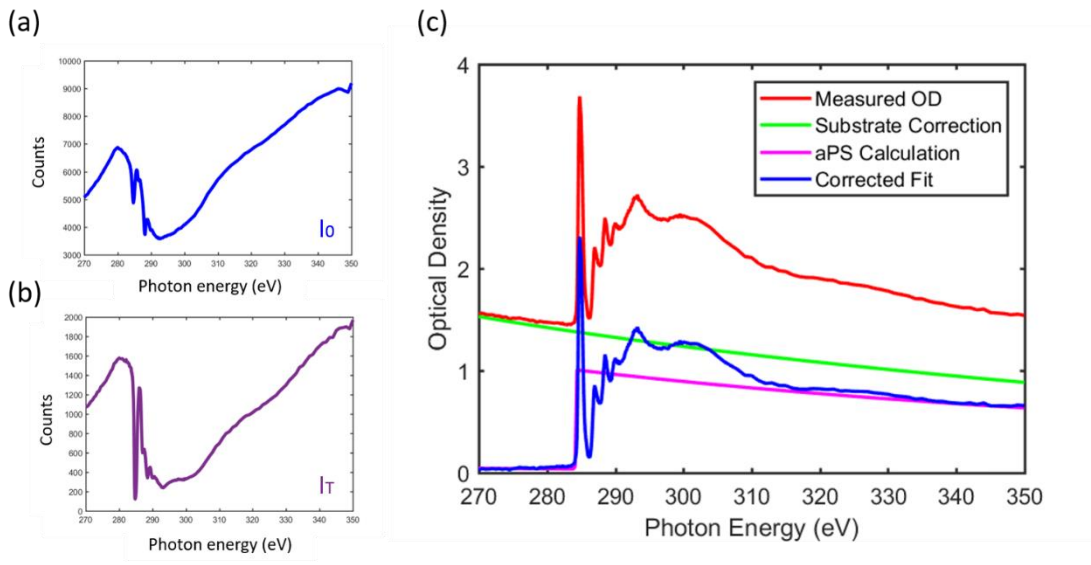

Figure A1.1 (a) Beam intensity as a function of photon energy measured with the sample removed. (b) Transmitted beam intensity as measured with the sample in place, over an unindented region. (c) Optical density spectrums obtained from (a) and (b). Red: The total effective optical density of the system. Green: Calculated Si_3N_4 optical density. Magenta: Calculated PS. Blue: Measured PS corrected for Si_3N_4 window.

Measuring the optical density of the polystyrene film exclusively is required to determine relative mass density changes. For a layered system the *OD*'s of the individual components are additive:

$$OD_{eff} = OD_{Si_3N_4} + OD_{PS} \qquad (A1.2)$$

OD_{Si3N4} may be accurately approximated through atomic scattering calculations. The primary interactions of soft x-rays with matter outside of absorption regions are cohesive elastic scattering and photoabsorption[2]. They are described using the atomic scattering factor $f = f_1 + if_2$. The atomic photoabsorption cross section μ_a is obtained from f_2 via:

$$\mu_a = 2r_0\lambda f_2 \qquad (A1.3)$$

Where r_0 is the atomic radius and λ the photon wavelength. The optical density of a sample of thickness h is therefore given by:

$$OD = n\mu_a h \qquad (A1.4)$$

Where n is the number of atoms per unit volume in the material. Using equation A1.4 and the scattering coefficients measured by *Henke*[3], approximations for OD_{Si3N4} and OD_{PS} may be computed. There are plotted as the green and magenta lines in figure A1.1 (c) respectively. While the fine structure of the polystyrene spectrum is missing in the

calculated case, it matches well with the window-corrected PS curve (blue) at off-resonance energies. To allow for some etching of the Si_3N_4 window, its thickness was calculated by setting the thickness of the polystyrene film to 203 nm (as measured) and fixing the blue and magenta curves at the pre and post absorption energies of 275 eV and 345 eV. This yielded a window thickness of 183 nm, physically reasonable for a pre-etch thickness of 190 nm.

The above background correction process yields OD_{eff} and OD_{Si3N4} as function of photon energy. These quantities are both used in the calculation of relative mass density around the indents. When an image of an indent is taken, an I_T map is produced. To calculate I_0, a mean intensity $I_{T_{mean}}$ is measured away from the indent and combined with OD_{eff} via:

$$I_0 = I_{mean} \exp\left(OD_{eff}\right) \tag{A1.5}$$

This I_0 is then used in conjunction with measured I_T map and OD_{Si3N4} to calculate the local optical density map OD_{local}:

$$OD_{local} = -\log\left(\frac{I_T}{I_0}\right) - OD_{Si_3N_4} \tag{A1.6}$$

This optical density map can then be divided by the AFM image to produce an absorption coefficient map at the scan photon energy, typically 384.8 eV. This method of producing local optical density maps effectively normalises the mean absorption coefficient of each individual scan to that which would be obtained from the blue line in figure A1.1 (c). However, as all scans are relatively close together (the indent array is 60 x 60 µm in total area) and have all been subjected to the same history, no significant deviation is expected between areas, meaning this approach remains valid.

Bibliography

1. Watts, B., Warnicke, P., Pilet, N. & Raabe, J. Nanoscale measurement of the absolute mass density of polymers. *Phys. status solidi* **212,** 518–522 (2015).

2. Hubbell, J. H. *et al.* Atomic form factors, incoherent scattering functions, and photon scattering cross sections. *J. Phys. Chem. Ref. Data* **4,** 471–538 (1975).

3. Henke, B. L., Gullikson, E. M. & Davis, J. C. *X-Ray Interactions: Photoabsorption, Scattering, Transmission, and Reflection, E = 50 - 30,000 eV, Z = 1 - 92*. (1993).

Appendix 2:
Commonly Performed Indentation Procedures & Experimental Details

In the course of this work there are a number of commonly performed indentation operations which merit greater discussion than could be provided for in the content chapters. Principle amongst these are the creation of the 'peak stress' indent arrays, arrays of indents where each subsequent indent is loaded to a greater peak load/stress. Such an array created on a 190 nm PS film yielded the data contained in figures 3.4.3 and 3.4.4 in chapter 3, while a similar 25 indent array was used for the STXM studies in chapter 4. The workflow for the creation of these arrays is detailed here.

As well as this, the issue of reproducibility of stress-strain curves is discussed, for tests in the same film, and for tests into two equivalent (same production history) films. AFM data is provided for the thermal history experiments of section 4.4.1, showing how a near-identical flat punch film surface misalignment angle was obtained for both sets of tests. Finally, thermal drift data is included for the creep experiments of section 4.4.2.1.

A2.1 Peak stress indentation array creation

As was mentioned above, peak stress arrays are used to explore the CLCT geometry in both chapters 3 and 4. The basic process for the creation of such an array is detailed below:

- First, as in standard indentation of a supported thin film to a fixed maximum load, the sample must be mounted to the indenter stub and aligned to the flat punch, as described in section 2.1.2
- Following alignment, a custom 'peak stress indentation recipe/program is created. Whereas in conventional indentation the maximum load L_{max} for a test is specified, in this case an incremental load L_i is input, with each subsequent indent in the sequence being to a load L_i greater than the previous.
- The maximum load for each individual indent in the array is then given by the loop:

$$while\ i\ \leq n;$$
$$L_{max}\ = Li = (i-1) * Li \qquad (A2.1)$$

Where i is the current indent number and n is the total number of indents to be performed in the array. i is automatically incremented by the indenter software upon completion of each indent.

- Following this, the desired location of the indents is entered via the nanoindenter software. By varying L_i and n, the desired maximum load and load resolution may be chosen. An example of load-displacement curves produced by such a process is shown in figure 3.4.4 (a), while and AFM image of such an array is shown in figure 4.3.2 (b).

A2.2 Reproducibility of stress-strain curve in the same film.

While the peak stress configuration stress-strain curves shown in figure 3.4.4 generally show the consistency of the test over multiple indents into a single film (all curves lie on top of each other), it is useful to demonstrate that this reproducibility is achievable to the same max load, and that it does not merely apply to the 190 nm PS film. Figure A2.1 shows two load displacement curves for indents into films of 190 nm, 240 nm, and 300 nm thickness all loaded at the same rate (0.67 mN/s) and to the same maximum load (3.5 mN) with the 2050 nm diameter flat punch used in chapter 3. Surface detection was performed by monitoring the load and displacement hardware channels and determining contact to be when the slope of these two channels was greater than 50 N/m. Drift rates for all test were below 0.05 mN/s, and as the loading portion of each test was approximately 5 seconds, it can be assumed to be minimal. In each film the two indents were approximately 50 microns apart. As can be readily seen, the load displacement curves lie directly on top of each well to well past the extrusion limit, with excellent agreement between slopes and yield point. As such, the reproducibility of the test within the same film is confirmed.

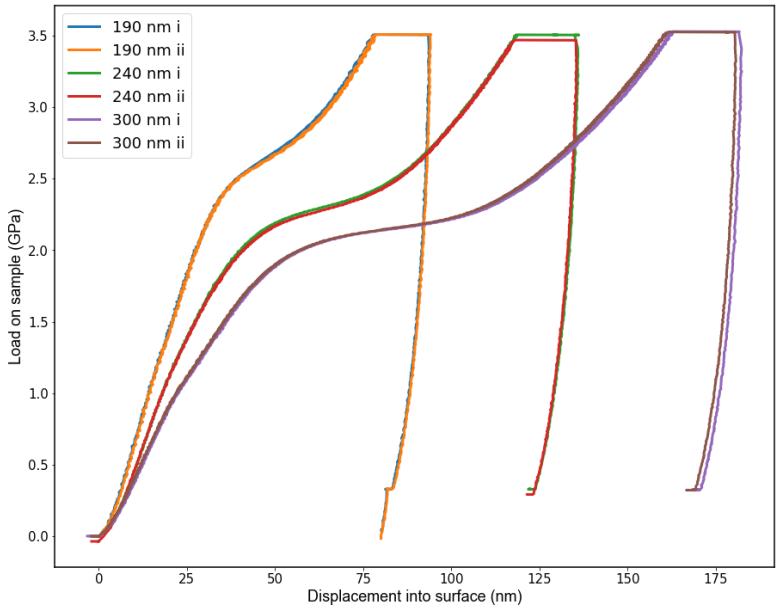

Figure A2.1 Load displacement curves for falt punch indentations into polystyrene films of thicknesses 190, 240, and 300 nm. As two curves exist for each thickness and sit directly on top of each other, the reproducibility of the test is confirmed.

A2.2 Reproducibility of stress-strain curve in different films

For the CLCT to be adopted as a standard test stress-strain curves and therefore constitutive behaviour, most be reproducible for similarly prepared samples. While this was not studied in detail in this work, some data indicating that this is the case is available and presented in figure A2.2. 300 nm amorphous selenium films were prepared on silicon and diamond substrates by physical vapour deposition by collaborators at Texas Tech University. Both samples have the same thermal history and were mounted to the same indenter stub via crystal bond. Indentations were preformed to a maximum load of 5 mN at a rate of 0.67 mN/s using the 2050 nm diameter punch. Following background stiffness corrections of approximately 120,000 mN for the silicon sample and 600,000 mN for the diamond (see section 3.4.2 for details) the stress-curves of figure A2.2 were obtained. Both samples show good agreement in the confined elastic and plastic zones, with yield occurring at approximately 0.55 GPa in both cases. Some divergence is noted at extrusion, however this is likely due to the Se-diamond and Se-silicon boundaries having different interaction properties and promoting stick, slip, or delamination. Unfortunately no misalignment angle data is available for this data set.

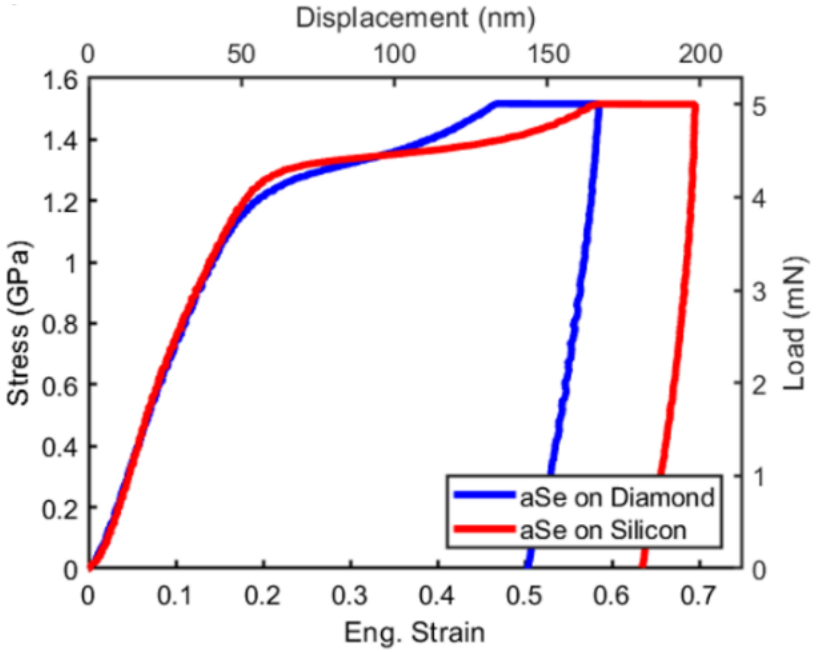

Figure A2.2 Stress-strain curves for 300 nm amorphous selenium films on diamond and silicon substrates. Following the substrate stiffness correction the two curves match well in the confined limit, with difference at extrusion likely emerging from the altered film-substrate boundary.

A2.3 Replication of indentation conditions following thermal cycling

As was detailed in section 4.3.1, an involved procedure was undertaken to ensure that no significant change to the mechanical support environment occurred between removing and replacing the 550 and 670 nm polystyrene films from the indenter for the anneal/quench heating processes. Central to this process was ensuring this mechanical reproducibility was ensuring that there was no significant change in the punch face to sample surface misalignment angle. This was accomplished via tapping mode AFM and adjustments of the tilt stage, as described in section 2.1.2. Presented in figure A2.5 are AFM micrographs of indents into the annealed (a) and quenched (b) films following realignment and using the 4,800 nm diameter punch. The angle of greatest misalignment is the vertical axis of the scans and the direction of the profiles displayed in (c) are indicated by arrows. In both cases the angle of misalignment (taken by evaluating the height of the two punch edges) is approximately 0.1°. As such, changes in mechanical response could be attributed to changes in the material behaviour due to the thermal ageing process, and not changes in tilt angle.

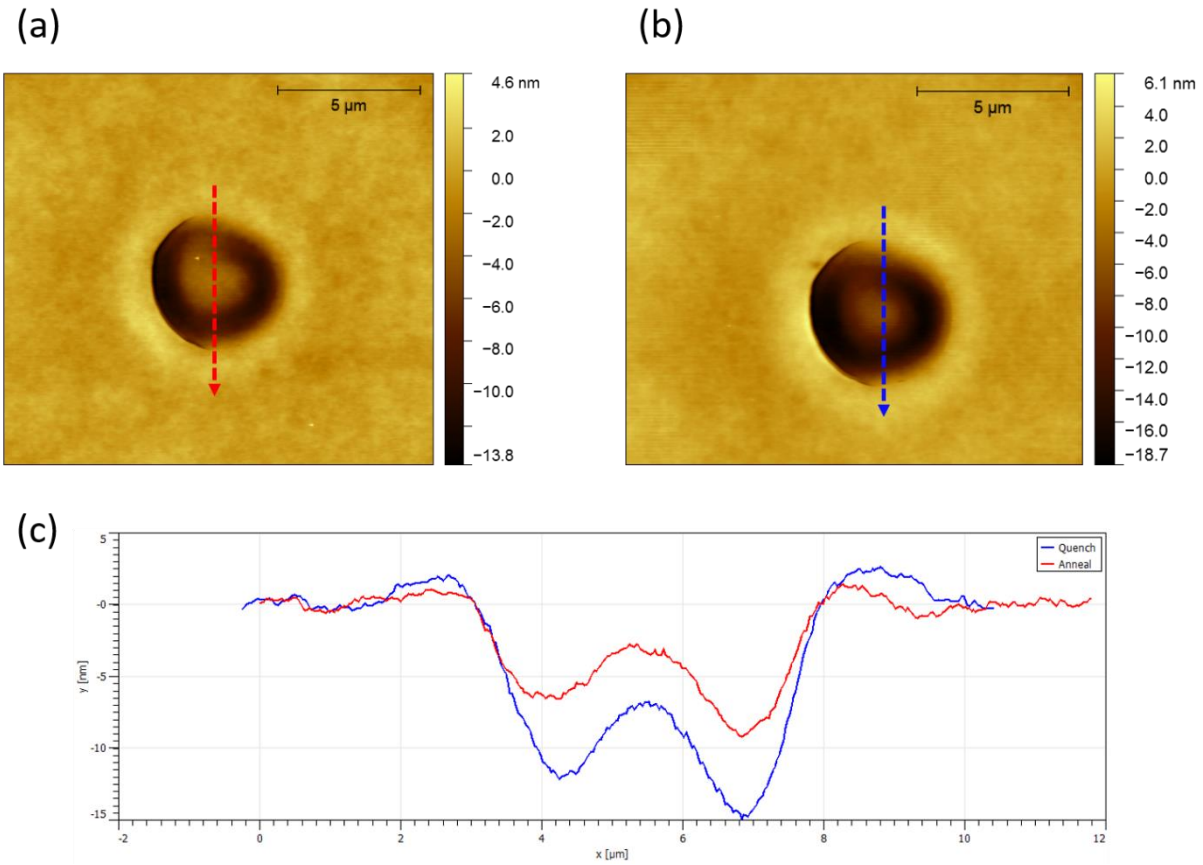

Figure A2.5 Misalignment angle between punch face and film surface for the 550 nm atactic polystyrene film considered in chapter four. (a) AFM micrograph of an indent into the annealed film following successful alignment. (b) Equivalent image for the same film following the quench thermal history. (c) Line profiles of the indents taken from (a) and (b). The arrows in those images indicate the directions in which the profiles were taken. In both cases, a misalignment angle of approximately 0.1° is observed

A2.4 Thermal drift measurements during creep compliance testing

Within section 4.4.2.1 creep compliance data is presented for indents into a 550 nm quenched atactic polystyrene film performed with a 4,800 nm diameter flat punch. The method for determination of thermal drift is discussed, however no data on the magnitude of drift with respect to the applied creep stress nor in the context of the total creep displacement is provided. This data is shown below in figure A2.4. Figure A2.4 (a) shows the measured drift rate as a function of the applied creep stress over a range of 0.1 – 0.5 GPa. No strong dependence of the applied creep stress is observed, indicating that the two quantities have been successfully decoupled. Drift appears to be relatively stable across all tests, falling between the limits of -0.04 and 0.04 nm/s. Figure A2.4 (b) presents a plot of the total displacement of the indenter during the creep

step as a function of the applied creep stress, as well as an equivalent drift displacement. This latter quantity is the measured drift rates of figure A2.4 (a) multiplied by 100 seconds, the duration of the creep step. This measurement helps to provide a sense of the impact of the drift correction on the total reading. As can be seen from (b), the equivalent drift is always smaller than the total creep displacement and is essentially insignificant at high loads.

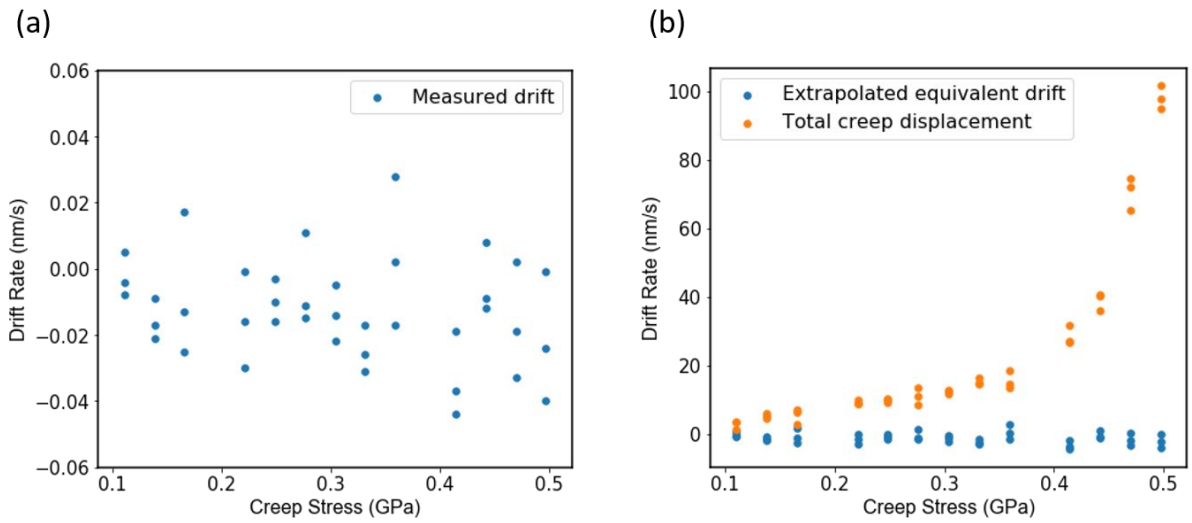

Figure A2.4 (a) Measured thermal drifts for indentations into a 550 nm thermally quenched polystyrene film on silicon, as obtained via the procedure outlined in section 4.4.2.1. Drift appears unaffected by the applied creep stress, indicating that it has been successfully decoupled from the creep measurement. (b) Total creep displacement as a function of applied creep load during the 100 second creep step (orange). Extrapolated equivalent thermal drift obtained by multiplying the values plotted in (a) by 100 seconds. Drift is typically much smaller than the total measured displacement.